DOE/CS/05315-1

A 50 kWp PHOTOVOLTAIC CONCENTRATOR APPLICATION EXPERIMENT: PHASE I

Final Report for June 1, 1978—February 28, 1979

By
H. J. R. Maget

June 15, 1979

Work Performed Under Contract No. ET-78-C-04-5315

Varian Associates, Inc.
Palo Alto, California

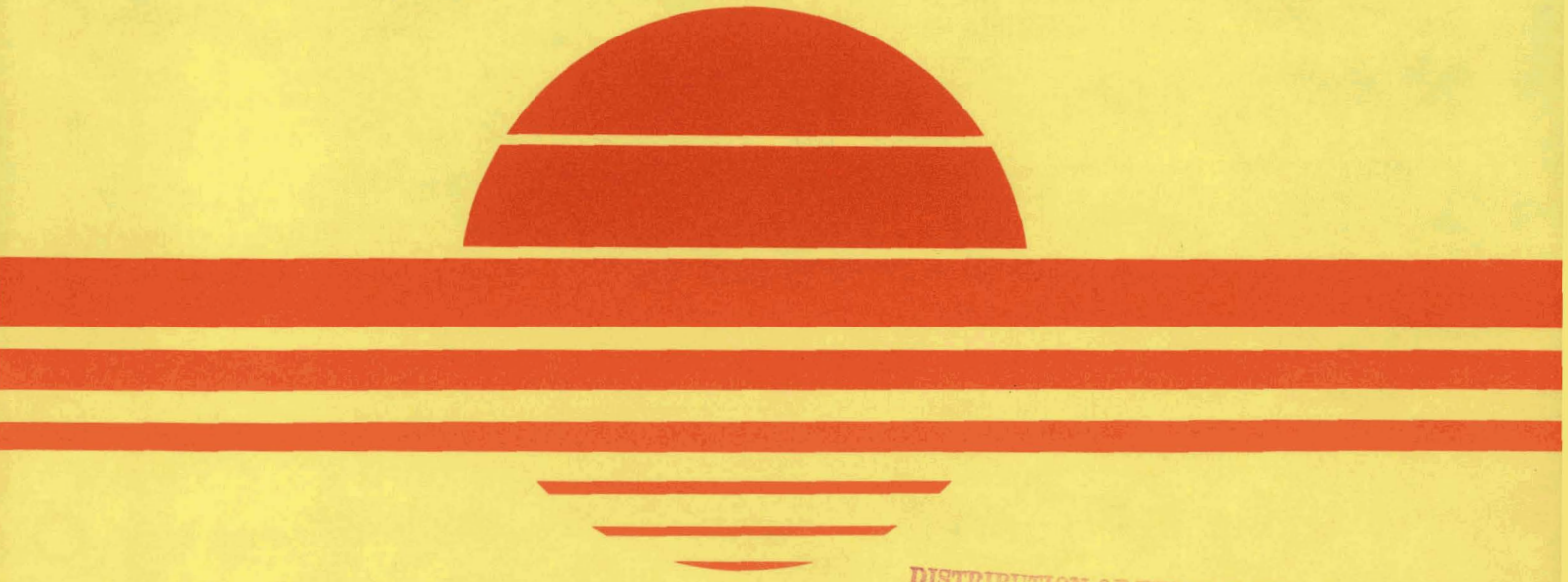

U.S. Department of Energy

Solar Energy

DISCLAIMER

NOTICE

Available from the National Technical Information Service, U. S. Department of Commerce, Springfield, Virginia 22161.

Price: Paper Copy $10.75
Microfiche $3.00

DOE/CS/05315-1
Distribution Category UC-63d

A 50 kWp PHOTOVOLTAIC CONCENTRATOR APPLICATION EXPERIMENT

PHASE I

APPROVED
FINAL REPORT

FOR THE PERIOD

1 JUNE 1978 TO 28 FEBRUARY 1979

H. J. R. MAGET

JUNE 15, 1979

WORK PERFORMED UNDER CONTRACT
ET-78-C-04-5315

VARIAN ASSOCIATES, INC.
611 HANSEN WAY
PALO ALTO, CA 94303

FOREWORD

This report presents the results of a Phase I design study of a 50 kWp photovoltaic concentrator application experiment, performed under DOE Contract ET-78-C-04-5315 with the Division of Solar Technology through the Albuquerque Operations Office. The program was monitored by Division 5719 of Sandia Laboratories, Mr. Eldon Boes and Mr. E. Burgess, project monitors. The performance period of Phase I was June 1st 1978 through February 28th 1979.

The prime contractor was Varian Associates, Inc., Palo Alto, CA in association with the operator of the experiment, Pacific Gas & Electric Company, San Ramon, CA. Subcontractors on this program were Nielsen Engineering and Research, Mountain View, CA, and Optical Sciences Group, San Rafael, CA. The program manager at Varian was H.J. R. Maget. Contributions were made by B. R. Cairns, L. W. James, R. L. Moon, H. Vander Plas, M. Nowak, R. L. Bell, O. Moore, and others of Varian; J. T. Wells, T. Hillesland, of PG&E; S. MacIntosh, R. Reed, and W. Miller of Nielsen; and J. K. Williams and J. R. Egger of Optical Sciences.

SUMMARY

Work carried out under DOE contract ET-78-C-04-5315, "A 50-kW Photovoltaic Concentrator Application Experiment--Phase I," is described. This Phase I program consisted of a design study and component development for an experimental 50-kWp photovoltaic concentrator system to supply power to the San Ramon substation of the Pacific Gas and Electric Company. The design team was PG&E (site installation, power conditioning, and utility interface) Nielsen Engineering (mechanical and thermal subsystems) Optical Sciences (lens design and fabrication) and Varian Associates (program management, system design and component development).

The photovoltaic system is optimized to produce peaking power to relieve the air conditioning load on the PG&E system during summer afternoons, and would therefore displace oil-fired power generation capacity. No electrical storage is required. The experiment would use GaAs concentrator cells with point-focus fresnel lenses operating at 400X, in independent tracking arrays of 440 cells each, generating 3.8 kWp. Fourteen arrays, each 9 feet by 33 feet, are connected electrically in series to generate the 50 kWp. The high conversion efficiency possible with GaAs concentrator cells results in a projected annual average system efficiency (AC electric power output to sunlight input) of better than 15%. The capability of GaAs cells for high temperature operation made possible the design of a total energy option, whereby thermal power from selected arrays could be used to heat and cool the control center for the installation.

Active water cooling of the cells was evaluated as most cost effective, with the cooling water for each array being stored in a collection of 55-gallon barrels for heat dissipation by radiation and convection over the entire 24 hours, including cool nights characteristic of the site. Detailed modeling was carried out for this system, using a model climatic year for the site, assembled from available local data and the actual obscuration conditions of the site. Using average cell conversion efficiencies of 21% typically achievable with earlier designs of GaAs concentrator cells, the model predicts generation of 100,000 kWH/year of electrical energy, with an average conversion efficiency of 15.8% as installed. An additional 280,000 kWH of thermal energy is discarded.

A revised design of solar cell, heat sink and package was required by limited performance of the optics, and by considerations of reliability in assembly and low-maintenance operation of the system. At the same time, fabrication processes for the cells were redesigned for scaleup of throughput by a factor of fifty to meet cell production objectives for the Phase II installation program. A number of engineering problems were encountered in these combined changes as a result of which development of the cell was not completed by the end of the Phase I program. These problems are in process of solution, but conversion efficiencies of the evolving "production" cell design had not exceeded 19.5% at 400 suns by the end of the program.

Independent control systems for the power conditioning unit and for each array of the photovoltaic system were evaluated as most cost effective for the experiment. The array control system is based on a lowcost microprocessor (Intel 8022) which controls the tracking, array status monitoring, and fault reaction functions. Extensive optimization of the fresnel lens design, the revised cell design, the thermal subsystem, and the site layout are reported, including interactions between the lens and cell designs. The required tracking accuracy derived from these studies was 0.2 degrees rms. The supporting tracking array structure, fabricated from large diameter thin wall tubular steel members, was designed for combined static and dynamic deflections (gravity and 30 mph wind loading) 0f 0.17 degrees in the worst case. The system is stowed for steady winds above 30 mph, and will survive 90 mph stowed. An optimized interconnection scheme for the 6160 cells of the system was devised, with series-paralleling and protective diode incorporation, resulting in series grouping of 560 sets of 11 cells in parallel (110 amps at 50 volts).

Materials costs of $257/sq.m. or $1.70/peak watt were estimated for the design, using standard materials costing for large scale production where applicable. Detailed costing studies showed that for the 50-kWp experiment, materials costs (mainly solar cell and package) would amount to approximately $30/watt. At the 6-megawatt level, this is reduced to approximately $5/watt, with the cell and package accounting for only 20% of the total. Labor and overhead for assembly and installation represent a small fraction of the materials costs.

A detailed fabrication and installation schedule (Phase II) is presented. This embodies initial fabrication and testing of a prototype array, and subsequent design modifications as required. The complete 50-kWp installation with spares would require a 15-month program. A plan for operation of the system (Phase III) is outlined.

TABLE OF CONTENTS

TABLE OF CONTENTS (Continued)

TABLE OF CONTENTS (Continued)

TABLE OF CONTENTS (Continued)

FIGURES-CAPTIONS LIST

FIGURES-CAPTIONS LIST (Continued)

FIGURES-CAPTIONS LIST (Continued)

1.0 INTRODUCTION

This report describes a design study for a 50 kWp photovoltaic concentrator system to supply power to a utility substation for redistribution to the utility's customers. The design team consisted of:

Pacific Gas and Electric Company (design of the site installation, power conditioning and utility interface);

Nielsen Engineering and Research (design of mechanical structures and thermal subsystems);

Optical Sciences Group (design and fabrication of fresnel lenses); and

Varian Associates (program management, system design, and component development).

The system (Fig. 1-1) is designed for installation on property owned by Pacific Gas and Electric Company (PG&E) adjacent to its San Ramon (California) substation. The substation is surrounded by a rapidly growing middle and upper income residential community supplied by distribution lines emanating from the substation. This base-line experiment is typical of a large number of applications for dispersed types of generation which can supply power directly to distribution customers at a time when their demand is highest. The connection of small solar generating plants to distribution circuits reduces losses in the transmission system.

The photovoltaic solar system, designed to deliver utility power only under conditions of insolation, consists of five main subsystems; collector, support and tracking, structure, thermal processing, power conditioning, and data acquisition subsystems. The solar system, specifically operating as an electric power generator, is not encumbered by thermal or electric storage subsystems. Such a design focuses attention on key elements, such as sun tracking, solar conversion efficiency, and utility interface.

Since the principal objections to photovoltaics are the high costs of the solar arrays, the approach here has been to explore the possibilities of attaining low life cycle energy costs for the arrays by exploiting the high efficiency and operating temperatures of GaAs concentrator cells. Cell costs themselves are lowered by using high concentration, which is therefore desirable as long as other costs (tracking, structural rigidity) are not driven up. The design considers

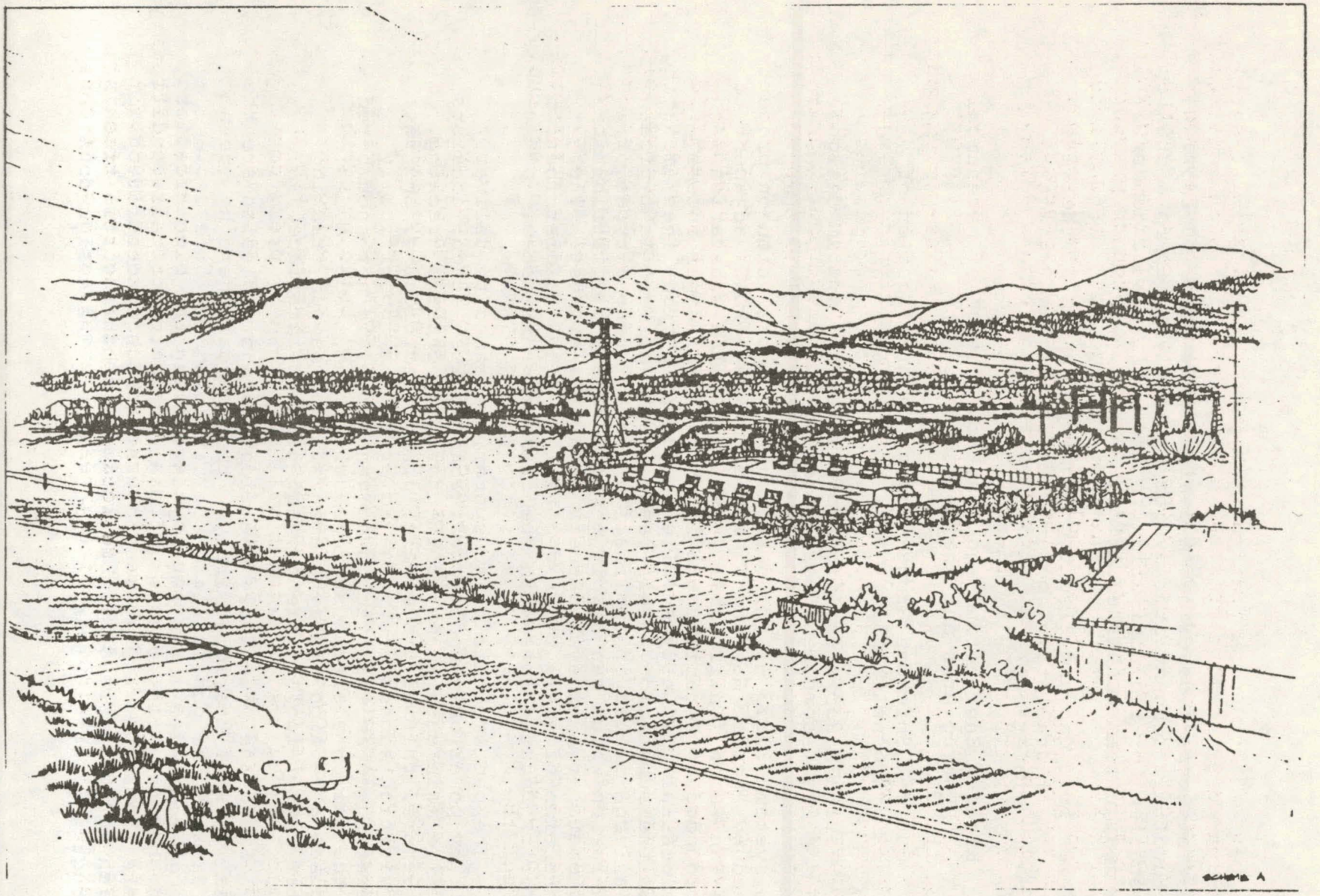

Fig. 1.1 Sketch of Site Installation

the use of high concentration (400:1 average) fresnel lenses, fabricated in acrylic, for the optics, together with moderately accurate tracking. Waste heat from the arrays is disposed of by means of a closed-loop cooling scheme, consisting of a grouping of low cost barrels. These barrels have cooling water circulated during daytime hours, and are covered to prevent solar heat gain. Much of the heat is dissipated by radiation and convection during the cool nights at the site location. Both the cooling pumps and the inverter are designed to minimize noise and since neither operate at night, noise-related environmental problems are avoided.

The output of the photovoltaic station is interfaced with the 21 kV distribution circuit through a line-commutated inverter and step-up transformer system. The load for the inverter will be PG&E's 21,000 volt distribution circuit, San Ramon 2102. The inverter design chosen incorporates maximum power tracking for any normal operating conditions. The distribution line can easily distribute the power generated by the station to its load; no on-site storage is planned.

The experimental site lies in a shallow valley 25 km inland and to the east of the San Francisco Bay. The site, on the east side of the substation, is part of a large field in an existing transmission-line right-of-way. An area of approximately 2.5 acres has been reserved for the photovoltaic arrays. Ranges of hills to the northeast and southwest rise approximately 6.6 degrees above the horizontal, and will not significantly obstruct the operation of the solar arrays. Transmission towers on the site, and the substation structures to the west, offer sparse obstructions which will not seriously affect the operation of the photovoltaic system.

The site, which would be accessible to visitors by prior arrangement with PG&E or Varian, is located within 5 km of PG&E's San Ramon Research Center, where other solar and energy conservation experiments are conducted. The research laboratory would be the staging point for initial briefing prior to site visit. The control building of the photovoltaic power system has facilities for viewing data gathering instrumentation and descriptive panels. Public visibility of the experiment will be served by press coverage and corporate public relation activities. The site is visible from Highway I-680.

A significant portion of the residential electrical consumption in the summer in this area is due to air conditioning loads. The summer daytime temperatures can exceed 100°F for several days each year. The local loads during this time peak in the afternoon. Often, heat waves affect most of the

PG&E system, requiring the use of relatively expensive means of generation to meet the electrical demand. An alternative energy source such as a photovoltaic system peaking in the summer months and during midday, has the potential of considerable generating capacity and of a high energetic value to the utility, of 3.4¢/kW-hr. The quality of the solar generated power must however be properly regulated and conditioned in order to avoid degrading the service supplied to the customers on the line. The experiment offers the opportunity to evaluate the performance of this type of generation in conjunction with an inverter and interface with a commercial power line. The design capacity of the photovoltaic system, up to 50 kW, is not expected to affect the utility rate structure or service capability, but will provide useful operating information during peak load conditions. The baseline experiment, as designed, would not make use of the thermal energy available from the photovoltaic concentrator systems. Options considered included the recovery of thermal energy for heating and cooling the control room of the photovoltaic power plant.

On November 2, 1978, the Contra Costa County Planning Department advised PG&E that a land use permit would not be required for the photovoltaic solar system in San Ramon. A building permit would be required for the control building.

In summary, the design considered offers the following features:

* A concentration experiment using a relatively new solar cell material, gallium arsenide.

* A high projected array efficiency: 15%

* The use of high concentration ratio (400/1) Fresnel optics.

* A self-contained system for each array, which allows considerable flexibility, including a total energy experiment in the form of heating and cooling of the site control center.

It also includes the following special problems:

* The location of the experimental site in a residential area with its associated environmental, architectural, and application problems.

* The introduction of substantial new technology, including the establishment of a GaAs solar cell pilot/production line.

2.0 SYSTEM ANALYSIS AND DESIGN

2.1 Overall System Description and Specifications

The following general system specifications were established to provide guidelines in developing the component and subsystem designs:

*	Power Rating:	50 kWp
*	Environmental conditions:	
	Temperature:	30 - 115°F
	Wind:	30 mph steady operation
		40 - 50 mph transient
		60 mph survival
	Precipitation:	San Ramon conditions
		of rain, hail.
*	Array Efficiency:	$\geq$ 15%
*	Solar Cell Technology:	GaAs
*	Meet Requirements of:	
		Industrial Electrical Standards,
		Environmental Impact.

The 50 kWp design consists of an array field of 14 identical arrays, each delivering 3.8 kWp DC power. Each array is self-contained, i.e., with independent tracking and heat rejection subsystems. Therefore, each array can operate independently from adjacent arrays or the total field. Electrical inter-array wiring (main bus bar, AC power, tracking and control power) connect the array with the control room where power inversion from a nominal 540 VDC at 100 amperes to 3ϕ, 60 Hz 480 VAC is performed. In subsequent operation, a step-up transformer brings the voltage to 21 kV, the line distribution voltage.

The system block diagram is shown schematically in Fig. 2-1. The system is capable of unattended operation under the environmental conditions encountered at the site, e.g., the arrays will assume a stowed position at high wind velocities. The annual

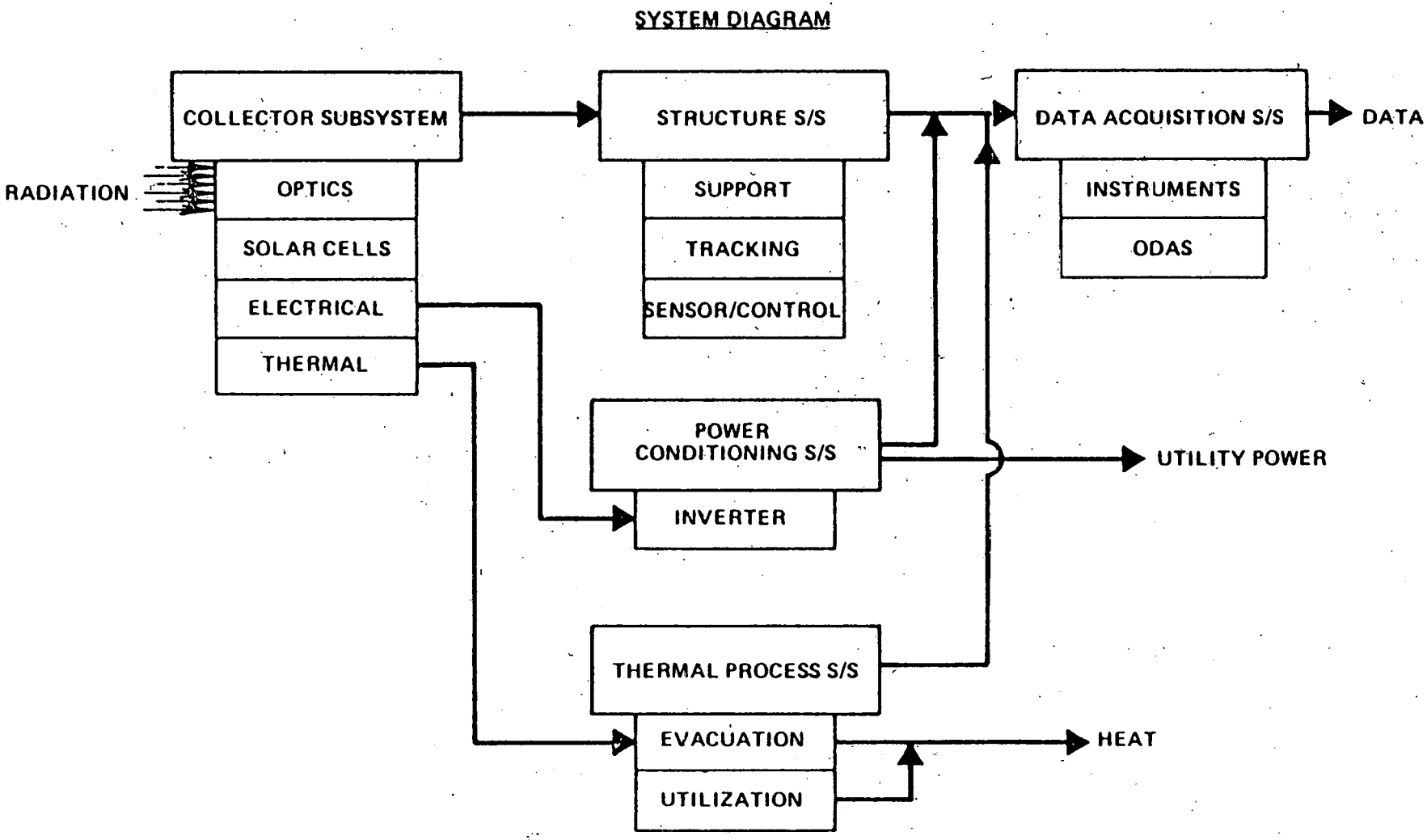

Fig. 2.1 System Block Diagram

AC electrical energy output is expected to be around 100,000 kWh. An additional annual thermal energy output of 280,000 kWh is discarded, since there is little local demand for this type of thermal energy.

The collector subsystem consists of hexagonal plastic Fresnel lenses designed to maximize array area utilization. Each array has 440 individual solar cell housings mounted in a honeycomb arrangement covering an area of about 295 ft^2. Troughs and manifolds on the tracking frame contain the electrical wiring and coolant piping. Water cooled solar cells are protected from the environment by a plastic housing.

A low cost distributed thermal subsystem (large heat transfer area) consisting of 55-gallon barrels is used to reject the thermal energy produced by individual arrays. Under conditions encountered at the site, the coolant temperature will not exceed 150°F. The parasitic energy requirements of the heat rejection system represent about 1% of the array electrical energy.

The solar cells, placed in 44 parallel modules of 10 cells each, are mounted on lightweight tracking frame capable of high pointing accuracy. The structural subassembly consists of a tubular H-frame (supporting all modules) connected to a Y-frame which also supports the elevation drive. Bearings for the Y-frame provide azimuth tracking. The complete structure is bolted to a reinforced concrete foundation. The tracking system has a calculated free play of less than 0.1° and a static deflection due to 30 MPH winds of less than 0.2°. Tracking power requirements are less than 12 watts/array. The power conditioning subsystem consists of a maximum power tracking inverter designed to operate with a variable input voltage of 100-650 VDC. The inverter DC-to-AC conversion efficiency is about 94% at loads above 25% of rated power. The data acquisition subsystem, in addition to meeting DOE established requirements, will also monitor one array specifically instrumented for studies of the distribution profiles of key parameters, component aging, response characteristics to transients, etc.

2.2 System Location

2.2.1 Site Topography - The actual topography of the experimental site is shown in Fig. 2.2. As shown, the location has a slight downward slope from north to south. Minimal land preparation is contemplated and the same slope topography will be followed. Figure 2-3 is a portion of the Diablo Quadrant U.S. Geological Survey map showing the location of the site.

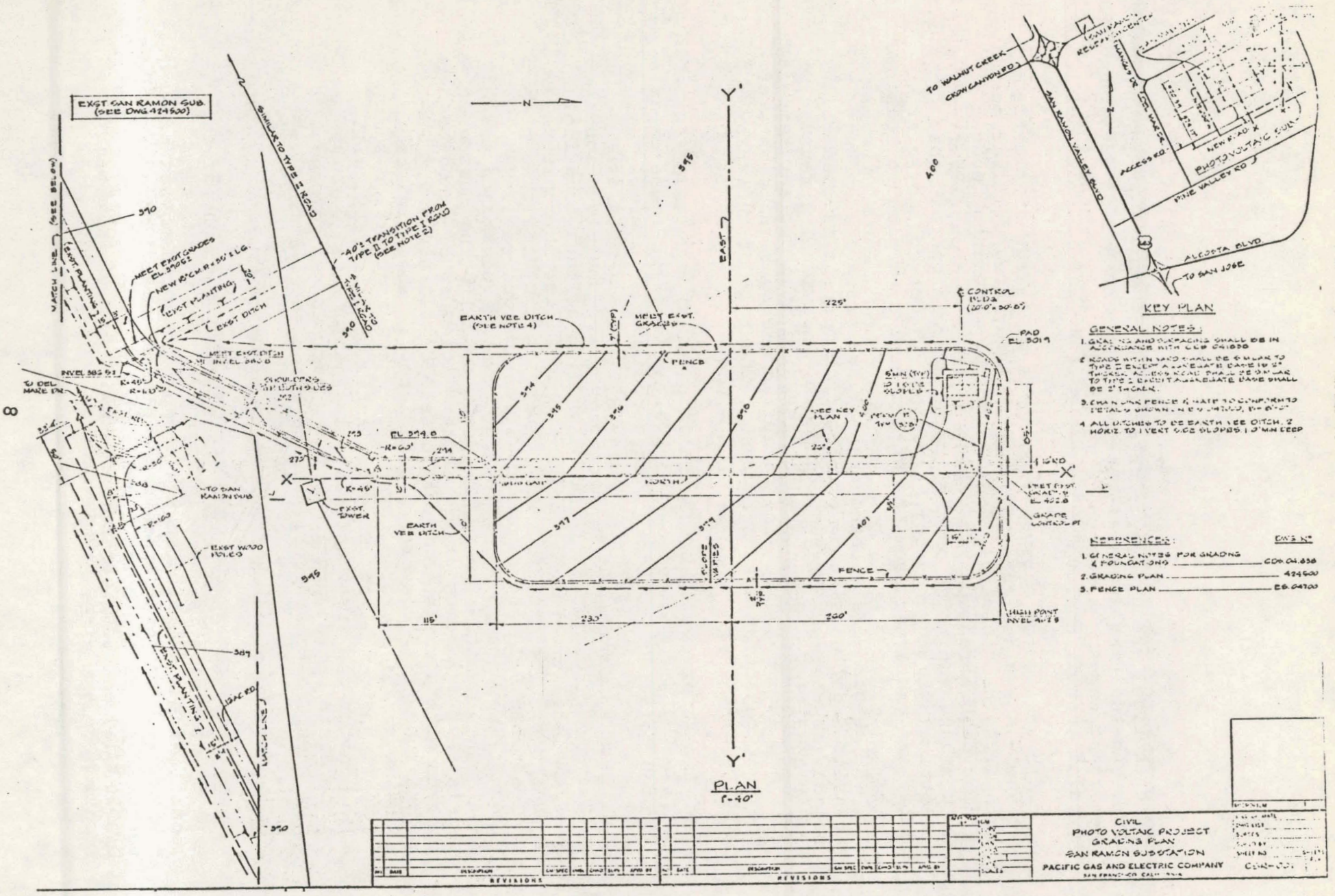

Fig. 2.2 Topography of the Photovoltaic Site

Fig. 2.3 Diablo Quadrant Showing Site of Experiment and PG&E Research Center

2.2.2 Array Field Layout - Several different locations for the 14 arrays within the site boundaries were studied. A north-south orientation was selected for this particular experiment so that shadowing from nearby arrays could be minimized. The large size of the vacant field allowed this orientation without the normally encountered constraints of a layout parallel with existing roadways and property line boundaries. Figure 2-4 shows the site layout. The original design utilized slightly more than one acre, but since land for this particular experiment was available, the arrays were spaced further apart to further reduce the effects of shadowing.

2.2.3 Site Preparation Requirements - Minor grading would be conducted to minimize overland storm drainage into the site. Drainage from the site and the surrounding area is designed to return to its natural drainage path. Cut and fill earthwork banks are designed to minimize erosion. The site yard surface is finished with 4" thickness of aggregate base material to reduce erosion, weed growth, dust, and afford a firm surface to allow access to equipment by light vehicles and maintenance personnel.

A paved roadway, consisting of 2" thickness of asphalt concrete over 6" of aggregate base, would be installed to allow access during inclement weather. Also, a paved area is designed for vehicular parking, vehicle turnaround and equipment.

2.2.4 Site Restrictions - Very few site restrictions exist for this particular location. The arrays and control building have been designed to blend aesthetically with the surrounding neighborhood. Noise emissions from the experiment were a concern during design stages, because of the nearby residential neighborhood. This restriction prevented the use of a cooling tower for waste heat disposal. No site size restrictions were encountered because of the use of a wide vacant transmission line corridor. Design considerations applicable to smaller sites are outlined in Appendix C.

2.3 Local Meteorological Conditions

Data for the site were drawn from the following sources: the 8-year record of the U.S. Weather Bureau at Livermore, CA, the 10-year hourly records of the FAA West of Livermore, recent discontinuous 3-year records from Sandia Livermore, and a few measurements from the Aerojet-General San Ramon site. This data was combined to yield a model climatic year shown in Figs. 2-5 through 2-7. The average model temperature is 18°C compared with the expected average of 15°C. On the

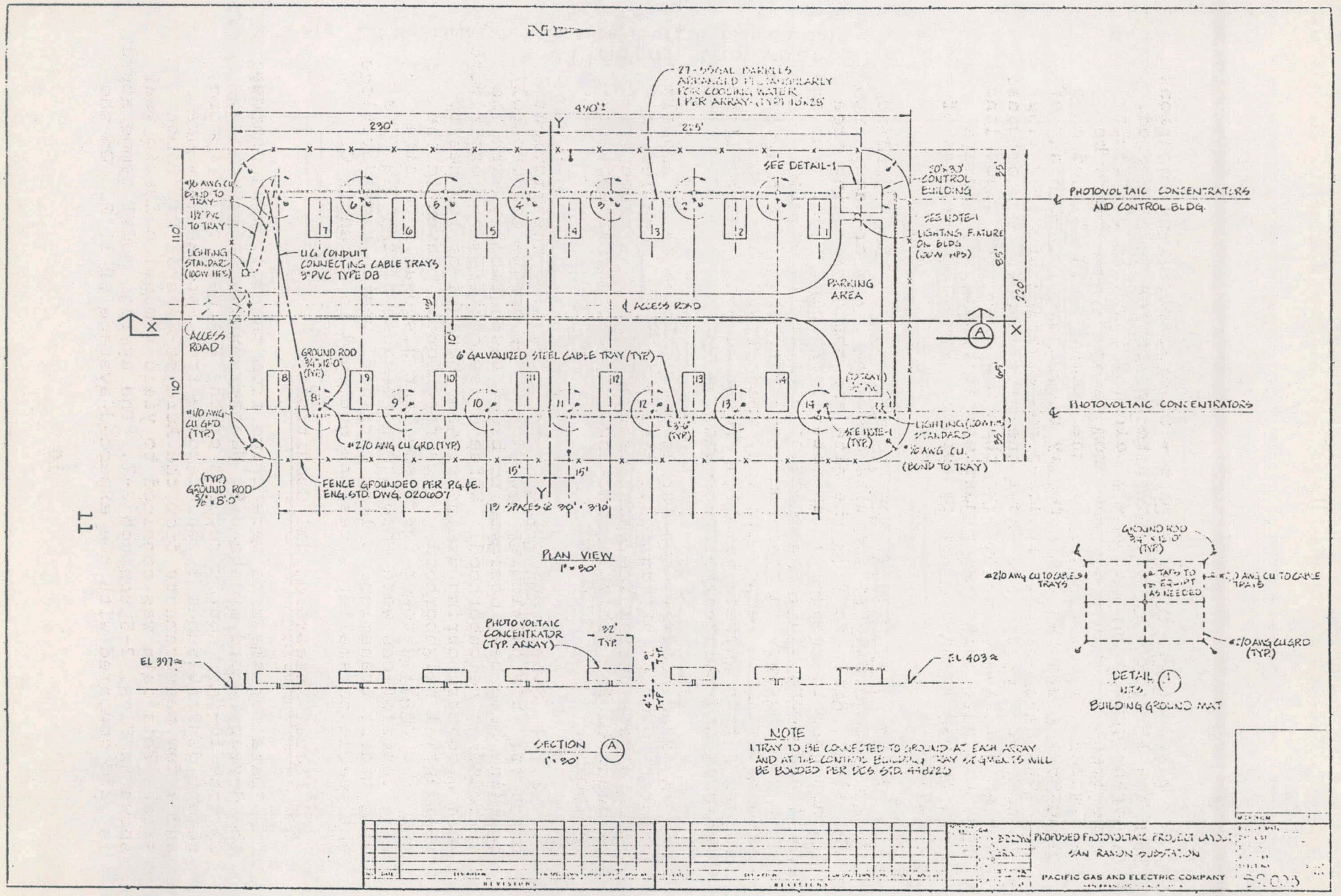

Fig. 2.4 Photovoltaic Project Layout

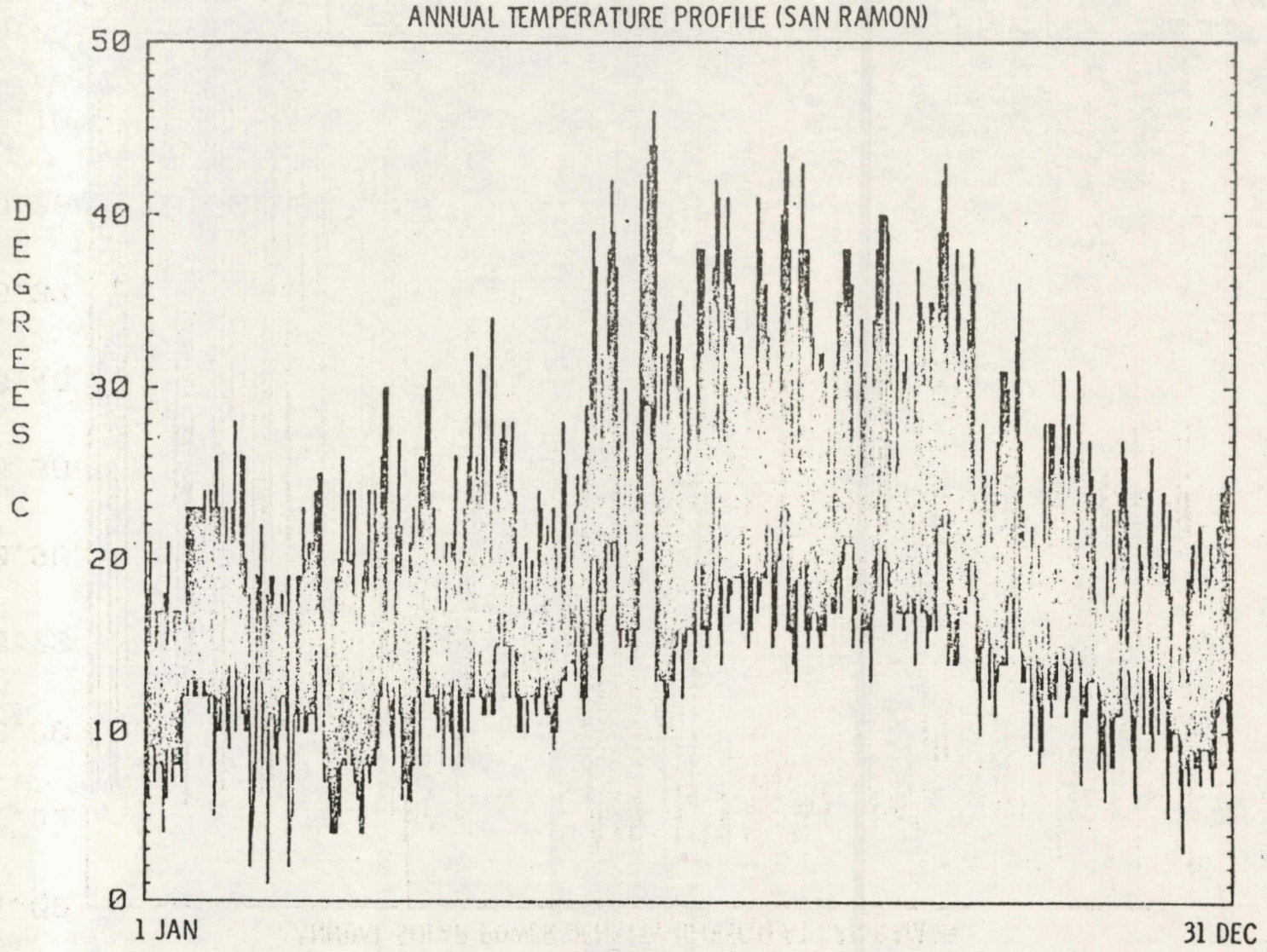

Fig. 2.5 Annual Temperature Profile (San Ramon)

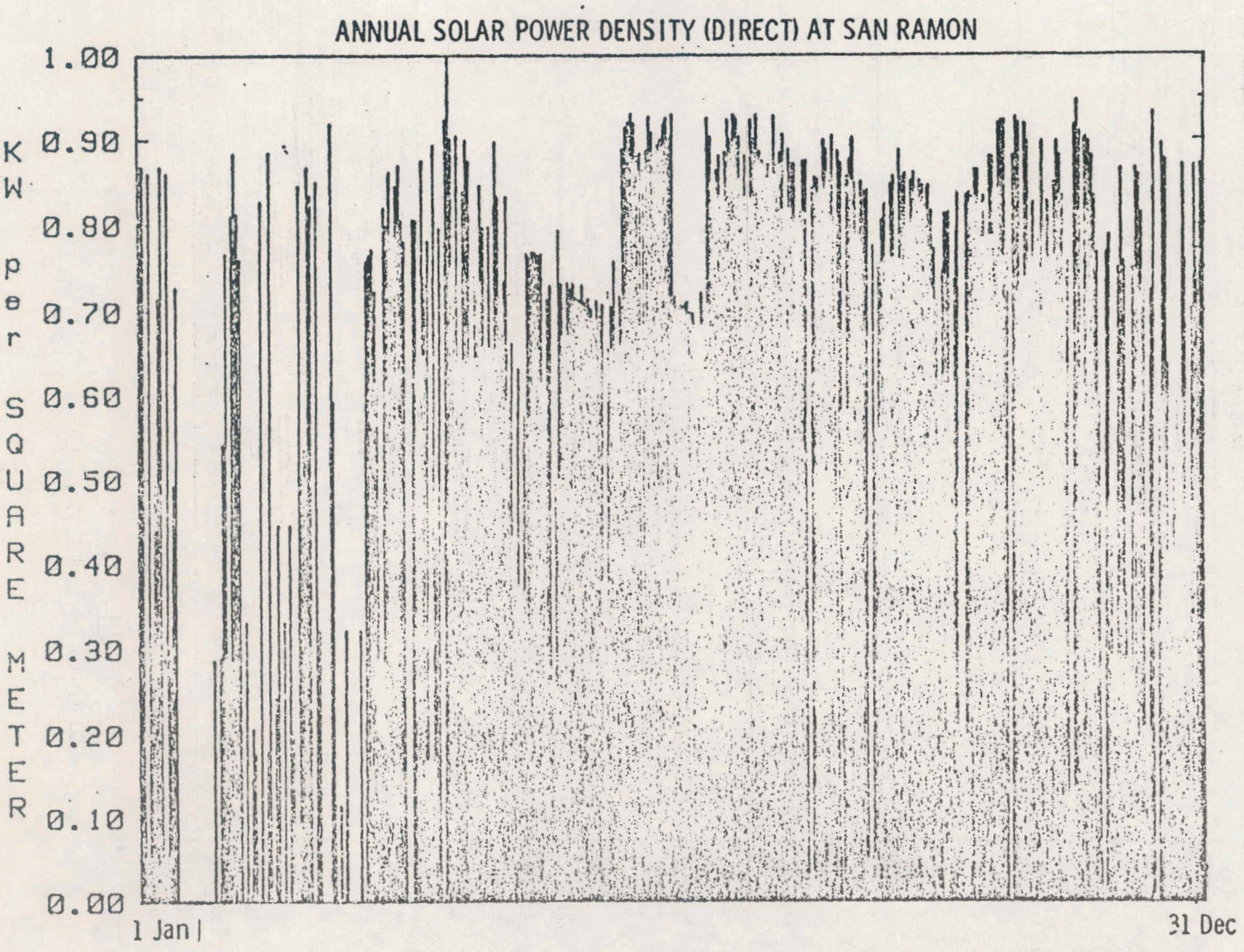

Fig. 2.6 Annual Solar Power Density (Direct) at San Ramon

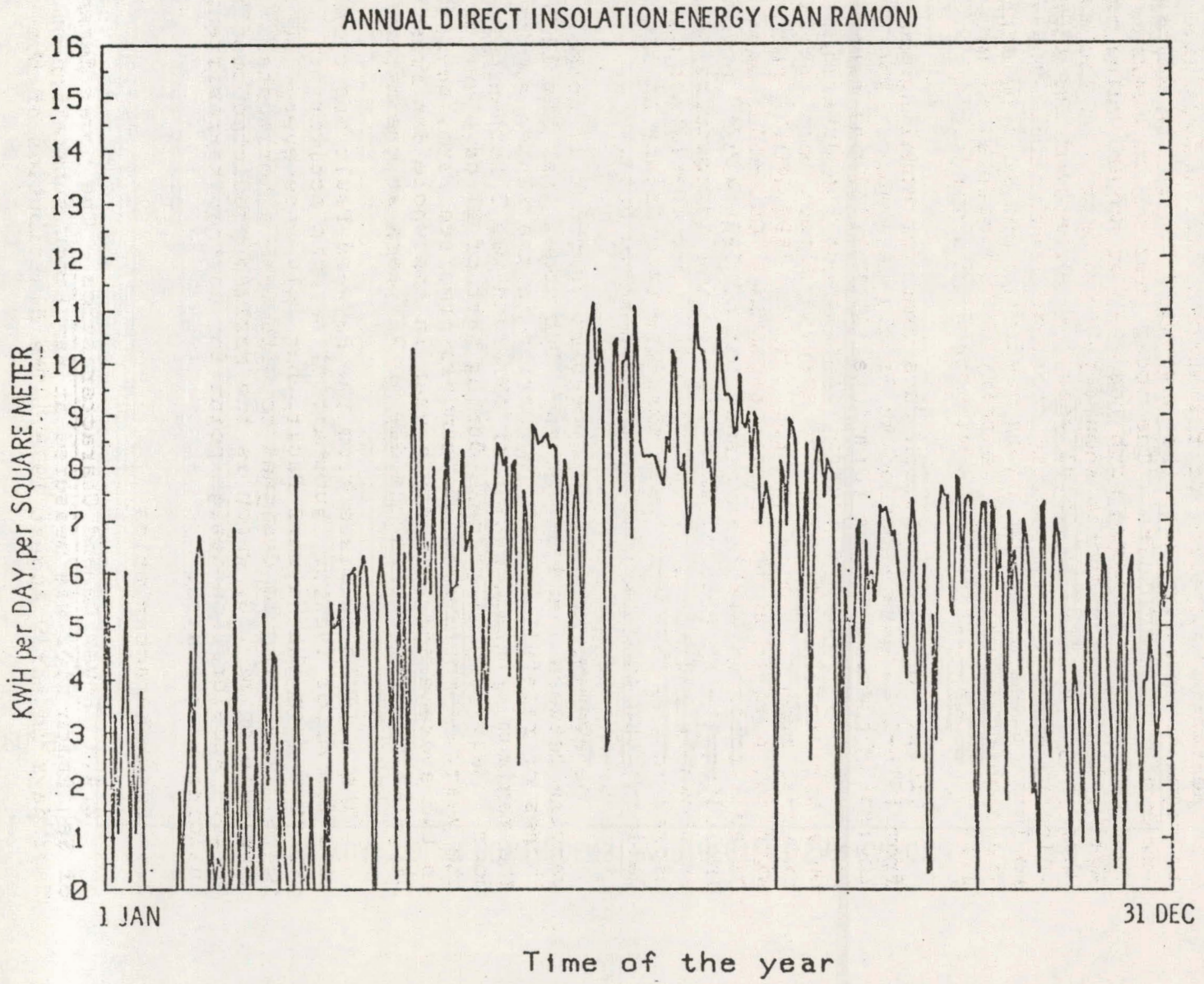

Fig. 2.7 Annual Direct Insolation Energy (San Ramon)

average, therefore, the cooling system performance will be better than projected here. Recorded temperature extremes are 45°C and -18°C. Below-freezing temperatures are expected 2% of the time in the winter months.

Heating and cooling of the surrounding valleys give rise to regular wind flow from the southwest during the daytime, with low probability of calms. The model year has an average wind speed of 6 mph, compared with the average annual value of 8 mph. Again, the cooling system should perform better on the average than projected for the model year. Winds exceed the stowing velocity (30 mph) only during overcast conditions. Therefore, no loss of power generation is predicted due to wind conditions. The highest recorded wind velocity at the site is 67 mph (in 1938). Stowed arrays would withstand this wind.

Direct normal insolation data used for modeling was taken from 1975-1977 data recorded at Sandia Livermore. The climatologically closest longer term data (1970-1976) was taken by the Bay Area Air Pollution Control District at San Jose (insolation on a horizontal surface). The average direct-beam insolation inferred from this data is from 1940 to 2690 kWh/M^2 per year with the horizon at 0° for all azimuths. Out model data year gives a total direct beam insolation of 1936 kWh/M^2 per year, including the effects of shadowing by the surrounding horizon, as shown in Fig. 2-8. Thus our model year insolation data is closer to the "average" year than the uncertainty in the data defining the average year at the San Ramon Site.

The average annual precipitation is about 15 inches, varying between 7 and 25 inches. Our model year has 12.6 inches of rainfall, mostly occurring in the winter months. The maximum rainfall rate ever observed was 3 inches per hour. Heavy fog is present during part of 27 days out of the year, on the average. Thunderstorms are rare, occurring on the average only one day a year in the whole San Francisco Bay area, and less than one day in 75 years at the site.

The site is 10 miles from the Hayward Fault and closer to a few minor faults. Substantial seismic activity is expected from the Hayward Fault, but only once every 100 years. The array is designed to withstand a horizontal acceleration of .5G, which is the maximum predicted credible bedrock acceleration design point for earthquake-resistant building at the site.

2.4 Load Characteristics

2.4.1 Power Demand Characteristics - The power demand of San Ramon 2102 was measured at San Ramon substation on four days in early August 1978. The distribution of the

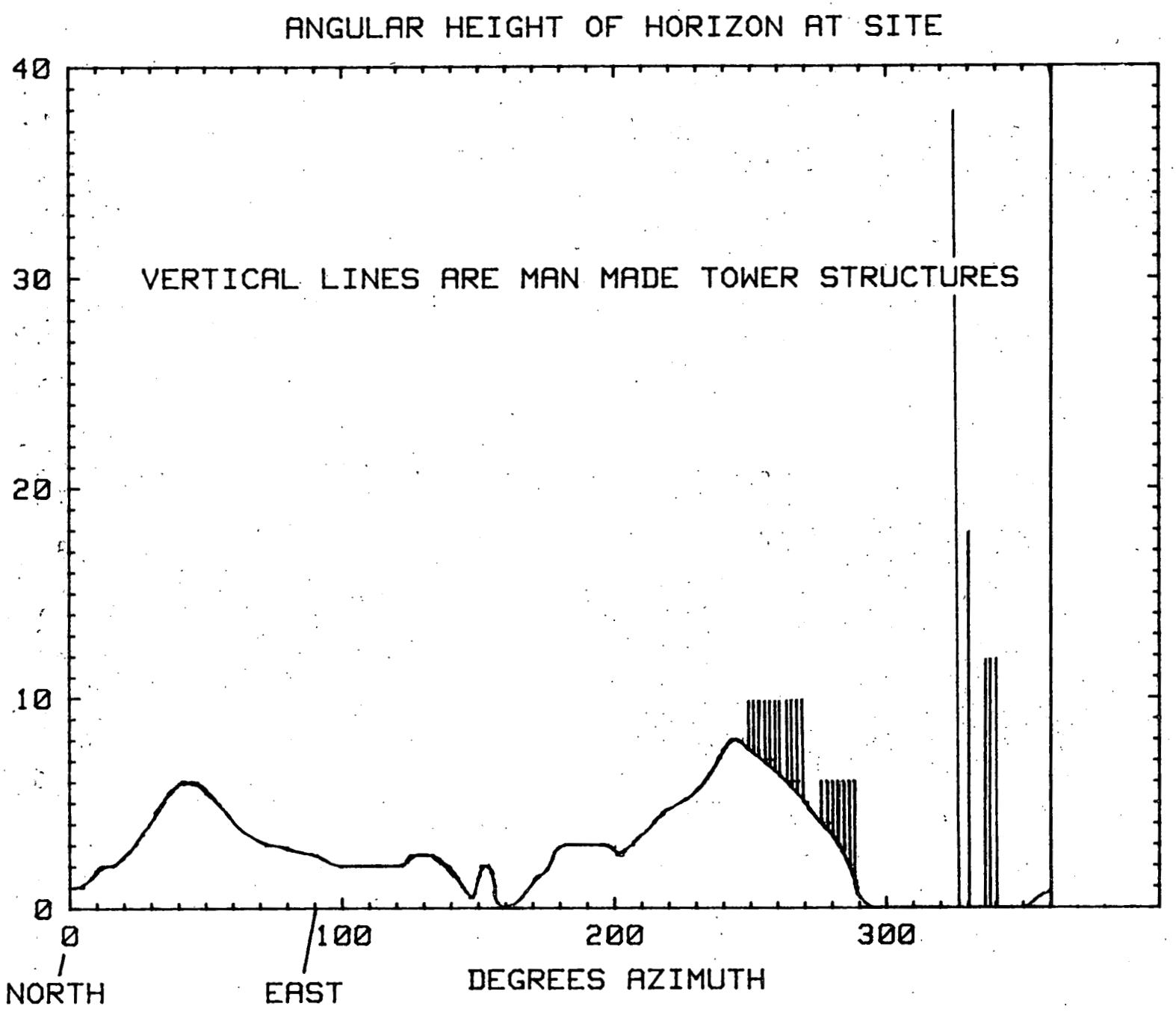

Fig. 2.8 Angular Height of Horizon Site

load on the circuit is shown in Fig. 2-9, averaged for the four days. The maximum value recorded was 9.4 megawatts at 6 p.m., and the minimum was 2.2 megawatts at 4 a.m. This circuit behaves like most domestic customer circuits in the area, with a peak load near 5 or 6 p.m.

The load curve of the entire PG&E system power grid on the peak day in 1977 (August 1) is shown in Fig. 2-10; note that the system peak occurs earlier than the residential peak.

2.4.2 Load Data Collection - Extensive instrumentation of the experiment is planned. Information will be available from the ODAS; if needed, further instrumentation would be added to monitor the various electrical parameters: DC array output; voltage, current, and DC watts, along with the inverter output; voltage, current, watts, vars and power factor. Figure 2-11 shows the measurement points and types of instrumentation used. Some of the information will be displayed at the control building, either in the observation area and/or at the equipment rack panels. Telemetered data will be transmitted to the PG&E Research Center to be collected by a PDP-11 based acquisition system. Auxiliary power used by the experiment for support and control will also be monitored. Measurements are planned on the 21 kv distribution circuit SR 2102. Current and potential transformers will be attached to the line to monitor the load parameters including time of day power consumption. This information would be compared to the array output to determine peak timing.

Additional "power quality" data would be collected during test phases of the experiment. Harmonic content, waveshape distortion, radio interference, and transient stability would be investigated to determine their effect on the distribution circuit and the surrounding community.

2.5 Operational Modes

2.5.1 Utility Interface - During normal operation, the solar facility will supply electric power to PG&E's power grid through a 480 V/21,000 V step-up transformer. The 480 V, 3ϕ output from the plant is linked via underground cables to a 75 KVA pole-mounted transformer for connection to PG&E's overhead distribution line at 21,000 volts. The system is capable of automatic operation including start-up, loading, and shut down on a routine basis.

The facility will serve the load in parallel with the PG&E system, reducing PG&E's energy demand from other generation sources powered by nonrenewable fuels. Except for a small amount of auxiliary power required by the facility, all the available power derived from the solar source will be delivered to the utility. The plant is designed to come on the line

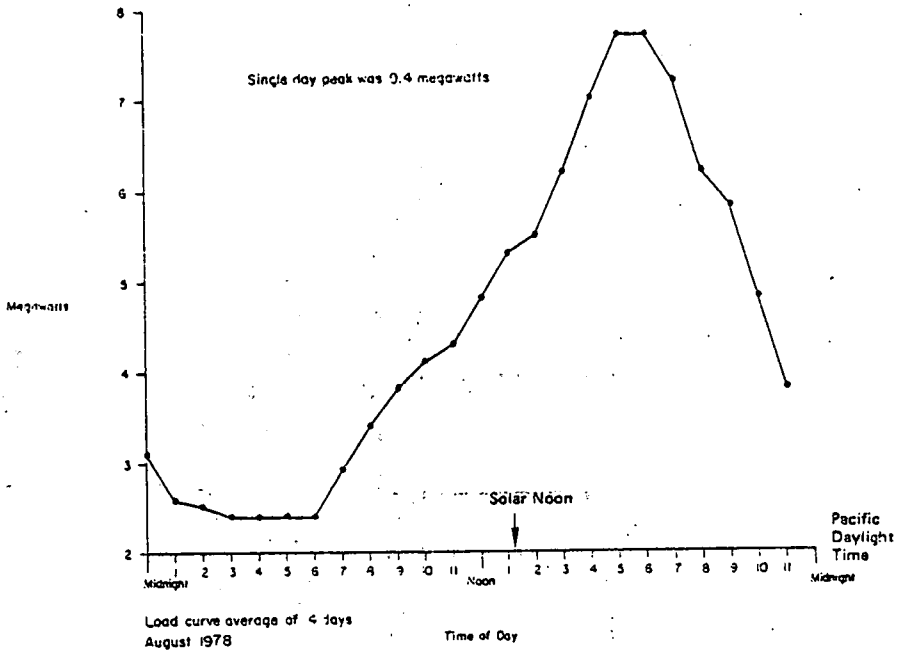

Fig. 2.9 San Ramon 2102 Circuit

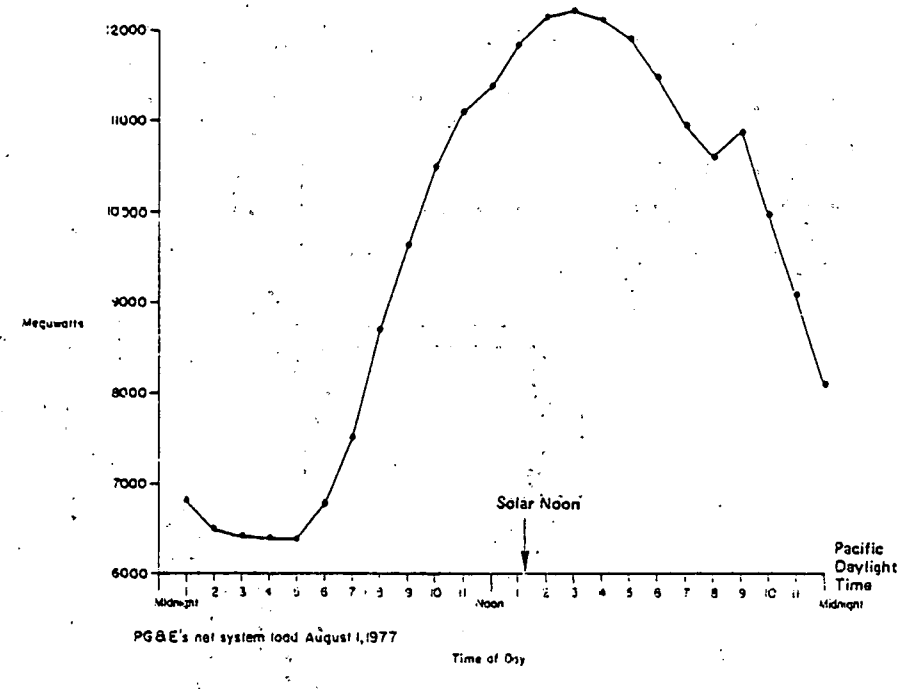

Fig. 2.10 PG&E's Net System Load August 1, 1977

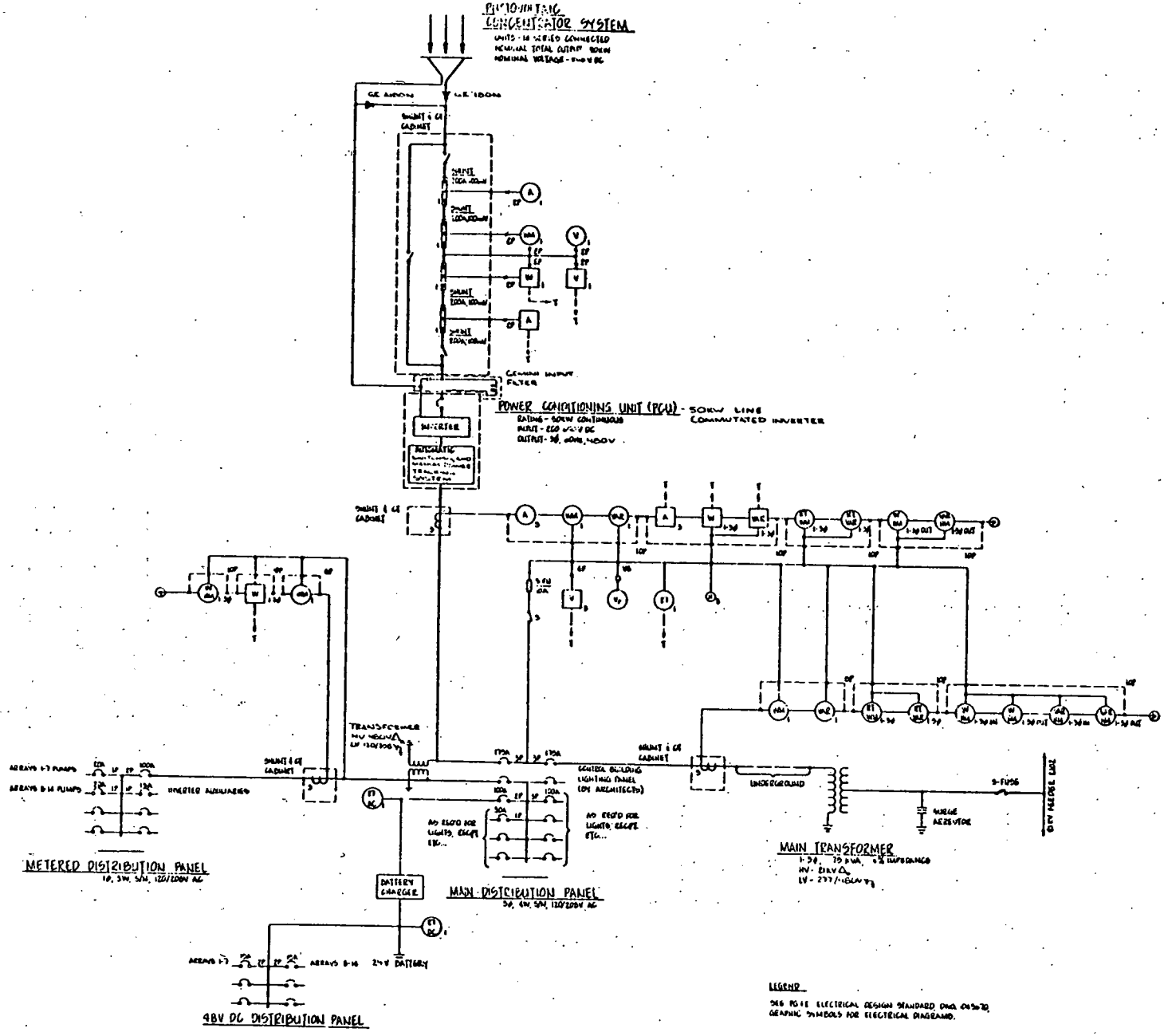

Fig. 2.11 Photovoltaic Concentrator System

whenever there is sufficient insolation for proper inverter operation. Similarly, it is capable of a safe shut-down when minimum insolation is no longer available.

2.5.2 Optional Total Energy--Operating Modes of Space System - An optional space heating system provides a reliable means of dissipating waste heat from the solar concentrators and using some of the thermal energy to heat the equipment building. In this option, an hydronic loop will transfer waste heat to an insulated storage tank whenever it is available. The system will maintain a datum temperature of approximately 50°C. If the storage tank reaches datum, the loop will circulate through an air-cooled heat exchanger, dumping unusable waste heat to atmosphere. In this way the loop will provide adequate heat removal from the solar concentrators, whether the heating system is operating or not. A secondary hydronic loop will transfer the heat from the storage tank to equipment building upon demand. The two loops operate independently, keeping the controls as simple as possible.

In the equipment building a ventilation system will be provided as the heating and cooling medium. An outside air cycle will optimize the use of outside air for cooling. The ventilation system will be inter-connected with the inverter to provide adequate ventilation and cooling. Cooling will be supplied by a commercially available refrigeration system. The cooling is necessary for maintaining the design tolerance temperatures of the solid state devices in the equipment building and the inverter.

Alternate Heating and Cooling Using Thermal Waste - A secondary loop would provide both hydronic heating and hot water for the absorption generator. As in the case of space heating only, this secondary loop would operate independently of the primary loop and provide an alternate means of heat dissipation. 90°C datum temperature would have to be maintained for proper operation of the cooling cycle.

Details of these options are described in Appendix D.

2.6 System Design

2.6.1 Conceptual Block Diagram - Figure 2-1 shows schematically the system elements and their inter-relationships. The full system consists of a number of smaller, practically self-contained photovoltaic arrays of optimized dimensions. Each array consists of a tracking frame on which are mounted 44 linear modules consisting of ten lens/cell submodules.

Each array is provided with an individual sun position sensor, guidance electronics, and elevation and azimuth drive units, with guidance override for stowage or emergency action and, as an option, clock override for cloudy conditions. Cells are interconnected by an internal array harness the cell interconnection scheme being designed to minimize the effects of cell and optics variations--Section 2.7. The cells are provided with active cooling, with ancillary circulation pumps and heat storage and dissipation system. Certain of the arrays are instrumented for mechanical and thermal monitoring, the outputs of which are fed to the data acquisition system, along with electrical data on array performance, inverter output, and data from the meteorological equipment.

2.6.2 Design Approaches - The central aim of the design is the attainment of low life cycle energy costs by exploiting the high efficiency and high operating temperatures of GaAs concentrator cells. Cell costs are lowered by use of high concentration, to which GaAs cells are well suited. The array configuration selected was of the "exposed" altazimuth tracking frame concept (Fig. 2-12).* This had previously been evaluated as more cost effective than the "bubble-enclosed" tracking frame or other concepts.[1] In particular, it appears to have significant advantages over the carrousel concept in installation costs (no extensive leveling of foundations, minimization of expensive assembly operations at the site) and in utilization of low sun angles (the carrousel suffers from partial self-obscuration for the major part of the day during the winter months; this reduces the annual energy collected, and increases the severity of cell shadowing problems in the design). The tracking frame concept selected, on the other hand, must meet high standards of rigidity under expected wind loading conditions. This was evaluated as relatively inexpensive to realize under near term cost conditions. Model experiments and calculations indicate that a low aspect ratio for the tracking frame gives minimum inter-array obscuration, and maximum use of the available land area. Hence the dimensions are chosen as long and low as compatible with the required rigidity in a low-cost structure. The frame concept allows the use of relatively small optical elements with single cells at their focus. Large optical elements increase in weight and cost faster than their area (for a given tolerance on mechanical rigidity). Furthermore, the use of series-connected cell clusters at the optical focus can be seen to involve illumination uniformity problems, and to require tracking accuracies that increase as the square root of the number of cells at the focus. An optics diameter and focal length in the region of 30 cm provide a conveniently manufacturable and handable two-axis focusing element, and result in a convenient cell size.

---

* The structural design is discussed in detail in Appendix I.

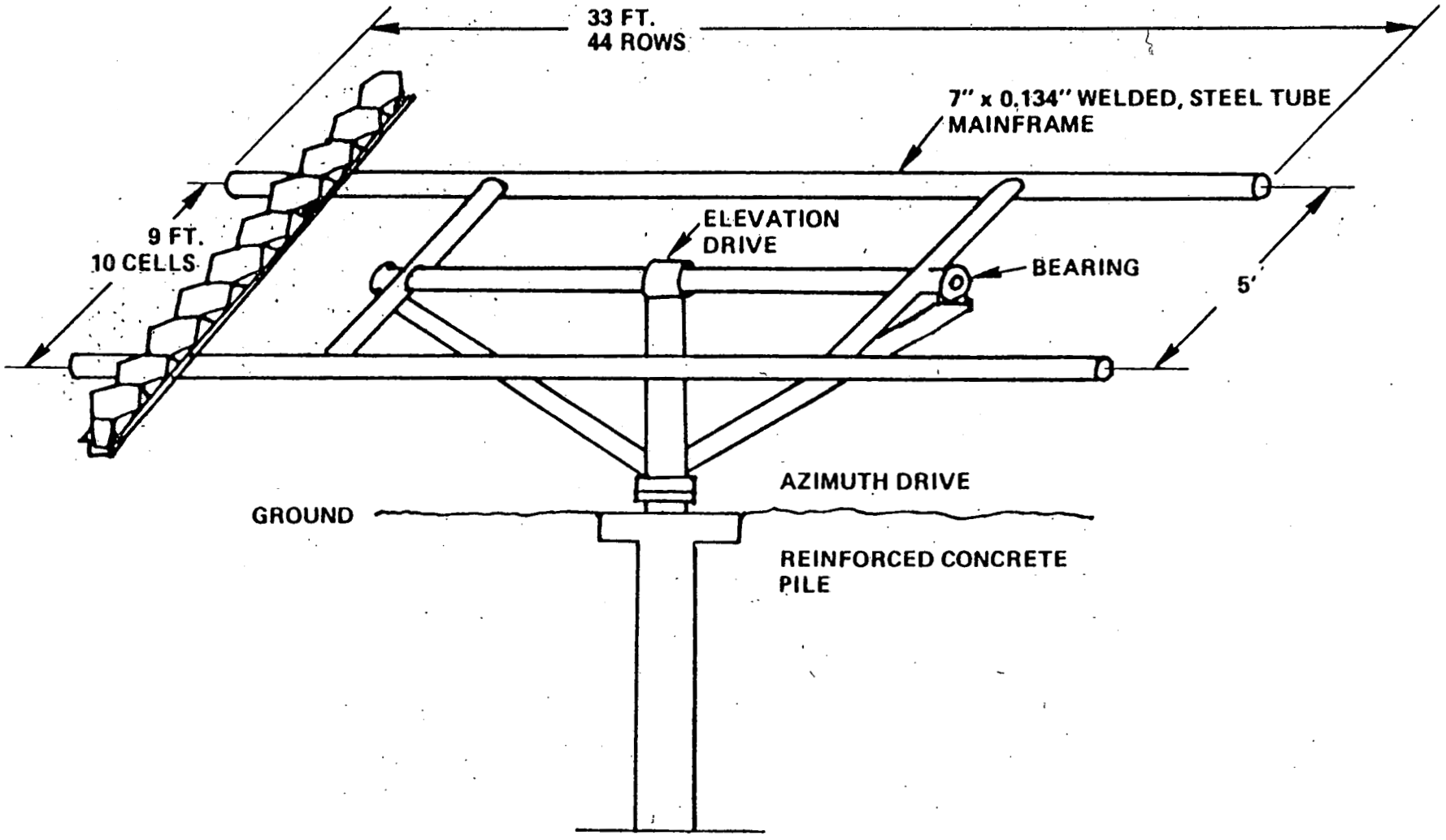

Fig. 2.12 Array Structural Configuration

The optics selected was a single, "grooves down" Fresnel lens (no secondary) realized in acrylic. This has advantages over reflectors in high transmission and relative insensitivity to dirt. The lens can also provide array closure and presents minimal problems with accumulation of snow and ice (by contrast with reflective trough concentrators). A disadvantage is the relatively low useful concentration (about 400 suns) available with a plano Fresnel acrylic lens.

At the 400 sun level, cooling of the cell by physical flow of the coolant is more cost effective than alternatives; active cooling was therefore selected. This has the added advantage of making waste heat available for some useful function or, in the case where the heat is simply dissipated, makes possible storage of the heat for dissipation during the whole 24 hours, including the generally cooler nighttime hours. This was found to be significantly more cost effective than passive cooling systems, or active cooling tower systems.

2.6.3 Major Subsystems

2.6.3.1 Optical Submodule - A number of optical designs were evaluated, including use of a secondary collector on the cell to increase concentration ratio while maintaining acceptable tracking requirements. This was evaluated as impractical in the Phase II timeframe, however, and the system adopted was the constant-groove-depth plano-Fresnel shown in Fig. 2-13. The relatively wide curved facets of the inner zones help reduce diffraction losses, and minimization of the number of steps reduces the optical losses at the steps. The mold for this design was fabricated by single-point diamond turning on numerically-controlled equipment. The photon distribution and other performance parameters for a lens of this type in hexagonal format, calculated by a Monte Carlo method for an AM2 spectrum with limits imposed by the cell of 1.4 and 3.0 eV are shown in Fig. 2-14. The measured transmission is 87% as compared to a theoretical value of 89%.

The lens design was optimized using extensive Monte Carlo ray trace modeling, considering flux uniformity, maximum allowable concentration, and minimum sensitivity to pointing errors.[2] The design requires maintenance of fairly tight tolerances in assembly and operation, both perpendicular to and in the plane of the lens. Fabrication of the mounting cone (Fig. 2-15) in the same acrylic as the lens ensures stability of the focus on the cell with uniform changes of temperature and humidity. Internal temperatures at representative points were checked experimentally to be uniform within a few degrees under typical operating conditions. Close-to-radial symmetry of the cone, lens and mounting arrangement maintains the axial alignment under temperature and humidity changes.

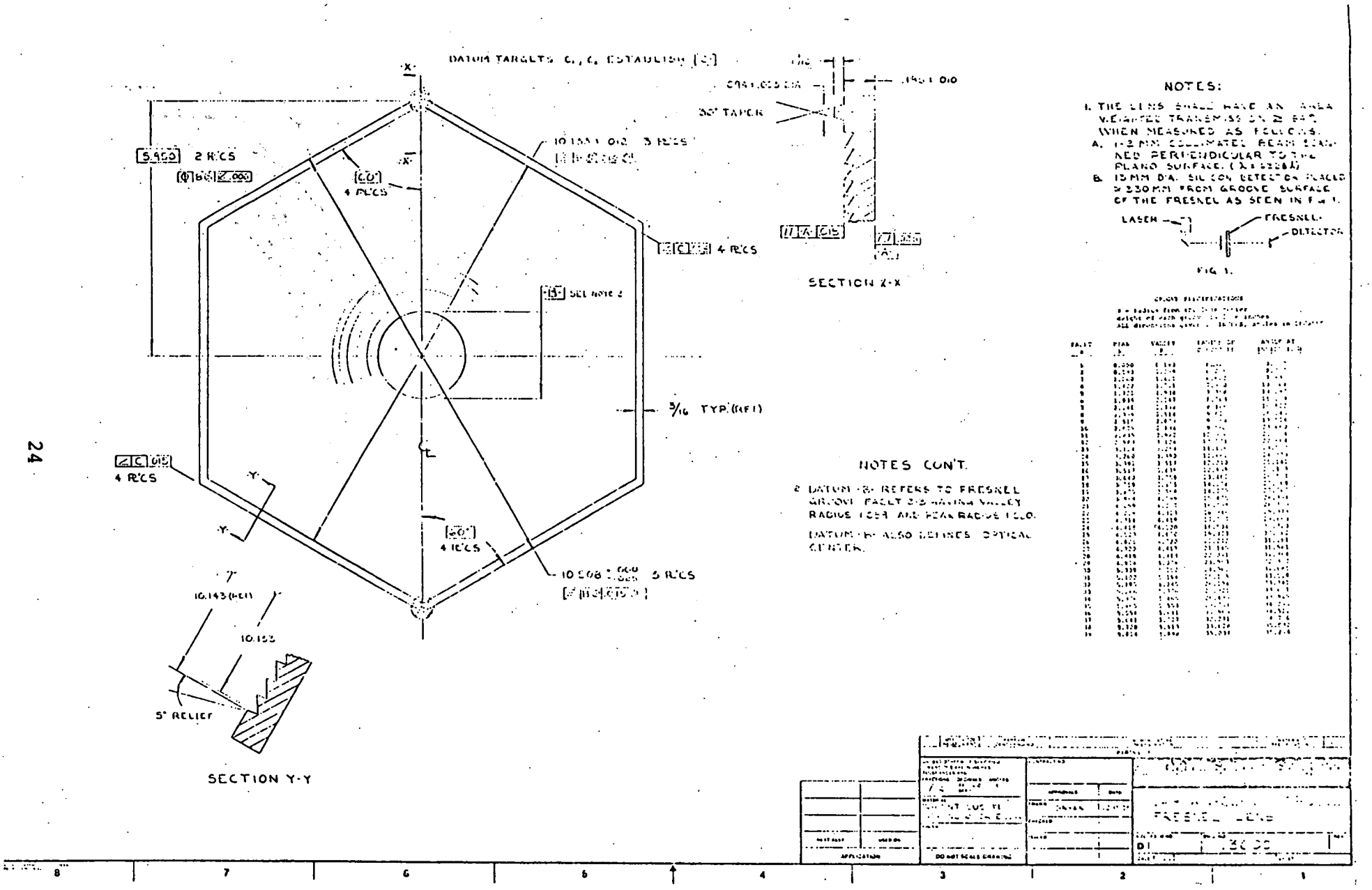

Figure 2.13 Curved-Groove Fresnel Lens

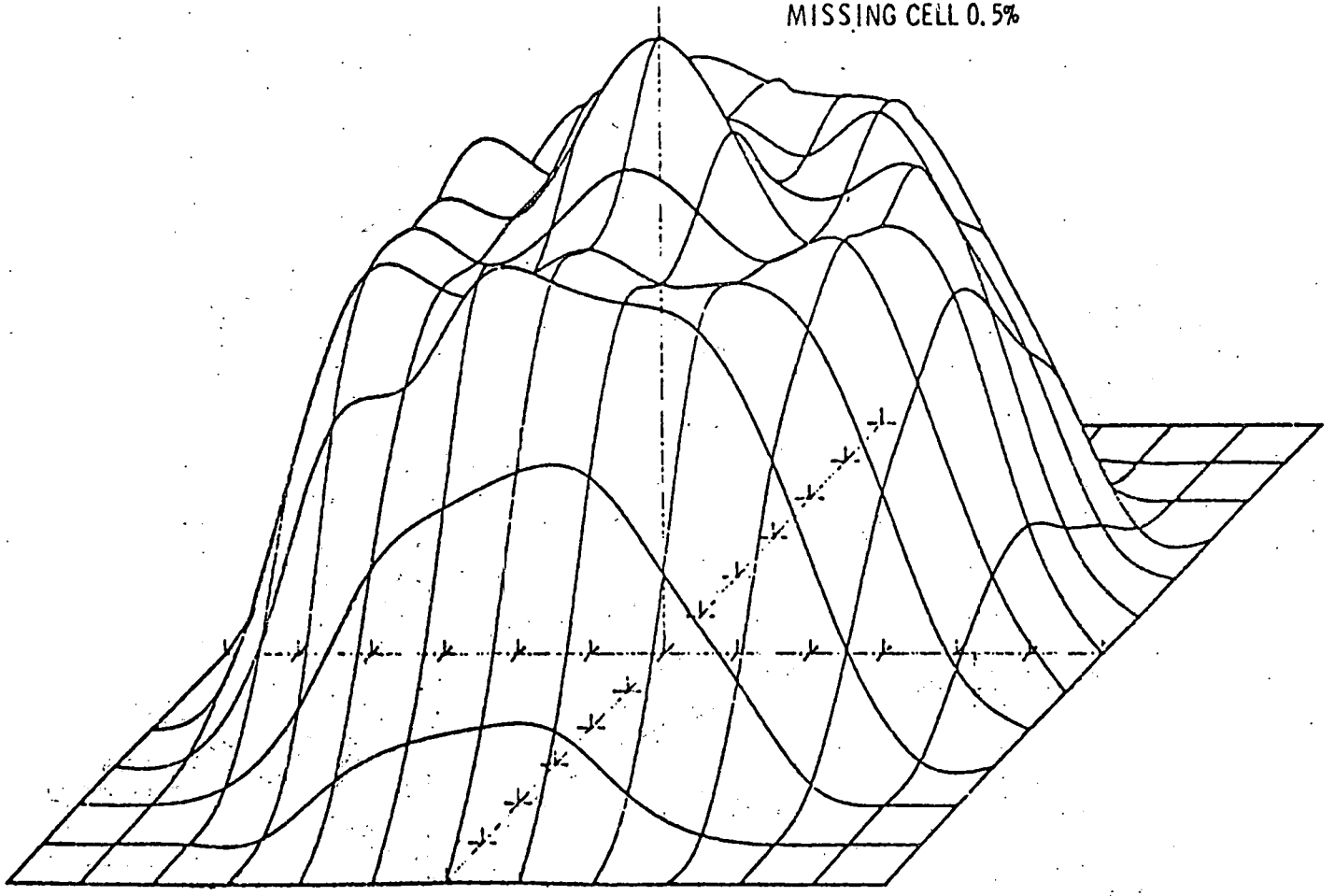

Fig. 2.14 Photon Flux Distribution

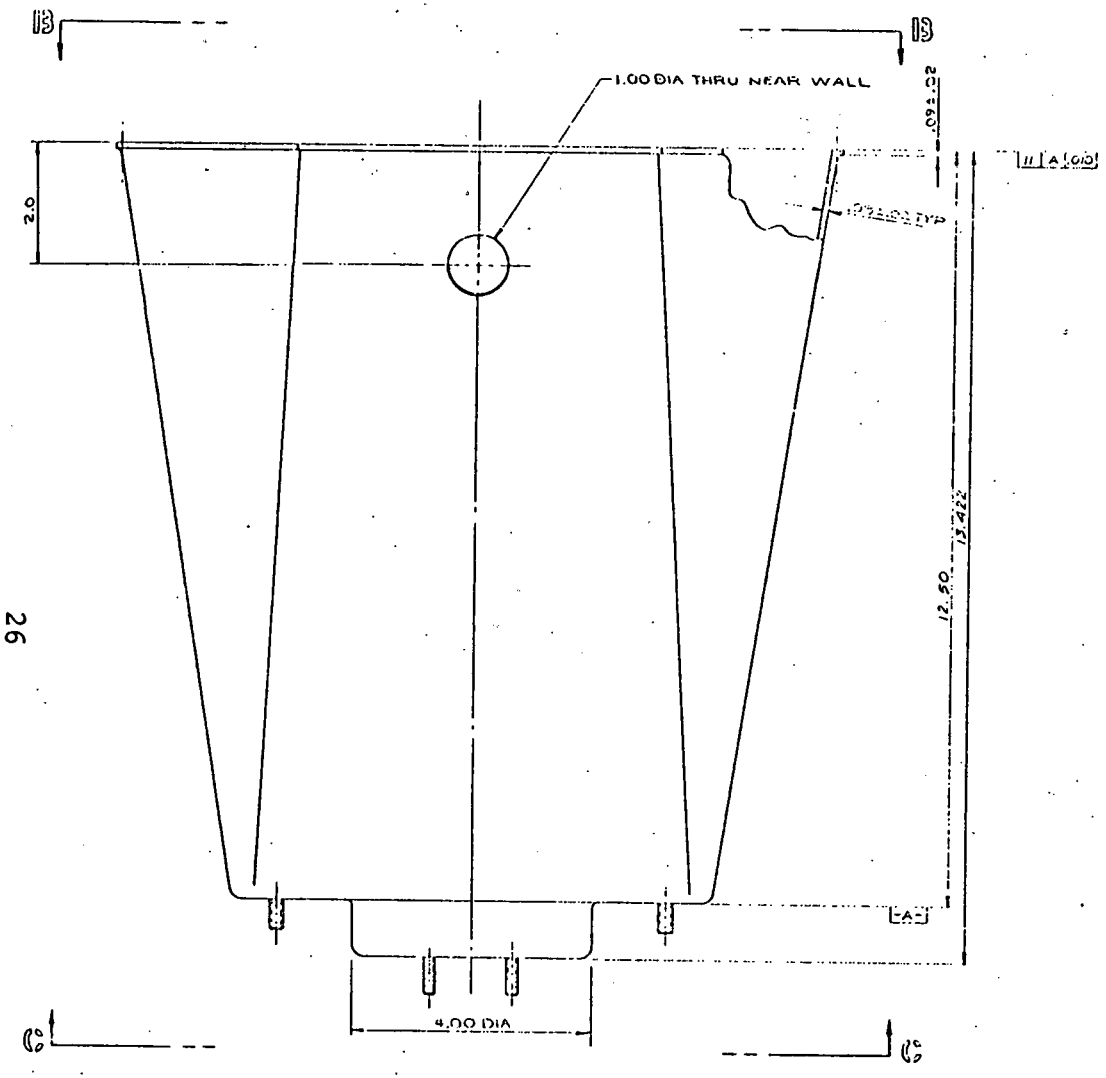

NOTES:

1. MATERIAL: ACRYLIC PLASTIC
   COLOR: CLEAR
2. FINISH: SEALED AGAINST MOISTURE

Nº REQ PER NEXT ASSY 4HO
Nº REQ PER ASSY 4HO

Fig. 2.15 Lens Mounting Cone

Two factors must be taken into account in alignment in the plane of the lens; the tilt of the lens from perpendicularity to the direction of the sun, and the position of the center of the cell relative to the center of the lens. Monte Carlo ray trace calculations show that it is possible to move the cell position to almost exactly compensate for small tilts of the lens, hence the lens cone assemblies are mounted without adjustment to the channels; a single adjustment of the cell position in the field after installation takes out all of the tolerances in the lens plane.

A tolerance problem arises from doming of the lens induced by humidity variations. Because the lens selected has fewer facets than conventional lenses, it has a smaller ratio of inside surface area to outside surface area, reducing the extent of this problem, which can, however, be controlled by proper choice of lens thickness (a thicker lens domes less). The thickness shown in Fig. 2-13 is based on 3-month measurements of doming on a roof-top prototype assembly, including both very dry and very wet weather.

Axial deflection measurements were taken at the center of the lens at regular intervals during the 3-month period, (November-January). At the start of the period, in a normal atmosphere with equal humidity on both sides of the lens, an inward deflection of .005 was measured. Intermittent rain on the exterior resulted in an outward deflection of .010 inch. As the lens dried slowly from the outside, a maximum inward deflection of .030 was recorded. With continued drying in a stable atmosphere, the lens returned to a .005 inward deflection.

The initial alignment of the lens/cell spacing can be done at the assembly plant. The lens mounting surface of the cone must be ground flat before the lens is mounted. This grinding is done in an accurate jig, setting the precise alignment.

2.6.3.2 Solar Cell - This is a GaAs/AlGaAs concentrator cell having an active diameter of 0.490 inch, and with a top contact pattern optimized for operation at 420 suns. Figures 2-16 and 2-17 show respectively optimized schematic cross section of the cell and top contact pattern. AM2 efficiencies in the region of 20 to 23% have been demonstrated with this type of cell fabricated by liquid phase epitaxy,[3] and 18 to 20% by organometallic vapor phase epitaxy.[4] In order to isolate the electrical circuit from the cooling fluid, the cell is mounted on an alumina ceramic (beryllia was evaluated as not cost-effective) which also serves as a package for the cell, to which a top contact lead frame and flying leads for power takeoff can be brazed (Fig. 2-18). The status of the solar cell and packaging processes is covered in more detail in Section 4.4.1 and Appendix G.

Figure 2-19 shows the effects of tracking error on the cell output for the selected optics. An allowable degradation of 3% was selected as a design criterion, corresponding to an allowable total tracking r.m.s. angular error of 0.2°. This in turn was divided up as follows:

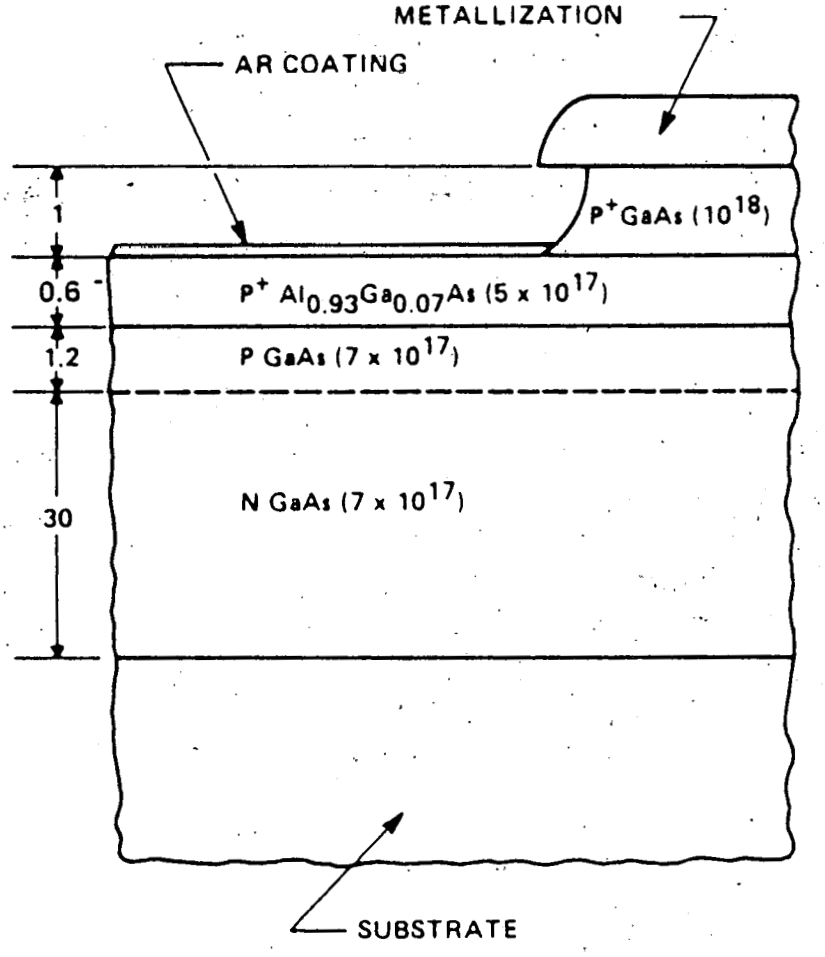

DOPINGS ARE IN UNITS OF (cm^{-3}).
DIMENSIONS ARE IN MICRONS.

Fig. 2.16 Schematic Cross Section of GaAs Solar Cell

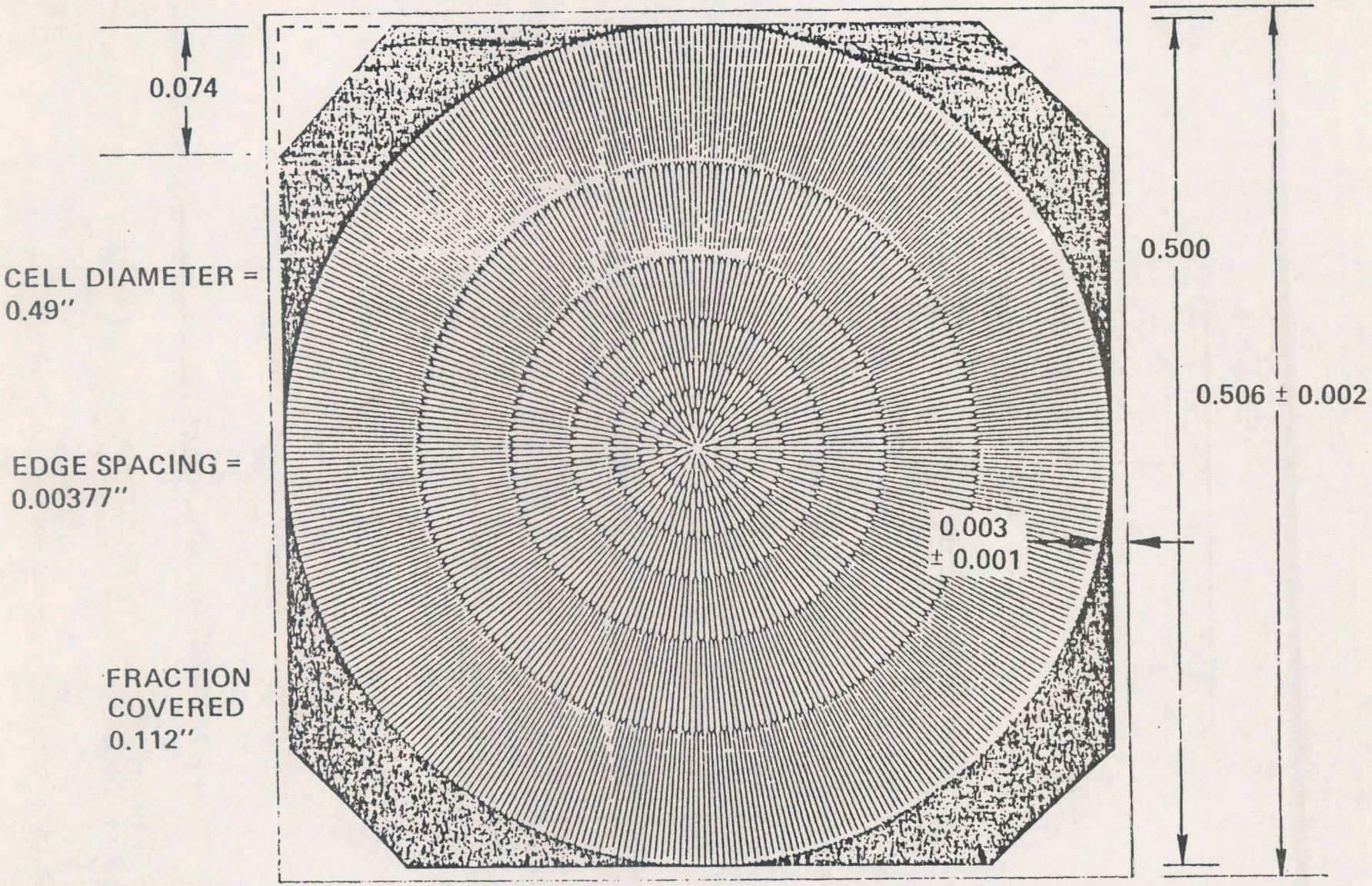

Fig. 2.17 Optimized Cell Mask Design

SOLAR CELL PACKAGING

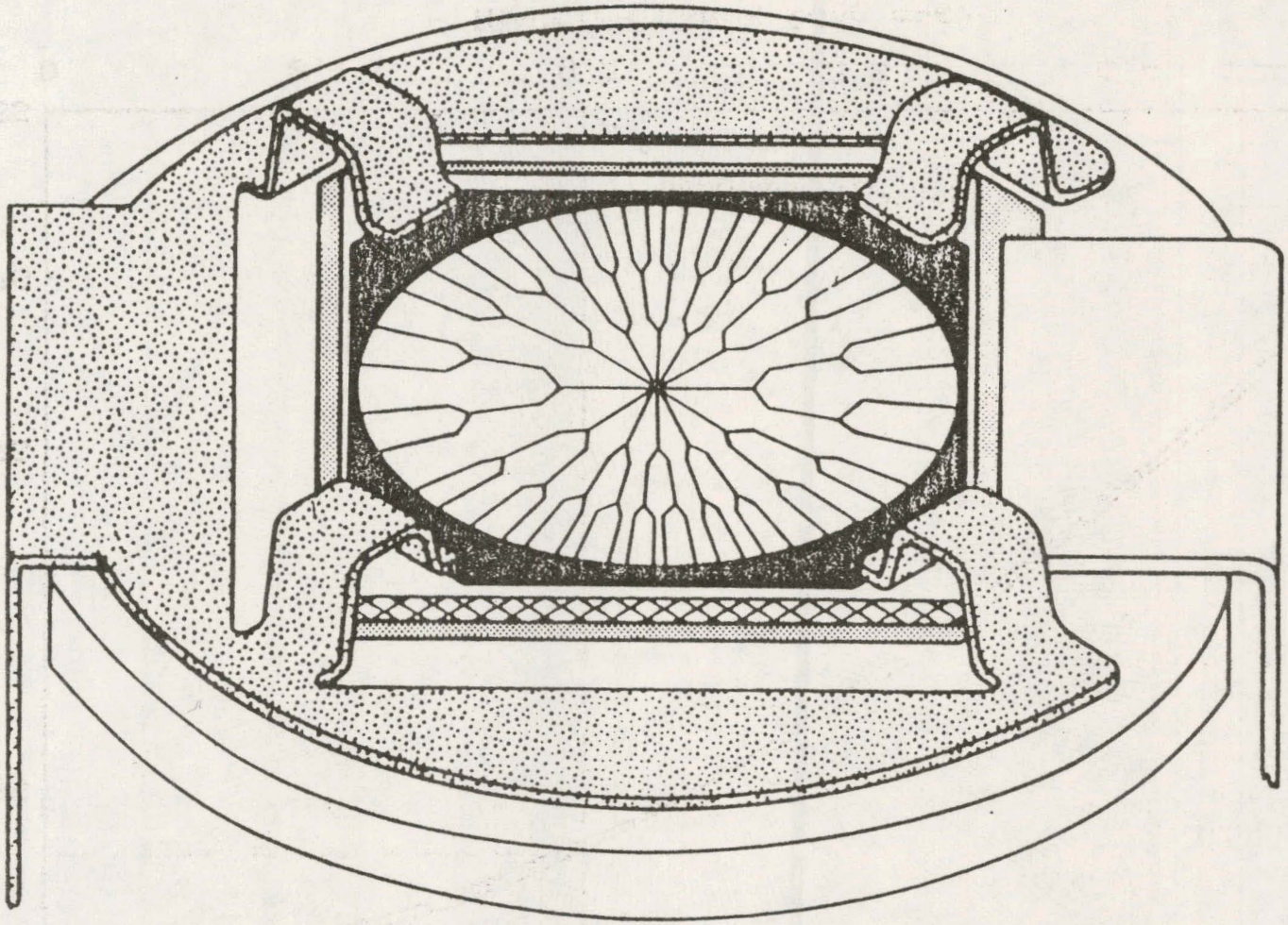

Fig. 2.18 Solar Cell Packaging

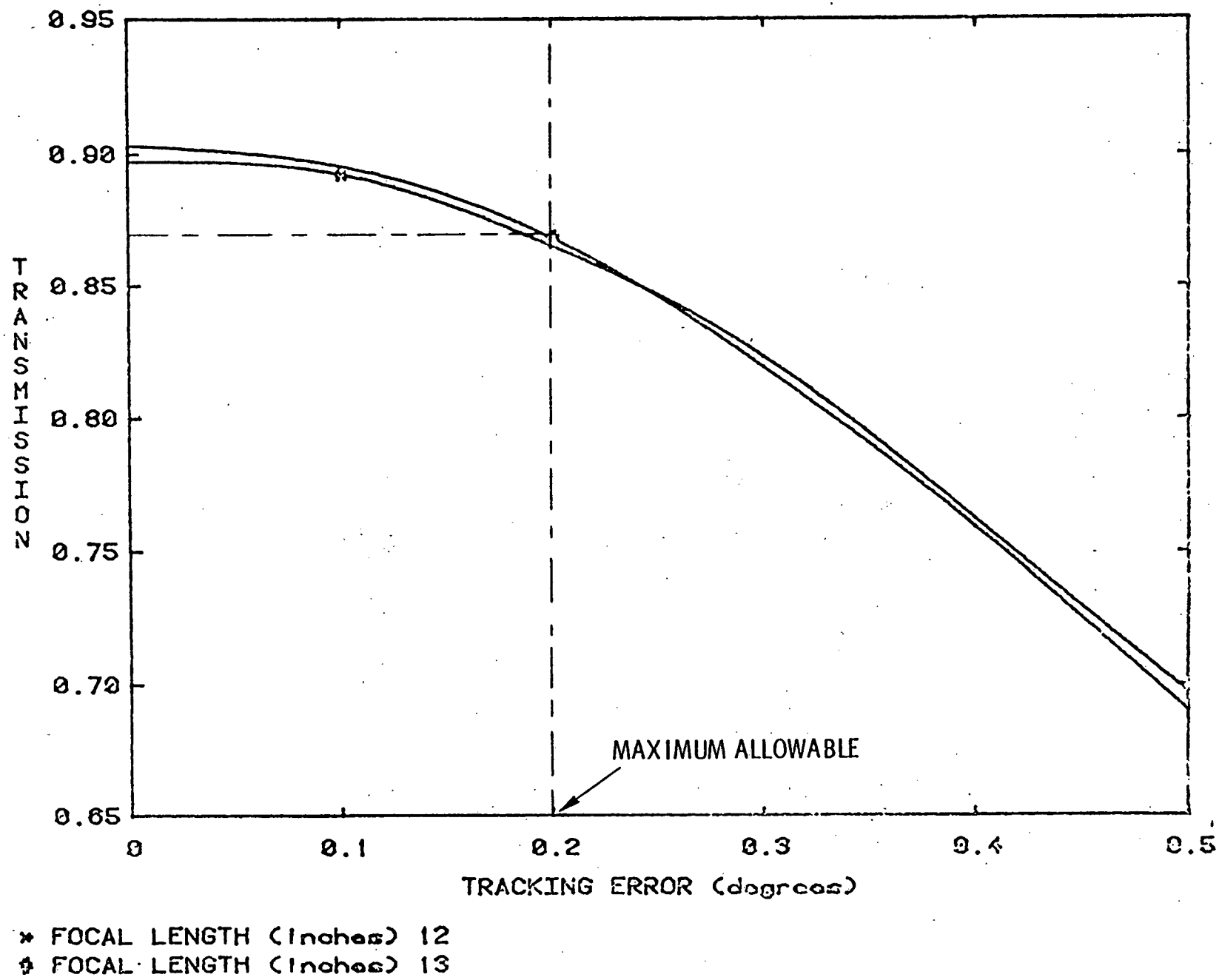

Fig. 2.19 Fraction of Photons Incident on Lens Producing Cell Current

Static Deflection of Tracking Frame	$\leq 0.05°$
Tracking System Free Play	$\leq 0.10°$
Static Deflection Due to 30 MPH Wind	$\leq 0.17°$

Assembly and tolerance errors can be removed by adjustment after assembly (Section 3.2.3).

2.6.3.3 Photovoltaic Module - Thermal expansion of the acrylic lens poses problems in utilization of multilens arrays (such as might be produced by casting) for high concentration. For the Phase II design, a short term solution was adopted of mounting each lens separately, with small inter-lens clearances to allow for independent expansion. Each lens of which mounts on a prefabricated aluminum channel (Fig. 2-15). The cell and its cooler are also mounted concentrically with the lower end of the cone, and can be adjusted in position for maximum cell output. The channel is long enough to accommodate ten of these lens/cell combinations which, when provided with electrical and coolant interconnections, form a linear, ten-cell photovoltaic module.

2.6.3.4 Array Structure - The required rigidity against gravity and wind loading is provided by a main bed of large diameter thin wall tubular steel members (H-frame), Fig. 2-20. This is supported, on bearings at intermediate distances from the ends, by the arms of a vertical Y-frame, also of tubular steel construction, which rotates on a vertical thrust bearing to provide azimuth motion. The entire structure of frames and channels is designed to allow maximum angular deflections under combined gravity and 30 mph wind of 0.17° in the worst case. Operation will be interrupted and the array stowed at wind speeds of greater than 30 mph, and the structure will survive wind speeds up to 60 mph, unstowed, and up to 90 mph, stowed (Appendix I).

2.6.3.5 Power Conditioning - Figures 2-21 and 2-22 show expected voltampere curves for the arrays under maximum and minimum temperature conditions. A line-commutated inverter has been specified to accept inputs over the ranges 100 to 650 volts and 15 to 125 amperes and to provide three-phase output at a nominal 480 volts. The inverter will be provided with circuitry for tracking the maximum power condition of the photovoltaic arrays. Further details of the inverter specifications are given under Section 3.3.1. The power conditioning unit is included in the schematic of Fig. 2-11.

2.6.3.6 Thermal System - In packaging, the cell is soldered to a high thermal conductivity ceramic chip, and the back of the ceramic is cooled by a water jet (Fig. 2-23) dimensioned to balance pumping power loss against loss of electrical output due to temperature rise of the cell. The ten cells of the collector module are series-connected for water flow, provided by top and bottom manifolds on the array frame. The coolant is pumped via flexible hose con-

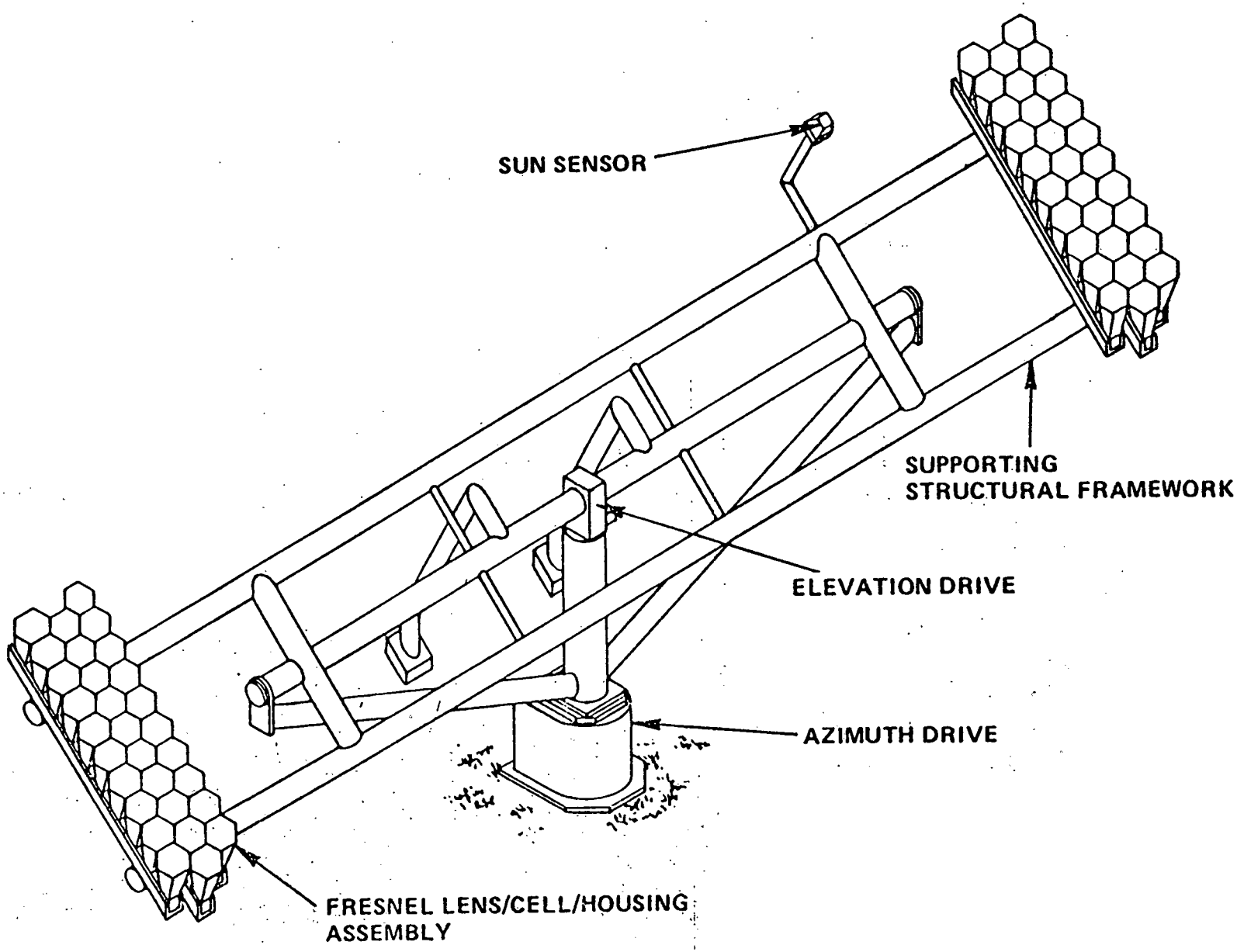

Fig. 2.20 Tracking Frame

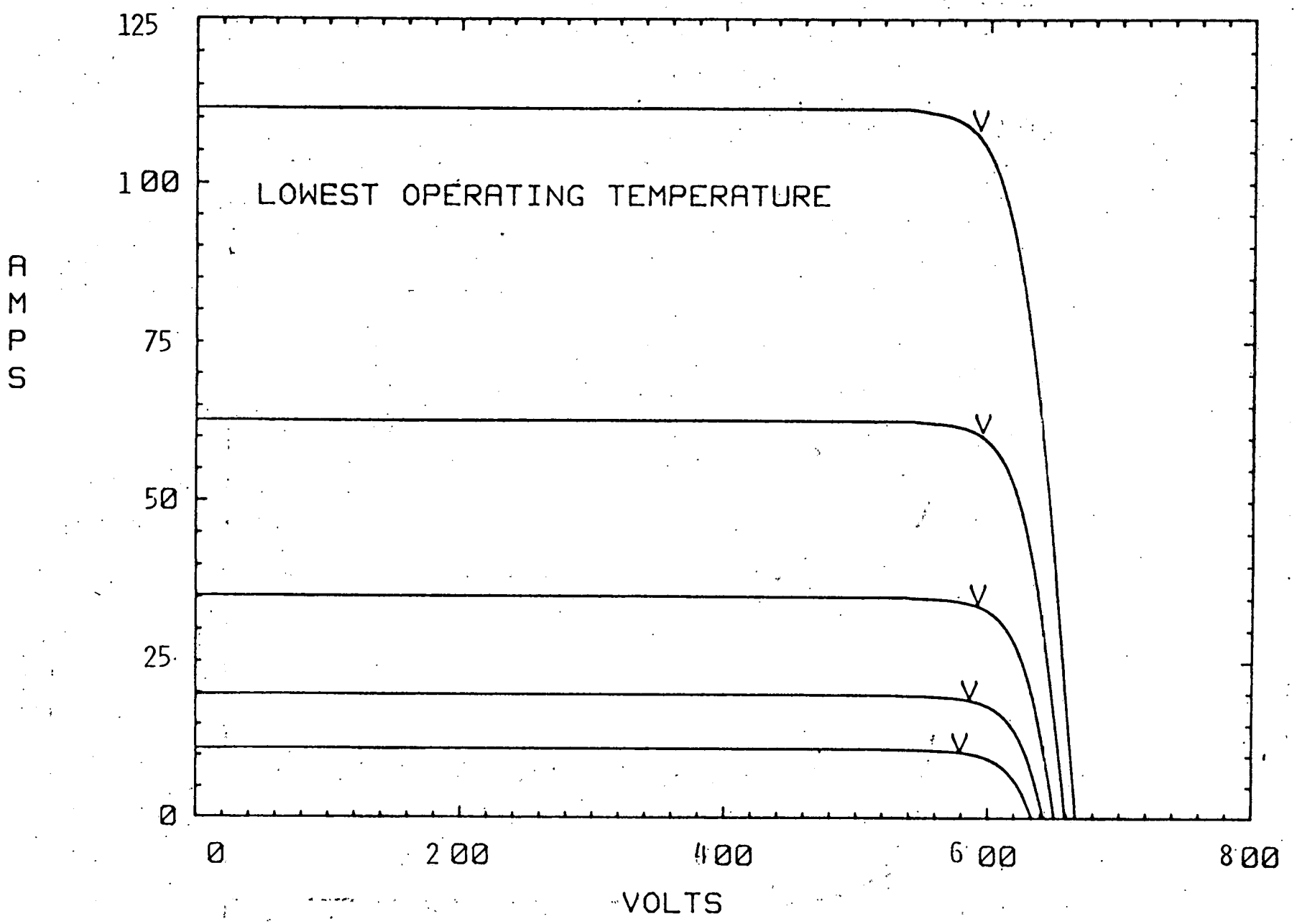

Fig. 2.21 Idealized I-V Characteristics of the Array Field (Various Insolation Levels-Lowest Temperature)

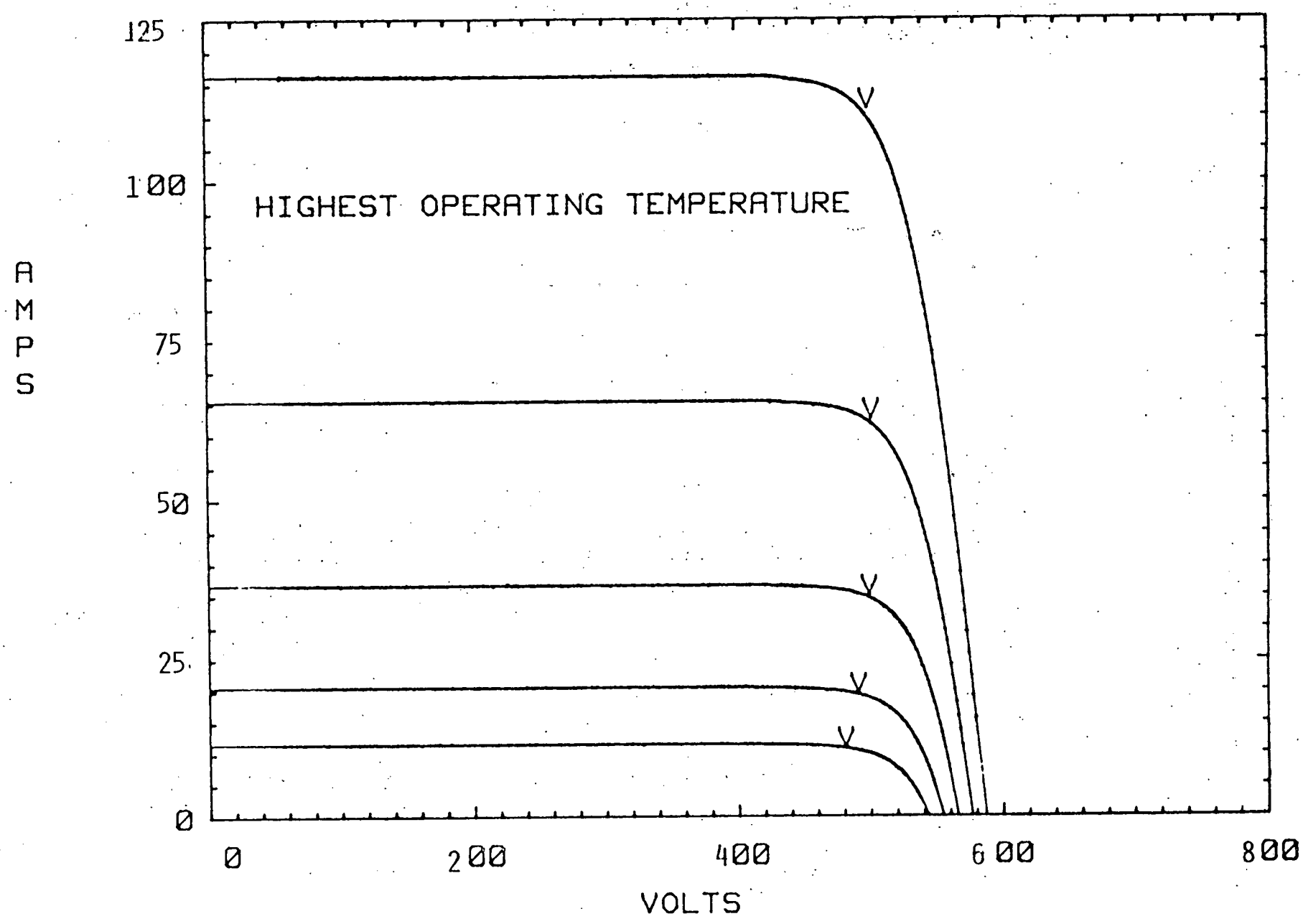

Fig. 2.22 Idealized I-V Characteristics of the Array Field (Various Insolation Levels-Highest Temperature)

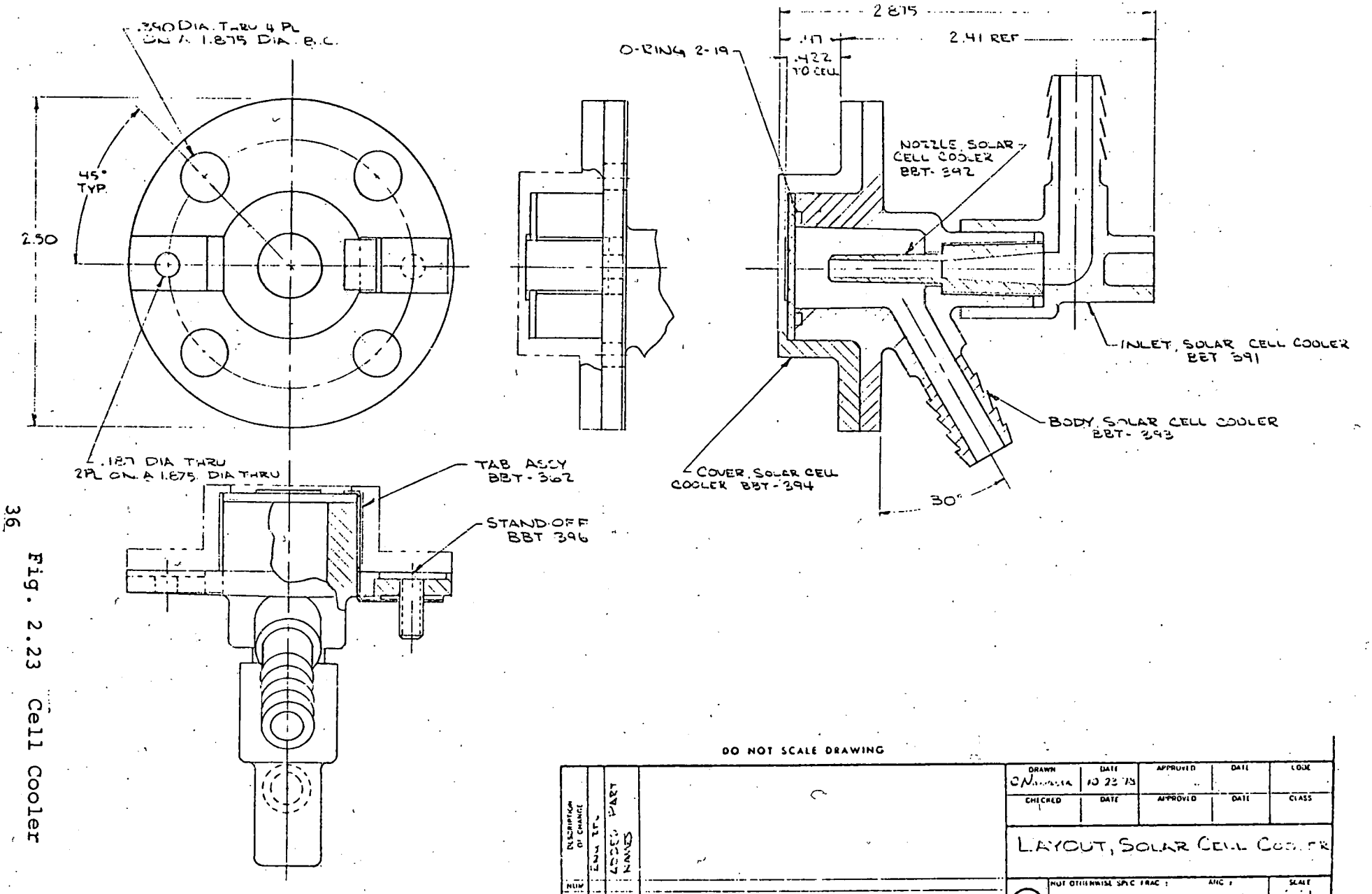

Fig. 2.23 Cell Cooler

nections to an array of 55-gallon drums disposed towards the north of each array, Fig. 2-24. Total coolant volume and storage surface area are such that temperature rise during the day is acceptable, and significant cooling occurs in the absence of circulation during the night. Design considerations for the thermal system are described in Sec. 2.7.4. Some modifications of the array design, mainly lagging of the internal coolant circuits, would allow 200°F water to be collected and used for heating and cooling experiments.

2.6.3.7 Control and Protective Subsystems - These subsystems were designed with the following requirements in mind:

1. maximum system power conversion efficiency,

2. complete protection of the system under the full range of environmental conditions expected, utility line conditions,

3. protection of personnel from high voltages or insolation levels,

4. low cost, consistent with satisfactory operation of the experiment.

These requirements are satisfied as far as possible in the basic design of all components, but received special attention in three areas: power wiring additions, the array control systems, and the inverter control system.

2.6.3.8 Power Wiring Additions - GE-type A180 silicon power diodes are incorporated to prevent damage to the arrays, preventing reverse breakdown of the cells and providing bypass of arrays under conditions of imbalance (e.g., shadowing) or inverter fault. Intra-array use of diodes has been minimized by paralleling, and by protection of rows of cells in pairs (Fig. 2-25). Safety is ensured by complete enclosure of high voltage leads (for example inside the channels, cable trays, etc.) and enclosure of the focal region of the optics. For protection of servicing personnel, each array can be disconnected by a manual knife switch in the locked junction box at each array.

2.6.3.9 Array Control System - Each array is provided with an independent control system to maintain optimum tracking, monitor hazards and take appropriate actions in alarm situations. Low cost and reliable operation were optimized by the following choices:

1. Independent control for each array (no central controller, no control cabling--duplication of low cost sensors in

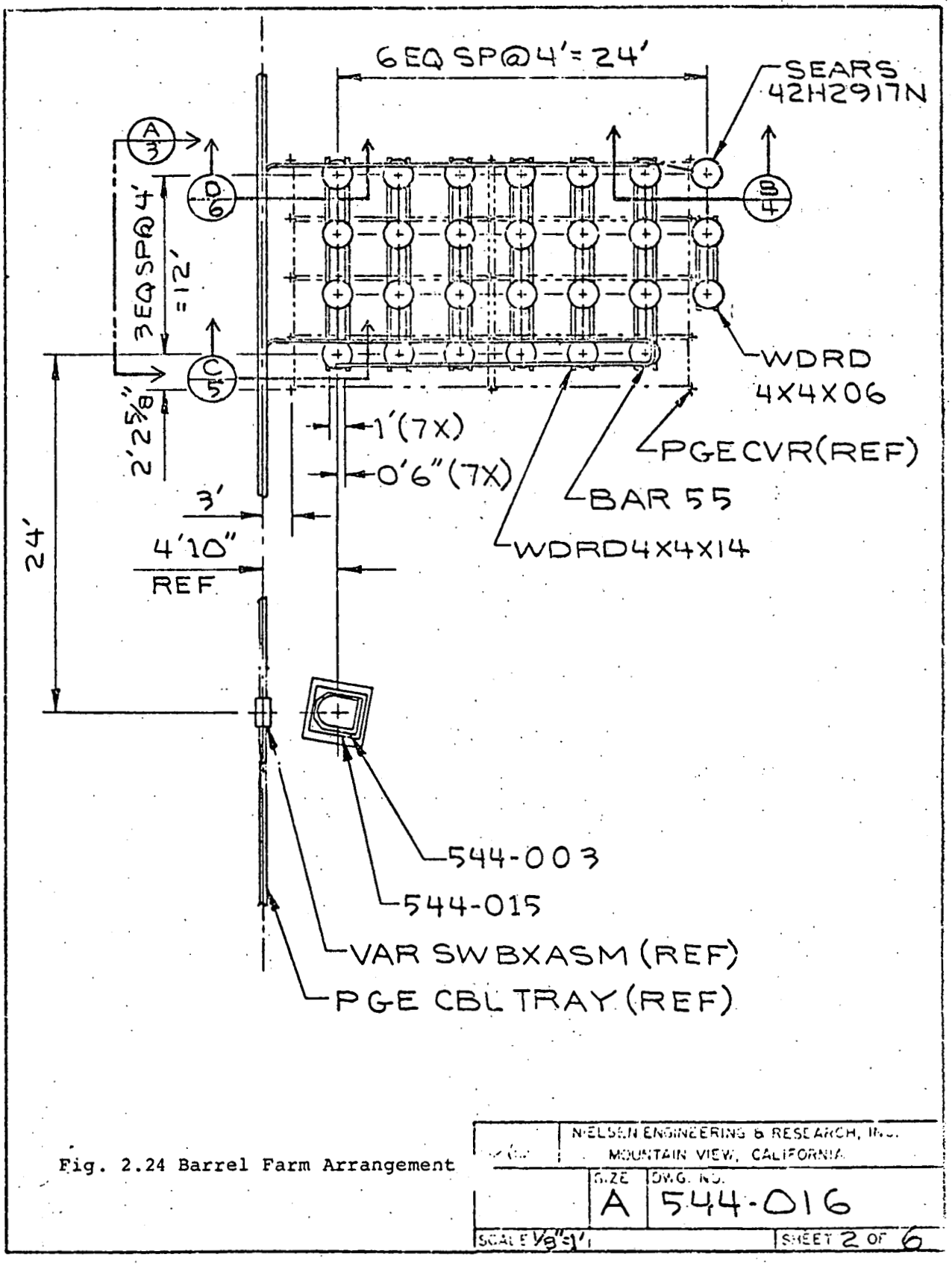

Fig. 2.24 Barrel Farm Arrangement

	NELSON ENGINEERING & RESEARCH, INC. MOUNTAIN VIEW, CALIFORNIA	
	SIZE A	DWG. NO. 544-016
SCALE 1/8"=1'		SHEET 2 OF 6

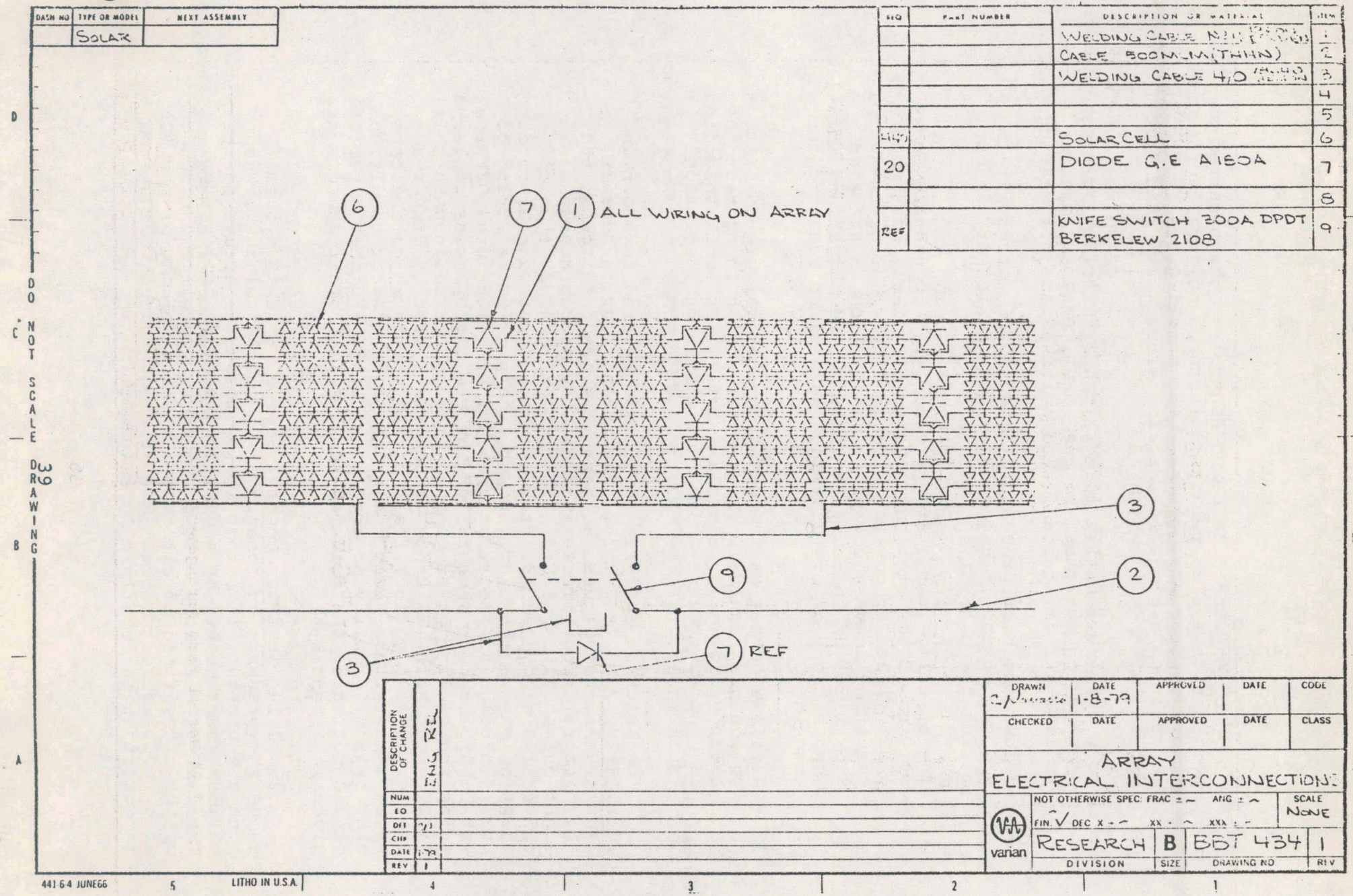

Fig. 2.25 Array Electrical Interconnections

conjunction with fine servo control on the observed sun position This also relaxes tolerances on array structures, lowering structural costs). The tracking electronics contributes negligible tracking error (less than 0.02 degrees).

2. Long term reliability is obtained by eliminating brushes, snap-action switches and the like. Stepping motors, solid state devices and reed switches are used throughout.

3. A low-cost microprocessor (Intel 8022) with built-in A/D conversion is used, to afford flexibility in optimizing the control algorithms.

4. The tracking gear trains are designed to prevent back-driving of the stepping motors (efficiency less than 0.5). Tracking power is required only during the step, resulting in very low power consumption in tracking. Slew rates of up to 0.1 deg/sec can be maintained for acquisition, or over 5 times the maximum required for tracking.

5. A fail-safe design is used such that failure of critical components results in a de-steer action to protect the solar cells (e.g., a coolant loss). Internal shielding is used to prevent other damage by high insolation intensities.

The tracking and array control subsystem is shown in Figs. 2-26, 2-27, and 2-28. Seventeen separate sensors (small GaAs photodiodes, a thermostat, reed switches, and thermistors) feed information into the microprocessor. Eight output lines provide (through integrated circuit drivers) 8 step, 4 phase drive to the azimuth and elevation stepping motors. A ninth output line provides a string of pulses through an isolation transformer which turns OFF the water pump motor. Thus failure of the microprocessor always turns the cooling water pump on, whether it fails with this line low or high. A tenth output line directly drives a single LED with various flashing sequencers which indicate by matching with a table the origin of any error condition that exists, simplifying troubleshooting. Further details of the software, the tracking sensors, and other sensors are given in Appendix A.

2.6.3.10 Inverter Control System - This system sense the presence or absence of DC and AC voltage. When both are present, it automatically loads the arrays to their maximum power point, by a dual feed back control system. The control circuitry also provides for complete disconnection of the array field if either the AC line voltage or the DC array voltage is too low. Operation of the control system is described in detail in Appendix B.

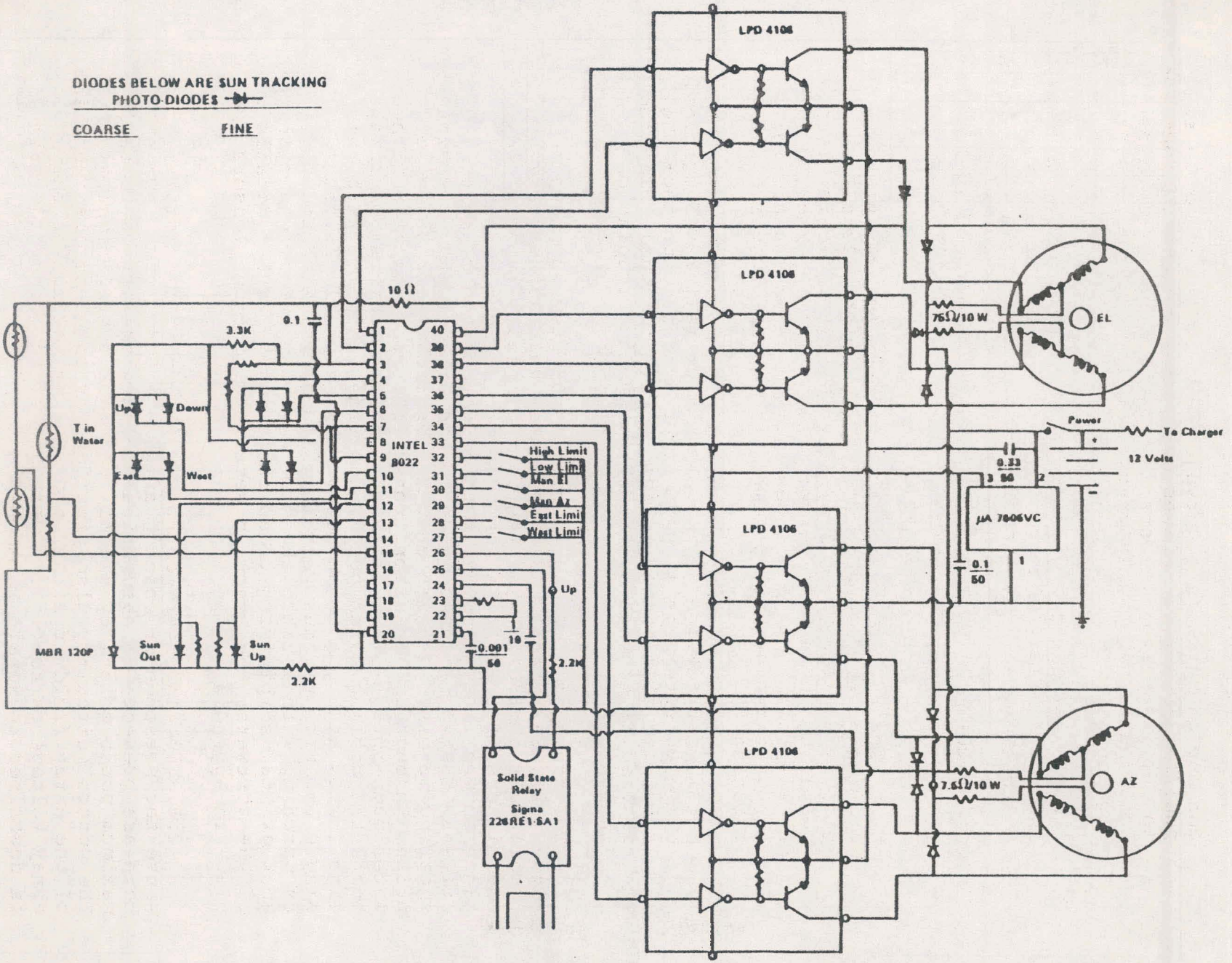

Fig. 2.26 Schematic of Tracking System

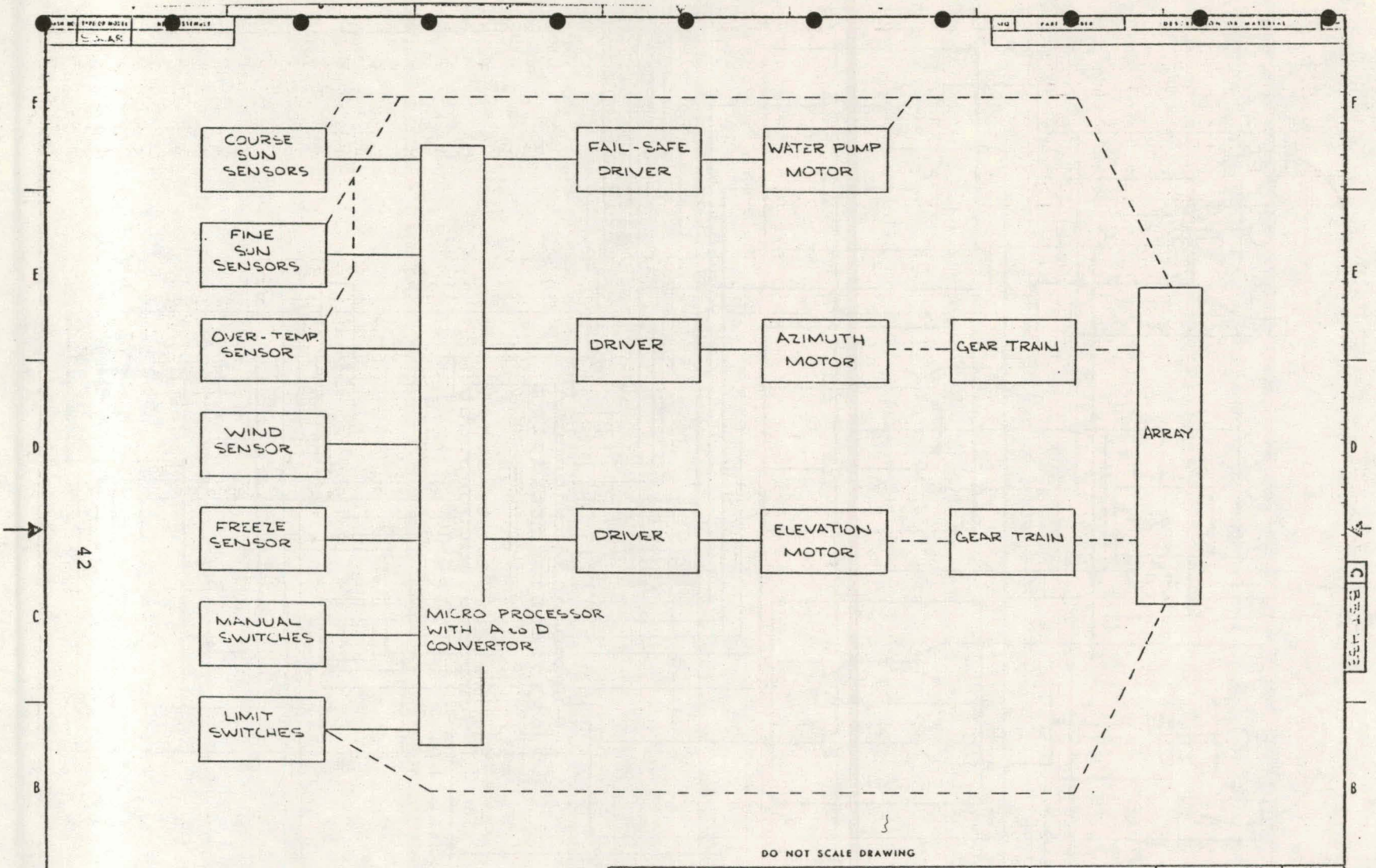

Fig. 2.27 Tracking & Control System Block Diagram

1. CONNECTIONS:
   SOLIDS LINES - ELECTRICAL
   BROKEN LINES - MECHANICAL

NOTES:

DRAWN	DATE	APPROVED	DATE	CODE
C. Navarra	1-8-79			
CHECKED	DATE	APPROVED	DATE	CLASS

TRACKING & CONTROL SYSTEM BLOCK DIAGRAM

varian | RESEARCH | C | BBT-433 | 1
DIVISION | SIZE | DRAWING NO | REV

SCALE NONE

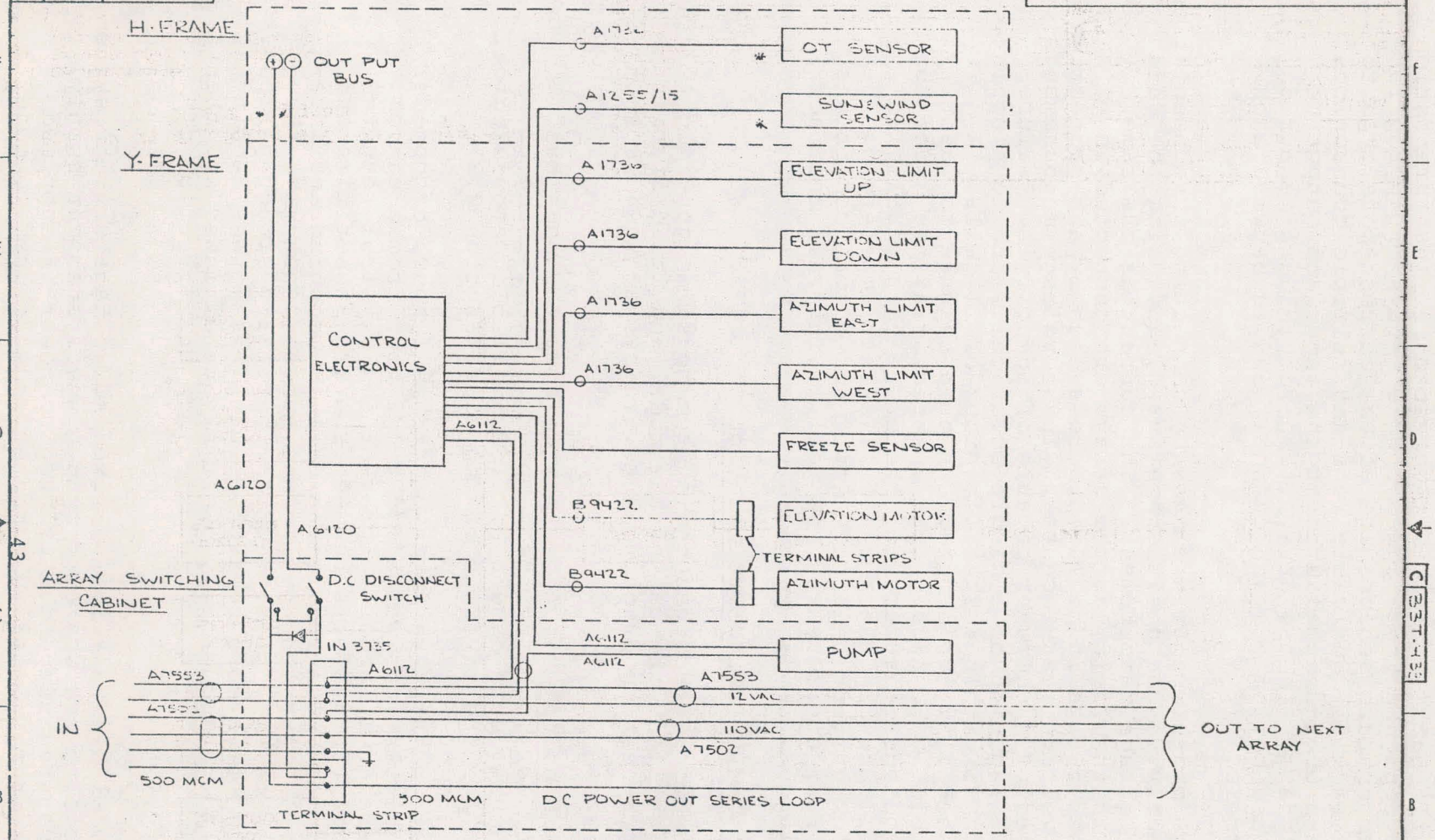

DO NOT SCALE DRAWING

4 MULTIPLE WIRES IN ONE JACKET INDICATED BY (-).

3. FLEXIBLE WIRE PATHS ARE MARKED WITH *

2a. A= ALPHA WIRE PART Nº
B= BELDEN WIRE PART Nº

1. INSTRUMENTATION CABLING NOT YET SHOWN.

NOTES:

Fig. 2.28 Control Wiring Array

DRAWN	DATE	APPROVED	DATE	CODE
CHECKED	DATE	APPROVED	DATE	CLASS

CONTROL WIRING, ARRAY

varian RESEARCH | C | B&T-433 | 1

DIVISION | SIZE | DRAWING NO | REV

SCALE NONE

2.6.3.11 Data Acquisition Subsystem - Instrumentation sensors are designed to be added to the arrays in appropriate places. Temperature sensors are of the current-mode type to prevent errors with long cable runs and multiple connections. Water temperatures are measured at the input and output of each barrel farm. In one array, temperatures are measured at the top and bottom of each channel, and in between each pair of barrels.

Voltage measurements are made by connecting instrumentation cables directly to the position measured, and using the data logger for voltage measurement. The current is the same everywhere in the field, as the arrays are connected in series. The voltage is measured across each bypass protection diode (574 voltage measurements). These voltage measurements are monitored by a computer capable of identifying failure or severe degradation of a single solar cell, and to pinpoint its location to within a specific group of 11 cells. A Hall-bar based clamp-on ammeter can then be used to identify the exact cell. The highly instrumented array has twice the number of voltage measurements; therefore each paralleled group of cells can be checked. Hall effect ammeters can be used to check current balance. Input and output conditions of the inverter are measured, as well as internal feedback control voltages.

2.7 System Analysis and Optimization

This section describes the system model in general terms, and outlines the use of the model and its different parts in optimization of components, subsystems, and system layout.

2.7.1 Modeling - An extensive computer code has been written for modeling the complete system, using 12 months of hourly data assembled from available meteorological information for the environs of the site (Section 2.3).

All data points are taken on the half-hour, except for shadowing calculations which add ± 1/2 hour from a random number generator in order to prevent non-physical results due to correlation effects between sunrise-sunset time and modelling times. The insolation data is measured and integrated over an hour long period and hence cannot give the actual power density present during partially cloudy periods. In order to obtain more correct results, the power density is calculated for moderately clear sky conditions, and then the isolation data is used to calculate what fraction of the hour the sun is out.

The model has as a load a fixed AC voltage utility system which is able to use whatever output the system can supply, and will operate independently when no power is supplied from this system. Detailed computer code is used to model

any shadowing of the lens, the cell, the electrical interconnections and wiring, the inverter, and all of the thermal system components. The array structure is accurately modelled only for static deflections, as the Q of the mechanical resonances, and their coupling to the wind is unknown. Times of array failure or non-tracking are neglected (except for intentional stowing) for modelling purposes.

2.7.2 Optimization Studies - A number of the subsystems outlined were subjected to optimization at various levels of sophistication. Elements undergoing intensive computer modelling and numerical optimization included the solar cell, the lens design, the thermal subsystem, and the site layout (shadowing). Optimization of the solar cell design was undertaken prior to and under Sandia Contract 05-4413 and reference is made to the Final Report under that program for details of the approach.[5] The computer programs developed, which are now incorporated in the system modelling program, were used here to provide an optimized design of cell for 400-sun operation, dictated by the performance of optimized Fresnel lens designs in available formats (plano-Fresnel). The lens design was also optimized as far as possible in respect of concentration ratio, given the restriction of a maximum non-uniformity of the radiation distribution on the cell (peak less than 1.9 times the average). The Monte-Carlo ray-trace procedure for this work has been described in Ref. 2. The concentration ratio was chosen by trading off cell cost and performance vs an estimated cost of increased tracking accuracy, using the Monte Carlo lens modelling to define the tradeoff performance parameters. The f-number of the lens was optimized for cell illumination uniformity and minimum sensitivity to tracking error. The lens size (and hence the cell size) was chosen by considering assembly and alignment costs, cell manufacturing costs and cell efficiency vs size, lens manufacturing costs, and size limitations of available production equipment. Results of individual optimization procedures have been given in earlier figures. Figure 2-29 is an example of how the interaction between the lens performance and the cell performance determines an optimum lens-to-cell spacing and the spacing tolerance. Other parameters of the system, for example the overall dimensions of the array frames, were chosen on a more qualitative basis, the absence of firm data making particular optimization processes (e.g., cost optimization) of questionable value. These parameters were generally selected on the basis of engineering experience. In many cases an early choice was necessary in order that dependent optimization processes (e.g., the structural design of the array frames to meet deflection specifications) could proceed. Optimization of the site layout and the thermal system are discussed below.

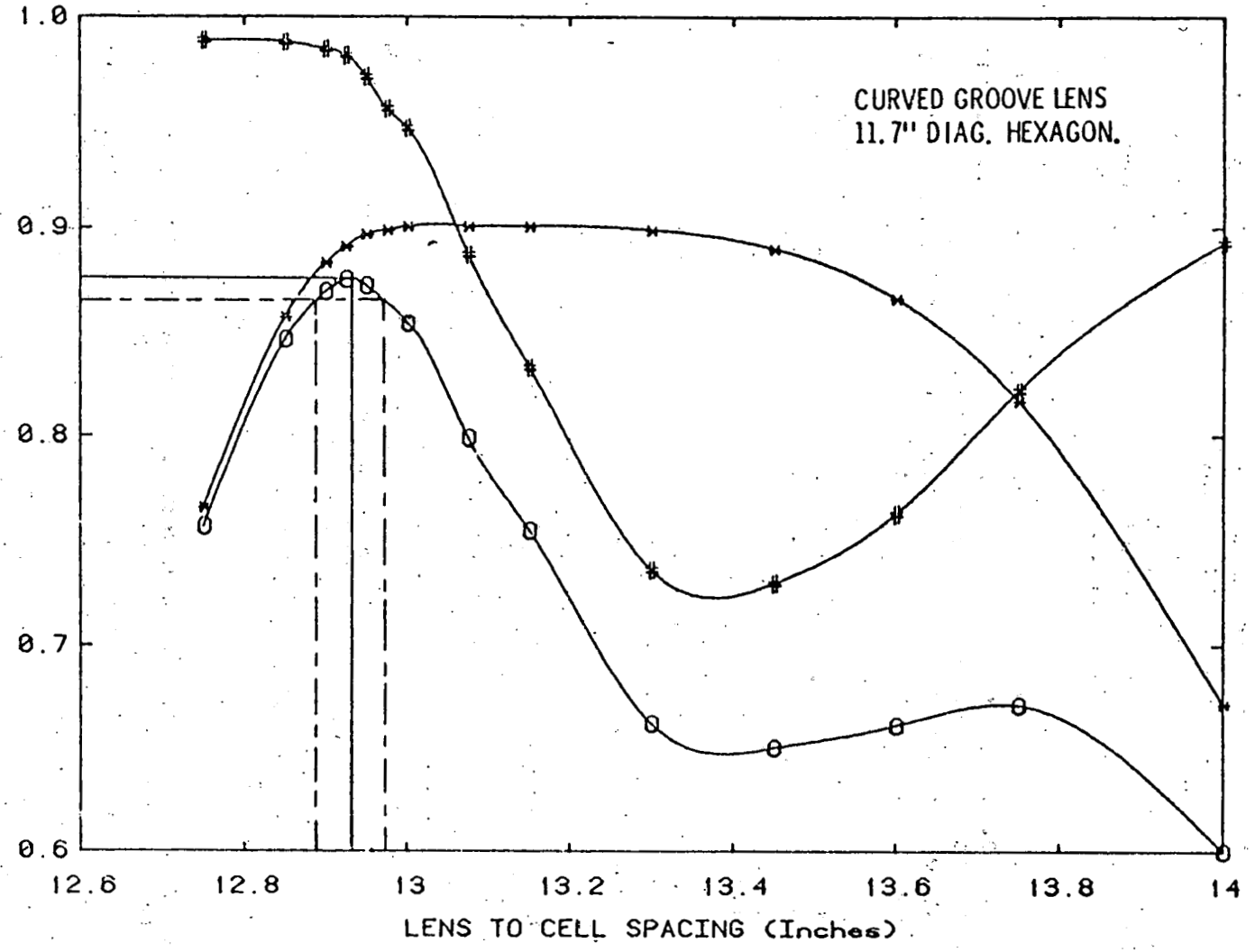

Fig. 2.29 Influence of Lens to Cell Spacing on Optics Efficiency

2.7.3 System Layout - Given the site topography, the array outlines and the model year insolation, it was possible to compute the annual loss of energy due solely to inter-array shadowing, Fig. 2-30. The asymmetry is due to the slight slope of the site (Fig. 2-2). Figure 2-31 shows the loss contours for inter-array shadowing. A preliminary low-loss layout resulting from superimposition of these contours for a multiarray field is shown in Fig. 2-4. The total shadowing loss for this layout is 0.6% in annual energy terms. This computed data can be used to construct an approximate analytical treatment of the economics of the land use (Appendix C). The indicated spacing is optimum for a ratio of array costs to land costs of about 100:1 ($/watt: $/sq.ft., e.g. $25/watt arrays on $10,000/acre land) appropriate for a first experimental system. Since the inter-array land area may be usable for other activities, the definition of land "use" depends on circumstances.

2.7.4 Thermal System - The choice of an active cooling system is dictated by the high cost and limited performance of passive cell coolers, and by the potential application of GaAs concentrator cells to a total energy experiment. Stagnation-point cooling by a liquid jet was evaluated as the highest performance, lowest cost, means of transferring heat to the coolant[6]; Figure 2-32 illustrates the factors involved in optimizing the cooler design--low flow rates conserve pump power, but allow the cell temperature to rise, with loss of generated power; high flow rates involve rapidly increasing pump power, but diminishing returns in the way of extra power from the cell. The storage layout (see below) and coolant inter-connection sizing were selected to minimize parasitic pumping losses. Optimum conditions require a total flow rate of 7 gpm (resulting in about four passes of the coolant through storage per 12-hour day) a pumping requirement of 28 watts per array at 25% pump efficiency and a maximum water temperature of 60°C (35°C initially plus a rise of 25°C). Figure 2-33 compares the radial distribution of heat flux into the coolant with that incident on the cell (taking the lens characteristics into account). An excellent match is apparent. The cooler design is shown in Fig. 2-23.

From the cells, the coolant is pumped to an array of 55-gallon drums which act both as storage for excess heat during the day, and as convectors and radiators during the cooler nights. Figure 2-34 shows the computed performance of such a system under the site conditions, using generalized parameters. It turns out that 55-gallon oil drums have close to optimum surface/volume ratio for the application and are available at lowest cost (Fig. 2-35). The optimum ratio was calculated by equating the heat added to the reservoir during the day to the heat dissipated by convection/radiation. Solving for the surface-to-volume ratio yields an optimum value of 2.6. The ratio for a 55-gallon barrel (including only one

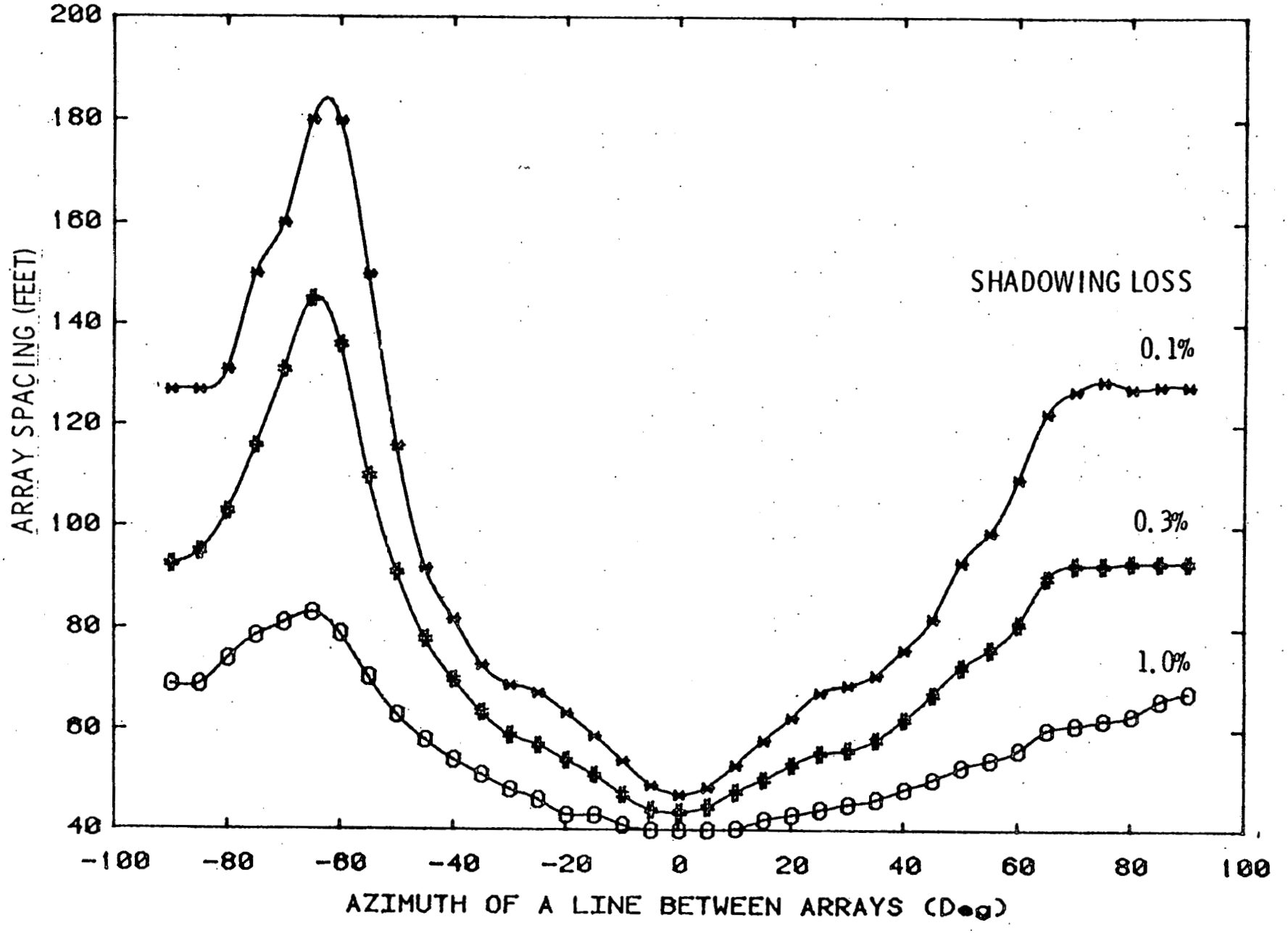

Fig. 2.30 Array Field Power Losses from Shadowing

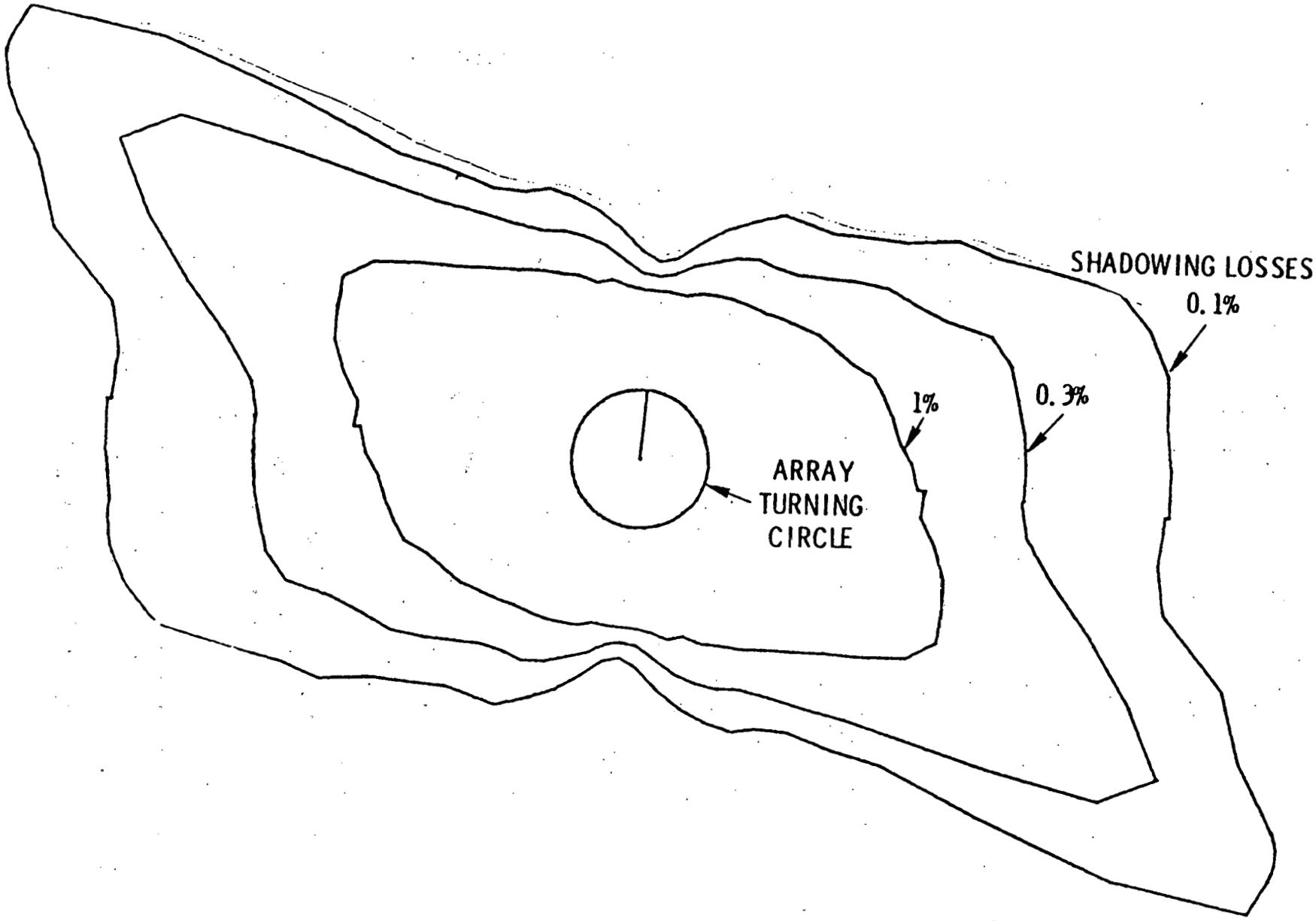

Fig. 2.31 Shadowing Contours for Two Adjacent Arrays (San Ramon)

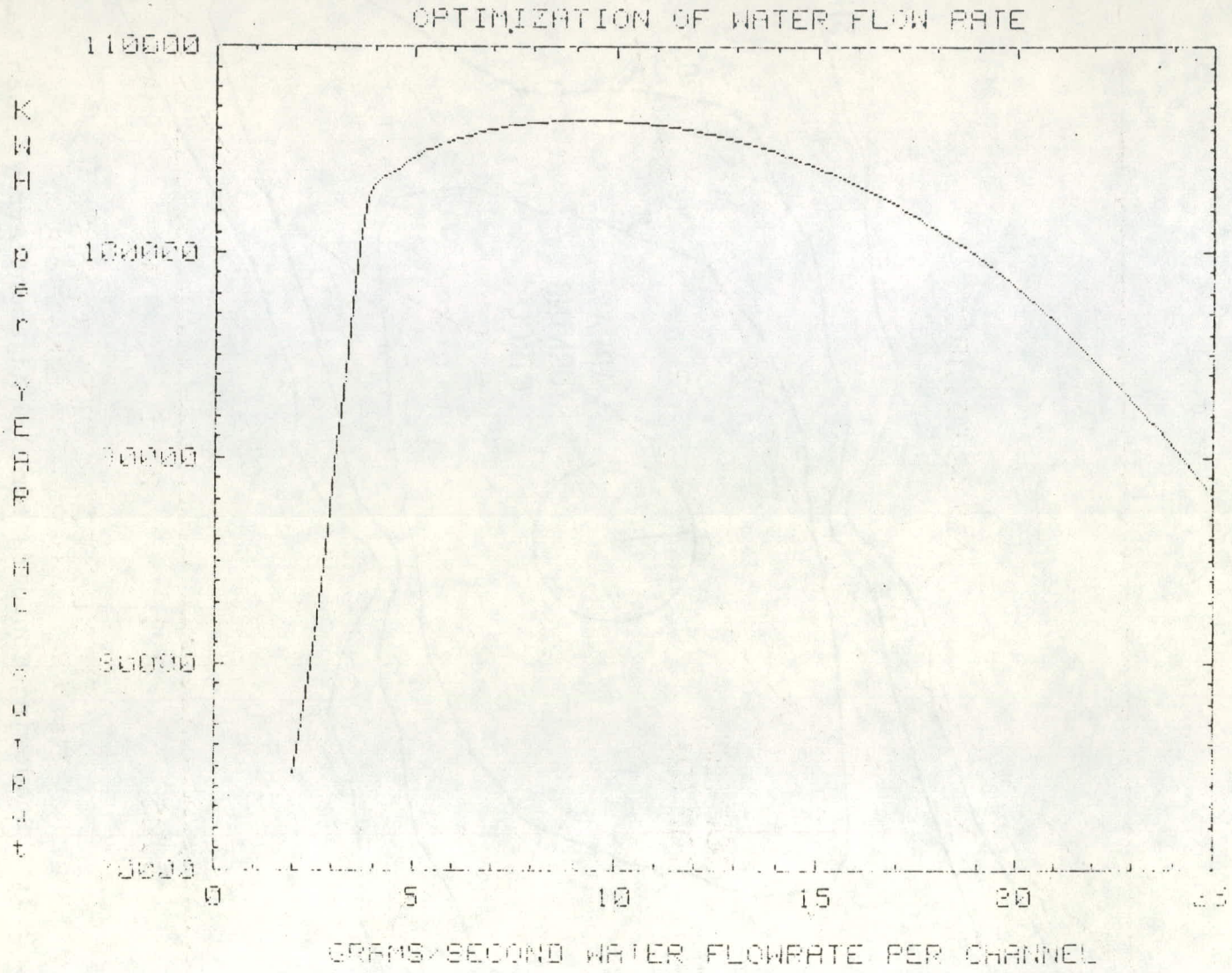

Fig. 2.32 Optimization of Water Flow Rate

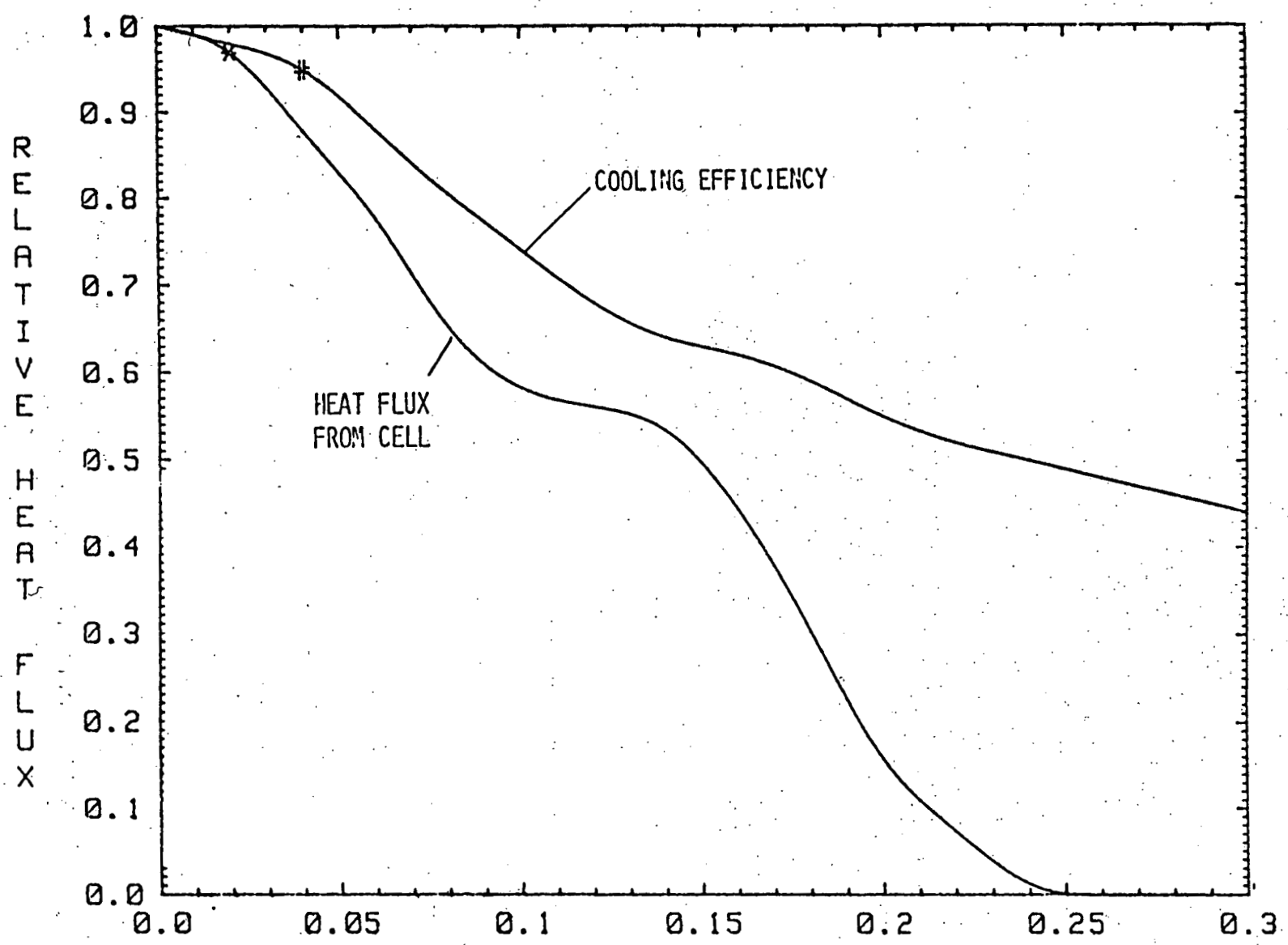

Fig. 2.33 Cell Heat Flux Distribution

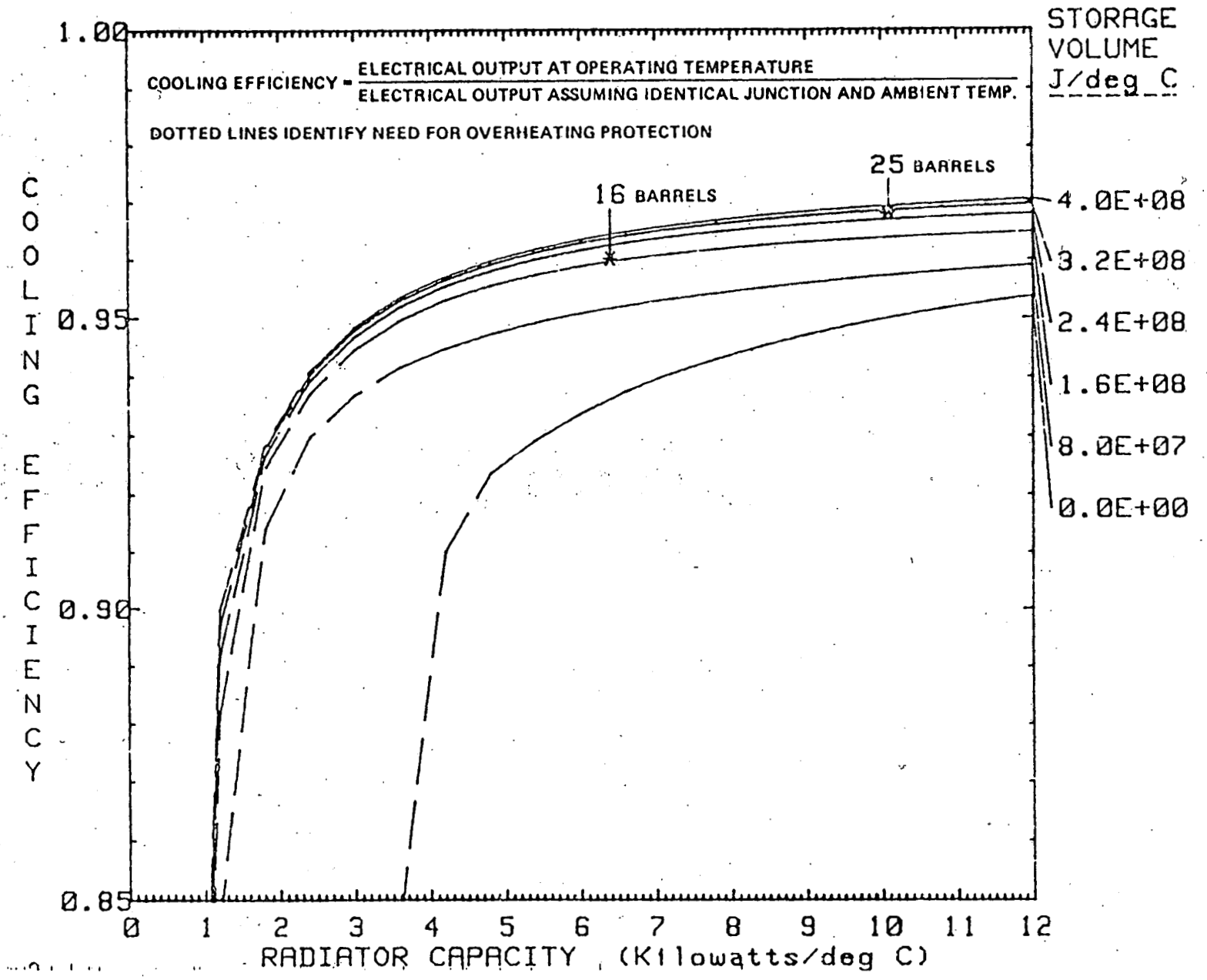

Fig. 2.34 Dependence of Cell Cooling on Radiator Size

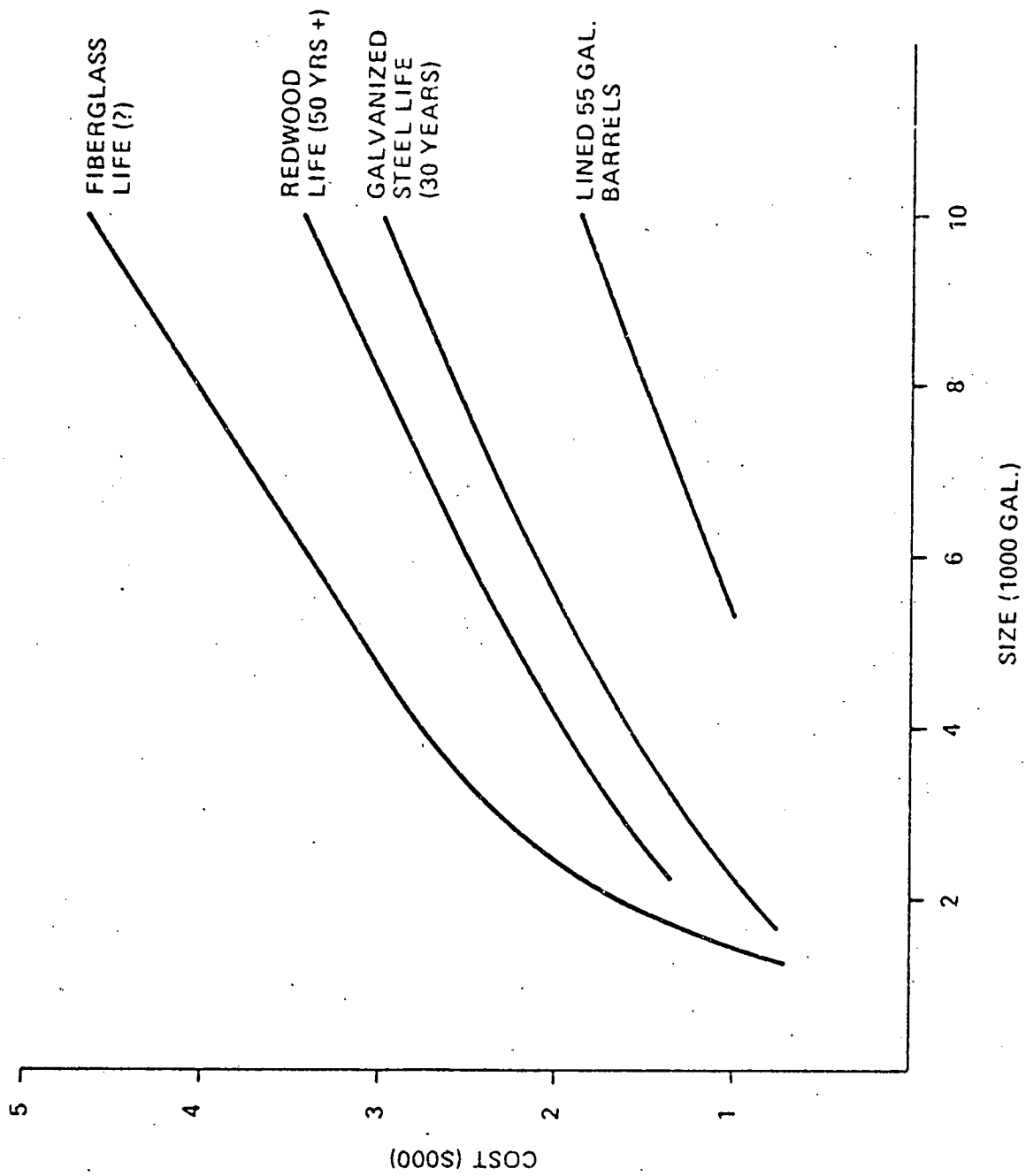

Fig. 2.35 Cost of Water Storage Containers

end in the area calculation) is 2.72. An array of about 26 barrels is close to optimum from the viewpoint of cost-effectiveness. (It can be seen that a much larger array of barrels would give little improvement in system performance.) This type of system is also advantageous from an environmental standpoint.

2.7.5 System Interconnection - The system contains 6160 solar cells which must be interconnected in some fashion. The system model for the solar cell includes the statistical variations in cell performance expected from the cell production line. Fig. 2-36 shows the ratio of system fill factor to average cell fill factor as a function of the number of cells in parallel. The paralleling averages out the mismatched cells, permitting loading of each cell closer to its maximum power point. This same effect can be used to average out lens variations and alignment errors in the optics, if present. Protecting bypass diodes are required only for each two groups of paralleled cells, so increasing the number of cells in parallel reduces the cost of the protection diodes.

The tradeoff in the direction of increased paralleling comes from the cost of the large cross-section interconnecting wiring (from array to array) and a reduced inverter efficiency resulting from a lower operating voltage and a higher operating current. The final choice was for 11 cells in parallel, and 560 of these groups in series (Fig. 2-25). Copper wire costs are significantly reduced by using a 480-volt inverter instead of a 208-volt inverter. On the other hand, use of a significantly higher voltage would substantially increase insulation costs, while at the same time decreasing the effectiveness of cell paralleling in relaxing cell costs.

2.7.6 Overall System Performance - Figure 2-37 summarizes graphically the tradeoffs arrived at as a result of optimization processes on the various components and inter-component relationships. A yearly average system efficiency (inverter AC output to solar insolation input) between 15 and 16% is predicted for the system at the time of installation.

2.8 Safety/Reliability/Availability/Maintainability

2.8.1 Allocation of Reliability Goals - At the beginning of the design phase, reliability goals were allocated to all elements of the array field, and were explicitly considered in the design process.

2.8.2 Failure Modes Effects and Criticality Analyses -

Detailed fault trees were constructed, see Fig. 2-38. These trees are structured with the undesired general event at the top, followed (below) by the undesired sub-events.

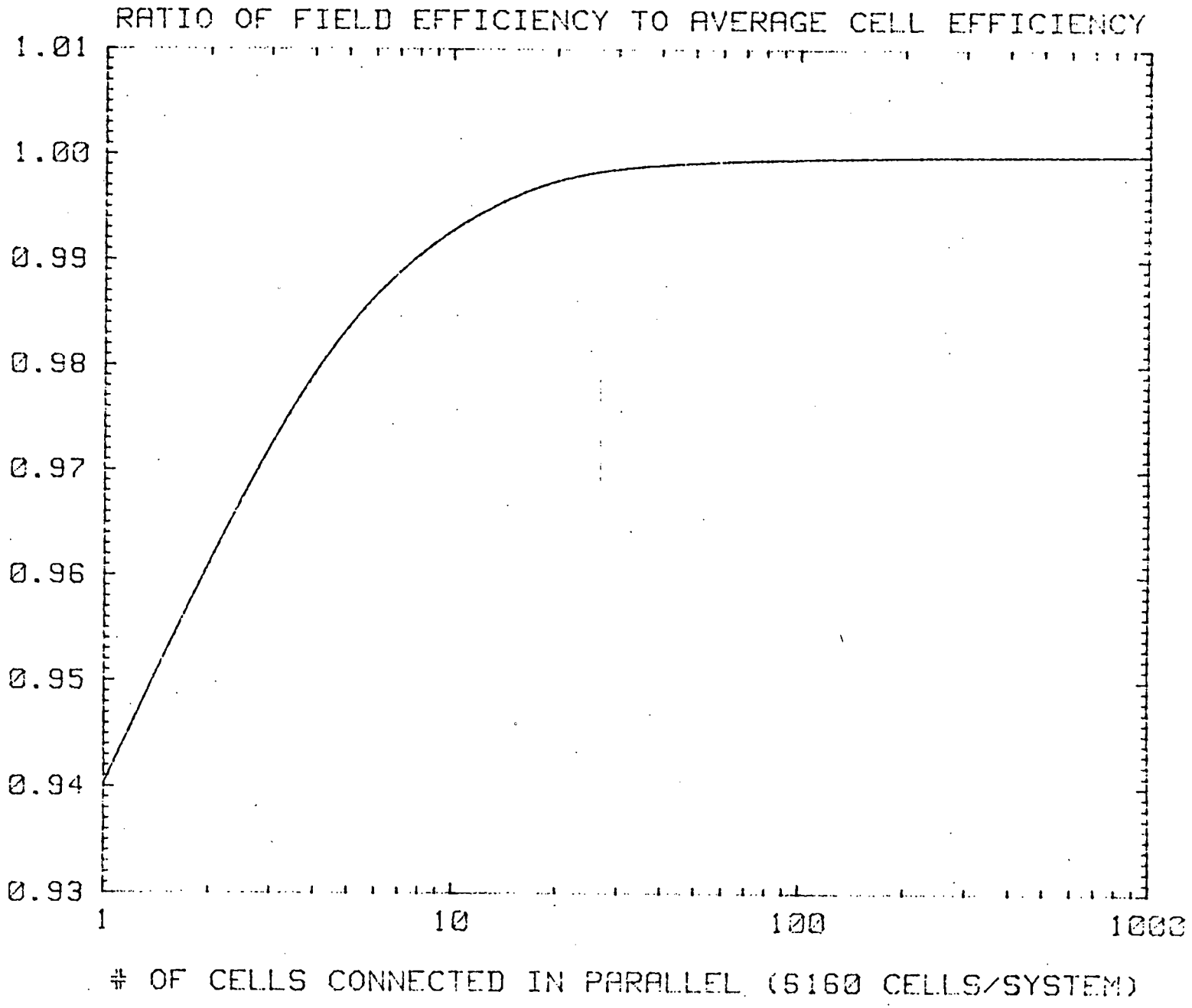

Fig. 2.36 Ratio of Field Efficiency to Average Cell Efficiency

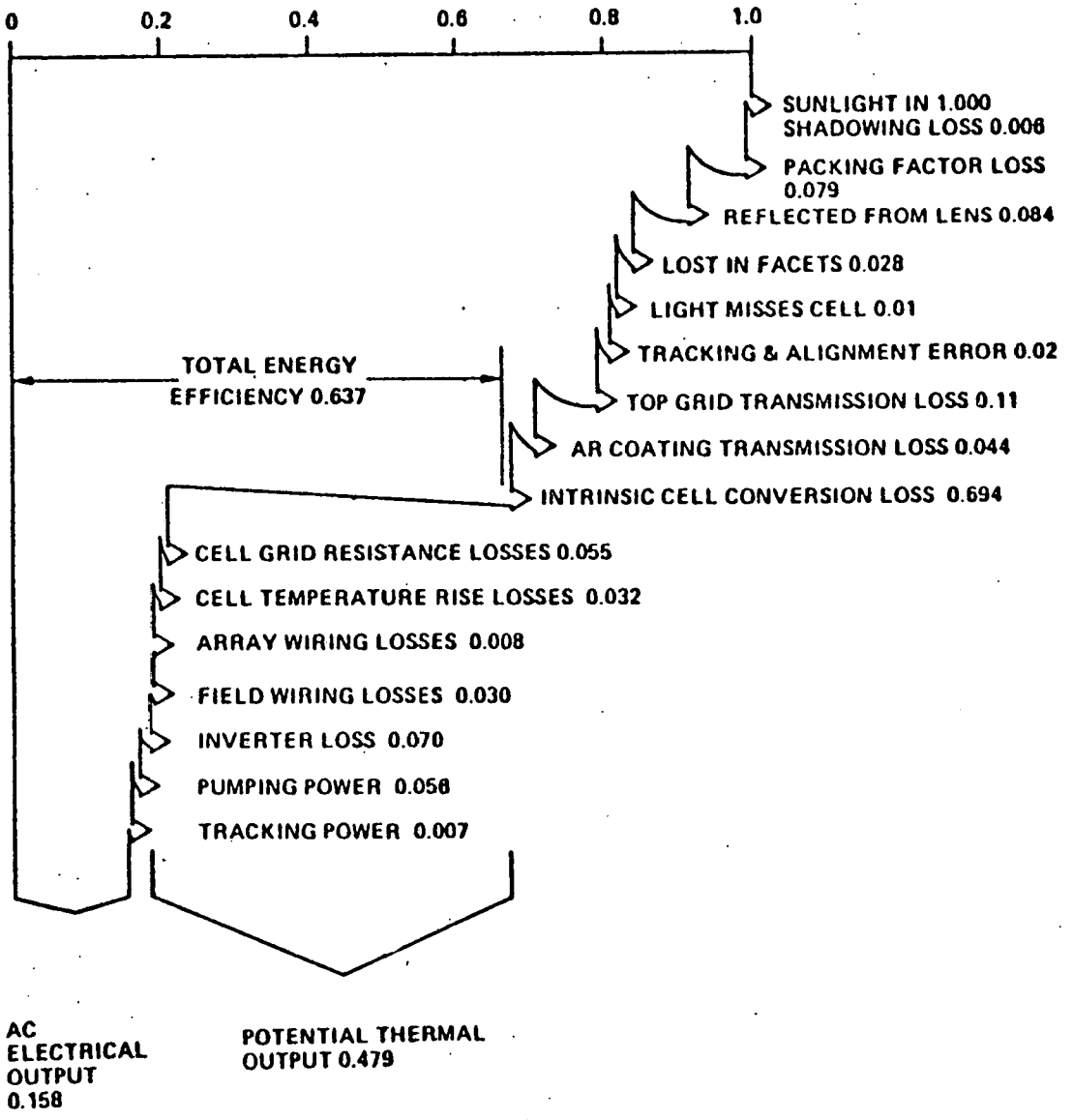

Fig. 2.37 Ideal Theoretical Efficiency at Each Point in the System (Yearly Average)

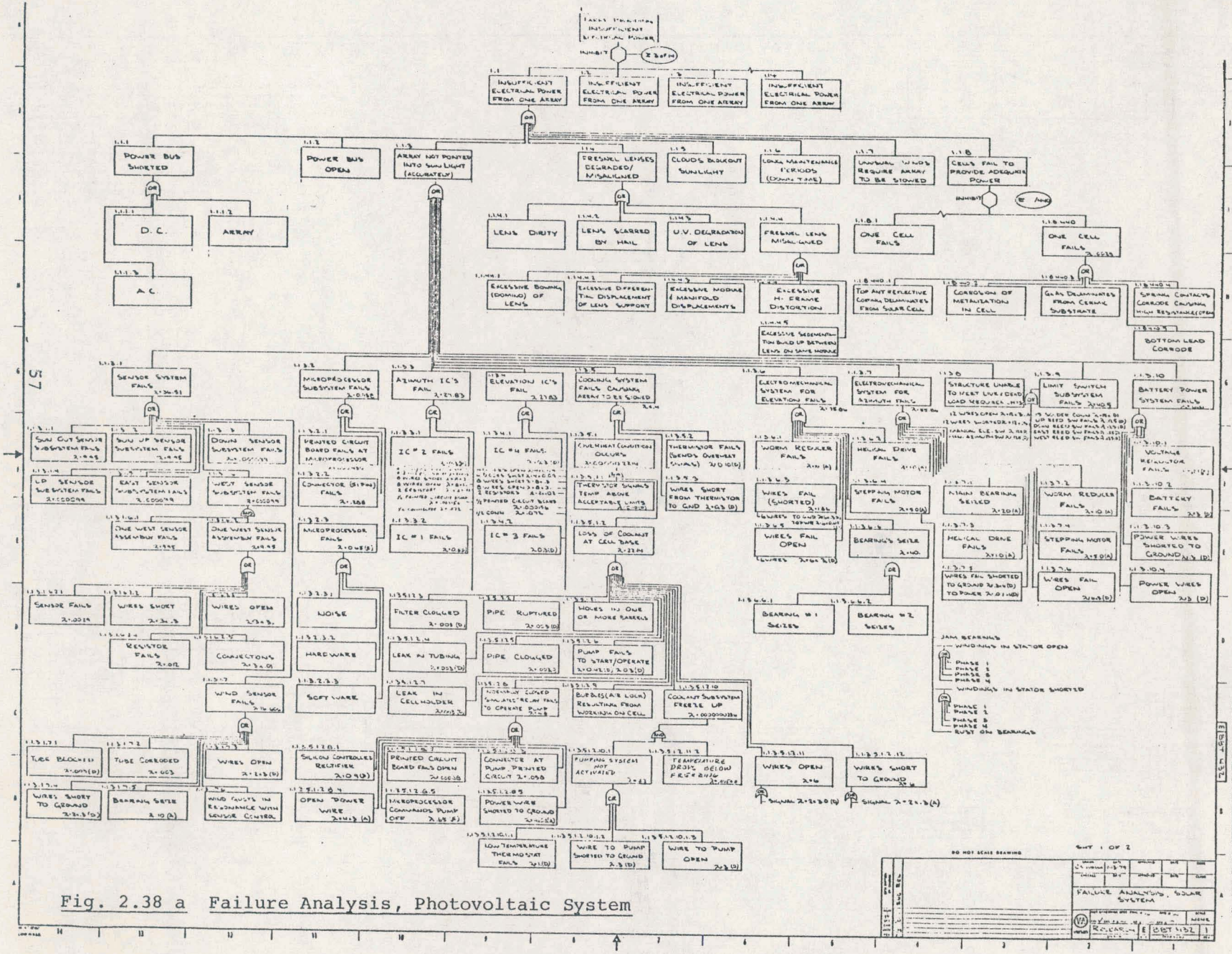

Fig. 2.38 a Failure Analysis, Photovoltaic System

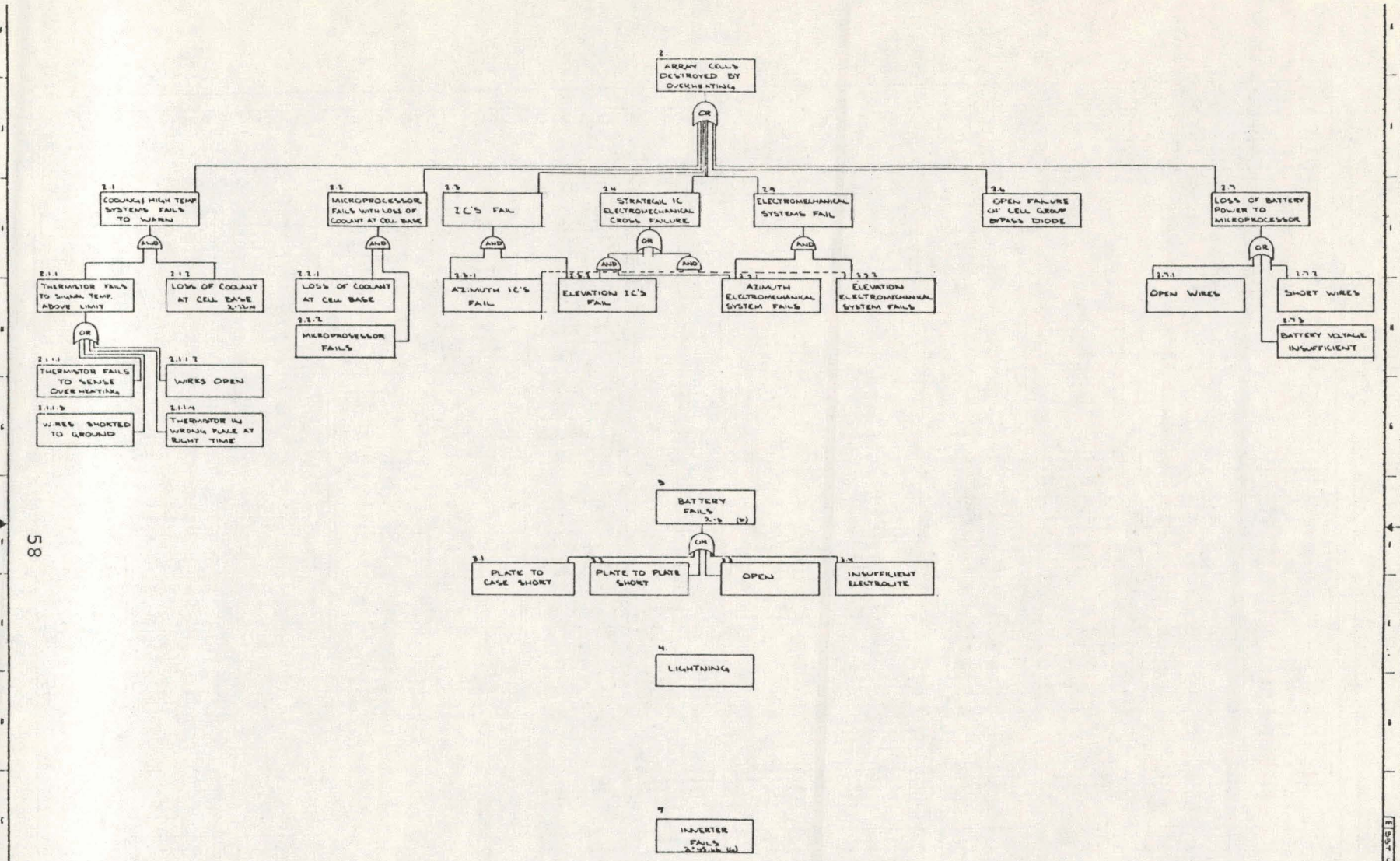

58

2. DATA:
A. A.E. GREEN & J. BOURNE "RELIABILITY TECHNOLOGY" WILEY INTERSCIENCE (1972)
B. C.O. SMITH INTRODUCTION TO "RELIABILITY IN DESIGN" MCGRAW HILL (1977)
C MIL. HDBK. 217 B "RELIABILITY PREDICTION" DOD (1974)
D "REACTOR SAFETY STUDY" WASH 1400 US. NUCLEAR REGULATORY COMMISSION (1975)
E PHONE CALL WITH DR CRAIG BARRET, QUALITY DIRECTOR, INTEL
F PHONE CALL WITH MR WARD ENERGY QUALITY MANAGER, FAIRCHILD.
G PHONE CALL WITH MR HANS MEYER QUALITY MANAGER, WIND WORLD Co.

1. ALL FAIL RATES IN FAILURE / 10^4 HOURS

NOTES:

SHT 2 OF 2

DO NOT SCALE DRAWING

SEE SHT 1

FAILURE ANALYSIS, SOLAR SYSTEM

Fig. 2.38 b Failure Analysis, Photovoltaic System

These include the potential hazards and failures that are the immediate causes of the top event. These events may be inadvertent or unauthorized functions, or the failure of the system to perform a required operation, and are determined from analyses of specific safety and reliability considerations. The analysis works down from the array field to determine combinations of events (for example, steady state winds in excess of 30 mph, unusually cloudy days, etc.) and component failures (electrical, electronic, mechanical, hydraulic) which could bring about the undesired result.

The fault tree is quantitative as well as qualitative. This quantitative evaluation includes the failure rate, λ, in failures per 10^6 hours, the mean time to repair, τ, in hours and the probability, π, of occurrence of an event. The rates for common piece parts (i.e., resistors, diodes, capacitors, etc.) are defined by MIL-HDBK-217B (including Change Notice 1) including appropriate derating corrections. Data on some unique hardware, such as the Fairchild 5-Volt Positive Voltage Regulator, the Intel Microprocessor, Lambda Dual Power Driver, etc., were derived from actual failure test data. The requirement for detailed reliability prediction was passed on to all participants in the experiment. For example, the 50-kW line commutated inverter received a full MIL-HDBK-217B analysis.

During the course of the design phase, conceptual and development design reviews were held. The fault trees played a part in guiding this process and in the minimization or elimination of single point failures. For example, a solid state relay had initially been planned to turn on the water pump either during operation or freezing weather. Such a normally open relay would fail open causing system degradation. During a design review, this concept was replaced by the present normally closed simulated relay which would cause the water pump to be and remain activated. This is a "fail safe" system. The fault trees also form the basis for the hazard analyses which comprise safety studies.

2.8.3 Reliability - Quantitative analysis of the fault tree has been performed using the Varian Fault Tree Program. Figure 2-38 contains the results of this quantitative analysis: the likelihood of occurrence of all intermediate and top events, the probabilities of the critical paths and an importance ranking of the component failure modes and minimal cut sets. Cut sets are any set of system components which, when they are fail simultaneously, cause the system to be in the failed state. A minimal cut set is the smallest set of system components which will cause the system to be failed. The system is in the failed state if at least one of its minimal cut sets is in the failed state. The components of a particular minimal cut set act as if they were in parallel, while the group of all minimal cut sets act as if they are in series.

Examples of the quantitative analysis of the Solar Energy Tree by the Varian Fault Tree Program appears in Appendix E. The first table provides the λ and τ data for components and where applicable π data for inhibits and probabilistic events. Table 2 indicates that the system will be analyzed with resultant outputs at start of operation, two weeks, one month, one year, and three years. Table 3 identifies the components associated with each of the 139 cut sets found in the system. Table 4 provides for each of the 139 cut sets at all five times: failed probability (Q), minimum cut set failure rate (W), minimal cut set failure intensity (per hour) (L), expected number of failures in that cut set to time T (WSUM), and the probability of one or more failures to time T (FSUM). Table 5 provides the system evaluation of each of the above parameters for all five times. Table 6 orders all 139 cut sets from most likely to least likely, for all cut sets with failure probabilities greater than 10^{-12}. Finally, Table 7 provides X and Y coordinates on the fault tree of Fig. 2-38 for all the elements in the tree, which are listed for convenience in alphabetical, then numerical, order. Appendix E only lists a portion of the program output. Once having the total output, Table 6 provides the probability of failure for each cut set. Table 3 can then be used to identify the components that make up a particular cut set under study. Table 7 then provides drawing coordinates (drawing BBT-432), so that the location of the components within the system can be identified. Drawing BBT-432 is attached and is an improved version of Fig. 2-38. It contains all component identification numbers referred to in Appendix E.

The fault tree shown is the best available prediction of system performance. As data becomes available from Production Assessment Testing (Post ATP reliability testing) and actual field experience, this information can be introduced to the fault tree and the results reassessed.

3.0 COMPONENT DEVELOPMENT AND SPECIFICATION

3.1 Specification Methodology

Software was developed under the Phase I program to describe the components and subsystems of the photovoltaic solar system, consisting of drawing package and a materials list, all included in the Phase II Installation Proposal furnished separately. The materials list (indented bill of materials) includes over 800 items required for the fabrication of the photovoltaic system. It is intended for: (1) procurement of components and subassemblies; (2) identification of order of assembly; and (3) as means for costing individual subassemblies. For that purpose, a cost allocation code (VPC) was used, as defined by the ERDA/EPRI evaluation methodology.[7] The completed materials list includes components costs at various procurement levels, and can be used to determine the cost elements associated with capital plant investment.

3.2 Photovoltaic Array Development

Under Phase I, the development of this subsystem was carried only to the stage of detailed design and preparation of working drawings. The first full prototype would be fabricated under Phase II; however, subcomponents (lens/cell cluster assemblies) were fabricated and tested.

3.2.1 General Characteristics - The array is shown schematically in Figs. 2-12 and 2-20. Overall dimensions of the fully assembled tracking array are approximately 10.3 meters long by 2.8 meters high (34' x 9') and weight 2200 kilograms (4800 lb). The mechamical structures are fully described and specified in the separate Installation Proposal. Development status of critical subcomponents are described in the following:

3.2.2 Collector Subsystem

3.2.2.1 Fresnel Lens - As discussed earlier, this will be a novel design of constant-groove-depth curved-facet plano-Fresnel in hexagonal plan form, 25.74 cm across the flats of the active area, and realized by compression molding in DuPont Lucite 147K-NC10 or equivalent (see Fig. 2-13).

Production tooling was fabricated and twelve lenses from this tooling were delivered to Varian; preliminary testing indicates that they perform close to theoretical expectations (Section 2.6.3.1).

3.2.2.2 Lens Support Cone - This part is illustrated in Fig. 2-15. It will be fabricated by injection molding of acrylic plastic (in order to match the thermal expansion of the lens). A number of vendors are available for design and fabrication of the tooling, and for volume production of the part, which has been designed with the injection molding process in mind. Prefabricated parts have been assembled from flat acrylic sheet stock in the approximate final form, for use in testing of prototype lens/cell combinations (see photograph, Fig. 3-1). In order to avoid over-heating of the cone before acquisition of tracking, it is provided with a thin aluminum internal heat shield, heat-sunk to the array frame via the attachment bolts.

3.2.2.3 Solar Cell and Package - This assembly is schown schematically in Figs. 2-16, 2-17 and 2-18. The package is shown separately in Fig. 3-2. Cell specifications are tabulated in Table 3-1.

Table 3-1. Solar Cell Specifications

AR Coating Material	Si_3N_4
Quarter Wave Photon Energy	2.06
AlGaAs Window Thickness, microns	0.6
Al in AlGaAs, %	93
Photolith. Line Width, microns	3.5
AlGaAs Diffusion Length, microns	0.5
p-GaAs Difsusion Length, microns	5
Junction Depth, microns	1.2
n-GaAs Diffusion Length, microns	3
n-GaAs Thickness, microns	30
Bandgap, eV @ 30°C	1.415
Grid Lines Spacing, Cent. to Cent., microns	80
Grid Line Width, microns	8.7
Cell Diameter, cm	1.245
Contact Metal Resistivity, ohm/cm	1.59×10^{-6}
Carrier Conc. of AlGaAs, cm^{-3}	5.0 E + 17
Doping Conc. in p-GaAs, cm^{-3}	7.0 E + 17
Tin Conc. in n-GaAs, cm^{-3}	5.0 E + 17
Ohmic Contact Resistance, ohm/cm^2	1×10^{-4}

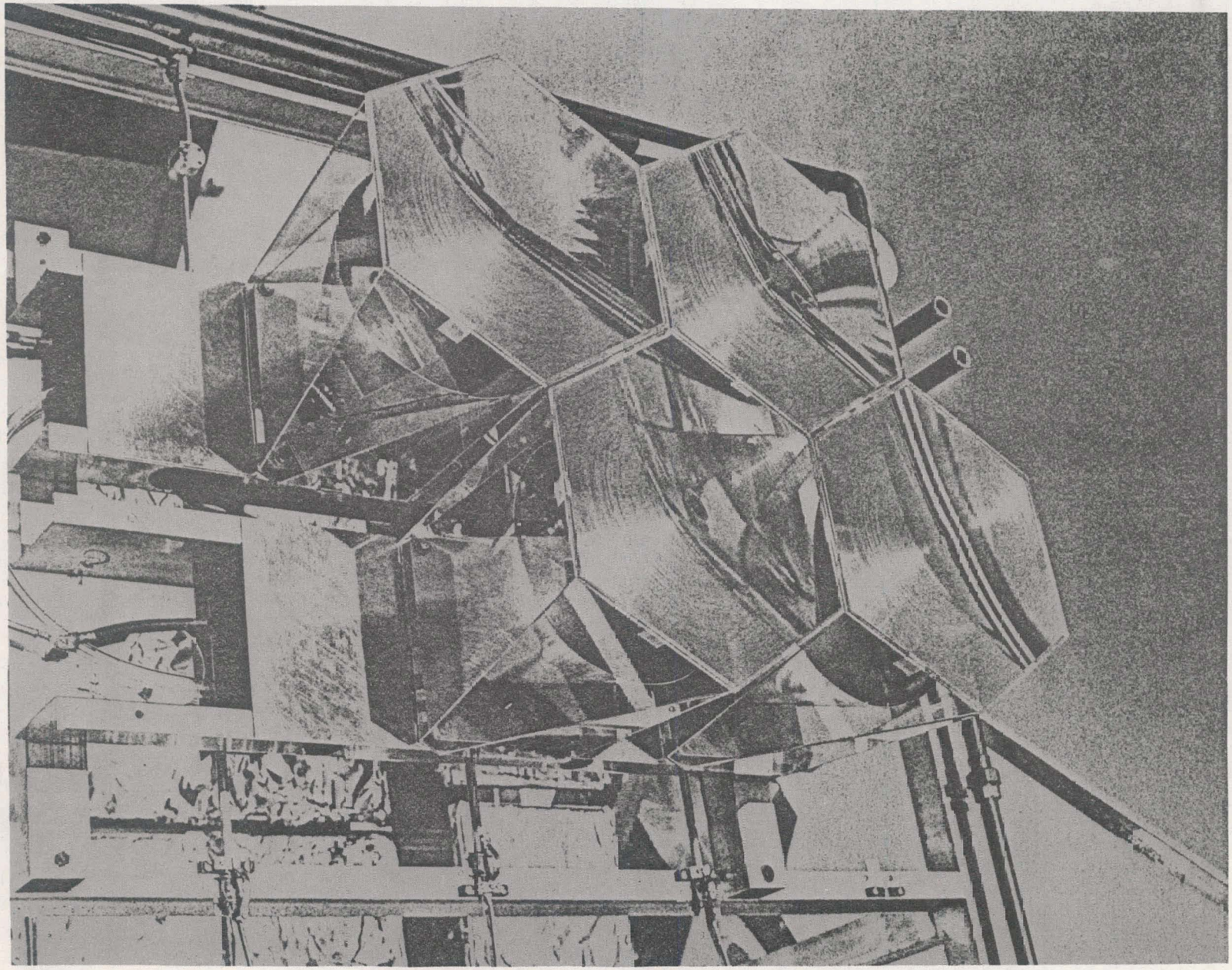

Fig. 3.1 Prototype Fresnel Lens Assembly & Photo

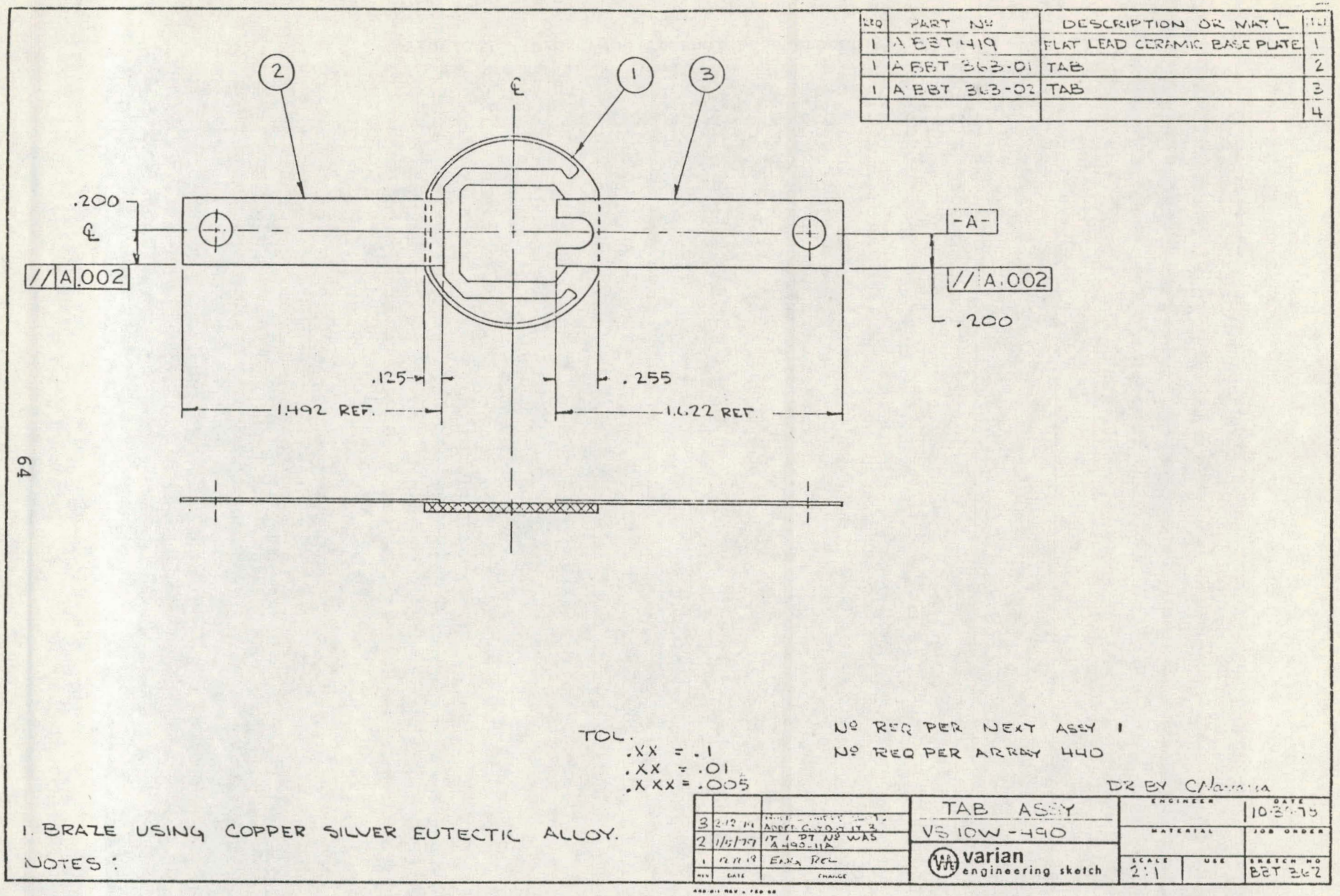

Fig. 3.2 Cell Package

Al_2O_3 heat sinks are fabricated by Wesgo (Belmont, Ca). Metallization is carried out by the Eimac Division of Varian. The lead frames are procured from Chem-Etch Corp., Torrance, CA. These consist of Ag-plated 0.007" Cu, photoetched and formed to shape. The GaAs cell is fabricated on n^+ substrates grown internally at Varian. The epitaxial layers are presently grown by both liquid phase and organometallic methods, which are being scaled up for higher throughput. These developments are described in Appendix F. Part of the effort under the design phase was devoted to startup of a pilot production facility to achieve the throughput of completed cells required for the projected installation phase. The facility and the results of the program are described in Section 4.4 and in Appendix G.

3.2.2.4 Cell Cooler - The cell and ceramic heat sink package are clamped in a plastic (polysulfone) holder, Fig. 2-23, with provision for jet cooling the back of the ceramic. The flying tape leads from the cell package are captured under threaded terminal bolts below the radial flange on the cooler. This flange bolts to the base of the cone and can be adjusted transversely for optical alignment before clamping in final position. The cooler is designed for injection molding. Machined parts have been fabricated for prototype testing. The plastic parts are protected from concentrated sunlight by the aluminum heat shield of the main lens support cone. Design of the cooler is based on detailed design data in the literature on stagnation-point cooling by jets (Section 2.7.1) and is similar to the design used successfully on our rooftop array, operating at 1000 suns.

3.2.2.5 Prototype Collector Cluster - A cluster of two lens/cell collectors from one module together with two adjacent collectors from the neighboring module was constructed for a test of assembly and operating performance of the new features introduced into the design (Fig. 3-1), to be carried out under Phase II.

3.2.2.6 Optical Alignment - The rear of the cell holder is provided with a hole to accept simple adjustment tool for transverse alignment of the cell after assembly of the array. Depending on experience with maintenance of alignment during shipping, arrays could either be fully aligned at the factory, or finally aligned at the site. Preliminary design concepts have been evolved for a microprocessor-automated alignment equipment, Section 4.6.2.

3.2.3. Module Assembly - Low assembly costs demand a design approach allowing factory assembly of low-cost multicell modules, which can be rapidly mounted and interconnected on the frame to form a complete array. This requirement is met by using a low-cost lightweight aluminum box channel as the structural support for a string of ten lens-cell collectors. The channel is a 4" x 5.75" U-shape with flanges, bent up from 0.063" 5052-H32 aluminum stock, the box being completed for stiffness by bolting

the cone across the open face. Adequate accuracy in fabrication of this channel on conventional equipment was verified by formation of prototype parts and dimensional inspection. The limited number of parts for the 50 kW installation could be fabricated in the same way. For large scale production, utilization of a mill run of extruded channel is envisaged. An aluminum channel was evaluated as more cost effective in this weight-sensitive application than steel. To form the array, forty-four of the completed modules are bolted vertically, side by side in a staggered close-packed configuration, across the tubular arms of the H-frame (Fig. 2-20), with allowance for differential expansion. In assembly, the flange of the cell cooler bolts to the base of the lens mounting cone, with the cell protruding into the interior of the cone, and with the aluminum radiation shield and lens already in position. This sub-assembly is then bolted to the channel using four studs protruding from the base of the cone. The use of oversize holes in the cooler flange allows the cell position to be adjusted transversely to center the solar image on the cell, using the adjustment tool. If accumulation of tolerances exceed the available cell motion, individual studs for the cone mounting can be shimmed to realign the cone.

Three-inch holes punched in the back of the channel allow access to the back of the cell for cell replacement, alignment, and electrical and coolant connections. These holds are closed by plastic covers. Likewise the ends of the channels are closed off, leaving electrical and coolant circuits enclosed in the channels, but the back of the array generally open to allow convective cooling of the shaded sides of the cones. Thermocouple measurements of temperature at typical points inside the cone show negligible rise above ambient in operation.

Cells of the ten-cell module are connected in series for power takeoff and also for cooling. Cells of adjacent modules are also paralleled to reduce non-uniformity effects (including shadowing), and every second row is provided with shunt diodes for shadowing protection (Fig. 2-25). Coolant connections are made by 3/8" ID neoprene tubing. The flexibility of the coolant and electrical lines is adequate to allow cell optical alignment and avoid strain on the cell clamping arrangements. Electrical busbars and coolant manifolds are provided at top and bottom of the array. Power takeoff for the complete array is achieved by hanging flexible cables terminating in an adjacent junction box. The coolant connections are made by flexible hose terminating on the pedestal.

3.2.4 Structural Subsystem - Details are shown in Fig. 2-20. This subsystem consists of pedestal, Y-frame, H-frame, channels, cones and lenses. With the exception of the lenses all structural elements are constructed of readily-available materials, by standard techniques such as molding, welding, etc. The design

is such that tolerances are readily achieved without sophisticated manufacturing techniques.

The first 15 resonant modes of the structure were calculated, with frequencies up to 20 Hz. The lowest two modes, torsional oscillations of the array on the pedestal with the frame vertical and horizontal respectively, lie at about 2.5 Hz. The next highest, a symmetrical bowing of the H-frame in its fundamental mode, occurs with the frame vertical at 3.7 Hz. None of these resonances are expected to give rise to instabilities in the tracking feedback loop.

3.2.5 Pedestal and Foundations - The pedestal is shown in Fig. 3-3. The foundation will be formed by drilling a 30-inch standard auger hole 10 feet deep at the appropriate site location, setting reinforcement rods and anchor bolts, and pouring concrete. The foundation is designed for the array to withstand a 60 mph wind, unstowed, taking into account the expansive soil conditions of the site (low allowable stress when wet). Arrays will be transported to the site complete with pedestal, which contains the azimuth drive mechanisms, and installed by bolting to the foundation.

3.2.6 Heat Exchanger - Dissipation of reject heat to the atmosphere is accomplished over 24 hours by a semi-passive system for each photovoltaic array, with storage. The storage/cooling element is an array of 26 drums and one expansion tank disposed for efficient cooling by radiation and convection (Fig. 3-4). The barrels are standard storage drums with plastic linings, widely available from commercial sources. These are mounted on redwood 4 x 4s laid on gravel. The coolant is circulated through the solar cell array and the barrels during the day, using a commercial high efficiency pump and interconnecting PPVC conduit sized to reduce pumping losses to a negligible level. Each array is provided with an expansion tank to allow for relative thermal expansion without loss of coolant. Direct solar heating of the barrels is prevented by an open lattice-type sunshade (Fig. 3-5) constructed from low cost metal siding.

Circulation is turned off at night to conserve pump energy, unless freezing conditions are detected, when the circulation is restarted to prevent freezing of coolant behind the cells, and cracking of the cell heat sinks.

3.2.7 Power Cable and Grounding - A 500 MCM copper power conductor has been selected to provide negligible voltage drop between the arrays and the inverter assembly located inside the control building. The grounding for the project, shown in Fig. 2-4, is divided into four separate areas: (1) array grounding; (2) building grounding; (3) array-building interconnection; and (4) fence system.

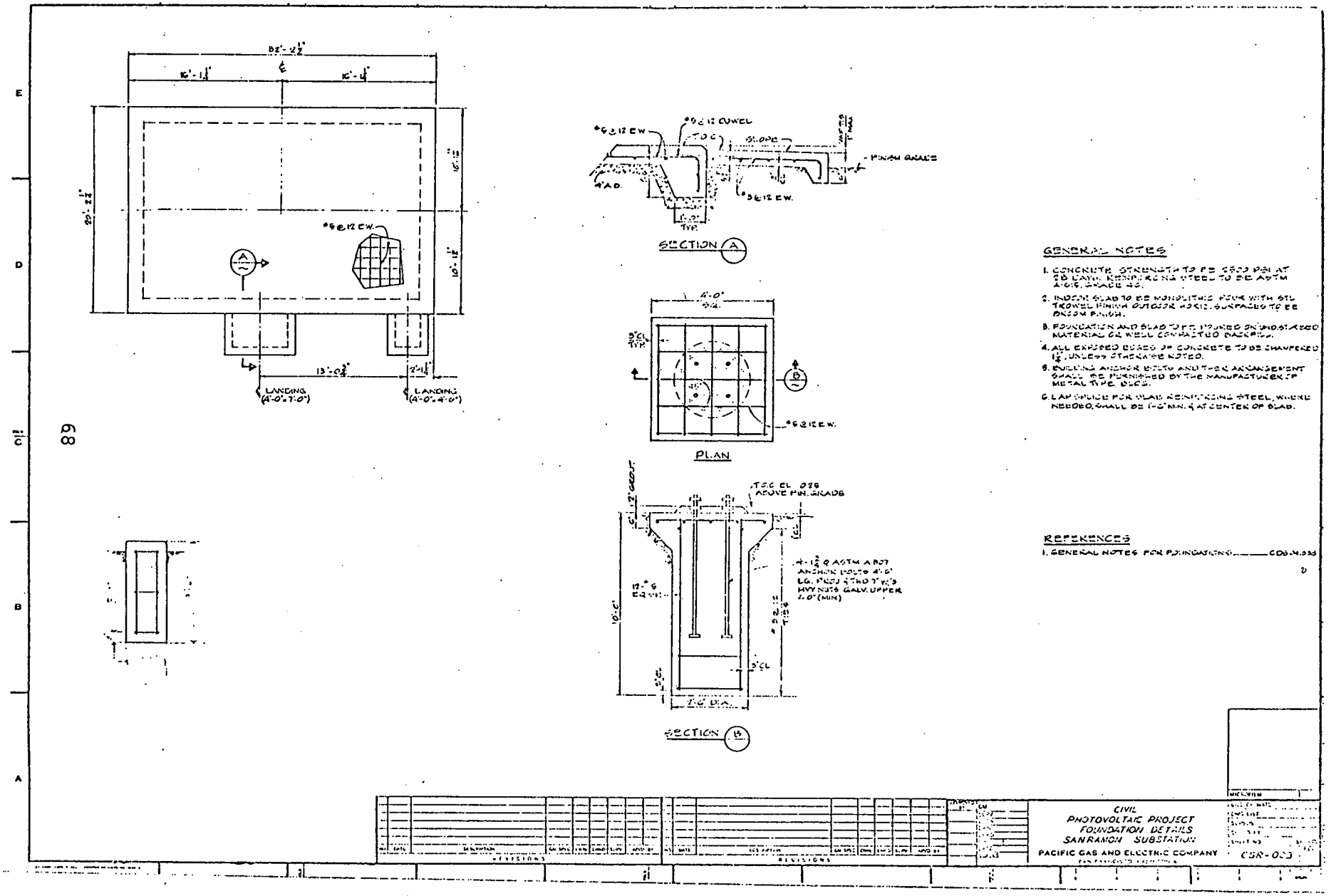

Fig. 3.3 Foundation Details

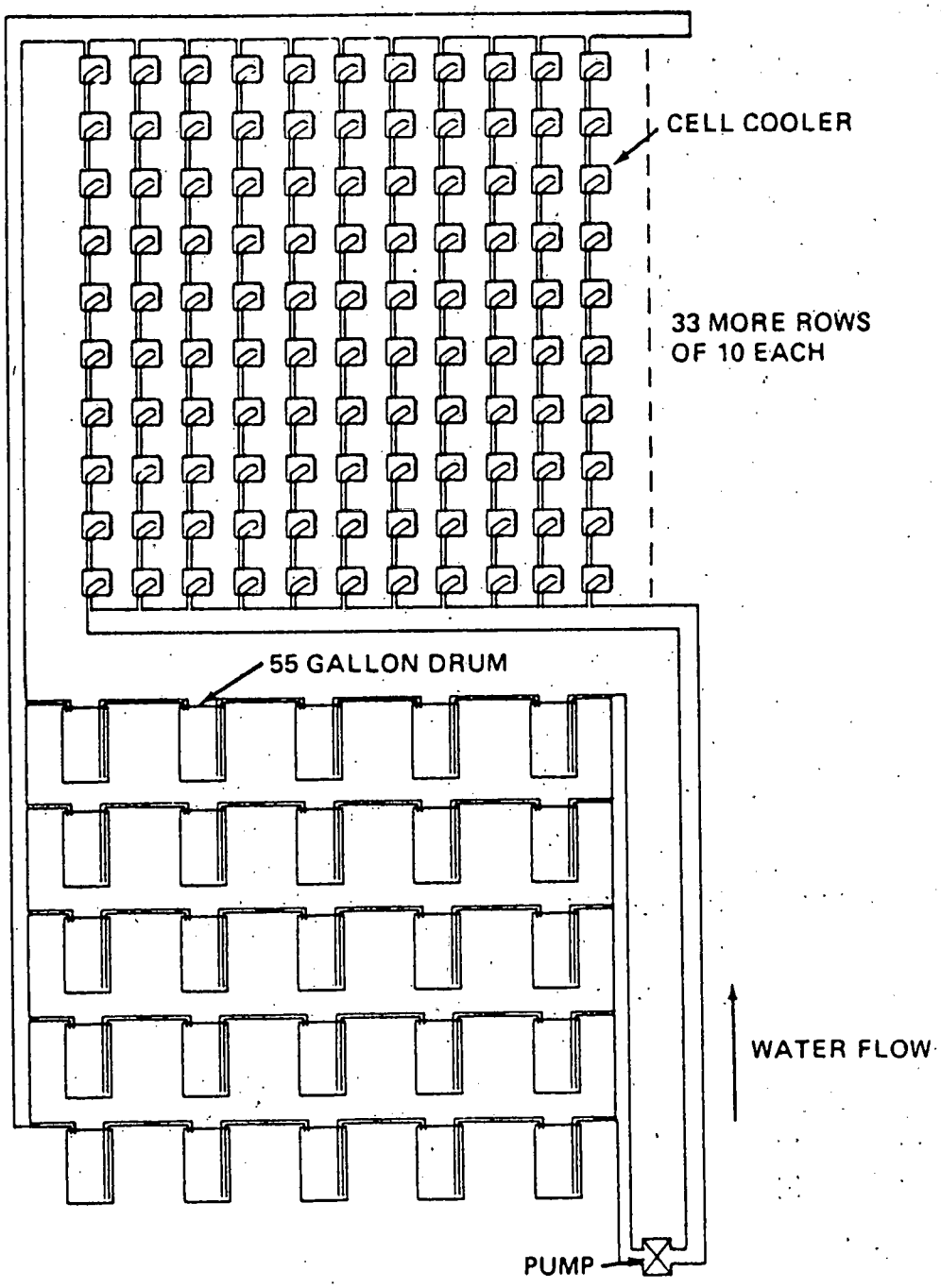

Fig. 3.4 Cooling Subsystem Plumbing Diagram

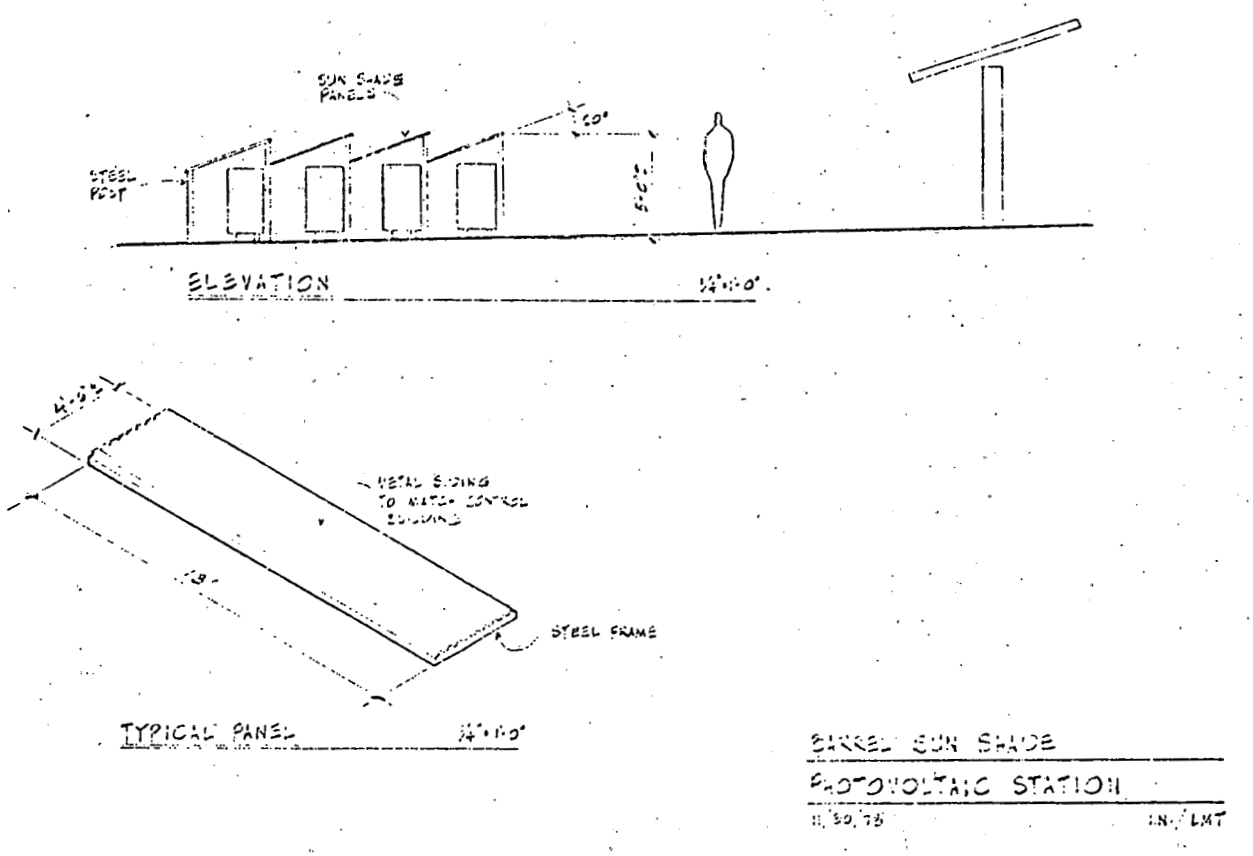

Fig. 3.5 Barrel Sun Shade Photovoltaic Station

(1) Array Grounding - Each array is grounded to a 12-foot long, 3/4" diameter, copper covered steel core ground rod by No. 2/0 AWG copper welding cables. The ground rod is adjacent to each array and is cad-welded to the connecting cable. The welding cable, because of its flexibility, is used to ground the arrays, the connection being made to the superstructure which moves as the array tracks the sun.

(2) Building Grounding - The control building ground mate is No. 2/0 AWG copper embedded in the foundation in a rectangular shape with one No. 2/0 AWG copper cable bisecting each of the parallel cables in the rectangle. Five 3/4" diameter, 12-foot long, copper covered steel core ground rods are utilized, one at the center of the grid and one connected to each corner of the rectangle, located outside of the foundation. All ground taps to the equipment inside the control building are made to this grid and are precast into the foundation.

(3) The individual array grounds are interconnected with each other and are tied to the building ground grid via the cable tray system. The building grid and each individual array ground is bonded to the tray system with No. 4 AWG copper. All tray lengths, bends, tees and other fittings are bonded to each other with No. 4 AWG copper cable to provide ground continuity.

(4) Separate from the ground system described in numbers 1, 2 and 3 above is the fence grounding system. The fenced area is rectangular, 490 feet by 220 feet with one 20 foot gate. The fence fabric is No. 9 wire, galvanized with a 2" mesh supported in tubular metal posts. At each corner and halfway down the long side of the fence on each side a 5/8" diameter, 8-foot long, copper covered steel core ground rod is connected by No. 1/0 AWG copper cable to the nearest fence post. The double 20-foot gate is grounded on both sides to its supporting pole with flexible copper braid and the supports are then connected to each other with No. 1/0 AWG copper, providing a shunt. One ground rod is connected to the shunt.

3.2.8 Tracking and Protective Subsystem - Commercial components would be purchased and assembled to realize the system outlined in Section 2.6.3. An Intel 8022 microprocessor could be used to give low ultimate cost and flexibility in experimenting with control algorithms, in high volume production. However, an EM2 emulator board will be used in the system as designed because of the low volume (14 units) and the ability to make program changes. In order to circumvent possible availability problems of the EM2 board, an emulator board, known as the "SLUSH-22" was built to Intel specs, guaranteeing the near-term availability of an emulator.

A combination of helical and worm drive reduction is chosen for the mechanical linkage between stepping motors and array elevation and azimuth motions, in order to avoid possible backdriving of the motors. Commercially available components are used in the drive train, packaged by the manufacturer to suit the present design. The azimuth drive is covered; both are readily accessible for servicing. Specified backlash on array orientation is 8 minutes of arc in azimuth and 12 minutes in elevation. The latter is eliminated by static imbalance in the array and will be evident only under gusting conditions.

3.3 Power Conditioning Unit

3.3.1 Inverter - The inverter is line-commutated and designed to convert 540 volt nominal DC power to 480 volt AC, 3Ø, 60 Hz power. The DC current on the input side of the inverter is approximately 110 amperes during maximum insolation and the current diminishes as solar insolation is reduced. The inverter is capable of satisfactory operation with variation in input voltages (400 to 600 volt) as well as variation into the PG&E line voltage (480 + 10%, -15%). If the utility voltage varies by +10% and -15%, a tap-changing transformer will be required to maintain utility voltage at 480 volts in order for the inverter to operate at high power factor and efficiency. However, it is expected that the utility 480 volts will remain within ± 5%, in which case a fixed ratio transformer will provide satisfactory operation for the inverter.

The inverter consists of a 6 pulse SCR bridge, coupled with a firing control circuit and a damping network. Given a stable AC voltage, varying the firing angle of the inverter adjusts the DC load on the arrays to the maximum power point. However, the firing angle must be kept within certain limits in order to obtain a reasonable power factor for the inverter operation. Investigation of the state-of-the-art for the power conditioning equipment led to the identification of a number of qualified manufacturers for this equipment. These vendors have been inspected by PG&E's Quality Control group and have been approved as qualified bidders.

A comprehensive review and evaluation process was used in the selection of a successful bidder. The proposal favored was judged to offer the best design and reliability. The important criteria in the evaluation included cost, vendor experience, design of the maximum power reliability, efficiency, safety, and power quality.

3.3.2 Other Equipment - Since the solar DC source is a low impedance circuit, an input filter will be required to provide satisfactory inverter operation. For an experimental installation, multiple-tap air core reactors and multi-valued capacitors may be used to determine the optimum filter configuration for system performance, particularly since the filter contributes losses.

An output filter may be required to prevent undesirable harmonics from entering into the utility grid. Because of the relatively small size of the San Ramon solar plant compared to PG&E system, the harmonics generated by the inverter at San Ramon are not expected to affect the PG&E system adversely. However, the harmonic level would be evaluated in operation in order to determine the need of the output filter equipment. The inverter is equipped with sensors which are connected to the control circuit for automatic operation including startup, loading, and shutdown in a safe manner. A control actuated contactor will isolate the inverter, when desirable. Fuses on both the AC and DC side of the inverter provide back up projection in case of contactor failure.

3.4 Thermal Subsystem

3.4.1 Operational Characteristics - The thermal subsystem has two operating cycles. During the day, the cooling reservoir is used as a heat sink for the approximately 30 watts per cell that must be dissipated. During the night, when the pump is off and the array is not operating, the heat in the reservoir is dissipated through the barrel walls. The reservoir volume required was determined by assuming that all of the heat to be dissipated from the cells on a hot summer day goes into the reservoir, and calculating the volume needed to limit the temperature rise to approximately 50°C (90°F). No allowance was made for heat dissipation from any of the array components or the barrels during the day. The required reservoir surface area was determined by calculating the area needed to dissipate the heat stored during the night and lower the reservoir temperature to 35°C (95°F). The ratio of reservoir surface area to volume thus calculated is matched almost perfectly by that of the barrels. The heat transfer coefficient used for the night-time calculations was measured by experiments on a barrel. (See Appendix J.)

The array cooling subsystem was analyzed in order to determine the flow rate for minimum power loss on a hot summer day. The power loss is from two sources--the pumping power, and the reduction in cell output due to an increase in cell junction temperature over the ideal value. Cell-cooler heat transfer data were obtained from Ref. 6; these data were also used to size the cooler orifice. The optimum conditions require a total flow rate of 7 gpm, which results in approximately four passes of the coolant through the array per 12-hr day, a pumping power requirement of 28 watts at 25% pump efficiency, and a maximum water temperature of 60°C during the hottest part of the model year.

A computer model was established to predict coolant temperature for various levels of insulation and for each week of the year. An example is illustrated in Fig. 3-6.

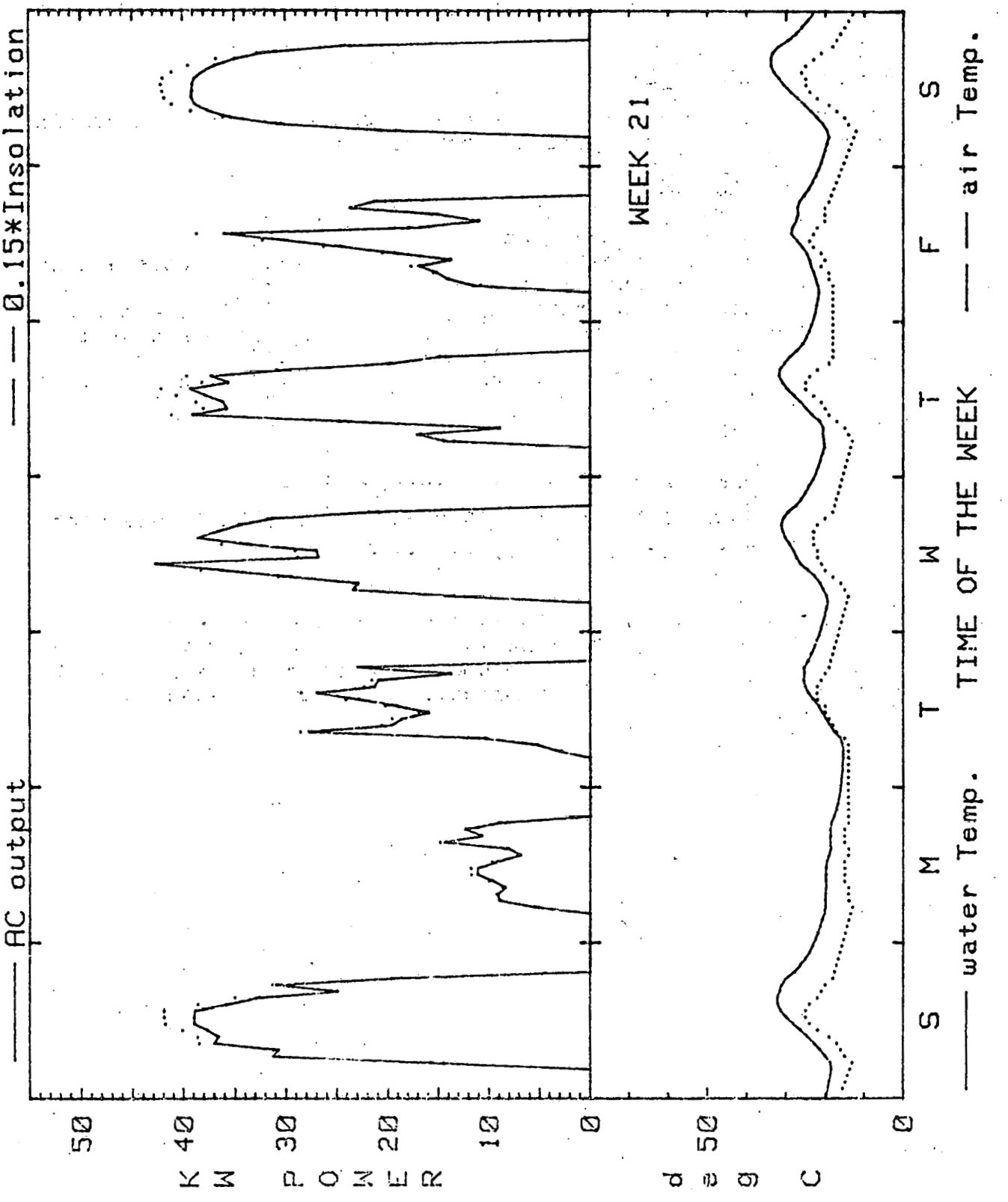

Fig. 3.6 Coolant (Water) Temperature Dependence on Ambient Temperature

3.5 Materials Costs

The following are the materials costs per array according to the values from Appendix B of Ref. 8:

Aluminum	$ 484	
Structural Steel	2,003	
Gears and Bearings	2,600	
Acrylic Plastic	864	(lenses and cones)
PVC or Equivalent	46	
Lead (counterweights)	192	(current cash price used)
Copper (array and field)	217	
Concrete Foundations	444	(2.22 cu. yd.)
Alumina	57	
GaAs	540	
Total/Array	$7,447	
Nominal Array Area 29.0 sq. m.	(27.35 m^2 intercepted)	
Cost/Nominal Sq. m.	257	

At an array efficiency of 15%, this corresponds to a materials cost of $1.70/peak watt. The cost of GaAs, $1.0/$cm^2$ is assumed to be the high volume price of high quality single crystal material. The raw material cost in the GaAs is $117/array.

4.0 SYSTEM FABRICATION AND INSTALLATION

4.1 Fabrication and Installation Plan

Figure 4-1 shows a PERT chart developed for the fabrication and installation of a 50-kWp experiment adjacent to the PG&E San Ramon substation, including adequate spares for the Phase III operation. The first or prototype array module (MOD 0) would be fabricated in the early stages of the program, installed at a site to be selected, and tested to verify the design. Volume procurement for the remainder of the system would be delayed until test results of MOD 0 indicate satisfactory performance. Procurement, fabrication, and installation of the remainder of the system would then proceed, along the lines discussed in earlier sections.

4.2 Make/Buy Decisions

Most of the components required to build the system would be procured from external sources, with the exception of the packaged GaAs solar cell, the sun tracking electronics, and the sun sensors. The major components and subassemblies are shown in Table 4-1. The plan includes in-house assembly of the collector module, the supporting mechanical structure, and the complete array.

4.3 Procurement Plan

Vendor selection would be made on the basis of quotations received during the cost estimating activities of Phase I.

The production schedule, Fig. 4-1, has been based on information regarding long-lead items, such as tooling for the production of the lenses, cell plastic housing, coolant subsystem, and some electrical equipment. In some instances, the production of tooling requires a lead time of up to 26 weeks.

4.4 Fabrication Plan

Most of the components needed for production of the arrays and the total photovoltaic system do not require unique technologies or processes, with the exception of the packaged GaAs solar cells and the Fresnel lenses. These two components would be procured from single sources. As described earlier, packaged GaAs solar cells have been developed at Varian, and a pilot production line has been established to meet the requirements for the Phase II project. Methylmethacrylate Fresnel lenses will be procured from Optical Sciences Group, Inc. (OSG), a subcontractor to Varian during Phase I of this project. A high-transmission curved-groove Fresnel lens (Section 2.6.3) has been designed and will be manufactured by OSG.

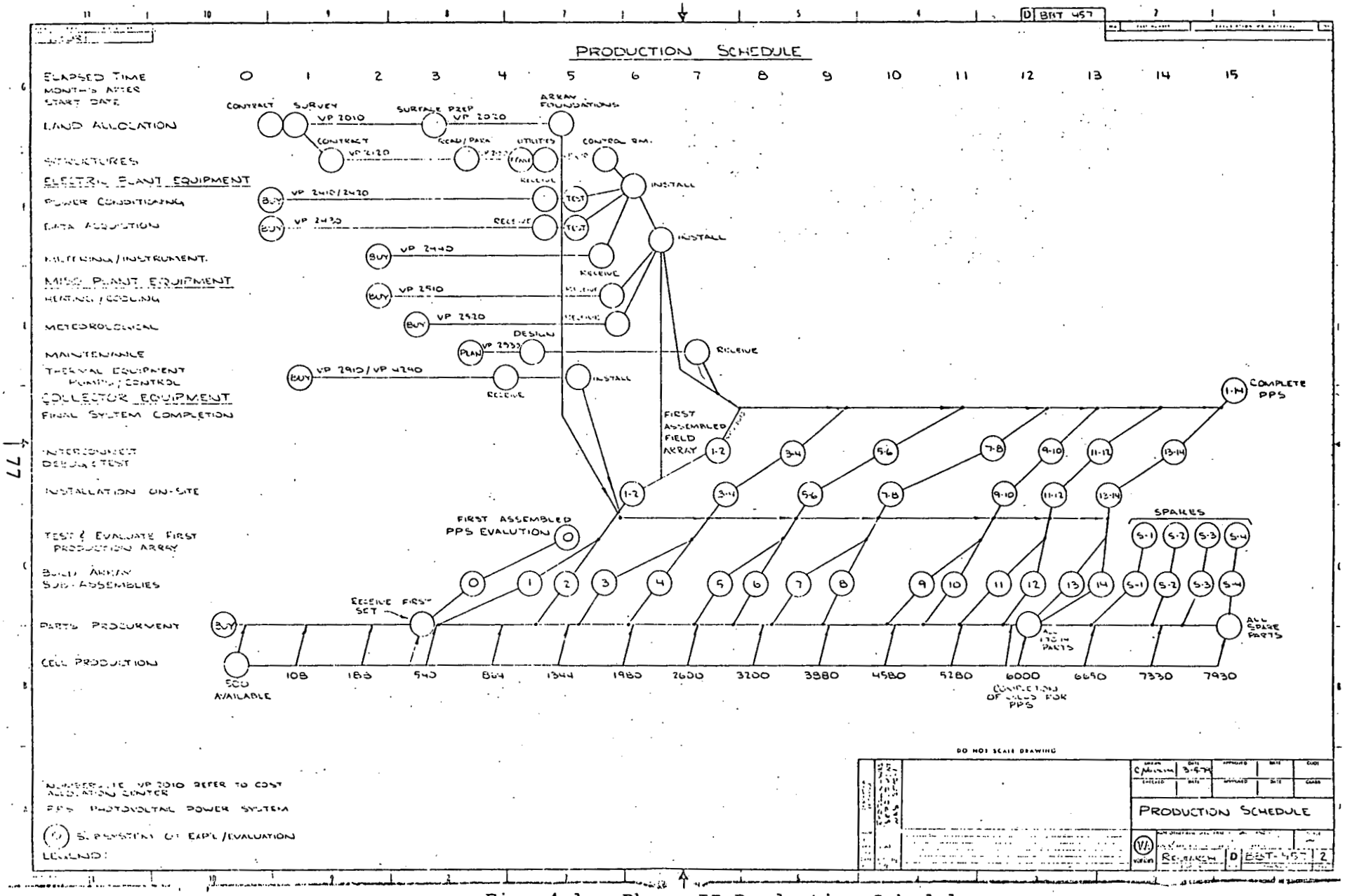

Fig. 4.1 Phase II Production Schedule

TABLE 4-1 FACTORY LEVEL MAKE/BUY DECISIONS

SUBSYSTEM	COMPONENTS		SUB-ASSEMBLIES	
	MAKE	BUY	ASSEMBLE	BUY
COLLECTOR EQUIPMENT (Incl. Structure)				
HOUSING ASSEMBLY	GaAs Solar Cells	Fresnel Lens Housing Reflector Cooling S/A	Module	
STRUCTURAL SUPPORT		Trough Manifold	Structure Array	H-Frame Y-Frame
DRIVE SYSTEM		Elevation Azimuth		
TRANSDUCERS	Sun Sensor Tracking Electronics	Thermocouples Torque Sensors Wind Sensors	Electronic Tracking	
ELECTRIC PLANT EQUIP.				
POWER CONDITIONING		Inverter Modulators Transformers		
CABLING		Power Bus Bar AC Equipment DC Instrumentation Data Acquisition		
DATA ACQUISITION	Software	Equipment		

TABLE 4-1 FACTORY LEVEL MAKE/BUY DECISIONS - Page 2

SUBSYSTEM	COMPONENTS		SUB-ASSEMBLIES	
	MAKE	BUY	ASSEMBLE	BUY
METERING EQUIPMENT		Power Instrumentation Miscellaneous		
MISCELLANEOUS		Meteorological Station		Environmental Control (Optional) Heating/Cooling
TERMINAL PROCESSING		Pumps Controls Piping/Valving/ Fitting Barrels		

4.4.1 Solar Cell and Package - The solar cell and package assembly shown in Fig. 2-18 would be fabricated in the Varian Pilot Line Facility (Fig. 4-2). Production equipment is in operation for the entire cell fabrication process. Equipment has been positioned to give a smooth flow through the process steps. This is indicated by the number sequence 1-14 in Fig. 4-2. Substrate and epitaxial growth operations are located close to this facility in the same building.

The materials and solar cell fabrication process flow and single shift equipment capacities are shown in Figs. 4-3 and 4-4, and discussed in more detail in Appendix G. The process is vertically integrated from polycrystalline GaAs growth to final packaged cell testing. Several well-established, high-volume, major equipment items are in use for contact metallization. These include an automatic photolithography system with mask aligner, a Varian 3120 metallization evaporator, and an allow belt furnace. This makes possible a consistent yield of low-resistance contacts essential for high-efficiency cells.

Cells are tested at 1-sun to select those to be soldered to the ceramic package. All package components are held in a single fixture and soldered in a belt furnace. The final test is a 400-sun pulse test. Selected samples are also tested under solar concentration and compared to pulse test data. In addition several process quality assurance steps and measurements are made during cell fabrication to insure quality and increase yields.

Detailed consideration of equipment throughput and production buildup was generated for the fabrication schedule shown in Table 4-2. Cell output is expected to gradually increase during Phase II, primarily owing to increasing experience and ongoing production engineering during Phase II.

4.4.2 Fresnel Lens Fabrication - Phase II lens fabrication would be initiated by making a new Fresnel master die based on improved master die substrate, since previous attempts have shown that substrate porosity lowers tools and lens quality. To produce the required quantity of lenses for Phase II, additional electroformed busmasters and stamper tools would be fabricated. Two submaster electroforms would be made by metal-to-metal electroform. The second generation submaster would be machined by EDM techniques to produce the grooveless order of the lens tooling and other lens housing features to be molded into the production lenses. This submaster would be replicated by electroforming to produce the required number of stamper tools for lens production.

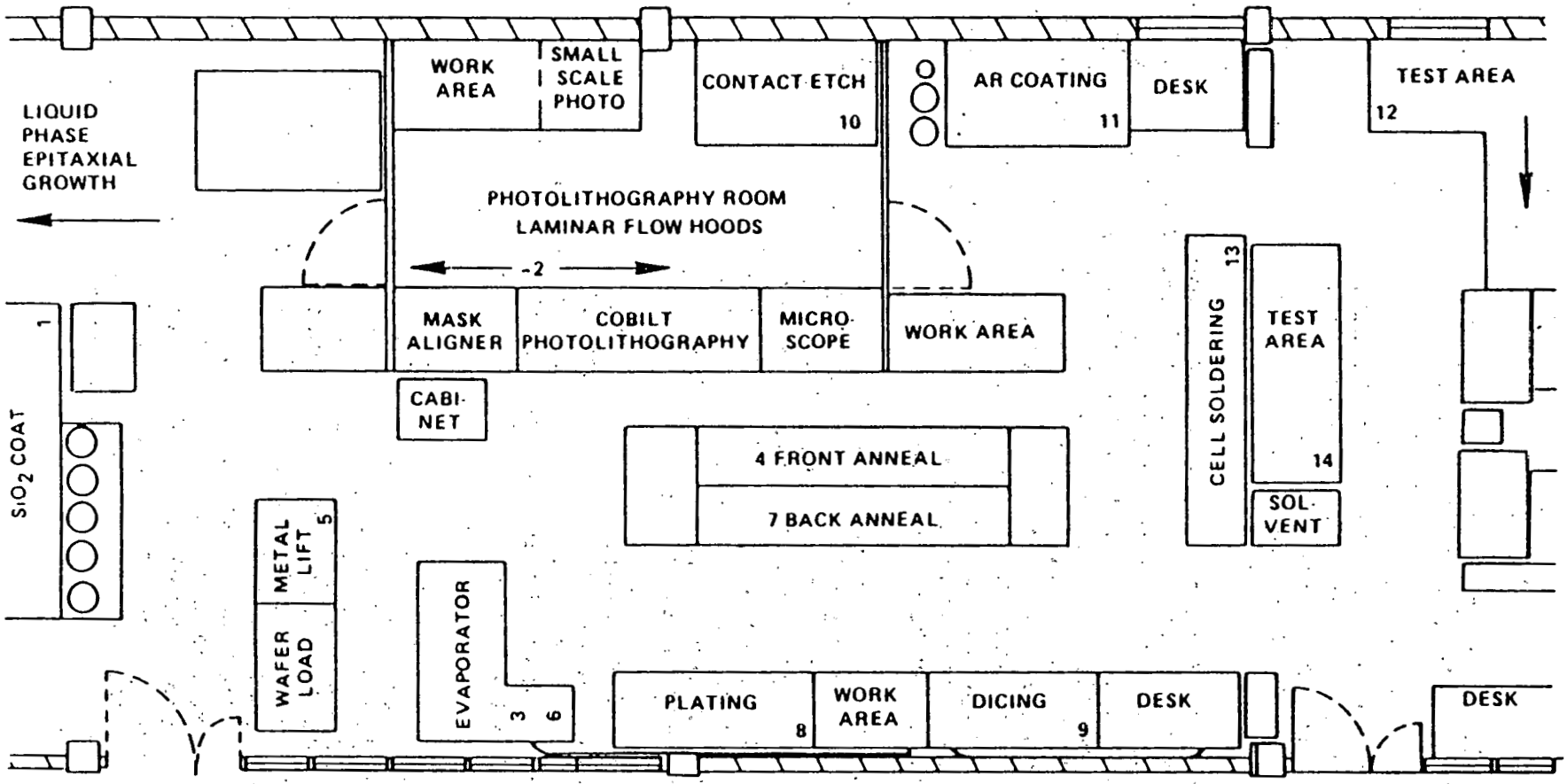

Fig. 4.2 Solar Cell Pilot Line Facility

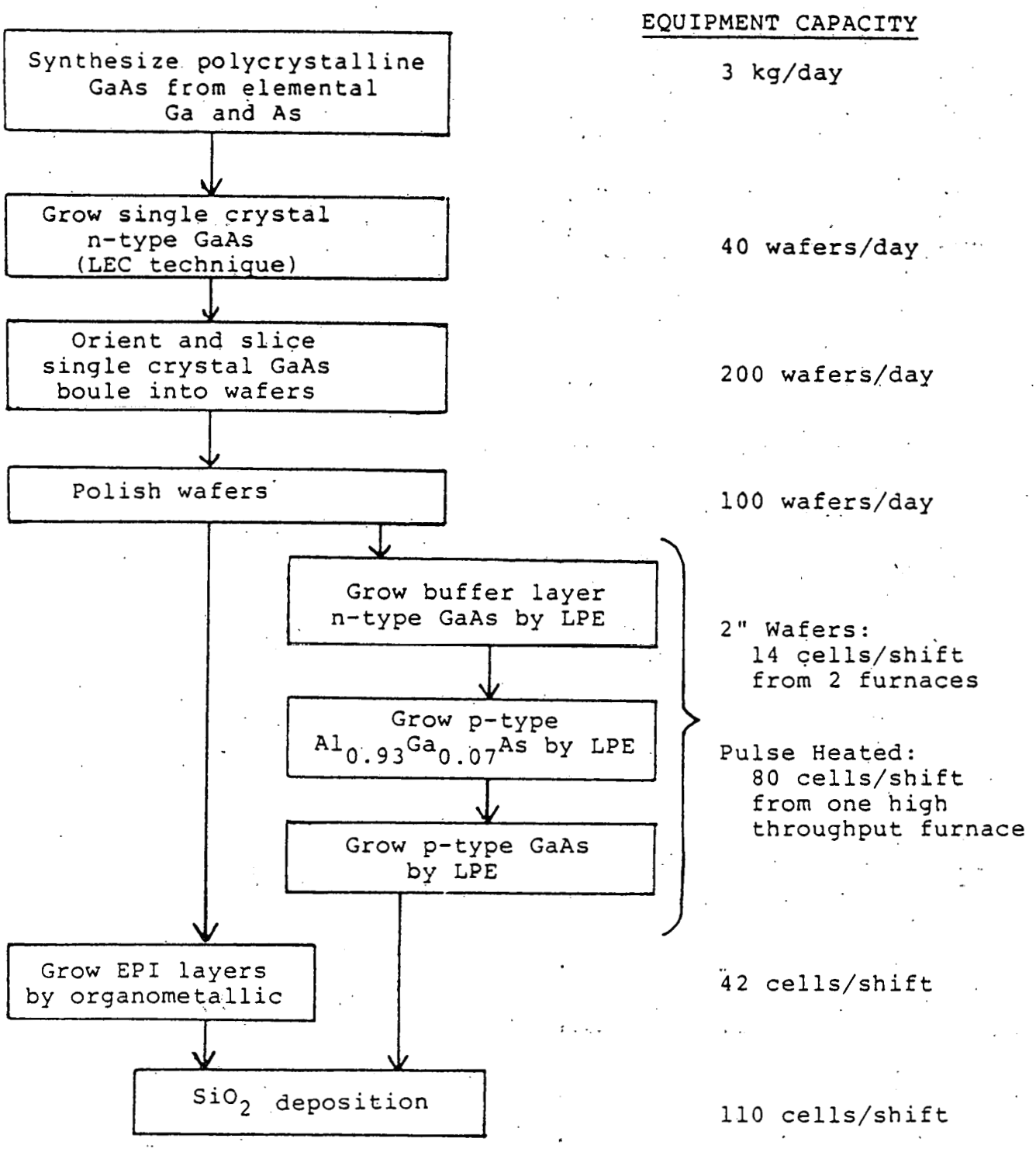

Fig. 4.3 Solar Cell Pilot Line Materials Flow

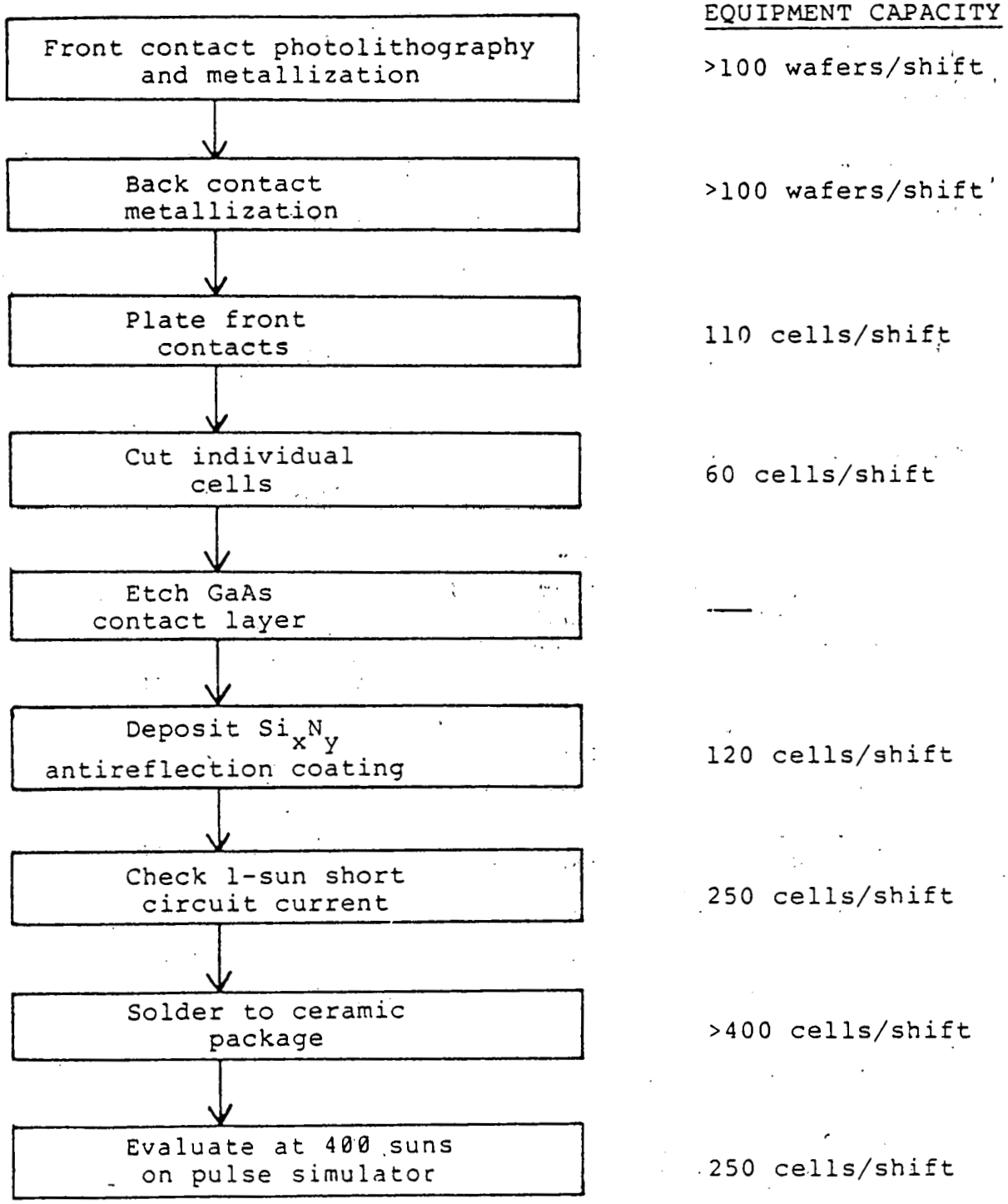

Fig. 4.4 Solar Cell Pilot Line Fabrication Flow

Average Efficiency: 21%(AM2) at 400 Suns

MONTH	1	2	3	4	5	6	7	8	9	10	11	12	13	14	15
Wafer Starts/Day	3	5	7	10	14	16	12	18	18	18	19	19	14	14	14
Cell Starts/Day	12	20	28	40	56	64	48	72	72	72	76	76	56	56	56
Overall Yield (%)	38	40	43	46	48	51	53	53	55	55	55	57	57	58	58
Yielded Cells/Day	4.55	8.0	12.0	18.4	26.9	32.6	25.4	38.2	39.6	39.6	41.8	43.3	31.9	32.5	32.5
Yielded Cells/Month	91	160	240	368	538	652	508	763	792	792	836	866	638	650	650
Cumulative Cell Output	91	251	491	859	1397	2049	2557	3320	4112	4904	5740	6606	7244	7894	8544

TABLE 4 - 2 FABRICATION SCHEDULE
SOLAR CELL & PACKAGE

In-press tooling was designed and fabricated in Phase I to mold prototype lenses from an electroform Fresnel stamper and to polish press plate plano tools. In Phase II, the original tool plus two additional units of the same design would be used to reproduce from 6000 to 10,000 lenses.

A high temperature grade of optical quality acrylic molding materials used in Phase I would also be used to produce Phase II lenses. The material, a Dupont molding and extrusion-grade lucite, has a heat deflection temperature of 92°C. This material will produce lenses with relatively high resistance to creep or deformation under long-term, low-loading conditions. These characteristics are important for lenses with high resistance to deformation or bowing. After production, the lenses would be permanently marked for traceability. Each Fresnel production tool would also be coded for subsequent tracing.

4.6 Assembly Plan

4.6.1 Procedure - Production will be facilitated by a product structure, commonly known as a "Christmas tree." This shows the practical procession of parts which make each assembly from the lowest level to the highest (final system) level.

The assembly plan is to produce one complete array every two weeks. For the first several months, cell production will slow the manufacturing cycle. Owing to the large size of an assembled array, it is planned to build to the H and Y frame levels in the manufacturing plant and then, on site, to install the Y-frame on the pedestal, H-frame onto the Y-frame, complete electrical and water connections and make final system adjustments. Low-level parts, such as cables and hoses, will be made in advance. Frame assembly then becomes more of an assembly of parts rather than "make and assemble". This will speed assembly time.

The cable assembly line will have responsibility also for short plastic water hoses; the cone assembly line will also produce the sun/wind sensors and printed circuit boards used in the control circuitry; the channel assembly line will make all smaller mechanical parts such as switch boxes. The H and Y frame assembly personnel will fabricate (solder) all copper water lines used in their units. Assembly jigs and fixtures are also required in these operations, and to support the cones, channels and the H and Y frames during assembly; these are planned for the early (MOD O) phase of the fabrication plan. In addition, adjustable height platforms will be required for assembly of the large H-frame. This will be performed by a two-man team, one man on each side; two platforms will be required.

4.6.2 Alignment Plan - Optical alignment for the small installations under consideration will be done with the arrays tracking the sun. The MOD 0 array will be aligned manually using the tool discussed earlier, with the alignment operator adjusting the cells for a centered spot as visually observed. Simultaneously, with the construction of MOD 1, an automated microprocessor-based alignment tool would be constructed. This tool consists of two major parts; a power supply, logic and controller box which sits on the ground behind the array; and an alignment head which is placed consecutively in the holes in the channel behind each cell location. The alignment head contains two DC motors, 2 stepper motors with hear heads, a solenoid, and a current shunt. The alignment head is placed through the 3"-diameter hole in the back of the channel, oriented by guide bars with respect to the channel edges so that the flexible extended shafts of the DC motors fit over the position locking nuts on the cell holder, two spring-loaded current measuring probes contact the DC output screws of the cell holder back. After a constant, non-zero current has been measured continuously for 2 seconds (which signals proper positioning), the solenoid locks the tool onto the channel. The stepping motors then scan the cell position, alternating X and Y movements, until the highest SSC output point is found. The DC motors, which are operated at a voltage such that their stall torque equals the required torque of the position locking nuts, tightens these nuts. The solenoid then disconnects the tool from the channel, and the tool is moved to the next hole. If the peak current position appears out of the adjustment range, an error lamp will go on, indicating the direction of the required manual shimming. This is expected to be a rare occurrence. It is estimated that this tool will permit to align four cells per minute, or two hours per array.

In case re-alignment is ever necessary, the DC motors can be run with reverse polarity at a higher voltage and higher torque, loosening the position locking nuts, and allowing rapid realignment. Barring physical damage to a channel, re-alignment is not expected to be needed.

4.6.3 Test - Factory testing will be performed by production personnel and monitored by Quality Control. The test will consist of continuity checks of electrical circuits, leakage checks of all water lines, and alignment of the cells to the lens, using the built-in mechanical devices. Final lens adjustment to the sun will be done at the site installation.

4.7 Quality and Reliability

Statistical reliability estimates for the design were discussed earlier (Sec. 2.8.). The numerical reliability

objectives for major elements of the system, apportioned down through design levels to a numerical reliability objective for each lower level of hardware assembly design work package, would be adjusted to the maturing design, in order to identify critical areas for further engineering improvement. Design reviews were conducted at scheduled intervals during Phase I to assess the adequacy of the design with respect to requirements, and should be continued under Phase II, as part of the complete quality assurance programs required in a manufacturing operation.

4.8 Transportation Plan

The design calls for a transport truck with lowbed (39" above ground), 40-feet long, by 8-feet wide. This permits moving the subassemblies for two arrays. Support fixtures are required during assembly of the H and Y frames, and similar fixtures would be used as the main support of the frames during transport. At the installation site, a crane with a minimum capacity of 2 tons would be used to lift the assemblies from the truck to the mounting pedestals.

4.9 Installation Plan

4.9.1 Site Preparation Requirements - Site preparation requirements and certain site restrictions have already been discussed in Sec. 2. A site perimeter fence (chain link) with a double swing gate is provided for security. There are no plans to further landscape the site.

4.9.2 Utilities--Electric-Water - A low-voltage feed is required at each array for its solar tracking system and array cooling pump. Water faucets are provided at convenient locations in the yard for the purpose of initial filling of the coolers as well as for washing the lens during maintenance. The water piping system is supported on the side of the cable tray system to minimize obstruction and installation cost. Minimal yard lighting is provided for security reasons and for access to the station at night. Telephones are installed in the control building to provide a telephone data link from the ODAS to the San Ramon Research office. A voice phone would also be provided during the construction and operation period of the facility.

4.9.3 Control Building - The control building (Fig. 4-5) consists of a main control room, a battery room, and an observation room. The main control room contains the power conditioning unit (PCU), associated metering and control equipment (including instruments, transformers and shunts), AC and DC switch panels, telephone termination equipment, a work table and a desk. An area is also provided for heating, ventilation and air conditioning (HVAC) equipment. Electrical access is provided by an overhead tray system passing through the building which connects to the outdoor tray system, and

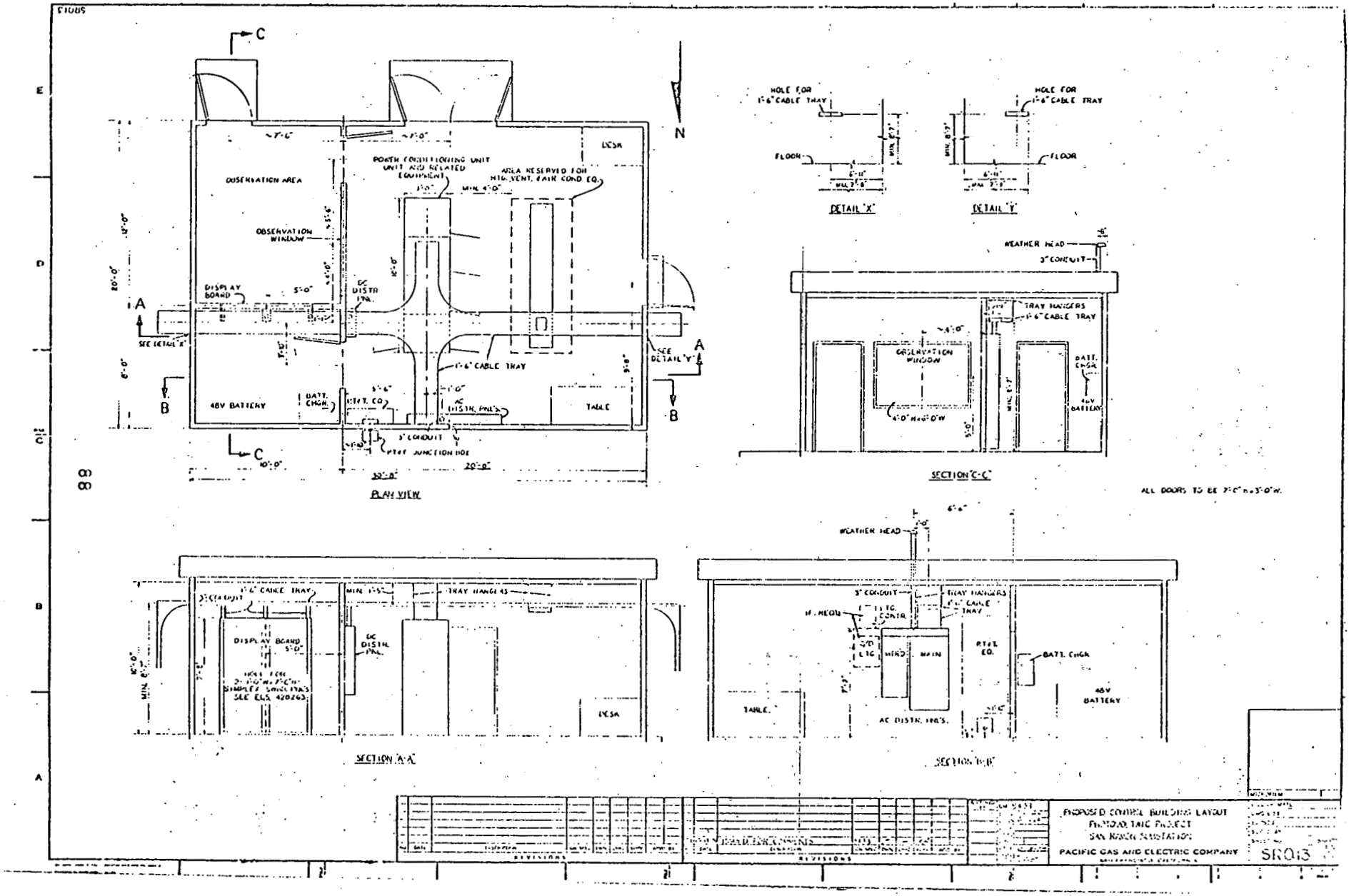

Fig. 4.5 Control Building Layout

an underground conduit for connecting to the main station transformer. Physical access is provided by one three-foot-wide single and one six-foot-wide double door. Another three-foot single door is provided between the observation room and the main control room.

The battery room contains a 24-V battery and a battery charger. Access is provided by a three-foot single door to the main control room. The observation room has a window for viewing the main control room and a display panel to show various aspects of the station. Electrical access to the display panel is through the battery room. Physical access to the observation room is provided by a three-foot single door to the outside and the above mentioned door to the control room.

4.9.4 Tray System - All electrical connections, main DC, instrumentation and motor power, between each array and to the control building are made via an above-ground cable tray system. The arrays are arranged in two N-S lines of 7 arrays each. Two tray runs, each serving 7 arrays, are connected to the building. The runs are located to avoid tripping hazards; their ends are connected underground by a 3" PVC plastic conduit. A conduit connection is required since the run crosses a road and the arrays are connected in series.

The ventilated (ladder type) trays are 6 inches wide, with a 3-inch loading depth. The covers are flanged (solid type) to protect the cables from the rain or other hazards. All horizontal elbows, vertical elbows, and tees have radius bends of 24 inches in order to accommodate the main DC cable which is 500 MCM copper and has a bending radius of approximately 18 inches. The trays have an internal barrier to separate the instrumentation from AC or DC power cables. All trays and fittings are steel, hot-dip galvanized after fabrication.

The trays are supported at 12-foot intervals by unistrut columns mounted on concrete piers. Tray height is 15 inches above concrete. Between the arrays, which are 60 feet apart, an expansion connector is used which permits 1.5 inches of movement.

At each array, the tray terminates at a 24 by 24 x 12 inch, NEMA 3R, hinged cover box. The box houses a knife switch to which the main DC cable is connected and provides a means of bypassing the array. From this box the connections are made to the array from a cable service entrance at the top. The cables are looped to provide flexibility as the array rotates when tracking the sun.

4.9.5 Maintenance Plan - A preliminary maintenance schedule is outlined here; experience with the MOD O array will no doubt lead to further refinement.

Bearings (azimuth and elevation): grease fittings -- 6 months

Drives (sealed): inspect for leaks -- 6 months

Water pump (sealed): replace on failure

Lens housing: inspect bond -- 12 months

Hoses (flexible): check for wear -- 3 months

Electrical connectors: inspect and retorque -- 12 months

Rubber gaskets: check condition -- 12 months

Channels: inspect and clean if needed -- 6 months

Coolant circuit: check barrel and header connections -- 6 months

Coolant level in barrels (air leaks): check and refill according to experience Lenses:

Lenses: wash periodically according to season and experience

Site: cut weeds, spray under arrays -- Spring

The detailed failure tree, Fig. 2-38, in addition to generating system reliability information, will also be used in establishing a preventive maintenance program. For some components, such as the Fresnel lens and the solar cell, adequate information is not yet available to establish a meaningful program. The array design is such that field repair and replaceability can be executed on solar cells, individual cell housings (although not individual lenses), some housing components and modules.

Structural damage, resulting in permanent misalignment, will require replacement of an array. For that purpose, four spare arrays would be produced as part of the Phase II production program. Additional spare solar cells, housings, etc., will also be maintained in inventory. The parts list, (Section 3.1), represents the first step in establishing inventory control. This will be used in identifying critical long-lead items, which need to be inventoried in order to insure short array or system down-times. The list will also become a means to track inventory and availability.

Current estimates for parts, components, and sub-assemblies replacement are less than the nocturnal down-time of the system. Current estimates for the replacement of an entire array will be about two days, assuming availability of the spare array at the factory, located in Santa Clara, approximately 30 miles from the San Ramon photovoltaic array field.

4.9.6 Safety - The system will shutdown automatically if AC line voltage is lost in order to prevent it from energizing into a downed power line. As a backup, fusing is provided at both the DC and AC sides of the inverter to protect against overloads and faults. The site is completely fenced in to provide controlled entry into the facility with PG&E approval and supervision. The array structures will be solidly grounded for personnel safety. The power conductor and other wiring will be properly insulated and protected in a tray system for added safety. The inverter, as well as other station equipment, are required to meet PG&E specifications, which generally equal or exceed applicable industry standards for this type of equipment.

5.0 ENVIRONMENTAL ASSESSMENT

5.1 Land Use Review

A summary of the proposed experiment was presented to the staff of the Contra Costa County Planning Commission by PG&E. PG&E was subsequently informed that this experiment would not require any permits or any detailed descriptive documents for land use approval. Normal building permits for the control building are required. The County planners expressed their desire that the potential for adverse visual impact upon residents in the vicinity be carefully considered and ameliorated. Several planners from the county showed strong interest in the project and requested tours of the facility when constructed.

5.2 Environmental Design Considerations

5.2.1 Visual Conditions - The project location is in a gently sloping, rectangular open area surrounded by houses, the San Ramon substation, a golf course, and Alcosta Boulevard. There are several transmission and distribution structures leading to the substation. The designed facility is located away from houses to reduce visual disturbance. This in combination with the low profile design and careful color control minimizes visual impact, although the project is in plain view from Alcosta Boulevard. The array field has a simple rectangular shape requiring minimal grading. The features within the yard (arrays, cooling system, building, etc.) are organized in a simple geometric pattern. Due to the short duration of this project, a pre-engineered, pre-fabricated, metal building was selected for use as a Control Building. This type of building is quickly and easily erected or disassembled.

The Control Building is 20 feet wide, 30 feet long, and 10 feet high. It houses the controls and instrumentation for the photovoltaic experiment as well as the heating/ventilating/air conditioning equipment and an observation room, Fig. 4.4. A tan color was chosen for the roof and exterior wall panels for compatibility with the surrounding area. The roof and walls are insulated to R-19 and R-11 respectively.

5.2.2 Noise - Noise impacts on the surrounding residential community are expected only during the actual construction phase of the facility. Land preparation will require some heavy equipment at the site. This impact will be minimal as the construction will be of short duration (3 to 4 months) and all activity will occur during the daytime.

Normal operation of the photovoltaic experiment is not expected to cause any noise disturbances in the area. Any noise producing equipment (small pumps and motors for cooling) will only operate during daytime hours, and they are not expected to be audible at the nearest residence. Some repairs to the equipment may occur during evening hours, but such maintenance is not expected to create noise levels which would impact the local area.

5.3 Traffic

Access to the site will be by prior arrangement. Visitors will be guided by personnel from Varian or PG&E. PG&E's Research Center, 5 km to the north, will serve as a staging area for tours. Traffic to and at the site can therefore be controlled.

6.0 PHASE III PLAN

6.1 Objectives

Overall Phase III objectives are to collect data which will promote:

(1) development of system and component designs leading to lower life-cycle energy costs (i.e., designs having higher reliability, lower maintenance, and lower fabrication costs),

(2) improved acceptance of concentrating photovoltaic power generation equipment (dependability of generation, minimization of environmental objections, etc.), and

(3) improvements of the system modelling capability initiated under Phase I of this program, for potential future applications.

Item (1) implies a continuation of design activities, under the stimulus of an existing operating system, and the operating, maintenance and other problems it reveals. Since the system design objective is a relatively small, unattended source of power, fed continuously into a relatively large, 24-hour load network, the target operating protocol is one of automatic operation with no operator intervention, coupled with minimum maintenance attention. The system is therefore designed to be instrumented for remote monitoring of performance both at the PG&E Research Center (5 km distant) and Varian (40 km distant). Attendance of operating or maintenance personnel will be minimized, except during performance of specific short term experiments. Some system maintenance, required to restore performance, will provide the design information needed to better meet the objectives of the Photovoltaic Program.

6.2 Technical Plan

6.2.1 Technical Evaluation/Tests - The photovoltaic station will normally be operated at its full capabilities except during testing. Initial tests will be run to confirm the effectiveness of the control and protective features of the system, e.g., the station's response to cloud passage, individual array bypassing, and related distribution line voltage changes. The efficiency, power factor, and harmonic generation of the inverter as a function of input and output changes, with automatic or manual power tracking, will be monitored.

6.2.1.1 System Evaluation - The contribution of the electrical output of the photovoltaic station will be compared with the peaking load on that distribution line and PG&E's system summer daily peaks, in order to assess photovoltaic power as an energy resource, and its application to distributed power generation. Overall system stability is not expected to be a problem when the inverter and array controls are properly adjusted. Time constants will be chosen to avoid overcompensation to array transients by the maximum power tracking feature of the inverter. The station's response to temporary loss of utility power would be evaluated.

6.2.1.2 Total Energy Option--Computing Thermal Recovery and System Efficiency for Space Heating System - The temperature control of the space heating and cooling will respond automatically to space design requirements. An analog of heat energy will measure and record the amount of thermal waste available and the amount of thermal waste recovered through the operation of the space heating system. The cooling system is provided by a commercially available refrigeration split system, i.e., condensing unit and DX coil. Since it is only a functional component, there is no need to monitor its operation. Since the site of the experiment is unsupervised, the waste heat recovery system will be inspected weekly for proper operation and temperature control response.

Alternate Space Heating and Cooling with Thermal Waste - Since both the heating and cooling cycles would use thermal waste from the solar concentrators, both systems would be monitored separately for the energy recovered for cooling and heating as well as waste heat generation. Because the datum temperature of the combined cooling/heating recovery system is higher than for heating, a strict service and maintenance program would be required, i.e., weekly inspection and service record.

6.2.1.3 Power Conditioning Equipment - The performance of the power conditioning unit will be carefully monitored during the operation and test period. In the component area, failure rates of SCRs, electronic devices, control circuitry, cooling equipment, and other accessories will be documented in order to determine if there are areas that require design improvements. Spare parts requirement, repair cost, availability, and redundancy level of key components will be evaluated in order to provide inputs to the design of next generation of inverters. Attention will be placed on the maximum power tracking system and tests will be conducted to verify its proper operation. All the key electrical quantities are monitored and recorded so that the power and efficiency of the inverter operation under varying

AC and DC voltage conditions can be determined. Tests will be conducted with and without the input and output filters to determine their effect on efficiency, power quality, and the operation of the inverter.

6.2.2 Economic Evaluation - Concentrator photovoltaic power generation such as being developed as part of this experiment will have the following major economic values to a utility system:

1. Reduction of system peak generation capacity requirements to the extent that the PV system coincides with the system load peaks.

2. Displacement of fuel derived energy which would otherwise be required to serve area loads.

3. Reduction in transmission and, in some cases, distribution capacity requirements (where the PV systems are connected to the distribution network).

4. Lowered transmission and/or distribution energy losses.

5. The possibility of sharing facility costs where customers have use for the waste heat of the system.

Photovoltaic systems will have particular value to PG&E in the Sacramento and San Joaquin River valleys where peak loads occur on hot summer days and transmission and distribution equipment ratings are minimal. Since the system load tends to peak at the same time as these loads most of the energy displaced will be from inefficient oil-fired generation plants which is substantially more expensive than from efficient base load sources. As part of this project, PG&E will correlate the energy output of this photovoltaic facility to local and system loads and establish its economic value.

A related objective will be the derivation of some accepted valuation parameter for energy generation systems of the type discussed, such as levelized busbar energy cost, through application of discounted cash flow analysis. The format presented in the ERDA/EPRI study (ref. 7) of utility-owned energy systems will be used, to derive a single criterion by which the system can be compared with other power sources. Capital investment inputs to the analysis will be derived from Phase II experience. Relevant activities under Phase III will be: (1)

(1) an evaluation of system lifetime, from experience of repair and deterioration, if any,

(2) operating costs,

(3) maintenance costs, and

(4) miscellaneous factors.

6.3 Data Collection

6.3.1 System Operation - The design incorporates transducers for measurement of the parameters listed in the uniform data requirements (ref. 8) (voltages, currents, temperatures, flow rates, etc.) at the intervals required, except where obviously not applicable (e.g., no significant battery storage is contemplated; use will not be made of conventional heat exchanger or cooling towers). Accordingly, all required transducer data will be recorded at the intervals specified, for transmission to the DRC.

In order to validate the structural design, static and dynamic tests are envisioned on the MOD 0 structure. Influence coefficients of the assembled H-frame, Y-frame, and pedestal will be measured in order to ensure that this structure is stiff enough to meet the deflection constraints posed by the pointing-accuracy requirements. The fully assembled array will be subjected to vibration tests in order to measure the natural frequencies, mode shapes, and damping in the low-frequency end of the modal spectrum. Information from these tests will be used to update the theoretical model of the structure. The response of the system to various types of turbulence inputs, broadly representative of the atmosheric turbulence expected at the San Ramon site, will be calculated in order to identify any potential pointing-accuracy problems associated with dynamic response.

The instrumentation on array No. 1 at San Ramon includes strain gauges and accelerometers on the H-frame and Y-frame. These data will be monitored in order to identify potential fatigue and dynamic-response problems under in-service conditions. Response data on other arrays will also be taken on windy days with a portable accelerometer system in order to assess the response of arrays that are in the downwind wakes of other arrays. Should it be necessary, low-level atmospheric turbulence in the vicinity of the array field will also be measured. Depending on shadowing configurations, it may also be advantageous on an experimental basis to monitor voltages and currents at different points of the arrays, including protective diode currents, to verify expected operation.

One of the arrays will be instrumented in considerable detail to investigate expected operation of balanced coolant flow, balanced solar cell outputs, etc. Provision will be made for acquisition of design data for further component improvement. This will include as a minimum items listed below. Others may be added as a result of Phase II experience.

Design information will be required for conditions of system perturbation. An important experiment in this category is determining the consistency of the focal spot positioning on the cell. In order to determine this, in each of three rows of one array, instead of installing 22 parallel cells, it is planned to install 21 parallel cells chosen to have short circuit currents near the top of the production distribution, leaving three unconnected cell holder locations in which to install special measurement cells producing no power. These cells will have five electrically isolated active areas as shown in Fig. 6-1. Area 1 has a 0.490" diameter, the same as a normal cell. The ratio of I_{SC} of Area 1 to that of the sum of Areas 2,3,4, and 5 will detect any problems caused by lens doming. The ratio of I_{SC} in Area 5 to Area 3, and Area 2 to Area 4, will detect any changes occurring in alignment, or any tracking error. These cells will have a grid coverage of about 95% in order to reduce the I_{SC}s to readily measured levels.

Also, it is planned that system operation be briefly interrupted at suitable intervals (daily or weekly) according to experience) and the following data acquired in order to assist detection of performance deterioration:

Arrays:	I_{SC}, V_{OC}, fill factor
Field:	I_{SC}, V_{OC}, fill factor.

These observations will supplement the data available from the cell, array, and field monitoring systems specified under the uniform data requirements. They will also substitute for the full array current-voltage characteristics measured during the Phase II shakedown period as a verification of correct array operation. Since many array outputs are combined to feed the inverter, maximum power tracking by the inverter does not guarantee optimum loading of any given array, unless the field of arrays is carefully balanced. Individual array characteristics will be continuously monitored (power, voltage, current, and fill factor) in order to detect incipient imbalance. It will also be necessary as a minimum, in order to evaluate the effects of mutual shadowing of the arrays and effects of external shadowing, to monitor in real time the outputs of all 14 individual arrays as well as the total field.

As regards the thermal system, coolant flow will be monitored on all 14 coolant loops. In addition, pump power and storage field temperature will be monitored on one or more representative arrays in order to verify the system model used in calculating the cooling system performance. If indicated, it would be feasible to substitute different sizes of components (both in the thermal system and elsewhere) in order to verify the correct choice of the optimum parameters.

As already mentioned, options exist under Phase III for the use of thermal output from one or more array for heating and/or cooling of the control room (see Appendix F). In that event, instrumentation of this experiment would also be connected to the on-site data system.

Requirements for Class I archivable data from the GFE meterological station are noted: these imply frequent calibration and in some cases, daily maintenance of transducers.

6.4 Miscellaneous Phase III Activities

Plans were also formulated under Phase I for routine accumulation and recording of maintenance and safety information during Phase III operation, together with reporting of corrective measures taken. Also to be monitored on a formalized basis are institutional, environmental, social and legal issues, public and user acceptance etc., some of which have been touched on in earlier sections of this report.

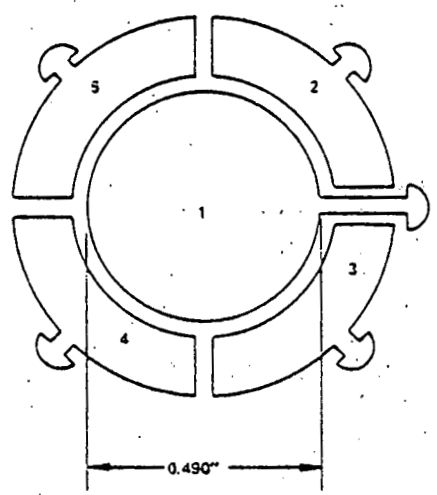

Fig. 6.1 Measurement Cell Configuration

7.0 COST PROJECTIONS

As mentioned earlier, a computerized materials list was established during the design process in order to keep track of all components needed for fabrication and installation of 14 arrays (50 kWp). This list was used for obtaining bids at the 50-kW level, and at higher levels of 3 and 6 megawatts. Since the design is expected to undergo considerable evolution before even these levels are reached, it was not felt relevant to obtain bids for still higher production quantities. Nevertheless, costs for the higher volumes decreased considerably, since initial tooling costs and preproduction and start-up costs have a strong impact on costs in early stages.

Figure 7-1 summarizes the relative distribution of material costs at the above production levels, corresponding to 19, 750, and 1400 arrays respectively. At the planned rate of production for Phase II, the cost of the photovoltaic submodule comprising the solar cell, heat sink and cooler, together with the lens and support cone, represents over 80% of the array materials costs; therefore, all other cost contributors are relatively small. At higher production levels (3 and 6 megawatts are not really distinguishable), the photovoltaic submodule contribution is 35-38% of the total array materials cost. Conventional subassemblies (such as structural supporting elements) are not susceptible to further substantive cost reduction and will, therefore, represent an increasingly more important cost contribution, i.e., 36-38% of the total array materials costs.

Figure 7-2 summarizes the contributions of the more important components to the materials costs, for the Phase II program, and for 3 and 6 megawatts respectively. At the latter levels, there is still substantial margin for further reductions in solar cell costs and structural costs. Design changes resulting from field experience would also be expected to produce further cost reductions at the higher levels. Figure 7-3 represents the cost/watt of the materials input (including solar cells) to the projects at the above production levels. Since labor and overhead for assembly and installation represent a small fraction (under 20%) of the total, the values quoted can be regarded as a representative of installed array costs, exclusive of the site preparation, power conditioning, etc. Solar cell costs at the various production levels are as follows:

Production Level, MW	Cell Cost, $/cm^2
.07	165
3	11
6	8

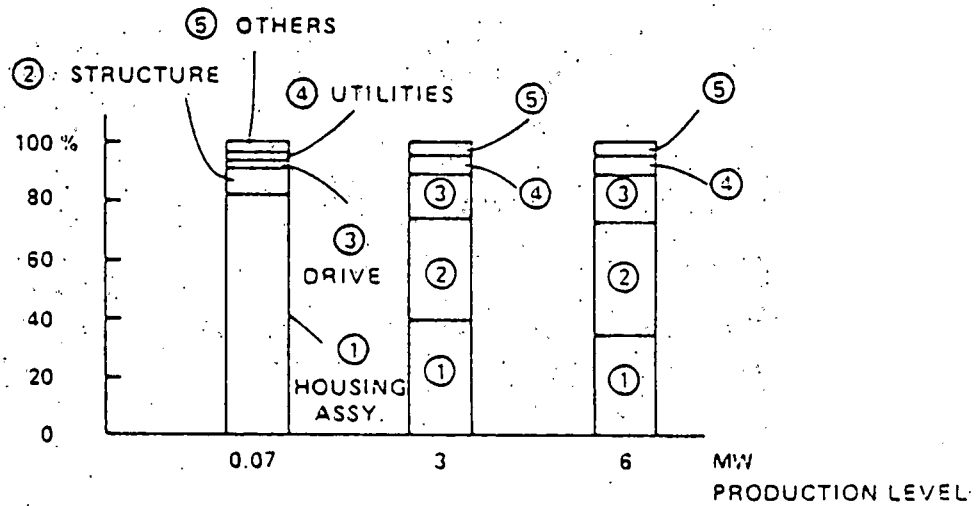

HOUSING ASSEMBLY (1):	SOLAR CELL, LENS, HOUSING, REFLECTOR
STRUCTURES (2):	STRUCTURAL SUPPORT, PEDESTAL
DRIVE SYSTEM (3):	ELEVATION, AZIMUTH
UTILITIES (4):	ELECTRICAL WIRING, COOLANT PIPING
OTHERS (5):	TRANSDUCERS, FASTENERS, DIODES

Fig. 7.1 Relative Contribution of Key Subassemblies to the Array Materials Cost at Three Production Levels

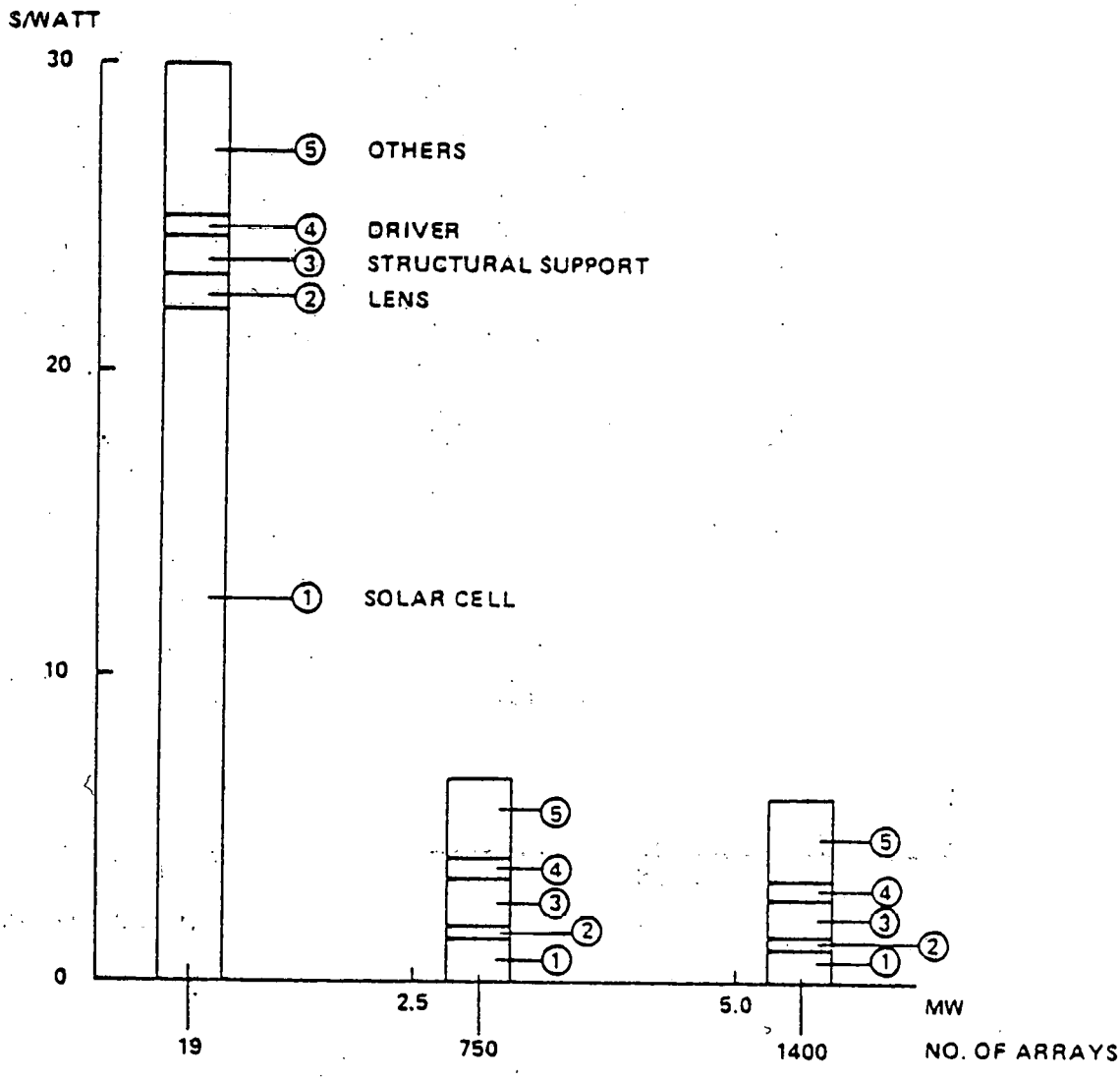

Fig. 7.2 Contribution of Costliest Single Components on Array Materials Cost, $/Watt, at Three Production Levels

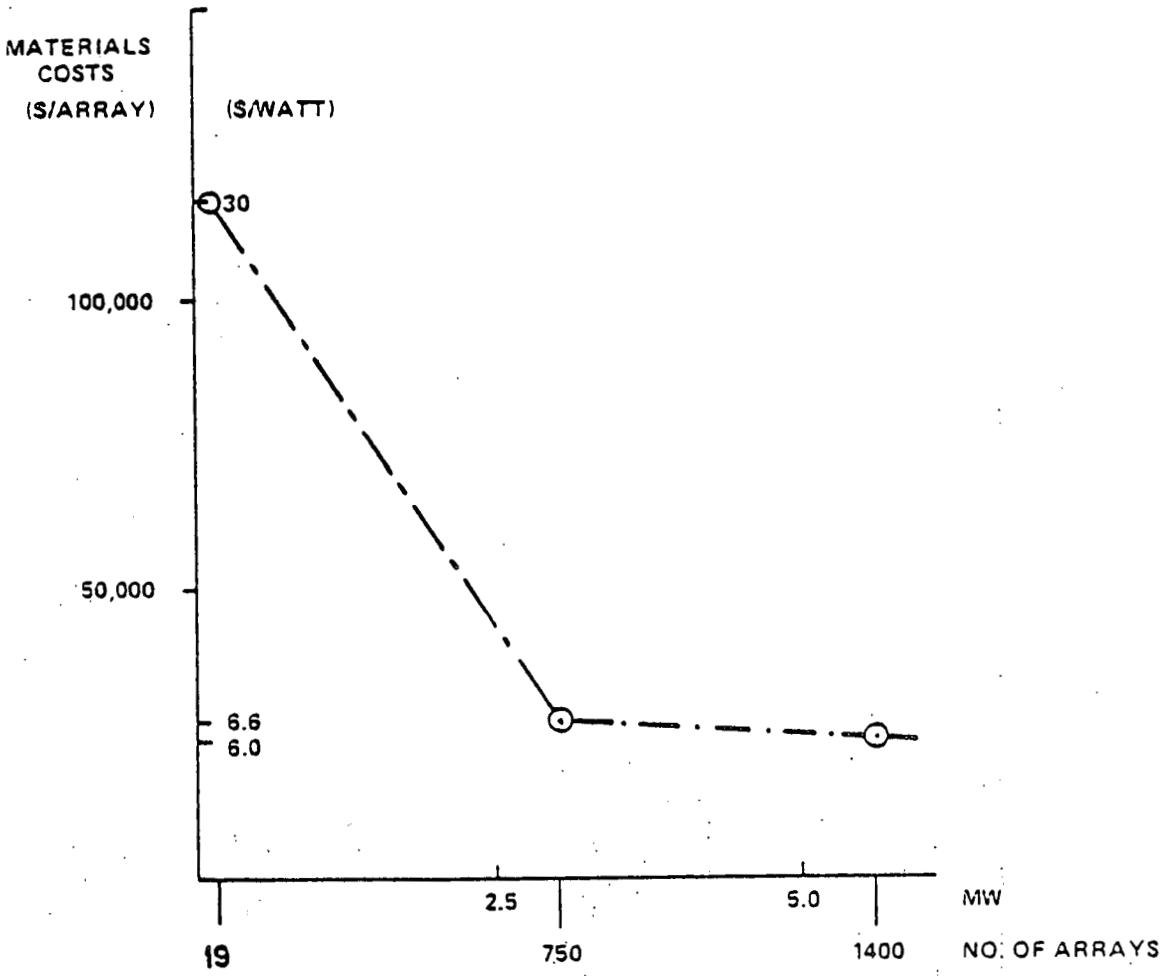

Fig. 7.3 Influence of Volume (Megawatts or Number of Arrays) on the Array Materials Cost or $/Watt

REFERENCES

1. D.K. Zimmerman and C.J. Bishop, "Concentrating Photovoltaic Solar Array". Final Report, Boeing Engineering and Construction Co, May 1977
2. L. W. James and J. K. Williams, "Fresnel Optics for Solar Concentration" (13th IEEE Photovoltaic Specialists Conference 1978,p
3. H. A. VanderPlas, L. W. James, R. L. Moon and N. J. Nelson, Proc. 13th IEEE Photovoltaic Specialists Conference, 1978 p. 934.
4. N. J. Nelson et al, Appl. Phys. Lett. 33 26 (1978) R. L. Moon et al., ibid 33 196 (1978)
5. L.W. James, H. A. VanderPlas, and R. L. Moon, Final Report, "High Performance GaAs Photovoltaic Cells for Concentrator Applications", December,1978, Sandia Laboratories, Albuquerque NM, Contract No. 05-4413,p 15-19.
6. D. R. Walz, Technical Report No. 61, Dept. of Mechanical Engineering, Stanford University, July 1964.
7. J. W. Doane et al., "The Cost of Energy from a Utility-Owned Solar Electric System" (ERDA/JPL - 1012 - 76/3)
8. "Proposal Preparation and Evaluation Guidlines", PRDA EG 77-D-04-0035, Department of Energy, Albuquerque Operations Office (1978)

APPENDIX A. SUN TRACKER SOFTWARE AND SENSORS

The software consists of an initialization section and two major program segments. The input and calculation loop is entered from the initialization sequence and alternately samples the inputs, and calculates and stores the action required by the 2 stepper motors, the pump switch, and the LED. A timer (internal to the 8022) interrupt calls the output segment as an interrupt service routine, and outputs the proper pulses as stored by the calculation routine. Control then returns to the input and calculation loop. Using a timer interrupt insures correct timing of the output pulses independent of the various length program branches taken during the calculation routine.

The initial tracking algorithm duplicates in digital form an analog tracking system which has been running successfully on the Varian roof for over two years. Other algorithms could be tried in Phase III. The cooling water pump is turned on if the array is tracking, if an over temperature condition is sensed, or if freezing air temperatures are sensed. The sun is located by first using the coarse sun sensors which have a 300 degree view, and then using the fine sun sensor with a limited field of view for accurate tracking. The array turns to the east limit switch and the horizontal (up) limit switch at night. The array is stowed at the top limit switch position (horizontal) in case of a high wind velocity component perpendicular to the array face, or upon an over temperature condition. The wind sensor is really superfluous at the San Ramon site, but is included to make the design more generally useful.

The sun sensor, shown in Fig. A-1, uses paired back to back GaAs photodiodes. GaAs devices are used rather than Si devices because their higher voltage output allows retention of the full 8-bit accuracy of the internal ADC, and they are available as a by-product of the solar cell production line. The sun sensor assembly is built in a square pyramid shape, with an internal pyramid shaped prism. The coarse sun sensors are mounted behind windows on the sides of the assembly. This back-to-back connection subtracts the two photocurrents and tells the microprocessor which half of the sky the sun is in. The front of the assembly shields the prism so that it sees only about 10 degrees of the sky. The prism, with back-to-back connected photodiodes behind it, is cut at the internal reflection angle, and gives the microprocessor a very accurate indication of the center line position of the sun.

1	2 EBT 403	BACK PLATE	1
1	2 EBT 405	ADJUSTMENT PLATE BOTTOM	2
1	2 EBT 425	ADJUSTMENT PLATE TOP	3
2	2 EBT 412	SIDE PLATE	4
2	B EBT 427	SIDE PLATE PRISM SUPPORT	5
1	2 EBT 421	PRISM ASSY	6
2	2 EBT 427	SHORT HINGE	7
2	B EBT 406	LONG HINGE	9
1	2 EBT 408	PLATE PRISM SUPPORT	9
4	B EBT 417	SPRING CLIP	10
1	B EBT 414	FILTER	11
12		ROUND HD SCR 2-56 x .25 LG	12
4		GLASS SLIDE	13
1	A004105	STEM ASSY (TUBE DIVISION)	14
4		SOLAR CELL (VARIAN)	15
2		CO-AXIAL LOCK SCREW	16

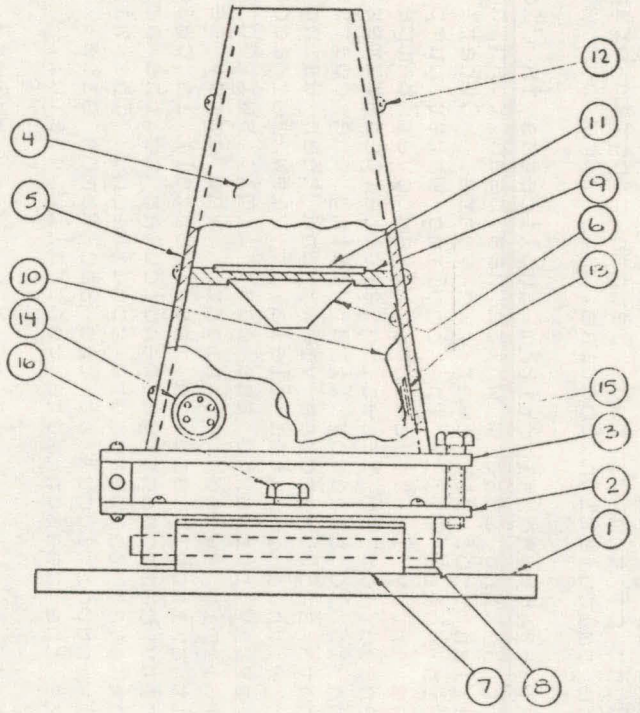

Nº REQ PER NEXT ASSY 1
Nº REQ PER ARRAY 1

DO NOT SCALE DRAWING

DESCRIPTION OF CHANGE	DRAWN-E REVISED
NUM	
TO	
DFT	CJ
CHK	
DATE	1/27/77
REV	2

DRAWN	DATE	APPROVED	DATE	CODE
CJ	1/27/77			
CHECKED	DATE	APPROVED	DATE	CLASS

SUN SENSOR, ASSY

varian | RESEARCH | C | EBT 418 | 2
DIVISION | SIZE | DRAWING NO. | REV

NOT OTHERWISE SPEC FRAC ± ANG ±
FIN √ DEC .x ± .xx ± .xxx ±
SCALE NONE

Fig. A.1 Assembly, Sun Sensor

A-2

EBT 418

4165 APRIL LITHO IN U.S.A.

The wind sensor works on the principle of increased cooling of a hot wire by wind; hence it has no moving parts. The hot wire (actually a thermistor) is baffled from wind blowing along the length of the array, but is exposed to wind perpendicular to the array. Thus, the array will only be stowed when it really needs to be stowed. The thermal type of sensor also provides a reasonable time constant so that the array will not stow on very short gusts.

APPENDIX B. OPERATION OF THE MAXIMUM POWER TRACKER

A normal feedback system seeks to establish its operating point by comparing the actual output of the system with some desired result. The magnitude and polarity of the error between the two quantities is used as the signal which causes the system to change its output in a direction which tends to reduce the magnitude of the error. A feedback system required to maximize the power output from a photovoltaic array is more complex, since a given system change in response to an error signal may cause either a decrease or an increase in power, depending upon which side of the maximum power point the system is operating. At zero current, the voltage is high, but no power is being supplied, since there is no current. At short circuit conditions, current is high, but again no power is delivered, since the voltage is zero. At intermediate points, power is supplied in varying amounts, depending on loading, and a point exists where the maximum power can be sensed.

The synchronous inverter control circuitry is capable of varying the output voltage of the array field by loading it at different levels in response to a standard feedback regulator which compares the actual operating voltage to a signal indicating the desired voltage. If a change to a lower voltage is signalled, the system increases the loading of the source until its voltage sags to the desired value. Voltage increases are accomplished by reducing the loading.

The correct voltage that corresponds to maximum power is tracked by the system. Basic elements are:

1. A wattmeter circuit that continuously measures the DC input power level and provides a signal output proportional to actual power.

2. Two sample and hold circuits, controlled by a timer, that alternately sample the wattmeter signal output and hold it for comparison with the next sample.

3. A comparator that works in combination with a logic circuit to determine if a given sample represents a power level that is greater or smaller than the previous sample.

4. A flip-flop circuit that changes state whenever a new sample is smaller than the preceding one, but remains in the same state if a new sample is larger than the preceding one, thus representing an increase in power level.

5. An integrator circuit that provides a constantly changing output, whose direction of change is increasing for one state of the flip-flop and decreasing for the other state of the flip-flop.

Operation of the second control loop is as follows: The output of the integrator is used as the signal which indicates to the first feedback controller the desired voltage level. It has limits which are set so that it does not attempt to control voltage beyond the range of the inverter or the array field. As indicated above, this integrator will constantly change its output in a direction determined by the state of the flip-flop. If, for example, the flip-flop is forced to remain in a state that causes a constantly increasing output of the integrator, the controller will sweep through the voltage range, starting at a low level and increasing to maximum as determined by its preset limit. If the state of the flip-flop is changed and forced to remain in the opposite condition, the integrator will cause the controller to sweep down the voltage range toward zero.

In automatic operation, the flip-flop is not held in any particular state, but is allowed to change as determined by the interpretation of successive samples. The sample rate is adjusted so that many samples are taken in the time it would take to make a complete sweep from zero to maximum or from maximum to zero.

Assume that the controller starts at zero voltage and is moving in a direction toward maximum voltage. As each sample is taken, the logic circuit and the comparator compare it to the preceding one. On the low voltage side of the maximum power point, as the voltage increases, each sample of power is larger than the one before it, and the flip-flop does not react. The voltage therefore continues to rise. Eventually the voltage reaches the value corresponding to maximum power and passes it. When this happens, the next sample of power indicates to the logic circuit and the comparator that the power has decreased from the preceding sample, and the flip-flop is told to change state. This causes the voltage to stop rising, reverse movement to a downward direction, and return toward the maximum power point.

From this time on, the voltage will cycle back and forth around the maximum power point, reversing direction each time it moves far enough to indicate a decrease in power. If the field DC output characteristics change, an automatic readjustment restores the voltage control to the new optimum point.

To provide minimum voltage swings in the area of maximum power and to allow optimum stability, the rate of voltage change as well as the time between samples is adjustable.

APPENDIX C. OPTIMUM LAND UTILIZATION

Figures 2-30 and 2-31 show that shadowing losses increase abruptly for North/South array spacings less than about y = 60 ft., and rather gradually for East/West spacings x. An approximate exponential relationship between spacing x and fractional energy loss L can be derived from these plots:

$$L = 0.6 \exp(-x/26) \quad (1)$$

Two arrays generating a rated 7200 watts occupy an area

$$y\,(x + y) \quad (2)$$

Where y (above) is about 60 ft. At a cost of $ B/sq. ft. or $43,560B/acre, the land cost is therefore approximately

$$\$60\,(x + 60) \quad (3)$$

For an array cost of $A/watt, the cost of the lost power is

$$\$4320\ A \exp(-x/26) \quad (4)$$

Minimizing the sum of (3) and (4) the optimum spacing becomes:

$$x = 26 \ln 2.77\,(A/B) \quad (5)$$

For A = $10/watt, for example, and

B = $0.50/sq ft. ($21,780/acre)

x = 104 ft.

Inclusion of other area-related costs (e.g., copper interconnects, cable tray costs, etc.) would obviously modify this value slightly, and would be worth including when more precise information is available on actual array costs and performance.

APPENDIX D. AIR CONDITIONING FOR EQUIPMENT/VISITOR'S BUILDING

Based on Proposed Control Building Layout, see Fig. 4-4. Insulation added to building for determining loads of heating and cooling: Ceiling: R-19 Walls: R-11 Concrete Floor Slab: R-5 perimeter insulation

ALTERNATE I -- Proposed Design Goal: Provide a heating and cooling system of commercial quality that would require minimum service and maintenance, incorporate some waste heat from the solar concentrators and give reliable temperature control for equipment/visitor's building (see Fig. D-1).

System Type: Mechanical refrigeration for cooling and hot water heating using waste heat from the solar concentrators. Hot water storage.

Power Requirement: Waste Heat -- 120°F hot water at 6 gpm; Electrical Energy -- 1300 kWh

ALTERNATE II - Proposed Design Goal: Provide a heating and cooling system totally dependent on waste heat from wolar concentrators and monitor the performance and reliability over experimental project life (see Fig. D-2).

System Type: Absorption cooling and hot water heating. Hot water storage and hydronic piping with circulating pumps.

Power Requirement: Waste Heat -- 195°F hot water at 15 gpm; Connected Electrical -- 5.0 kw, 120/240/1

Annual Energy Requirement: Waste Heat -- 134 MMBTU

Electrical Energy -- 900 kWh

Utility Requirements: Make-up water (10 gpm capacity) and drain connection.

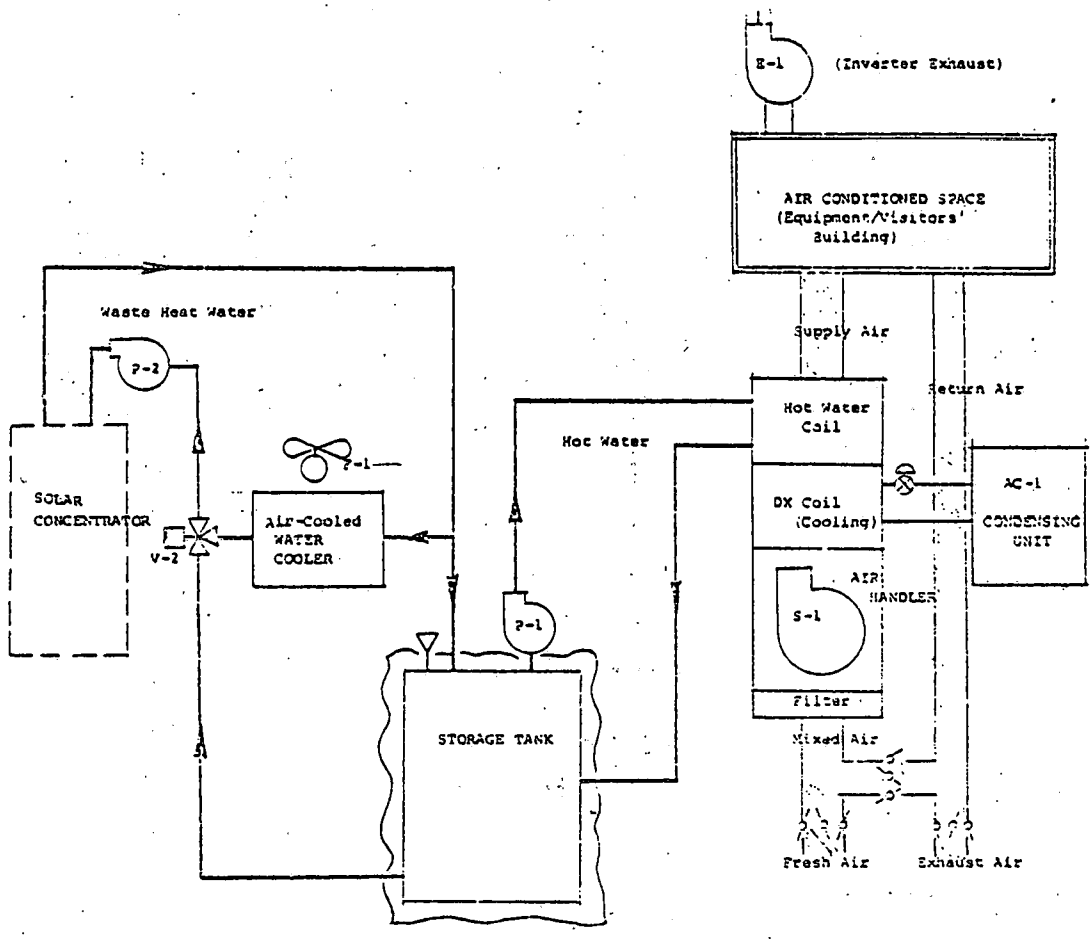

Fig. D.1 Alternate 1 - Mechanical Cooling and Hot Water Heating - Photovoltaic Project

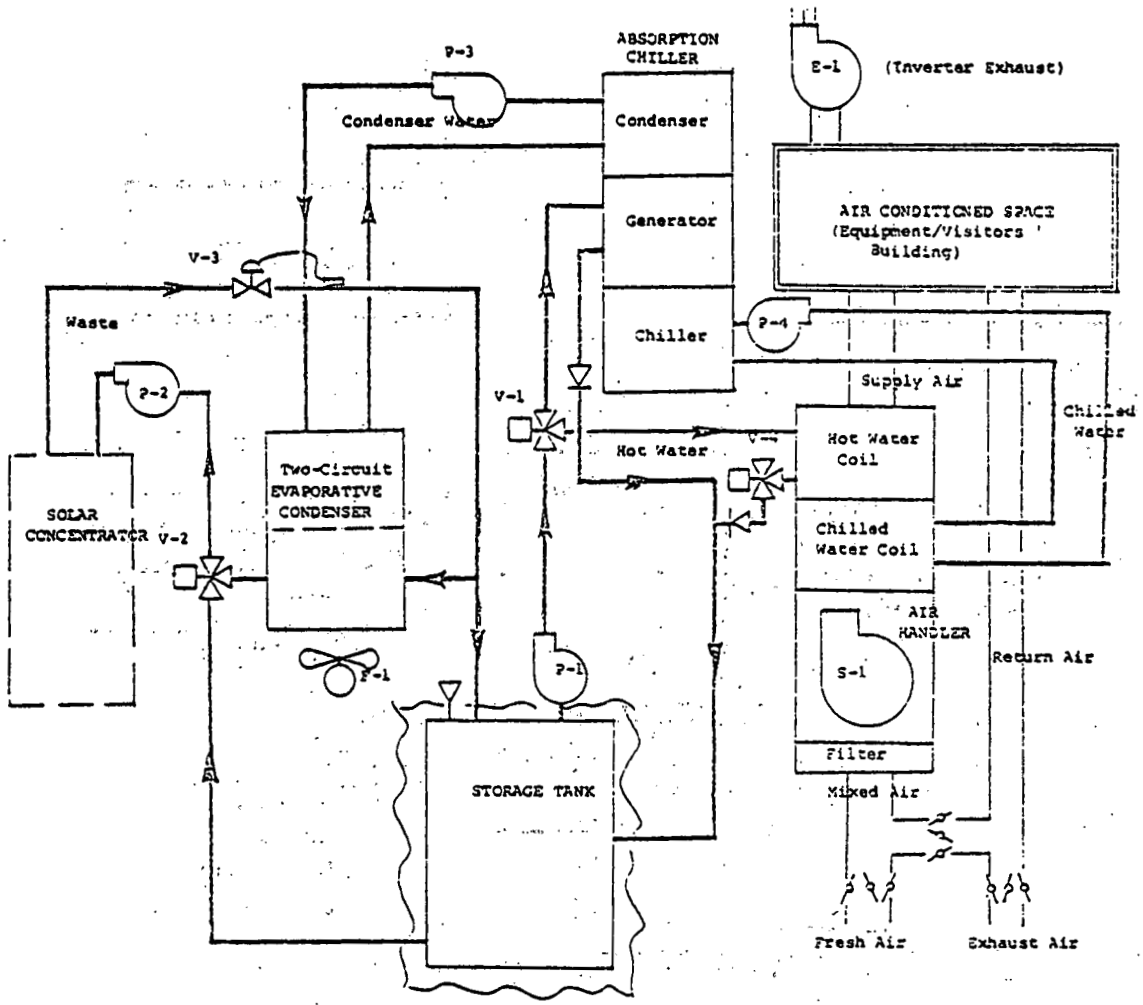

Fig. D.2 Alternate II - Absorption Cooling and Hot Water Heating - Photovoltaic Project

APPENDIX E

FAILURE ANALYSIS TABLES

TABLE 1

****

* PROBLEM TITLE FOR THIS ANALYSIS BY KITT-SOLAR ENERGY TREE 2 THURSDAY 1/18/79 *

****

NO. OF COMPONENTS AND INHIBIT CONDITIONS (NCOMP) = 152

COMPONENT DATA (LAMBDA AND TAU)
(NON-POSITIVE TAU DENOTES NON-REPAIR)
(NON-POSITIVE LAMBDA DENOTES INHIBIT CONDITION)

COMPONENT	LAMBDA	TAU
BTSA	0.30999973E-06	0.30000000E 01
BTSB	0.29999983E-05	0.60000000E 01
BTSC	0.29999973E-06	0.10000000E 01
BTSD	0.29999983E-05	0.10000000E 01
PRB1	0.0	0.99999994E-10
111A	0.59999957E-06	0.20000000E 01
111B	0.66219957E-06	0.20000000E 01
112A	0.59999957E-06	0.10000000E 01
112B	0.13697982E-05	0.30000000E 01
113B	0.99999943E-05	0.60000000E 01
114A	0.99999869E-12	0.60000000E 01
114B	0.99999869E-12	0.60000000E 01
114C	0.99999869E-12	0.60000000E 01
114D	0.99999869E-12	0.60000000E 01
114E	0.99999869E-12	0.60000000E 01
1141	0.99999869E-12	0.60000000E 01
1142	0.99999869E-12	0.60000000E 01
1143	0.99999869E-12	0.60000000E 01
115	0.0	0.92459992E-02
116	0.45599963E-05	0.33600000E 03
117	0.0	0.99999979E-02
118A	0.57999960E-09	0.20000000E 01
118B	0.57999960E-09	0.20000000E 01
118C	0.57999960E-09	0.20000000E 01
118D	0.57999960E-09	0.20000000E 01
118E	0.57999960E-09	0.20000000E 01
118F	0.97424936E-05	0.10000000E 01
118G	0.62317952E-07	0.10000000E 01
119	0.28399969E-04	0.20000000E 01
121A	0.99999852E-07	0.30000000E 01
121B	0.19999987E-07	0.10000000E 01
121C	0.66109959E-06	0.30000000E 01
122A	0.59999966E-05	0.10000000E 01
122B	0.13697982E-05	0.30000000E 01
122C	0.19999987E-07	0.10000000E 01
122D	0.60799948E-07	0.30000000E 01
13CA	0.21999983E-06	0.40000000E 01
13CB	0.21999983E-06	0.40000000E 01
13CC	0.21999983E-06	0.40000000E 01
13FA	0.99499939E-05	0.40000000E 01
13FC	0.28999982E-08	0.30000000E 01
13FD	0.59999957E-06	0.20000000E 01
13FE	0.89999949E-05	0.20000000E 01
13FF	0.11999990E-07	0.30000000E 01
13FG	0.29999978E-07	0.20000000E 01
13GA	0.29999980E-08	0.60000000E 01
13GB	0.29999980E-08	0.60000000E 01

TABLE 2

136G	0.19999978E-04	0.60000000E 01
136H	0.19999979E-04	0.60000000E 01
136I	0.12499986E-05	0.60000000E 01
136K	0.31249982E-06	0.60000000E 01
136L	0.31249982E-06	0.60000000E 01
136M	0.31249982E-06	0.60000000E 01
136N	0.31249982E-06	0.60000000E 01
136P	0.31249982E-06	0.60000000E 01
136Q	0.31249982E-06	0.60000000E 01
136R	0.31249982E-06	0.60000000E 01
136S	0.31249982E-06	0.60000000E 01
136T	0.12499986E-05	0.60000000E 01
137A	0.19999978E-04	0.60000000E 01
137B	0.99999943E-05	0.60000000E 01
137C	0.99999943E-06	0.60000000E 01
137D	0.49999971E-05	0.60000000E 01
137E	0.59999934E-07	0.30000000E 01
137F	0.17999977E-04	0.30000000E 01
139A	0.35999969E-04	0.30000000E 01
139B	0.35999965E-05	0.30000000E 01
139C	0.12499993E-06	0.30000000E 01
139D	0.12499993E-06	0.30000000E 01
139E	0.14999983E-06	0.30000000E 01
139F	0.12499993E-06	0.30000000E 01
139G	0.12499993E-06	0.30000000E 01
139H	0.12499993E-06	0.30000000E 01
139I	0.12499993E-06	0.30000000E 01
2111	0.99999852E-07	0.30000000E 01
2112	0.59999966E-05	0.30000000E 01
2113	0.59999957E-06	0.30000000E 01
2114	0.0	0.99999964E-01
212	0.22139982E-04	0.60000000E 01
221	0.22139982E-04	0.60000000E 01
222	0.93799940E-06	0.60000000E 01
231	0.27829970E-04	0.60000000E 01
232	0.27829970E-04	0.60000000E 01
251	0.55859942E-04	0.60000000E 01
252	0.75859934E-04	0.60000000E 01
26	0.14199991E-04	0.60000000E 01
271	0.59999966E-05	0.30000000E 01
272	0.59999957E-06	0.30000000E 01
273	0.29999983E-05	0.60000000E 01
31	0.74999957E-06	0.60000000E 01
32	0.74999957E-06	0.60000000E 01
33	0.74999957E-06	0.60000000E 01
34	0.74999957E-06	0.60000000E 01
4	0.0	0.10000000E-10
5	0.45659952E-04	0.60000000E 01

ISTOP= 1
NYPT 5
TIME POINTS FOR DELTA NON-POSITIVE (TOT(J))-IN HOURS...
0.0
0.336000E 03
0.720000E 03
0.876000E 04
0.262800E 05

```
NO. OF SETS (NCUT) =  139
SET INFORMATION

SET NO.   1, WITH COMPONENTS - 111A

SET NO.   2, WITH COMPONENTS - 212  2111

SET NO.   3, WITH COMPONENTS - 31

SET NO.   4, WITH COMPONENTS - 4

SET NO.   5, WITH COMPONENTS - 5

SET NO.   6, WITH COMPONENTS - 121A

SET NO.   7, WITH COMPONENTS - 134A

SET NO.   8, WITH COMPONENTS - 114A

SET NO.   9, WITH COMPONENTS - 115

SET NO.  10, WITH COMPONENTS - 116

SET NO.  11, WITH COMPONENTS - 117

SET NO.  12, WITH COMPONENTS - 112A

SET NO.  13, WITH COMPONENTS - 111B

SET NO.  14, WITH COMPONENTS - 221  222

SET NO.  15, WITH COMPONENTS - 231  232

SET NO.  16, WITH COMPONENTS - 232  251

SET NO.  17, WITH COMPONENTS - 251  252

SET NO.  18, WITH COMPONENTS - 26

SET NO.  19, WITH COMPONENTS - 271

SET NO.  20, WITH COMPONENTS - 32

SET NO.  21, WITH COMPONENTS - 33

SET NO.  22, WITH COMPONENTS - 34

SET NO.  23, WITH COMPONENTS - 122A

SET NO.  24, WITH COMPONENTS - 121B

SET NO.  25, WITH COMPONENTS - 121C

SET NO.  26, WITH COMPONENTS - 136A

SET NO.  27, WITH COMPONENTS - 131A
```

TABLE 4

MINIMAL SET INFORMATION

CHARACTERISTICS FOR SET NO. = 1

T (HOURS)	Q	W	L	WSUM	FSUM
0.0	0.0	5.9999957D-07	5.9999957D-07	0.0	0.0
3.3600000E 02	1.1999973D-06	5.9999883D-07	5.9999958D-07	2.0159973D-04	2.0157954D-04
7.2000000E 02	1.1999973D-06	5.9999883D-07	5.9999958D-07	4.3199928D-04	4.3190640D-04
8.7600000E 03	1.1999973D-06	5.9999883D-07	5.9999958D-07	5.2559899D-03	5.2422077D-03
2.6280000E 04	1.1999973D-06	5.9999883D-07	5.9999958D-07	1.5767969D-02	1.5644325D-02

CHARACTERISTICS FOR SET NO. = 2

T (HOURS)	Q	W	L	WSUM	FSUM
0.0	0.0	0.0	0.0	0.0	0.0
3.3600000E 02	3.9846599D-11	1.9923293D-11	1.9923294D-11	3.3471133D-09	3.3471134D-09
7.2000000E 02	3.9846599D-11	1.9923293D-11	1.9923294D-11	1.0997658D-08	1.0997658D-08
8.7600000E 03	3.9846599D-11	1.9923293D-11	1.9923294D-11	1.7118093D-07	1.7118093D-07
2.6280000E 04	3.9846599D-11	1.9923293D-11	1.9923294D-11	5.2023703D-07	5.2023693D-07

CHARACTERISTICS FOR SET NO. = 3

T (HOURS)	Q	W	L	WSUM	FSUM
0.0	0.0	7.4999957D-07	7.4999957D-07	0.0	0.0
3.3600000E 02	4.4999770D-06	7.4999622D-07	7.4999962D-07	2.5199929D-04	2.5196811D-04
7.2000000E 02	4.4999770D-06	7.4999622D-07	7.4999962D-07	5.3999784D-04	5.3985394D-04
8.7600000E 03	4.4999770D-06	7.4999622D-07	7.4999962D-07	6.5699674D-03	6.5486614D-03
2.6280000E 04	4.4999770D-06	7.4999622D-07	7.4999962D-07	1.9709901D-02	1.9517018D-02

CHARACTERISTICS FOR SET NO. = 4

T (HOURS)	Q	W	L	WSUM	FSUM
0.0	1.0000000D-11	0.0	0.0	0.0	0.0
3.3600000E 02	1.0000000D-11	0.0	0.0	0.0	0.0
7.2000000E 02	1.0000000D-11	0.0	0.0	0.0	0.0
8.7600000E 03	1.0000000D-11	0.0	0.0	0.0	0.0
2.6280000E 04	1.0000000D-11	0.0	0.0	0.0	0.0

CHARACTERISTICS FOR SET NO. = 5

T (HOURS)	Q	W	L	WSUM	FSUM
0.0	0.0	4.5659952D-05	4.5659952D-05	0.0	0.0
3.3600000E 02	2.7388451D-04	4.5647437D-05	4.5659945D-05	1.5339641D-02	1.5224658D-02
7.2000000E 02	2.7388451D-04	4.5647437D-05	4.5659945D-05	3.2868257D-02	3.2340647D-02
8.7600000E 03	2.7388451D-04	4.5647437D-05	4.5659945D-05	3.9987365D-01	3.2966730D-01
2.6280000E 04	2.7388451D-04	4.5647437D-05	4.5659945D-05	1.1996168D 00	6.9878873D-01

CHARACTERISTICS FOR SET NO. = 6

T (HOURS)	Q	W	L	WSUM	FSUM
0.0	0.0	9.9999852D-08	9.9999852D-08	0.0	0.0
3.3600000E 02	2.9999944D-07	9.9999795D-08	9.9999831D-08	3.3599941D-05	3.3599382D-05
7.2000000E 02	2.9999944D-07	9.9999795D-08	9.9999831D-08	7.1999862D-05	7.1997290D-05
8.7600000E 03	2.9999944D-07	9.9999795D-08	9.9999831D-08	8.7599821D-04	8.7561495D-04
2.6280000E 04	2.9999944D-07	9.9999795D-08	9.9999831D-08	2.6279946D-03	2.6245454D-03

CHARACTERISTICS FOR SET NO. = 7

T (HOURS)	Q	W	L	WSUM	FSUM
0.0	0.0	2.9999973D-07	2.9999973D-07	0.0	0.0
3.3600000E 02	1.7999946D-06	2.9999916D-07	2.9999971D-07	1.0079981D-04	1.0079483D-04
7.2000000E 02	1.7999946D-06	2.9999916D-07	2.9999971D-07	2.1599949D-04	2.1597647D-04
8.7600000E 03	1.7999946D-06	2.9999916D-07	2.9999971D-07	2.6279927D-03	2.6245473D-03
2.6280000E 04	1.7999946D-06	2.9999916D-07	2.9999971D-07	7.8839780D-03	7.8529953D-03

SYSTEN INFORMATION-UPPER BOUNDS

DIFFERENTIAL CHARACTERISTICS-UPPER BOUNDS

T (HOURS)	Minimal Cutset Failed ProbabilityQ	Minimal Cutset Failure Rate W	Minimal Cutset Failure Intensity(p.hr.) L
0.0	1.91545181D-02	4.11886095D-04	4.19929658D-04
3.36000000E 02	2.23602150D-02	4.11949242D-04	4.21371214D-04
7.20000000E 02	2.23590680D-02	4.11945247D-04	4.21370705D-04
8.76000000E 03	2.23590685D-02	4.11945247D-04	4.21370705D-04
2.62800000E 04	2.23590685D-02	4.11945247D-04	4.21370705D-04

INTEGRAL CHARACTERISTICS-UPPER BOUNDS

T (HOURS)	WSUM Expected Number of Failures to Time T	FSUM Probability of one or more failures to Time T
3.36000000E 02	1.38404337D-01	1.31804663D-01
7.20000000E 02	2.96592847D-01	2.61507989D-01
8.76000000E 03	3.60866479D 00	9.75052096D-01
2.62800000E 04	1.08260156D 01	9.99984480D-01

noc = NUMBER OF CUTSETS

$$Q(t) \leq 1 - \prod_{i=1}^{i=noc} (1 - q_i(t))$$

$$w(t) \leq \sum_{i=1}^{i=noc} w_i(t)$$

$$E(t) \leq \frac{\sum_{i=1}^{i=noc} w_i(t)}{\prod_{i=1}^{i=noc} (1 - q_i(t))}$$

Qi = Minimal Cutset Failed Probability

Wi = Minimal Cutset Failure Rate

TABLE 6

SOLAR ENERGY TREE 2 THURSDAY 1/18/79

MINIMAL CUT SET DATA IN DESCENDING ORDER OF PROBAB ILITY

NO.	CUT SET NO.	MAX FAILURE PROB.	COMPONENTS CONTAINED IN SET
1	11	.99999979E-02	117
2	9	.92459992E-02	115
3	10	.15298147E-02	116
4	5	.27388451E-03	5
5	93	.11998546E-03	136H
6	59	.11998546E-03	136G
7	51	.11998546E-03	137A
8	53	.10798823E-03	139A
9	18	.85192674E-04	26
10	72	.71994742E-04	133E
11	35	.71994742E-04	134E
12	97	.59996353E-04	13GE
13	78	.59996353E-04	1378
14	52	.59996353E-04	1138
15	26	.59996353E-04	136A
16	43	.56796707E-04	119
17	82	.53997006E-04	137F
18	58	.53997006E-04	136E
19	95	.35998673E-04	13GC
20	135	.35998659E-04	135D 135Z
21	80	.29999079E-04	137D
22	60	.19899584E-04	1318
23	19	.17999657E-04	271
24	87	.17999657E-04	BTSB
25	47	.17999657E-04	273

NAME = SOLAR ENERCY TREE
FAMILY = SOL DATE = 1/17/79
PAGE = 1

ELEMENT	PAGE	XPOS	YPOS	TYPE
A	1	7	A	OR
ALTA	1	16	C	OR
ALTB	1	18	D	OR
ALT1	1	6	F	OR
ALT2	1	14	F	OR
ALT4	1	6	B	OR
ALT5	1	7	B	OR
ALT6	1	0	E	OR
ALT7	1	2	E	OR
ALT8	1	8	D	OR
ALTS	1	11	D	OR
BTSA	1	12	E	COMPONENT
BTSB	1	13	C	COMPONENT
BTSC	1	13	E	COMPONENT
BTSD	1	13	D	COMPONENT
BTSY	1	13	F	OR
PRBB	1	8	J	COMPONENT
PRB1	1	10	H	COMPONENT
I	1	7	J	INH
IALT	1	11	I	OR
II	1	7	J	OR
III	1	3	I	OR
IIIA	1	2	H	COMPONENT
IIIB	1	3	H	COMPONENT
IIII	1	3	I	OR

APPENDIX F

DEVELOPMENT OF HIGH-THROUGHPUT EPITAXIAL GROWTH FOR SOLAR CELLS

F-1 Pulse-Heated Liquid Phase Epitaxy

Pulse-heated LPE is a new mode of growth potentially capable of mass producing solar cells. Operation relies on the production of supersaturation by the local heating of a growth solution in contact with a saturation wafer in a furnace held at constant temperature. Growth occurs by turning off the heat pulse, then placing a substrate under the solution on which a layer grows as the supersaturation is relieved. After one growth, the process is repeated with a new substrate, thus avoiding the time-consuming furnace heatup and cool down experienced with conventional LPE. Semicontinuous operation is possible by moving the substrates in and the grown cells out through an interlock system. A reactor which takes 1.2 inch square substrates has been built and tested.

Pulse-heated LPE provides an alternative to conventional LPE now used to grow AlGaAs/GaAs solar cells. Only 2 or 3 cells can be grown by conventional LPE per reactor per day, limiting the potential for scale up to practical power generation levels. Heat up time of the furnace to the growth temperature accounts for most of the time spent. In addition to inefficient use of labor and materials, the conventional process is not easily amenable to automation. The development of pulse-heating greatly increases the number of cells/reactor/day (throughput) and can potentially be automated.

The pulse method depends upon supersaturation in the growth solution for the deposition driving force. Supersaturation is effected by locally heating a saturation wafer in contact with the top of the growth solution. The process is carried out inside a furnace held at constant temperature. The solution heats quickly to a new steady state temperature determined by the heater power. As a result of heating, the solution becomes undersaturated and partially dissolves the saturation wafers. After turning off the heater power and placing a substrate wafer underneath the solution, deposition takes place as the excess nutrient concentrations are relieved, causing growth simultaneously on the top wafer and bottom substrate. All this occurs while the main furnace remains at a nearly constant temperature.

Apparatus

A pulse-heated boat assembly comprises a heater, solution well and a wafer carrier. The heater is mounted inside a graphite plug at the top of the boat. Below the heater is a saturation wafer that contacts the growth solution, underneath which a substrate holder slides when required. A number of such assemblies can be used, depending on the number of different layers necessary. For the solar cell, an assembly for the InGaAs contact layer follows the one for the AlGaAs window layer. Growth of a buffer layer requires a third heater assembly. Figure F-1(a) shows a schematic of a typical assembly and Fig. F-1(b) the complete boat used for experiments on 3/4-inch wafers. Figure F-2 shows the boat designed for 1.2-inch square wafers enclosed in its quartz reactor tube.

A complete reactor requires more than just a boat for operation. As Fig. F-3 shows, the additional equipment consists of a furnace, a quartz reactor tube which is connected to an interlock chamber, and a magnetically-coupled push rod. Operation begins by placing the substrates into substrate carriers which are then stacked into a cartridge. The cartridge passes through a vacuum interlock into the chamber area where the carriers now have access to a track leading to the pulse-heated boat, held at temperature in pure H_2. Each carrier and its substrate moves from the cartridge holder, down the track to the boat where growth occurs, then returns to the cartridge. After all the substrates have passed through the furnace, the cartridge with carriers returns through the interlock to the outside world.

Growth temperatures are between 800° and 900°C for the constant temperature furnace. The perturbation heater takes between 20-100 watts, depending upon the material grown and thicknesses required. Time for growth is nominally 5 minutes/layer, but has been as short as 1.5 minutes/layer.

Experimental Results

Experimental behavior of layers grown by PH-LPE suggests that supercooling is the dominant mode of growth. Layer thickness as a function of time after the heater is turned off shows a rapid increase in the first few minutes then a more gradual approach to a asymptotic value. Figure F-4 shows this behavior (reminiscent of supercooled growth) for the growth of GaAs on GaAs (111)B where the heater power and time on are kept constant. When the heater on time is varied, but the growth time and heater power are kept constant, the layer thickness again shows a rapid rise for short on-times, then is nearly constant for times up to 60 minutes; Figure F-5 shows this behavior. This is expected,

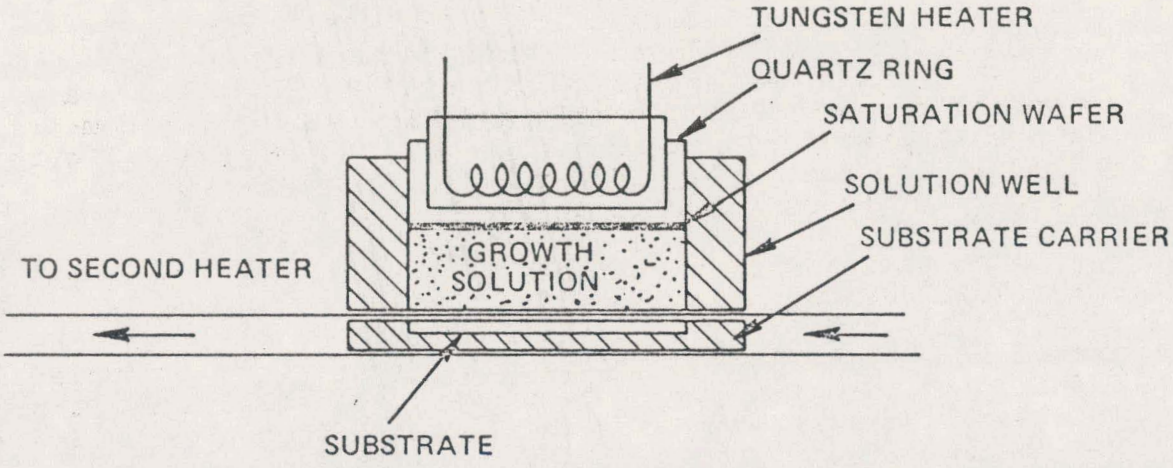

Fig. F.1 (a) Schematic of Heater Assembly for Pulse Heated LPE Boat

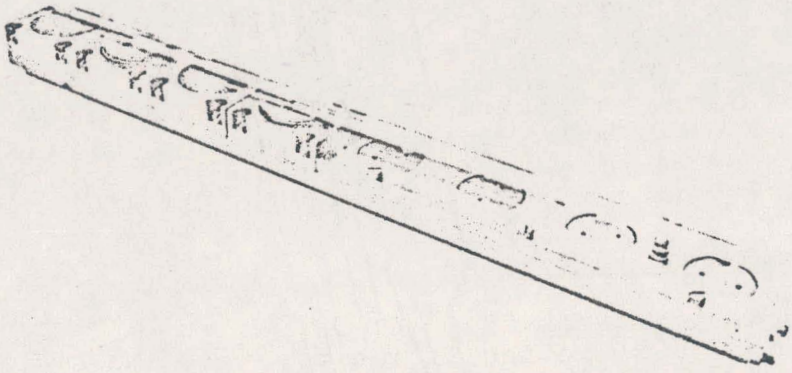

Fig. F.1 (b) Experimental Boat Using 3/4" Dia. Substrates

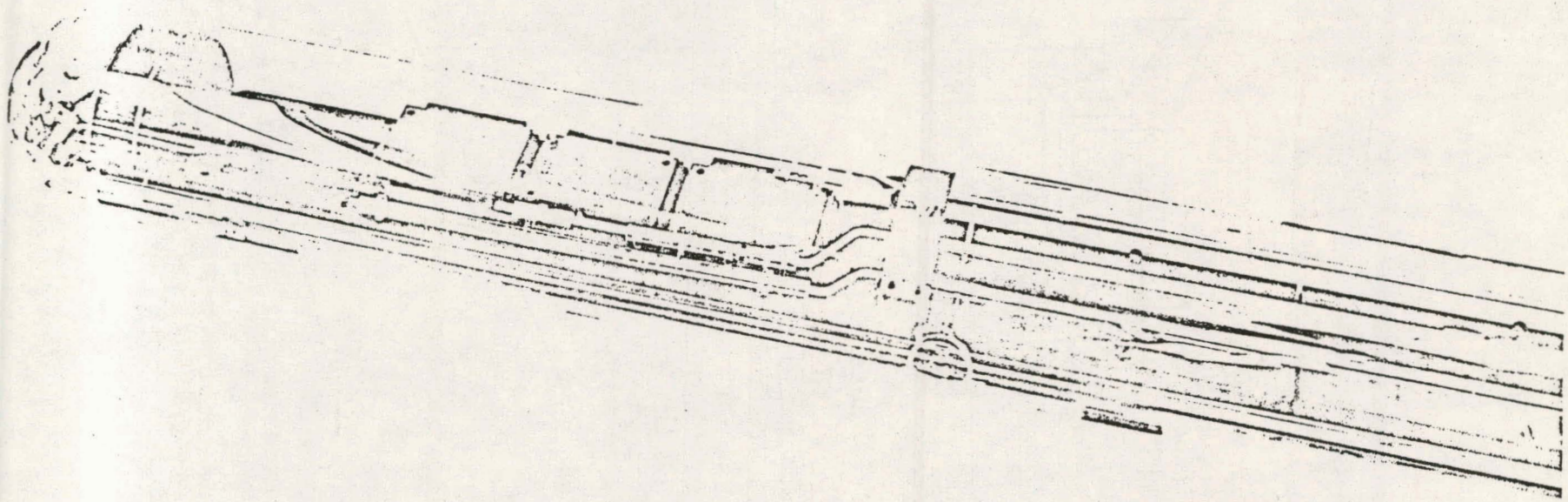

Fig. F.2 Pulse Heated LPE Boat for 1.2 inch Square Substrates in Its Quartz Reactor Tube

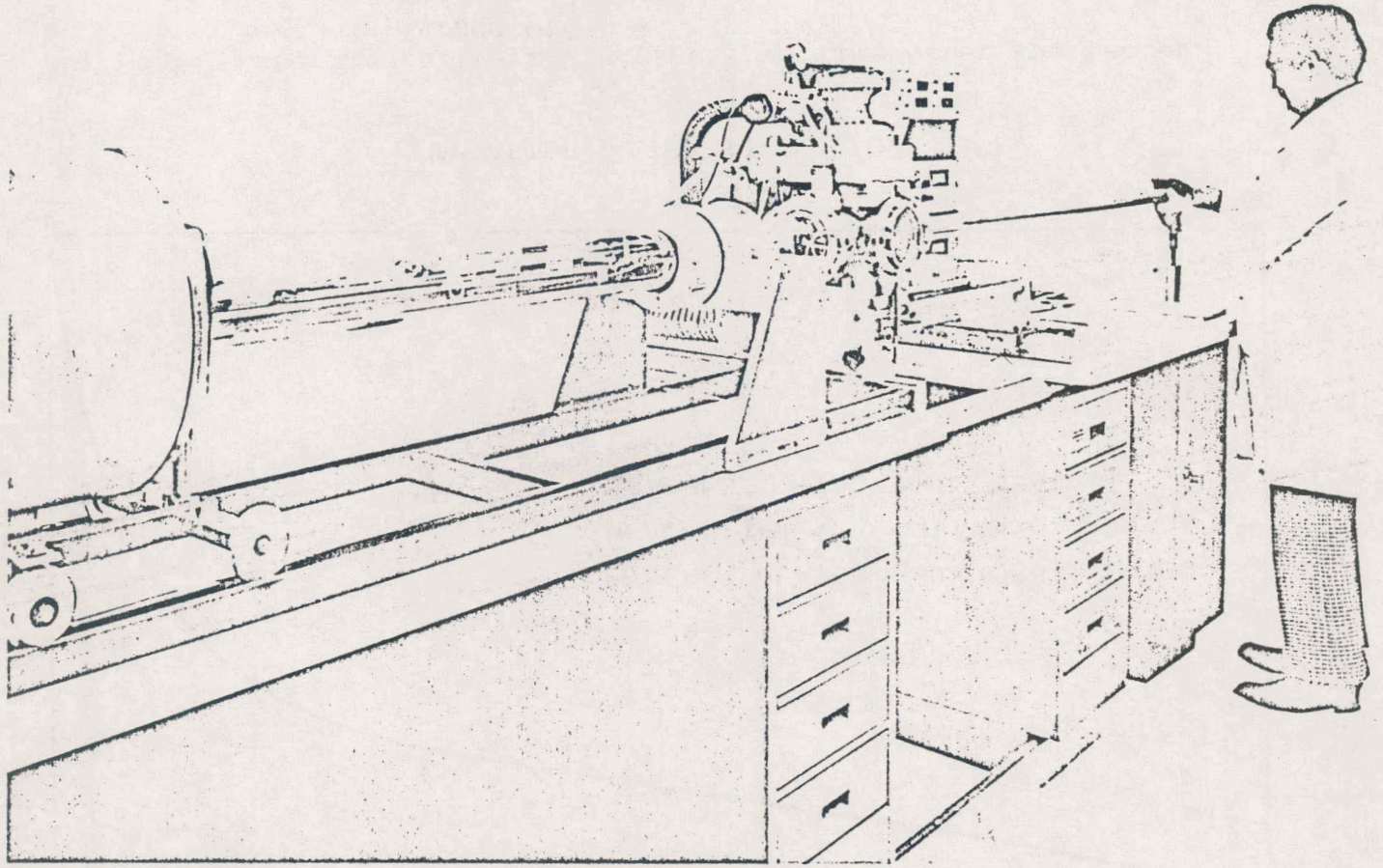

Fig. F.3 A Complete Pulse Heated LPE Reactor Showing the Furnace, the Reactor Tube, and the Interlock Chamber with Push Rod Assembly

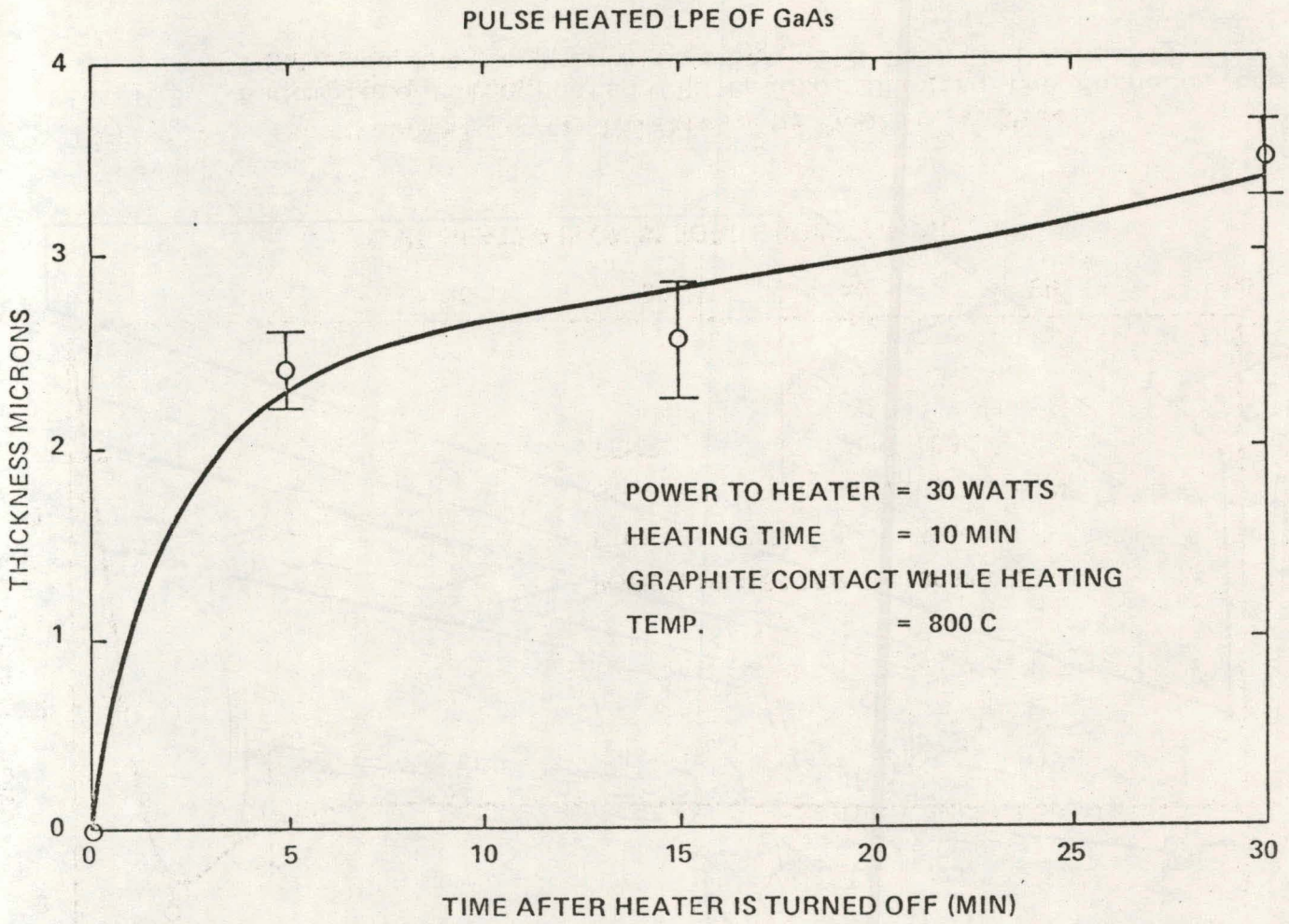

Fig. F.4 Experimental Layer Thickness vs Time After the Heater Power is Turned Off

Epi Layer: GaAs
Substrate: GaAs(111)B 3/4" Dia.

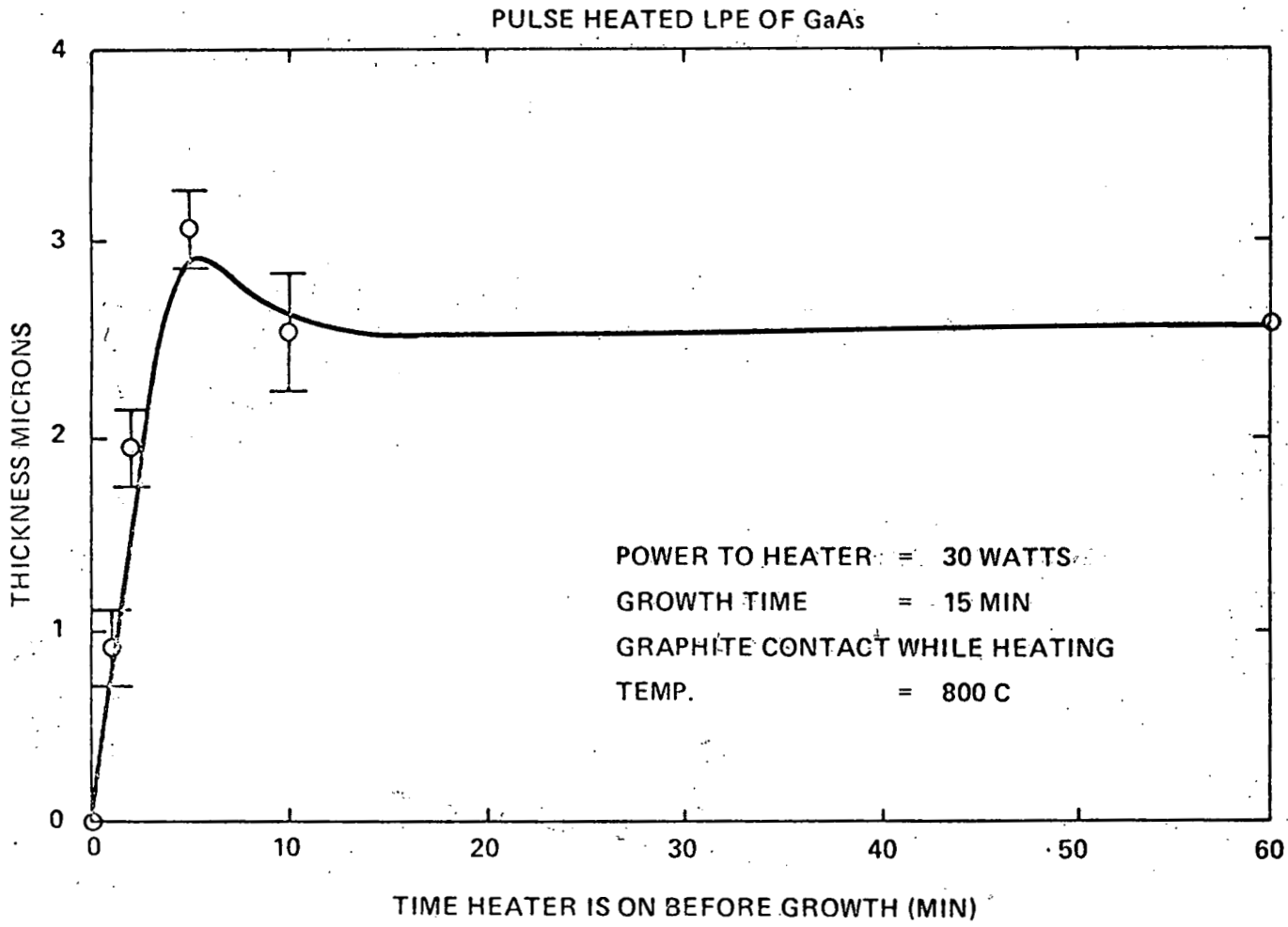

Fig. F.5 Experimental Layer Thickness vs Heater on Time

Epi Layer: GaAs
Substrate: GaAs(111) 3/4" Dia.

since once the solution is saturated at the new temperature, determined by the heater power and heat transfer dynamics of the system, no further supersaturation resulting in layer thickening can result.

Layers to be used for solar cells show a similar behavior, with the exception of GaAs on AlGaAs. Figure F-6 shows the layer thickness of AlGaAs as a function of growth time for two different heater power inputs. As can be seen, power input produces the necessary layer thickness control for solar cell growth. The variation in LPE behavior not seen in GaAs homoepitaxy occurs when (In)GaAs grows on AlGaAs surfaces as shown in Fig. F-7. Now, rather than rapidly increasing in thickness with time, the (In)GaAs layer thickness first increases relatively slowly then increases rapidly. Behavior of this sort suggests an interfacial kinetic limitation, where the time up to 3 minutes is a transient state before normal supercooled growth behavior sets in.

Solar cell characteristics are similar to those grown by conventional LPE. Figure F-8 shows a photomicrograph of a cleaved section of a PH-LPE AlGaAs solar cell, and Fig. F-9 shows the quantum spectral response for a 1/3" dia. cell. It is possible to grow all three layers by PH-LPE including the buffer layer. The spectral response of such a three-layered structure is in Fig. F-10.

Conclusion

In this program the concept of pulse-heated LPE was adapted to solar cell growth. A boat capable of using 3/4" diameter wafers was built and used for preliminary experiments in order to guide in the design of a much larger boat capable of using 1.2" square substrates. Such a boat and all the auxilliary equipment including interlock chamber, magnetically coupled push rod, vacuum system, and power supplies have been built and operated. Growth of three 1.2" wafers (GaAs and AlGaAs layers) capable of 4 cells/wafer required only 50 minutes total growth time under conditions that were not optimized with respect to heater power and time for heat up and cool down. So, at least, 24 wafers/reactor/8-hr day are presently available. This represents an order of magnitude increase over existing LPE methods. Further tests using the boat designed for the 1.2" square wafers are still necessary before the ultimate capacity can be established.

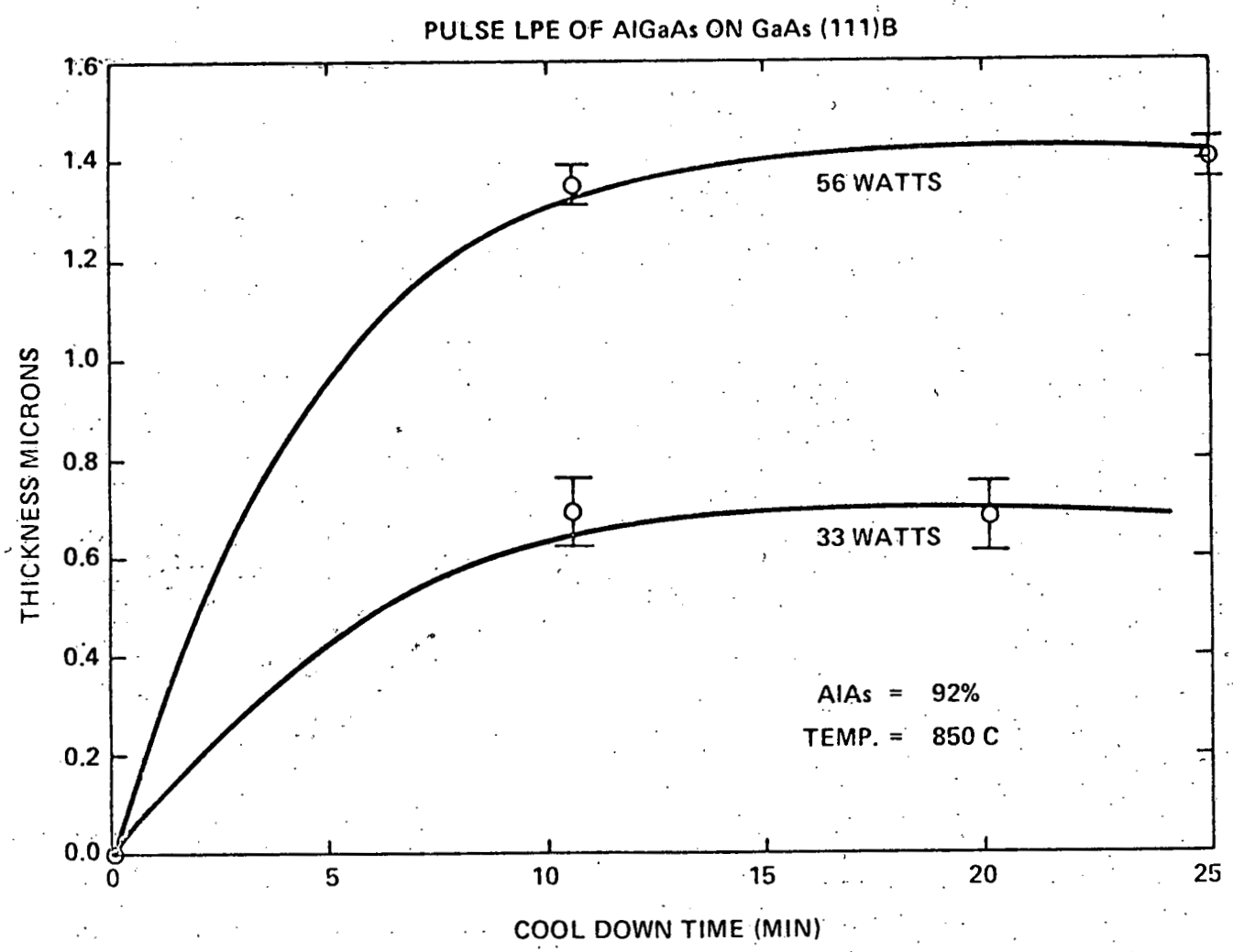

Fig. F.6 Experimental Layer Thicknesses vs Cool Down Time for Different Power Inputs to the Heater

Epi Layer: AlGaAs
.92 .08
Substrate: GaAs(111)B 3/4" Dia.

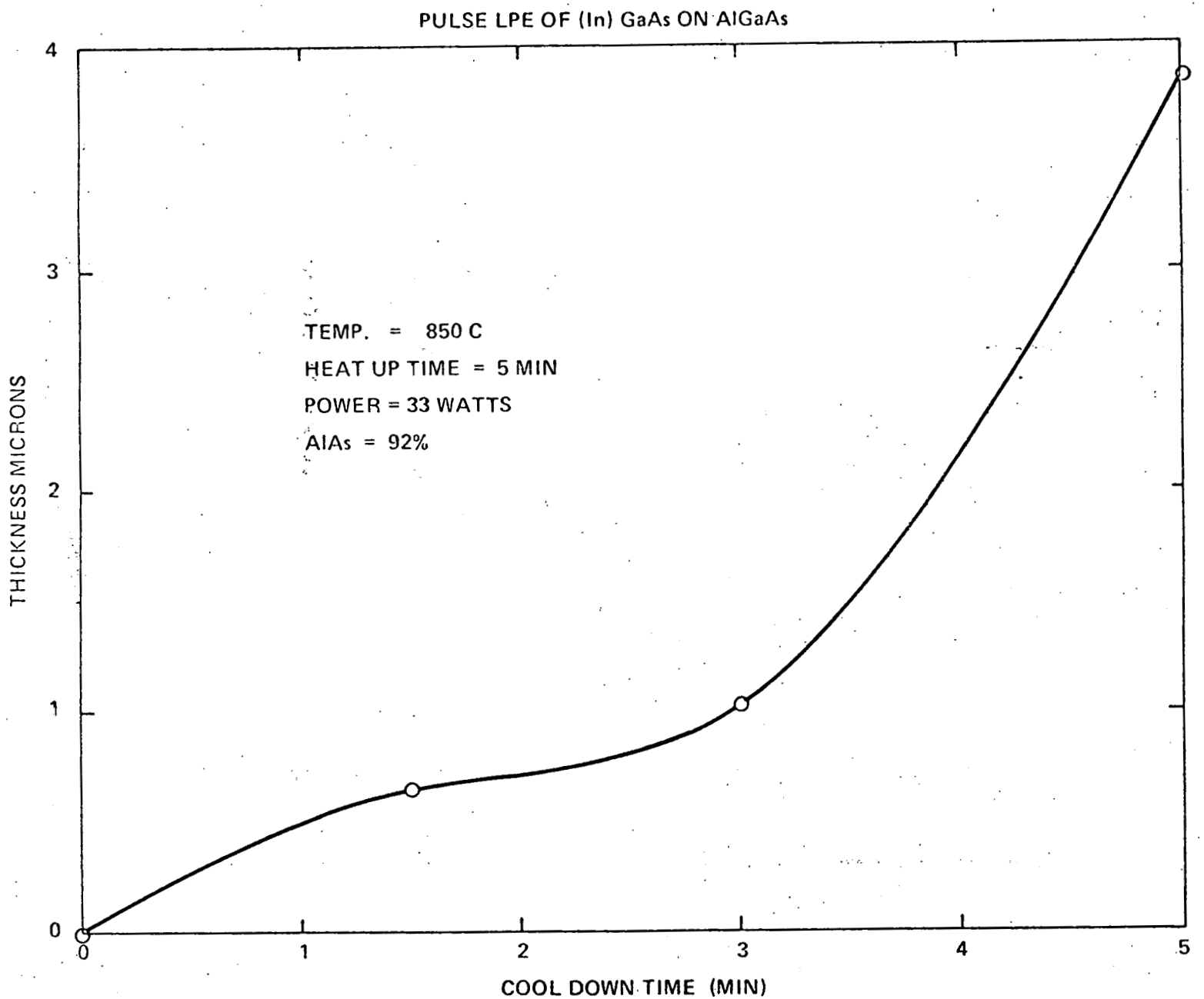

Fig. F.7 Experimental Layer Thickness vs Cool Down Time When Inter-facial Kinetic are Present
Epi Layer: (In)GaAs
Substrate: AlGaAs/GaAs(111)B 3/4" Dia.

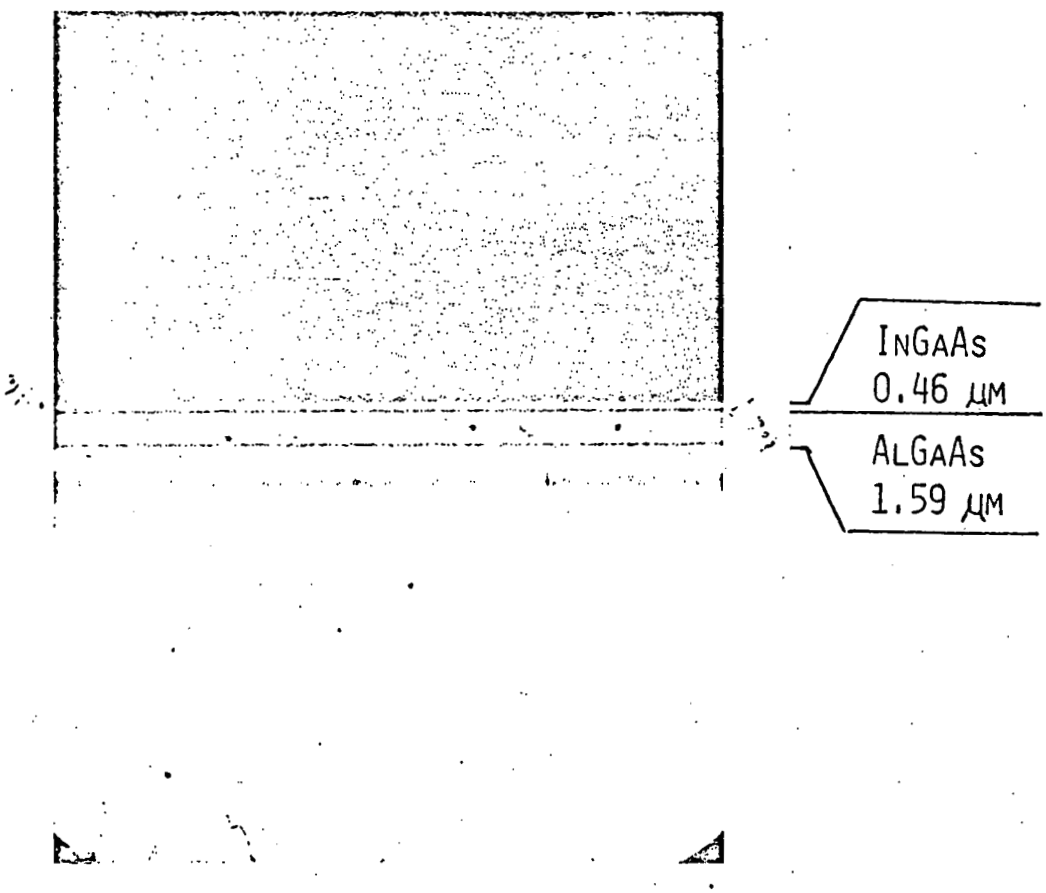

Fig. F.8 Cleaved Section of a Solar Cell Grown by Pulse Heated LPE

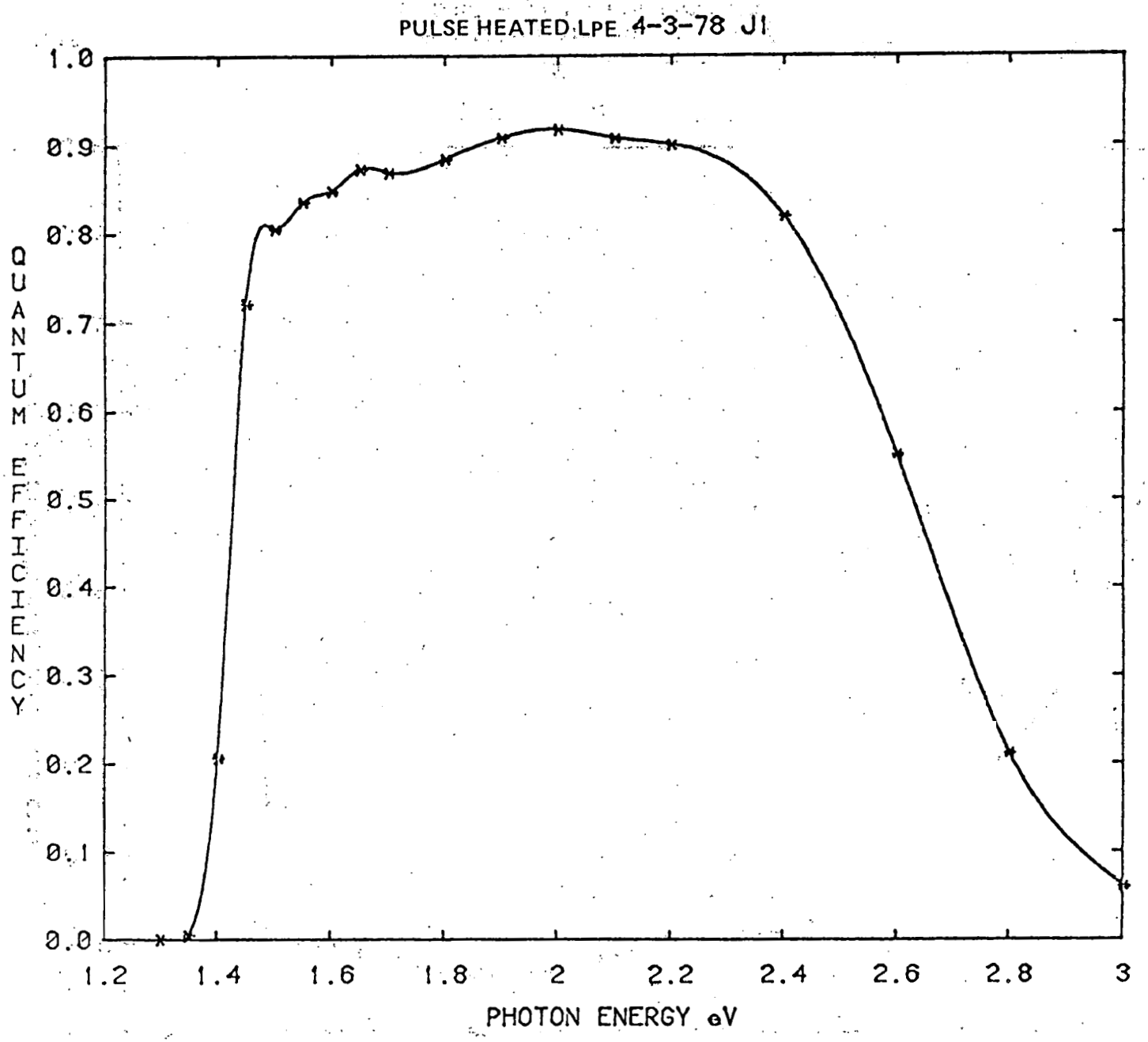

Fig. F.9 Quantum Efficiency vs Photon Energy for a 1/3" Solar Cell Grown by Pulse Heated LPE

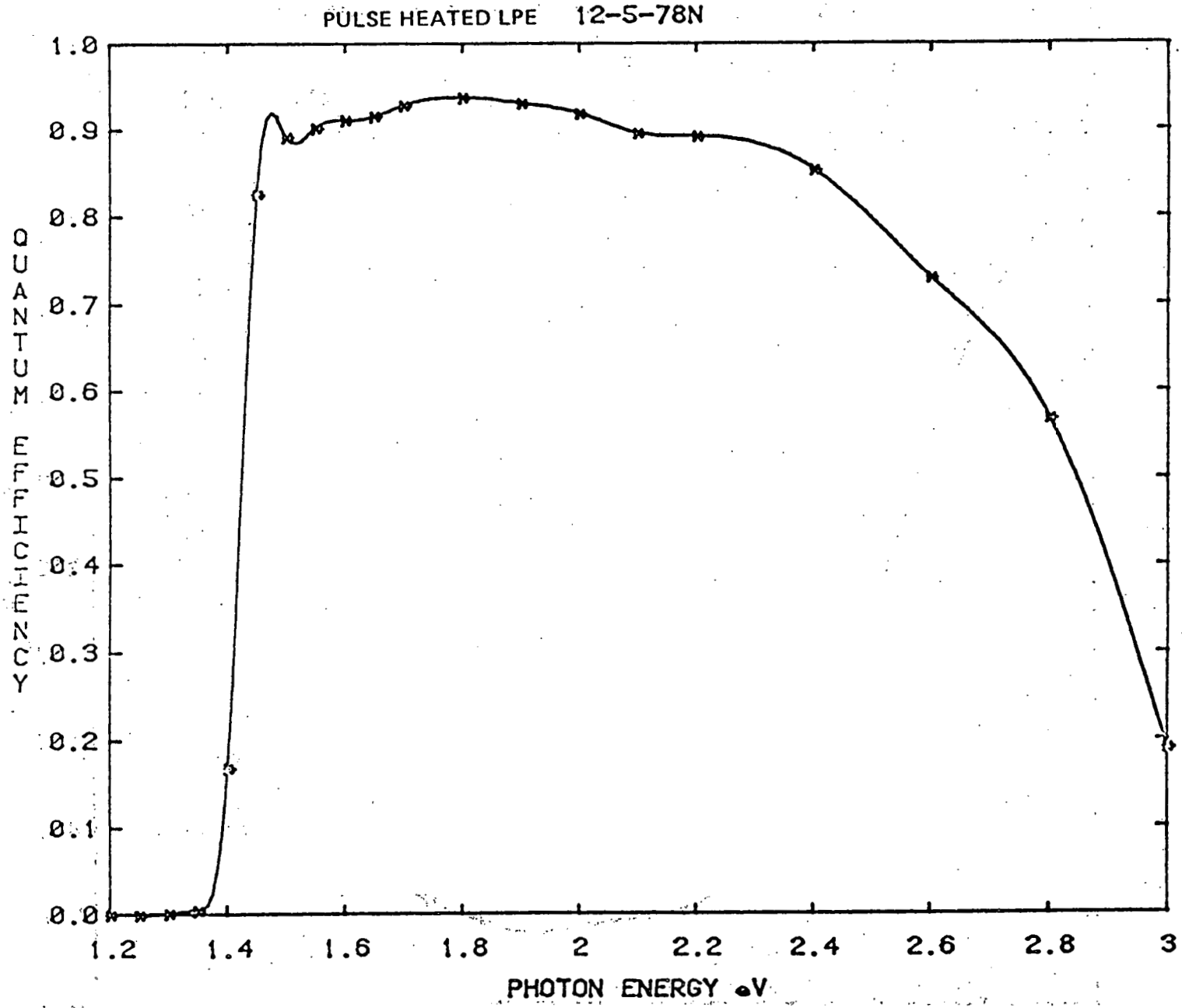

Fig. F.10 Quantum Efficiency vs Photon Energy from a Solar Cell Structure Where the Buffer Layer AlGaAs Window and GaAs Contact Layers Were All Grown in a Single PH-LPE Run

F-2 Organometallic Chemical Vapor Deposition

The organometallic chemical vapor deposition (OM-CVD) system was studied as part of the investigation into the low-cost, high-throughput production of AlGaAs/GaAs concentrator solar cells. A total of 95 experiments were conducted to study the material parameters important to concentrator solar cell performance, using an existing OM-CVD system. An additional 45 experiments produced material for the solar cell pilot production line. Some of these experiments explored the production characteristics and capacity of the system.

OM-CVD Materials Studies

Both n- and p-type doped layers of GaAs were grown and characterized. H_2S and diethylzinc (DEZ) provided the respective n- and p-type dopants used to dope the layers. Doping levels, n- and p-type, in the ranges required for solar cell production were reproducibly obtained (see Figs. F-11 and F-12). Minority carrier diffusion lengths of >3 microns for n-type and >2 microns for p-type GaAs was measured. The GaAs was grown at a growth rate of .065 microns/min. Characterization of AlGaAs layers has also been conducted. In particular work concentrated on the $Al_{.9}Ga_{.1}As$ composition required for the window layer in the cells. P-type doping was done using DEZ as the zinc source.

Growth uniformity experiments across the present susceptor (2.25" x 3.25") were conducted. Figure F-13 shows the variation in layer thickness from front to back of the susceptor. Variations in layer thicknesses on wafers placed along the length of the susceptor are <8% when the initial growth region is neglected. The thickness non-uniformity at the leading edge results from effects due to the establishment of a boundary layer in that region. Deposition efficiency in the present system is 18% when an untilted susceptor is used. The resulting raw materials (trimethyl gallium, trimethyl aluminum, arsine) growth cost per 1/2" cell, not including the GaAs substrate is ~$0.60.

OM-CVD Solar Cell Production and Studies

During the cell production experiments up to 12 1/2" cells were grown during each 2-1/2 hr. growth run in the OM-CVD reactor. On some days material for up to 24 1/2" cells was submitted to the cell fabrication area for processing. During one 14-day period, 95 1/2" cells were submitted for fabrication. In this period 4.5 days were spent on solar cell growth with the other reactor time allocated to other projects and to susceptor bakeout. The

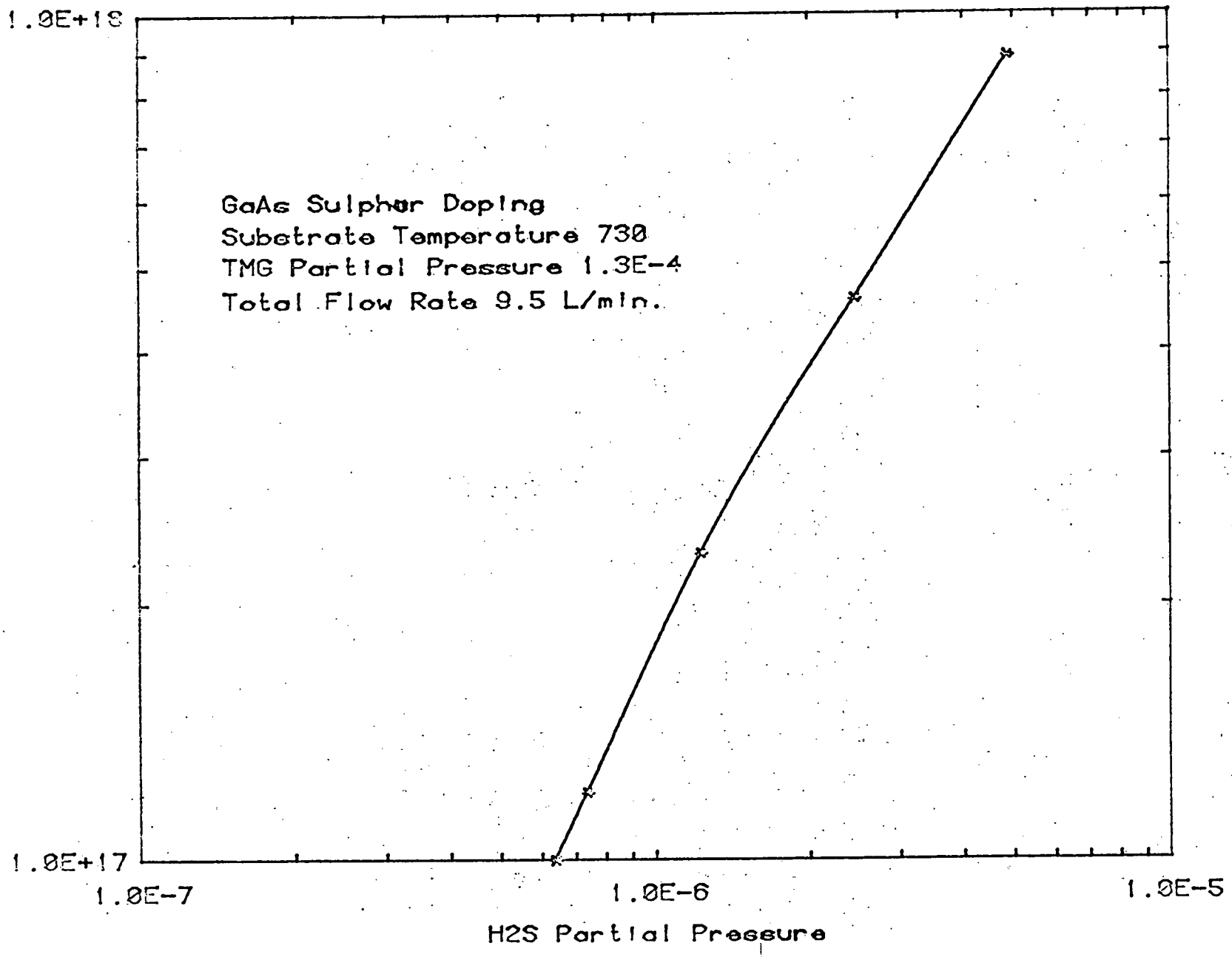
1.0E+18
1.0E+17
1.0E-7
1.0E-6
1.0E-5
GaAs Sulpher Doping
Substrate Temperature 730
TMG Partial Pressure 1.3E-4
Total Flow Rate 9.5 L/min.
Electron Concentration N
H2S Partial Pressure

Fig. F.11

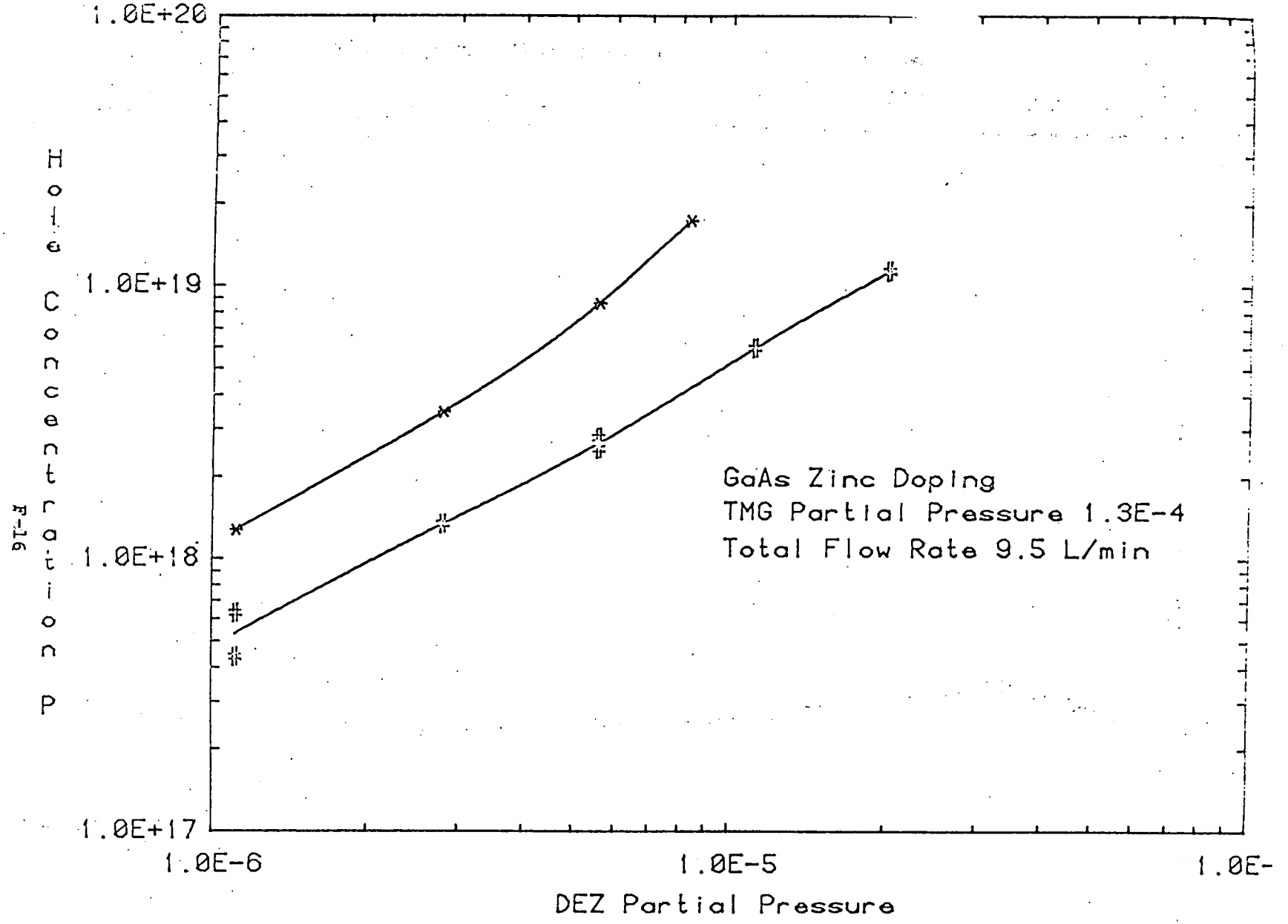

* SUBSTRATE TEMPERATURE 690
\# SUBSTRATE TEMPERATURE 730

Fig. F.12

Fig. F.13

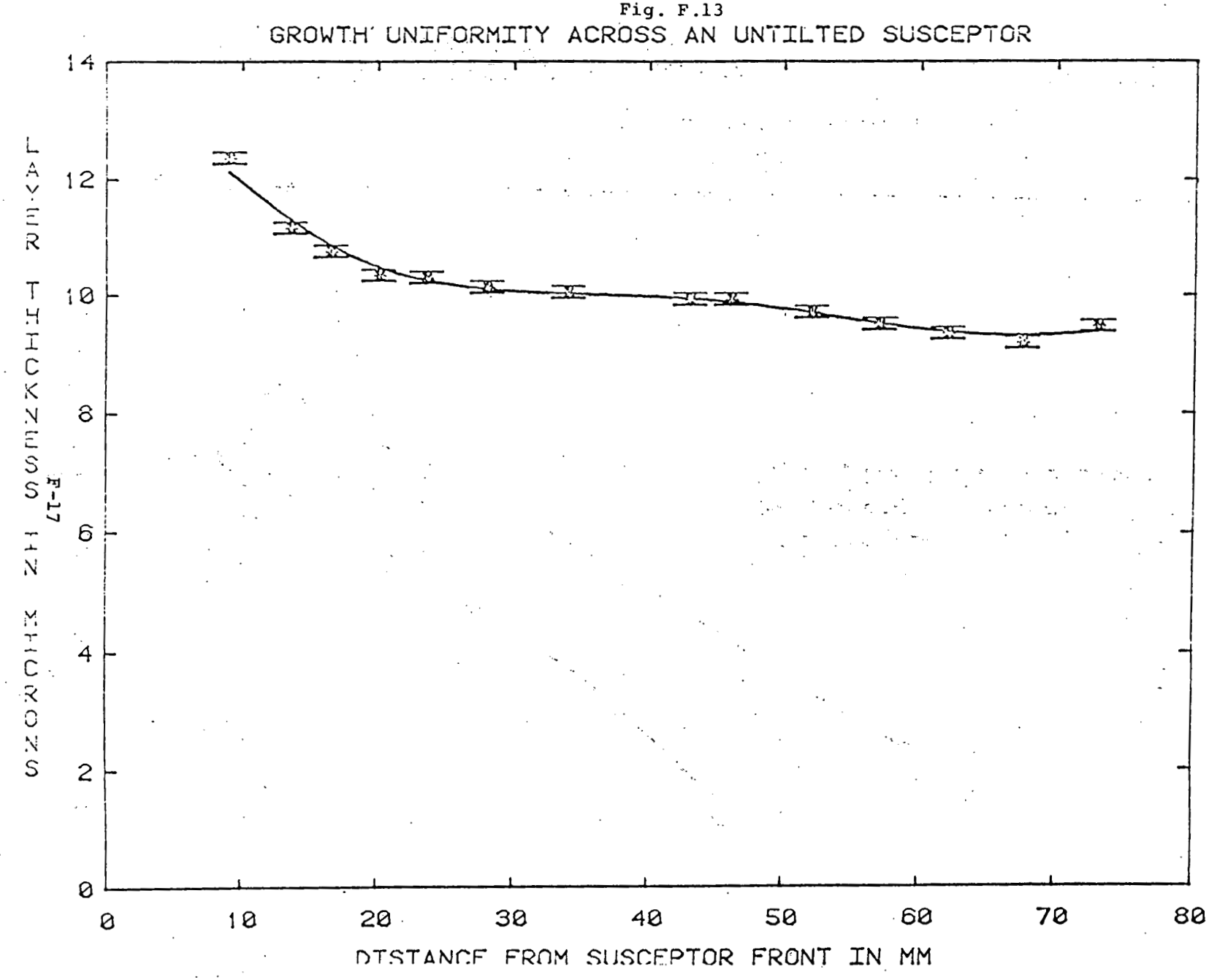
GROWTH UNIFORMITY ACROSS AN UNTILTED SUSCEPTOR
14
12
10
8
6
4
2
0
0
10
20
30
40
50
60
70
80
DISTANCE FROM SUSCEPTOR FRONT IN MM

grown layers had very good surface morphology. The good minority carrier diffusion lengths were further evidenced by the excellent quantum yield curves obtained from the finished solar cells, as shown in Fig. F-14.

Future modifications to the reactor would allow higher daily throughputs. These involve use of a larger susceptor and reactor tube in conjunction with the present gas handling system. These modifications would allow growth on ten 1/2" square substrates per run or 40 1/2" cells per run. The resulting capacity of the OM-CVD system would then be 120 1/2" cells per day, allowing for three 2.5 hr. growth runs per day.

Fig. F.14

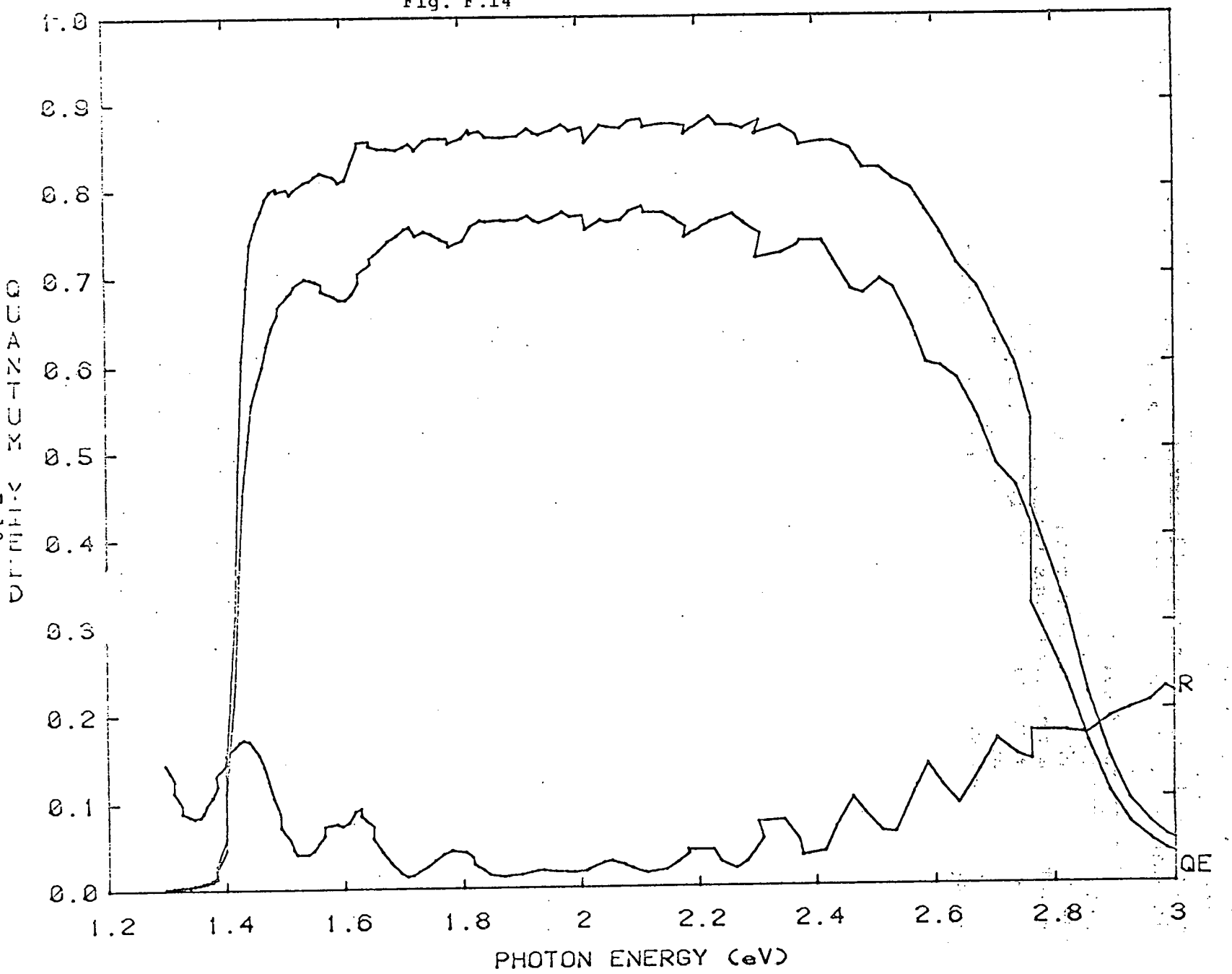
1.0
0.9
0.8
0.7
0.6
0.5
0.4
0.3
0.2
0.1
0.0
1.2
1.4
1.6
1.8
2
2.2
2.4
2.6
2.8
3
PHOTON ENERGY (eV)
R
QE

APPENDIX G: PILOT LINE AND PRODUCTION CELLS

G-1 Solar Cell Pilot Production Facility and Processes

A pilot line production facility was built and equipped to produce the 0.49" solar cell and package assembly shown in Figs. 2-16, 2-17, and 2-18. This primarily involved the expansion of a photolithography room and installation of the following major equipment items:

Cobilt automatic photolithography system Kasper

Kasper mask aligner

Varian 3120 metallization system

Lindberg belt furnace

LFE silicon nitride coating system.

The facility was designed to use high-volume commercially-available semiconductor processing equipment. This gives more than enough capacity to meet pilot production levels as well as allow process development using equipment which can directly lead to cost reductions as volume increases. All of the equipment can presently handle up to 2" wafers and 3" wafers could be processed with minor modifications.

The facility layout shown in Fig. 4-2 allows smooth flow through the process steps, which are numbered 1 through 14. This was the best flow possible in the present facility. A major activity in the design phase was installation of the equipment and performing functional tests on the major items. All of the equipment is functioning as designed, but each required a period of debugging during checkout. This is to be expected with automatic processing equipment of this complexity. Presently, one belt furnace is being used for the contact alloy (Steps 4 and 7) and cell soldering (Step 13) operations. To meet the Phase II production schedule, one additional belt furnace would be installed as well as one additional dicing saw and wafer preparation hood. All processing steps can be performed with the presently installed equipment and this additional equipment would complete the capacity to meet Phase II requirements.

The materials and solar cell fabrication process flow and single shift equipment capacities are shown in Figs. 4-3 and 4-4. The process is vertically integrated within Varian from polycrystalline GaAs to final packaged cell testing. The dicing saw to cut individual cells is the limiting

capacity item. An additional saw (a short lead-time item) would alleviate this limitation. The additional belt furnace (also available with a short lead time) will allow contact alloy and cell solder operations to be carried out simultaneously. The furnace is the same for these steps; however, the thermal profiles are different and therefore only one of the processes can be presently operated in a single shift.

The capacities of the contact metallization processes (>100 wafers/shift) are limited by the square footage of the available floor space and not by the equipment. In a larger facility greater than 400 wafers/shift could be realized for these operations. This also applies to the cell solder operation which could be increased by 2-4 times in a more spacious facility.

Several of the solar cell fabrication processes have required considerable process development. For some processes this has been due to scale up from a research piece of equipment to large volume production equipment. Other process development has been necessary because of cell redesign and packaging requirements. Much of this process development has been completed; however, some is still in progress. This will be discussed in the following description of the process flow.

Both organometallic and LPE wafers of various sizes were processed during development; however, the wafer designed for production is 1.2" square and contains four 0.49" cells. This has proven to be a convenient size for the present process. SiO_2 is deposited on the top surface of the wafer after epitaxial growth. The SiO_2 serves as a plating mask to limit plating to the metal grid pattern as well as protect the GaAs surface from contamination.

Front contact photolithography using positive photoresist defines the front contact pattern. The automatic photolithography equipment has been set up for this process. It has been checked out on GaAs substrates but not used on solar cell layers as yet. However, the photoresist characteristics are indentical to those processed by manual methods and this should only require the training of a technician for production operation. The 0.49" photolithography masks and mask aligner were both checked out and are routinely in use.

Once the front contact pattern is defined, SiO_2 is removed in the grid pattern and metal is deposited. After metal deposition the excess metal is lifted off by dissolving the photoresist. This is followed by back contact deposition

and subsequent contact alloying in the belt furnace. Silver based metallization is being developed for the 0.49" cell because of several potential advantages compared to the gold based system used on earlier cells. The silver based solders used to mount the cell to the metallized ceramic are soft compared to the brittle characteristic of Au-Sn previously used. The soft solder provides much less stress on the larger 0.49" solar cell and should increase reliability of the packaged cell. Silver has greater electrical conductivity than gold and yields higher device efficiency at high concentration. In addition, silver is considerably more cost-effective than gold. The ohmic contact metals directly on the semiconductor are still Au-Mg for the front and Au-Sn for the back; however, variations of subsequent metal depositions which are compatible with silver plating and Ag-Sn solder mounting are being investigated. A metal evaporation sequence has been developed which gives specific contact resistance less than 1×10^{-4} ohm-cm^2. This has been shown to be very important in obtaining high efficiency cells.[3,5] During the Phase I program, this process has been transferred from a single wafer, laboratory alloy heater system to a continuous flow belt furnace alloy. In addition, both front and back contacts are alloyed in one step, whereas separate alloy procedures were required in the single wafer system. Finally, the Varian 3120 metal deposition system has been completely checked out and is being used routinely.

After contact alloy the front contact is plated. A pulse electrolytic silver plating process is being developed. The Ag cross section and uniformity across a cell are adequate; however, the plating rate and plated metal adherence to the evaporated metal are current problems. Continued development efforts need to be directed towards a process which gives good adherence, as this is of utmost importance for high concentration operation. Good progress and improvements have been made, but more work is required. Plating rate reproducibility will be solved more easily once the process sequence is developed.

It should be noted that the analysis of the performance of early packaged cells from the pilot line (Sec. G-2, Fig. G-1) was made on a cell with the original gold evaporation and gold plating procedure. In addition, it was solder-mounted using Pb-In solder paste which was investigated as an alternate to Au-Sn solder. Cells with the complete Ag system and good plated Ag adherence have not been packaged. Once good adherence is obtained, a good evaluation of the complete Ag-based system will be possible. Cells mounted with poor Ag adherence have given low fill factors at concentration testing, as might be expected. However, a recent cell with reasonably good silver adherence has given improved performance as shown in Fig. G-2.

After plating, the wafers are cut into individual cells, the top GaAs layer is removed, and the silicon nitride AR coating is deposited on the cell. The etch process to remove the GaAs has been improved and is now very reproducible and operator independent. The etching stops very cleanly at the AlGaAs surface. A frequent evaluation of the silicon nitride films has been initiated to maintain correct process parameters for the plasma deposition. An ellipsometer is being acquired for this evaluation.

An AM2 one-sun short circuit current and open circuit voltage measurement are made prior to solder mounting. Short circuit currents measured on numerous cells indicate that if all other problems are solved (see Sec. G-2) cells of well over 20% efficiency are attainable in the new design. The one-sun test primarily serves as a screening test to eliminate cells which will not meet mounted cell concentration specifications. This saves labor and packaging materials.

The cell is solder mounted onto a metallized ceramic in a solder fixture which holds and properly aligns the ceramic, cell, leadframe, and solder. This entire assembly has been designed for a single pass through the belt furnace for soldering. However, currently the backside and topside solder processes are being done separately. This allows more detailed investigation of each solder process. Pb-In solder paste was investigated for gold metallized cells; however, this resulted in numerous voids in the backside solder and poor wetting for the topside solder connection to the leadframe. A low temperature Ag-Sn soft solder was used on 0.49" cells with silver metallization and greatly reduced the backside voids and gave excellent wetting and bonding to the leadframe. Ag-Sn solder results in 1/3" cells for another program [5] also have shown improvement over Pb-In solder. Therefore, Ag-Sn solder appears encouraging and will be used to mount cells with silver metallization. The exact effect of the remaining voids on electrical and thermal properties will depend on their size and distribution and remains to be determined. Work will continue to evaluate and improve the solder attach.

Currently cells are tested at 400 suns on a pulse simulator after mounting. A few of the cells have been tested at concentration in the concentrator demonstration module, but measured efficiencies mostly have been in the 15-16% range. An analysis of this performance which identifies areas for continued development is given in Sec. G-2. The recent cell with improved plated silver adherence was solder attached with AgSn and gave an improved AM1.6 efficiency of 19.1% at 490 suns.

The cells will be environmentally protected; however,

development is still needed in this area. Several cells were coated with a high quality transparent epoxy used for opto-electronic devices. No degradation in efficiency was observed under short-term testing but long-term reliability studies would be required before use. Another approach is to bond a glass cover to the cell with a transparent RTV compound. This has not been tried at Varian; sample materials are being obtained.

In summary, a pilot line facility has been built and equipment of the type required to meet PRDA Phase II production capacity has been installed and checked out. Considerable progress has been made on new process development required by volume production equipment, as well as a new cell and package design. All the development experiments were condensed into the last 2-3 months of Phase I as equipment, 0.49" photolithography masks, and ceramic packaging materials were not available until late in the program. Continued development is necessary to solve the remaining problems and obtain cells of greater than 20% efficiency.

G-2 Analysis of the Performance of Early Packaged Production Cells

As has been demonstrated in the past, both experimentally and theoretically,[3,5] AlGaAs/GaAs concentrator cells are capable of conversion efficiencies in the 23% range. For this to happen, however, everything about the cell must correspond to the theoretically optimum design. There are many places where a real cell can fall short of these optimum conditions. On a previous program[5] it was necessary to produce about one kilowatt worth of cells before any significant fraction of the cells had efficiencies exceeding 20% (AM2). For the present cell design almost every process in cell manufacturing has been changed from a research piece of equipment to a high volume manufacturing piece of equipment. In many instances the processes themselves have been changed to allow compatability with packaging requirements. Thus, it might be expected that the cell pilot line will not produce cells with theoretical efficiencies until it has been running long enough to zero in all of the processes to their optimum points. This expectation has been fulfilled, with early cells having measured efficiencies in the 15-16% range. One of these cells was analyzed in detail to indicate which processes were not optimized. The results of these measurements are shown in Fig. G-1. These results are compared with our computer model which has proven to give good correlation with the best experimental cells on other programs. (Some of the process steps responsible for the deficiencies noted below have been modified to correct the problems. However, these cells have not yet reached the stage of detailed evaluation under solar concentration.)

The first comparison was of predicted and measured short circuit currents. The actual cell had a short circuit current of 0.882 of that predicted. Further investigation by taking a quantum yield curve and a reflectivity curve of the cell showed that about one half of the short circuit current

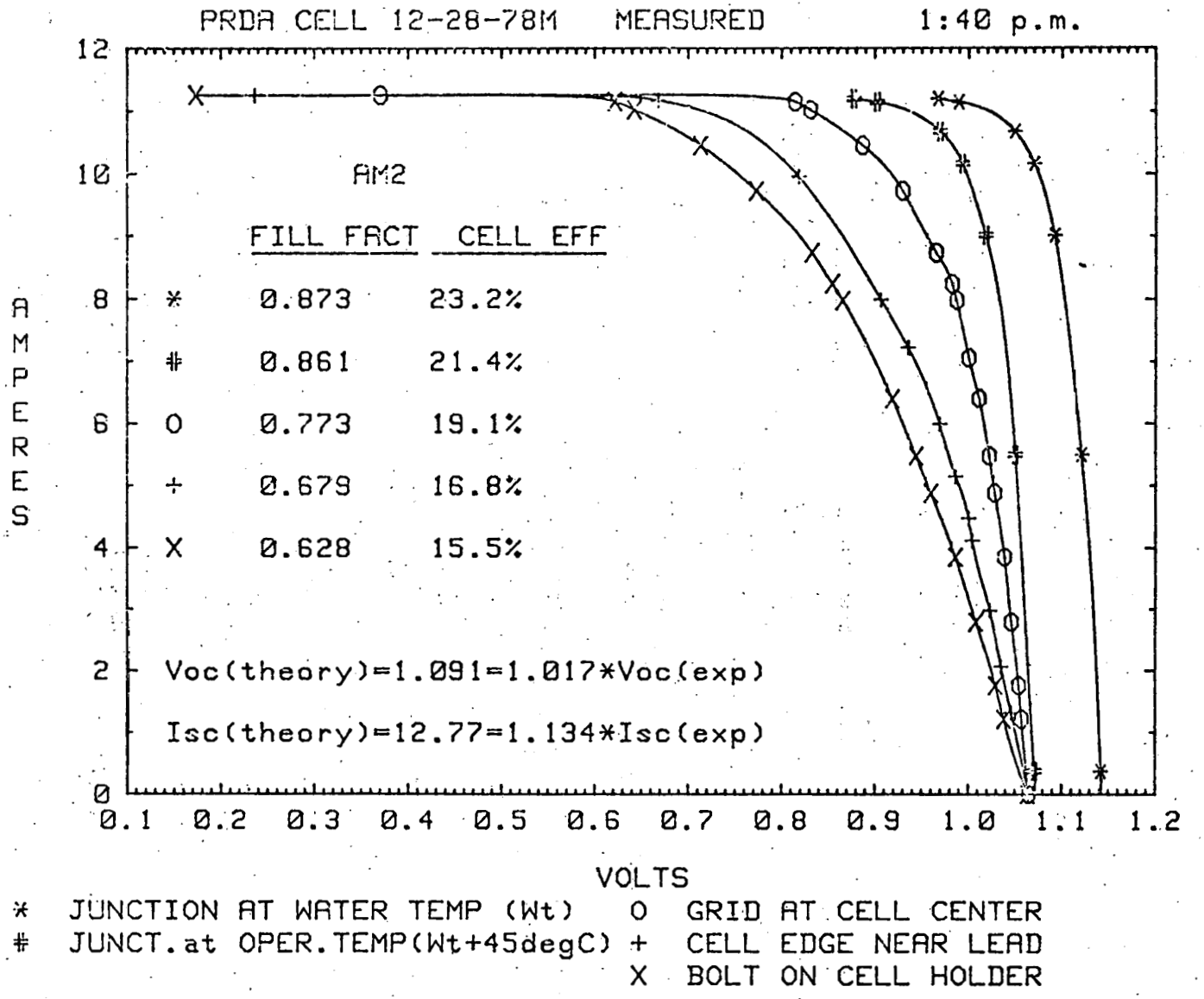

Fig. G-1 Evaluation of Early Production Cell

loss was caused by a defective Si_3N_4 AR coating. The process parameters on the new plasma deposition reactor had not been optimized and the coating as deposited had too low a refractive index, in addition to excessive absorption above 2.3 eV due to free silicon. The other half of the short circuit current loss was caused by a poor minority carrier diffusion length (less than one micron) in the n-type GaAs buffer layer. This may have been caused by a defective GaAs substrate wafer.

The second factor examined was the p-n junction I-V curve. This was measured by varying the illumination intensity in steps, and measuring at each step both the short circuit current and the voltage produced under open circuit conditions by that current flowing in the junction. Two I-V curves for the junction were derived from this data by correcting for the effects of temperature rise with illumination level. The high intensity points were corrected back to the cooling water temperature to give curve (*). The low intensity points were corrected up to the operating junction temperature to give curve (#). Two problems are apparent from this data. First, the open circuit voltage with the junction cooled to the water temperature is 0.983 of what it should be. This small degradation (1.7%) of the p-n junction characteristic could come from a number of causes, but is not very significant. The second problem is that the temperature rise of the junction is 45°C above the cooling water temperature instead of the 15°C expected. Further examination of the origin of this excess temperature rise disclosed that the solder used to solder the cell to its ceramics package had many voids, and the cell was in fact only soldered over a small part of its back area. This excess temperature caused a drop in open circuit voltage of 6.5% together with a drop in fill factor of 1.4%. Since the packaging technology was still in the early stages of development when this cell was processed, this result is not too surprising.

The third set of measurements involved measuring the I-V curve of the cell under load. The current was always measured at the load, while the voltage was measured at the following three points:

(1) at the bolts on the cell package where the interconnecting wiring will ultimately be connected (curve X),

(2) on the buss bar at the edge of the cell (curve +)

(3) using a fine tungsten probe to contact a grid line near the very center of the cell (curve 0).

By comparing the voltage measurements of these three points with the junction I-V curve, we can determine the location of any series resistance in the cell.

The voltage drop shown from the (#) curve to the (0) curve is caused either by sheet resistance of the p-AlGaAs and the p-GaAs layers, or by ohmic contact resistance. Some drop is expected in even an ideal cell, but the drop measured here is about twice that expected. The voltage drop from the (0) curve to the (+) curve is caused by the resistance of the grid lines. It is also twice the drop expected, pointing to a problem in the plating process. The efficiency at this point (16.8%) is comparable with the first batches of cells processed on an earlier contract.[5] These efficiencies were also measured using separate voltage leads on the cell buss bar. The voltage drop from the (+) curve to the (x) curve is caused by electrical resistance of the package. Most of the excessive drop here is due to soldering problems again, this time at the solder joint between the cell and the lead frame.

All of these processing problems are soluble, but will require allocation of time and effort before the pilot line will be capable of a high yield of production cells with greater than 20% conversion efficiency.

Figure G-2 shows the voltampere curve of a cell fabricated towards the end of the Phase I program. A considerable improvement is evident, with an AM 1.6 efficiency of 19.1% at 490 suns.

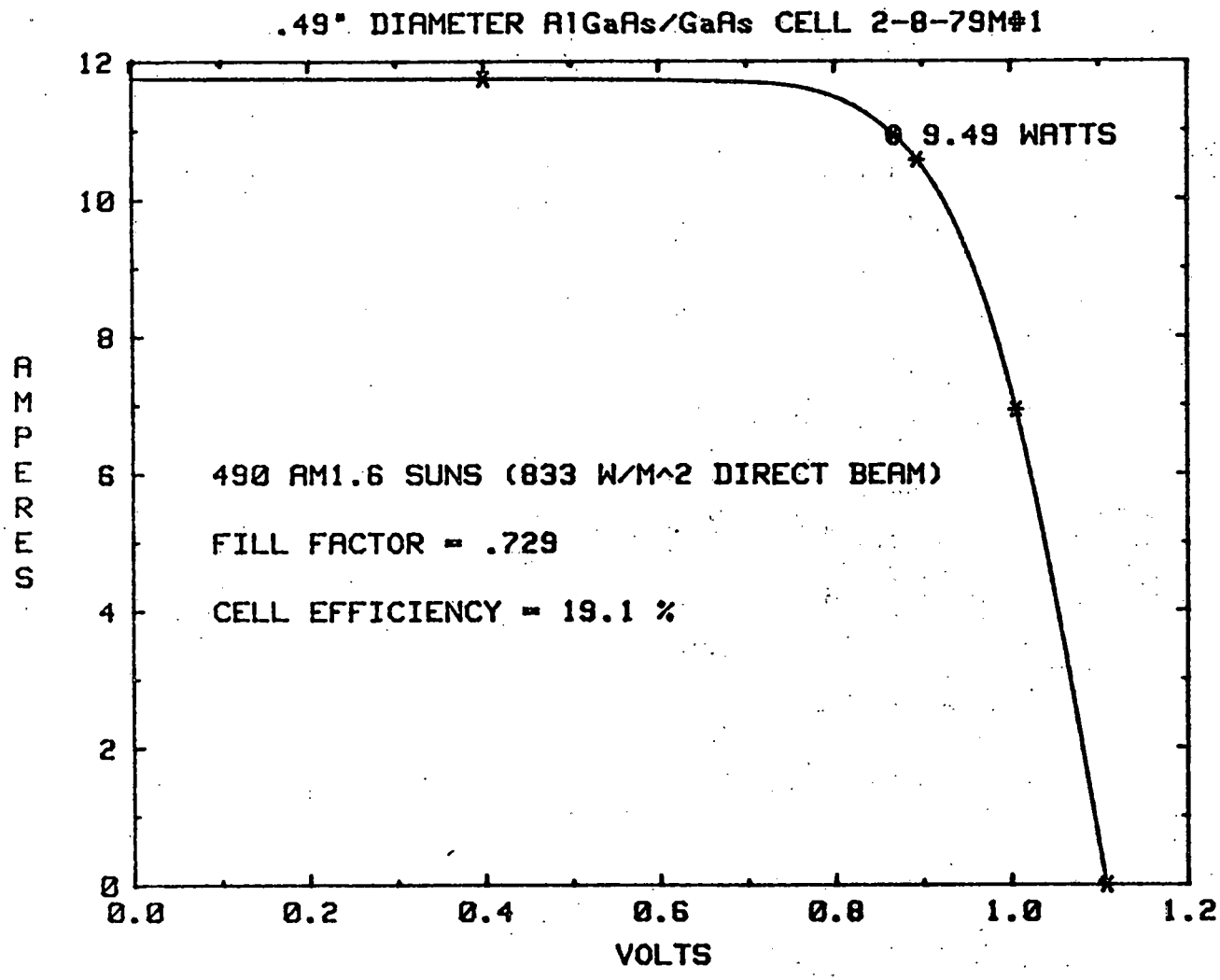

Fig. G.2 Voltampere Curve of Concentrator Cell With Improved Heat Sinking

APPENDIX H. FRESNEL LENS DEVELOPMENT (OPTICAL SCIENCES)

Optical Design Analysis and Optimization

The original design plan called for the manufacture of a curved grooved Fresnel lens made up of four to five distinctly different radius of curvature surfaces. The grooves were to be as wide as possible given the limitations of diamond tooling manufacture. This original design concept was abandoned late in June for several different reasons:

First, no tool manufacturer was capable of producing the range of radii necessary.

Second, all tool manufacturers were limited in the length of diamonds that they could obtain, thus drastically handicapping the benefits gained by going to radius surfaces.

Because of these problems, several alternative design configurations were developed. A plan was established that called for the implementing of four simultaneous designs. These designs were:

Design 1. Design 1 was to be cut in-house, a twelve inch diameter -- approximately twelve inch focal length Fresnel die using curved grooves with a constant radius of curvature of 8.5 to 9 inches out to a diameter of f/2. Then from f/2 to f/1 plano or flat grooves were to be cut.

Design 2. Design 2 was to be cut at OSG. This design was to be a twelve inch diameter lens with an eighteen inch focal length. The grooves were to be curved, if possible, but flat if it was determined the radius of curvature needed was longer than that obtainable from the diamond tool manufacturers.

Design 3. Design 3 was to be a single point diamond turned Fresnel lens cut out-of-house under the direction of OSG. Each groove was to have an optimum radius of curvature for that particular groove. The lens was to be twelve inches in diameter with approximately twelve inch focal length.

Design 4. The fourth design was also to be cut out-of-house under the supervision of OSG. It was to be a curved groove lens put on a base curve. That is a domed lens with curved grooves. The lens was to be twelve inches in diameter with approximately twelve inch focal length.

A decision was made to parallel work on all of these designs as long as possible. The most desired design was number 4, the curved groove based Fresnel lens. But, it also carried the highest risk of failure. The least desired design was the design number 1, which was an OSG cut flat-curved lens. The optical performance of option 1 was significantly lower than options 3 or 4, but the risk factor was much less. After analyzing the manufacturing difficulties encountered with option 4, it was dropped as a viable alternative for Phase I work. Option 3 was thus the primary option to pursue. Options 1 and 2 were to be pursued by OSG in the event that option 3 failed. At the time the decision was made to pursue three options simultaneously, it was felt that there was enough money in the budget to accomplish all three designs. The problems that were encountered in accomplishing design alternative number 3 were not anticipated at this time.

OSG was also requested to participate in discussions dealing with the lens mounting analysis. Several OSG people participated in joint discussions with Varian and Nielson Engineering. As a result of several preliminary discussions, Nielson Engineering and Varian proceeded along a path of designing an injection moldable, plastic cone. Once the initial design concept of this plastic cone was established, OSG was not asked to participate further in discussions leading to a detailed cone design. The intent was for the cone design to be patterned after the final lens design provided by OSG. At this time, the interface of the lens and the cone is still not completely defined. A revised lens drawing number 3600 is included in this report.

Prototype Fabrication

Fresnel Die Fabrication:

Design option number 1 was to be curved grooved out to f/2 and flat grooved from f/2 to f/1. But due to delivery problems and diamond tool manufacturing problems, this option was modified to be a flat grooved lens throughout its entire aperture range. The die was manufactured at OSG, and prototype parts were pressed and supplied to Varian.

Option number 2 was to be a twelve inch diameter, eighteen inch focal length lens to be used with a secondary concentrator. This was a secondary backup put into the system because it was felt that a secondary concentrator design would produce a more uniform intensity distribution on the cell. This design was also manufactured at OSG. The die was completely flat grooved. Prototype parts were manufactured and delivered to Varian.

Option number 3 was a curved groove Fresnel lens. This Fresnel die was to be manufactured outside OSG, but controlled directly by OSG personnel. The design was to be completely curved grooved and cut with a single point diamond turning technology relatively new as a Fresnel manufacturing technique. Several problems were encountered in manufacturing this Fresnel die. First, because OSG could not control the manufacturing process as carefully as it desired, several compromises had to be made in the manufacture of this tool. It had to be cut in a thick substrate that could be mounted on a magnetic chuck. This condition then dictated that a material that was diamond turnable had to be plated on top of a magnetic surface. This plating technique had never been used for manufacture of single point diamond turned Fresnel surfaces before. Perosity problems with the plated surface later caused serious electroforming problems which resulted in a final product performance below that which had been expected. The problems that were encountered in the manufacture of this Fresnel tool have been analyzed and solutions have been found. The problems that did occur during Phase I of this work can, and will, be corrected on any future work of this type. The problems encountered in the manufacturing of this Fresnel die did cause significant cost overruns to occur.

Press Tooling

The press tooling originally planned for this program was to be obtained by modifying tooling that was already in existence at OSG. After an initial analysis of this tooling was done, it became obvious that the modifications planned for this tooling were not adequate to provide the type of Fresnel parts desired for this program. Thus, a completely new tooling system had to be developed. This, again, caused cost overruns; but without this new tooling, the program would not have been a success. Two optical flats were ordered as part of this press tooling. These flats were to be used to produce the plano surface of the part. This portion of the tooling did not arrive in time to be used for Phase I work. Thus, the benefits of these optical flats are not known at this time.

Cost Estimates for Phase II and High Volume Production

The costs estimated for Phase II lens production were higher than initially estimated on December, 1977. The unit price for lenses produced in Phase II of less than $10 is reasonable for the quantities involved. The tooling costs are high for several reasons. First, perosity problems encountered in Phase I made it necessary to include the costs of producing a new master Fresnel tool for Phase II work. Also, the high performance and dimensional specifications that are thought to be required of these lenses at this time made it necessary to include costs for highly mechanized press tooling, as well as several extremely expensive quality control instruments designed specifically for the inspection of these solar lenses.

The work done in an attempt to predict the unit costs of high volume production of these lenses produced two significant results. First, it was determined that the compression molding process would not be capable of producing the quantity of lenses desired for a "high volume" production run within the cost expections of $2.00 per square foot currently set by D.O.E. Secondly, it was concluded that a modified type of injection molding process could possibly reach the cost objectives if a process could be developed that would produce a lens with the desired optical performance.

Conclusion

The Phase I Fresnel lens program has successfully demonstrated, via the production of prototype quantities of lenses, the manufacturability of very high optical transmission quality Fresnel lenses. As a result of the Phase I program, a new and improved method of producing Fresnel tooling for solar applications has been established. This single point diamond turning (SPDT) method of manufacturing Fresnel tooling has several advantages over the methods normally used to produce Fresnel tooling. The SPDT method enables the grooves to be curved instead of flat. This means that each groove now can have any desired radius of curvature. This ability enables each groove to have focusing power which gives an additional design freedom previously not obtainable. Also, the SPDT method removes the previous groove width limitations imposed on conventional Fresnel tooling because of diamond tool edge length limitations. Using SPDT Fresnel grooves can be made as wide as desired. For solar applications, this decrease in the number of grooves results in improved lens transmission. Even though the percentage of transmission increase is relatively small (a few percent), when dealing with the large numbers of lens elements that are needed to produce large quantities of electrical energy, this increase in lens efficiency is very significant.

The ability to meet a $2 per square foot cost for Fresnel lenses looks promising. An injection-compression molding type of process that is capable of producing shallow domed, thin, high quality Fresnel solar lenses appears to be possible. This type of process should be capable of producing the quality of lenses necessary for high concentration solar applications in quantities sufficient to meet the projected needs of this industry. The acrylic material used to make the Phase I prototype lenses has properties that make it attractive for use in solar lens applications. Data from material suppliers indicates that molding and extrusion grade materials are less resistant to ultraviolet radiation than cell cast or continous cast acrylics. Thus from a cost and life expectancy point of view, a molded Fresnel lens appears to be a very cost effective solar concentrator.

APPENDIX I

STRUCTURAL DESIGN OF PHOTOVOLTAIC SOLAR ARRAY

Contribution by NEAR, Inc.
to final report, draft copy

by R. E. Reed

NEAR TR 185

March 1979

Prepared under contract to
Varian Associates

Contract 08CCA-871885

NIELSEN ENGINEERING & RESEARCH, INC.
510 Clyde Avenue, Mountain View, CA 94043
Telephone (415) 968-9457

ACKNOWLEDGMENT

This work was accomplished through the efforts of many people at NEAR, Inc. including the following.

McIntosh, S. C., Jr. - Project Engineer
Reed, R. E. - Structural design and analysis
Miller, W. - Designer and coordinator
Mullen, J., Jr. - Alternative structural studies
Klopfer, G. H. - Cooling system design
Schwind, R. G. - Cooling system design
Synder, P. - Drive unit design

INTRODUCTION

This report describes the contribution of NEAR, Inc. to the design of the Varian Photovoltaic Solar Array. The efforts of NEAR, Inc.,primarily involved the structural and cooling system designs and resulted in the delivery of drawings for estimation of costs and a detailed computerized parts list with the software capability of listing the parts by different criteria including assembly order, part number and commodity code. A section is included in this report that discusses alternative design concepts. Although time was not available for studies of any depth to be made of alternative designs, reasons why they were discarded are discussed.

DESIGN REQUIREMENTS

The following requirements were established at the beginning of the program.

Pointing accuracy	0.2°
Lens-to-cell dimensional tolerance	±0.025"
Wind speed, operational	30 mph
survival	60 mph
Lens shape	hexagonal
Total electrical output	50 kw
Cell cooling	water cooled
Array length-to-width ratio	2:1 to 4:1

The following conceptual requirements were followed throughout the program.

- Maximize the lens area to total array area.
- Use standard, available components.
- Provide design with major components suitable for variety of locations.
- Maintain accessibility for repair and replacement of components including cells, lenses and drive systems.
- Retain option to assemble and adjust unit at off-site location.

DESIGN PROCEDURE

The time available for the design and preparation of detail drawings was 6 months. This meant that major decisions (general configuration, etc.) had to be made very quickly and little time was available to study alternative concepts. Once the overall configuration was established, the detail designs of the subsystems were started. The subsystems are the following:

1. Foundation - concrete structure below ground level
2. Pedestal Weldment - structure supporting Y-frame
3. Azimuth Drive - enclosed within pedestal weldment
4. Y-Frame - central column and struts
5. H-Frame - primary structural frame supported by Y-frame
6. Elevation Drive - connects H-frame to Y-frame
7. Channels - secondary members supporting lens-cell units
8. Cone - housing for lens and cell
9. Cooling System - closed water system to cool cells

The individual subsystems, denoted in figure 1, were designed without the use of a computer. However, the complete array structure including the Y-frame, H-frame and channels was modeled and analyzed on a computer using the SAP4 finite element computer program. Results of static analyses under gravity and lateral loads, and natural frequencies and mode shapes were obtained. These results are discussed in the following with details of analyses given in Appendices.

FOUNDATION

From information provided by Varian, the soil at the San Ramon site is known to be an expansive clay about 15 feet thick with the water table probably below a 20 foot depth. The area is in an active seismic zone where bedrock accelerations can be in the 0.4-0.5g range.

The type of foundation chosen is a single reinforced concrete pile, poured in place. It is 10 feet deep and 30 inches in diameter. This was chosen because of the ease of removal at the end of the program and because PG&E had auger equipment to drill the holes. The pile was designed to resist a lateral load of 3000 lbs., resulting from a 60 mph wind, a vertical load of 6,000 lbs., and a moment of 6,000 ft-lbs arising from the static eccentricity of the array. The lateral wind loading closely corresponds to a lateral acceleration of over 0.5g's so no additional seismic loads were considered.

The moment loading from the wind is the dominant load and can occur from any direction. It is transferred from the array to the foundation base plate and then through 4 anchor bolts imbedded in the concrete. The 4×4 ft. cap provides a base above grade for the

THIS PAGE

WAS INTENTIONALLY

LEFT BLANK

ELEVATION AND AZIMUTH DRIVES

Because the drive system is so closely linked to the overall configuration of the array structure, its conceptual form was one of the first design decisions made. A system composed of a single elevation drive and a single azimuth drive was chosen. This offered an approach that appeared straightforward and relatively free from possible hazards that could jeopardize the design with no time available for a redesign.

Stepping motors are used to drive the units and because of possible damage to the drive motors, it was considered essential to have an irreversible system. Therefore, worm and helical units are combined to ensure that the systems cannot be backdriven and that the required reduction is obtained. The elevation and azimuth drives are of the same design except that the azimuth drive has components rated for the higher loads that can exist.

It was desired to keep backlash to within 8 minutes of angle. The larger azimuth unit should satisfy this requirement. However the elevation drive may exceed this. To avoid significant errors in the elevation drive, the tracking commands can be programmed to ensure that the tracking maintains one direction and the system only reverses itself under wind gusts. A static unbalance is available to produce a torque which would return the system if blown off track by a gust. The effects of backlash would then be felt only momentarily when a gust loading larger than the unbalance torque reverses the system to the limit of the backlash tolerance.

The required operating characteristics of the gear units are:

	Elevation Drive	Azimuth Drive
Gear reduction	1500:1	1500:1
Operating range	0-90°	250°
Maximum slew rate	90°/15 min.	90°/15 min.
Operational slew rate	~90°/7 hours	~90°/7 hours
Operating torque	230 ft-lbs	750 ft-lbs
Survival torque	900 ft-lbs	3,000 ft-lbs

The operating characteristics of the drive stepping motors are:

Stepping rate	0-200 step/sec	0-200 step/sec
Step size	0.9°/step	0.9°/step
Holding torque	0.28 ft-lbs	0.78 ft

The gear reduction is determined by the maximum slewing rate (stowing maneuver) and the maximum stepping rate of the drive motors. The operating torque values were obtained by requiring the units to drive against a differential 15 mph wind acting on the upper or lower half (for elevation) and the right or left side (For azimuth) of the array. The survival torques are based on differential 30 mph wind on half of the array.

To reduce the loads that would be transmitted through the elevation drive, the struts of the Y-Frame were included in the structure. Bearings at the end of the drive tube allow its rotation. These bearings can carry thrust which could arise from differential thermal expansion of the structure. All of the torque applied to the array about the axis of the torque tube is carried by the elevation

drive. The torque on the elevation drive due to the static offset of the array can be removed with counterweights although some eccentricity in the gravity load can be left, as previously mentioned, to reduce backlash in the system. The torque about the axis of the central column caused by wind gusts is transmitted through the azimuth drive to the pedestal weldment.

The design is such that the stepping motors can be removed without further disassembly of the drive units and the drive units can be removed without disassembly of the array structure. The azimuth drive is mounted on cam followers and can be rolled in and out of the pedestal weldment. Details of the design are given in Appendix B.

PEDESTAL WELDMENT

The purpose of the pedestal weldment is to transfer all loads from the Y-frame to the foundation. All loads except torque in the central column are transmitted around the azimuth drive via the pedestal to the foundation. These loads are transferred to the pedestal through the pedestal bearing. The torque is transmitted through the drive unit to the pedestal. One side of the pedestal can be removed for access to the azimuth drive unit. The pedestal is designed to carry the loads with the door removed although operation would be degraded since wind loads would produce larger rotations and deflections of the array. The thick walls (3/4 inch) are to ensure that the base is rigid and does not produce rotations from wind gusts that would be felt throughout the entire structure. Also, the thickness provides sufficient material

THIS PAGE

WAS INTENTIONALLY

LEFT BLANK

FINITE ELEMENT ANALYSIS OF H- AND Y-FRAMES

Although many components of the array were designed without using a computer, the main structure including the Y-Frame and H-Frame were analyzed with the structural analysis program SAP4 which was developed at the University of California at Berkeley. SAP4 is a finite element program for static and dynamic analysis of structures. The structure was modeled using a beam element capable of carrying bending, torsion and axial loads.

The static analysis assumed the loading conditions of gravity with the array horizontal and vertical and a wind loading with the array vertical. The symmetry of the loading condition and the array was utilized by analyzing half of the array with symmetric boundary conditions imposed on the array centerline. A total of 42 nodes with 37 beams were used to model the structure. The stiffness and weight of the 22 channels and estimated weights for cones, etc., in half of the array were lumped into 5 channels to reduce the number of nodes. The nodal distribution is shown in figure 2. For the gravity loadings, the weights of the structural members were computed within the program. The weight of the cones, lenses, piping, etc. was estimated to be 5.5 psf or about 40 lbs. per channel. The total weight of the structure above the pedestal weldment, including the estimate for the cones, etc., is 4900#. The horizontal gravity loading was analyzed using the coordinate system shown in figure 2. The case for vertical gravity was obtained by rotating the pedestal 90° at the bearing nodes 5 and 7 and applying a gravity load in the y-direction.

The wind loading analysis was obtained by having the array in the vertical position and applying a gravity load in the z-direction. The stresses and moments were obtained by scaling the results to obtain the proper magnitude of wind loading. This was a good simulation of the wind loading because both wind and gravity apply a uniform distribution of load over the channels and the loads are transmitted along much the same loadpaths. A 60 mph wind was assumed to produce a pressure of 10 psf. This is equivalent to having the full dynamic pressure (actually 9.2 psf) act on the surface. The pressure varies as the velocity squared so a 30 mph wind produces 2.5 psf, etc. No allowances were made in the pressure distributions for the gaps between lenses or the decrease in pressure near the edges of the array.

The stresses are low in most of the members since stiffness was the primary concern. Members were sized to limit the maximum static rotation to about 0.001 radians. Maximum stresses in the tubular members in the range of 10,000-15,000 psi occur under the survival loading from a 60 mph wind acting perpendicular to the face of the array. This assumes the stowing mechanism has failed and the array is vertical. Under this loading, the shaft in the elevation drive has a bending stress of about 35,000 psi. However the shaft yield stress is 59,000 psi. A summary of the moments in members and rotation of joints is given in Table 1. The section properties and the stresses in the members are listed in Table 2.

An unsymmetric wind loading (acting on 1/2 the array) of 30 mph was considered by imposing antisymmetric boundary conditions at the array centerline. The maximum stresses were less than those from

the survival load except for the torsional shear stress in the central column which was about 1,500 psi.

The dynamic analysis was made to determine the natural frequencies and mode shapes of the lower modes. The complete array was modeled with the mass of the channels, cones, lens, etc., distributed along the outer members of the H-frame. The finite element model is shown in figure 3. The lowest 15 modes were obtained for the array being horizontal and vertical. These 15 natural frequencies are in the range of 2.5-25 Hz for both array positions. The lowest 5 modes are shown in figures 4-8. The lowest two modes (actually, the same mode with the array either horizontal or vertical) are modes where the array acts nearly as a rigid plate twisting on the central column, while bending the struts. To be excited, this mode requires a gusty wind to produce a torque about the central column. The worst condition would be to have the array in the vertical position in a heavy wind. The third mode is a flexural mode of the array when it is vertical. When the array is vertical, the struts bend out of their plane in a relatively flexible mode of deflection. Sharp gusts can excite this mode. Modes 4 and 5 are the same basic mode with the array either vertical or horizontal and the central column undergoing lateral bending. Little or no excitation from the wind should exist for these modes.

One source of periodic wind excitation is the shedding of vortices off cylindrical type bodies at a frequency given by the relation

$$f = 0.2 \frac{V}{d} \qquad (f \text{ in hertz})$$

This equation applies in the range of Reynolds number of $10^3 < N_R < 10^5$ where $N_R = \frac{Vd\rho}{\mu} = 6310\ Vd$. The frequency range of periodic excitation is, therefore,

$$f_{min} = 0.2\ (\frac{1000}{6310d}) = \frac{3.17 \cdot 10^{-2}}{d}$$

$$f_{max} = \frac{0.2(10^5)}{6310d} = \frac{3.17}{d}$$

Values of interest are given below:

d, ft.	f_{min}, Hz.	Vel., fps	f_{max}, Hz.	Vel., fps
0.5	.064	0.32	6.4	31.6
1	.032	0.158	3.2	15.8
5	.006	0.032	0.64	0.6

This shows that a body of 0.5-1 ft. in diameter sheds vortices in the frequency range of the lowest natural frequencies. Thus, the central column and the main structural tubes will be subjected to oscillatory forces near the system resonance. However, these forces should be insignificant compared to the stiffness of the structure since the structure is designed to withstand a 60 mph wind acting on the entire array surface.

CHANNEL ASSEMBLY

Each array has 44 channels which each support 10 cones. These channels are made from 0.063 inch thick aluminum sheet that is folded into a ⌐¬ section. Each channel is supported as an overhanging beam by the outer two members of the H-frame at the spacing which nearly minimizes the elastic rotation of the channel under a uniform gravity load. The nominal spacing used is that which sets the rotation at the supports to be zero. To show the advantage that is gained, the rotations resulting from typical support conditions are shown below.

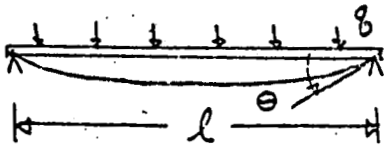

Simply supported

$$\theta = \frac{q l^3}{24 E I}$$

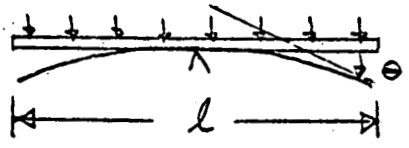

Double cantilever

$$\theta = \frac{q l^3}{48 E I}$$

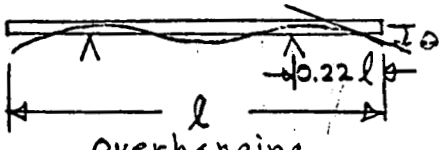

Overhanging

$$\theta = \frac{q l^3}{530 E I}$$

Both the channels and the H-frame members that support the channels are uniformly loaded and can be supported in this fashion as shown below.

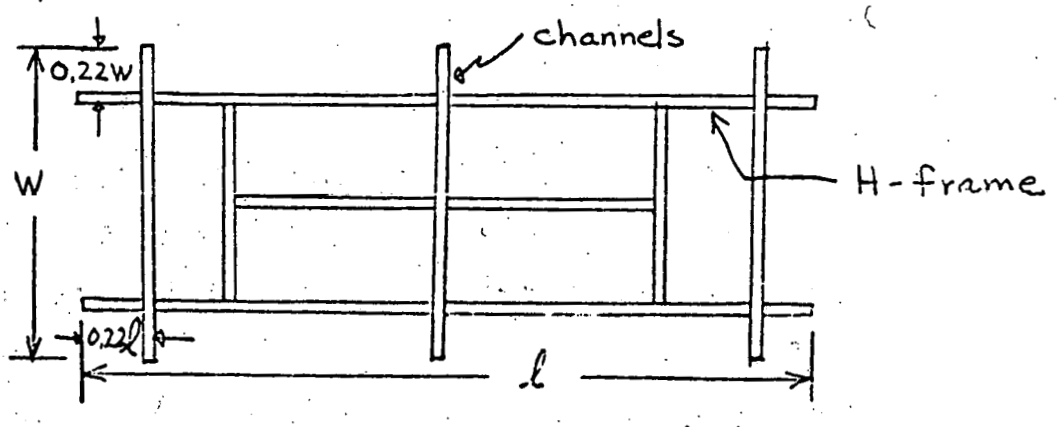

The connection to the H-frame at one end of the channel is designed to allow longitudinal slippage of the channel which will relieve thermal expansion and contraction arising from the difference in thermal expansion coefficient between steel and aluminum and changes in the ambient temperature. Also, the connections isolate the aluminum from the steel electrically to prevent corrosion. The ends of the channel are covered with a coarse screen to limit access by birds, etc. but the open screen allows convective air currents to aid in cooling the cells.

The cones are attached to the channel flange, with 4-point support. This increases the torsional stiffness of the assembly. Access to the solar cells is provided through 3 inch diameter holes in the bottom of the channel. The channel is stiff in bending but relatively flexible in torsion. The primary source of torque on the channels is the wind hitting the cones and channels. However, only two channels, one at each end of the array, are exposed to the wind. If winds produce excessive torsional rotation in the end channels, they can be tied to the adjoining interior channel across the bottom with short beam segments at, say, the middle and ends. This will cause the bending stiffness of the interior channel, which is large, to interact with the torsional stiffness and thereby reduce the rotations. The analysis of loading conditions given in Appendix D indicates that survival conditions of 60 mph winds will deflect the cones more than the 0.050" spacing and suggests that the exterior channels may have to be reinforced.

THERMAL EXPANSION OF CHANNEL:

The channel is supported so that it can expand longitudinally. However, a temperature gradient over the depth of the channel will cause it to bow. An estimate of the gradient is given here.

Assume channel can rotate at supports as illustrated in the sketch below.

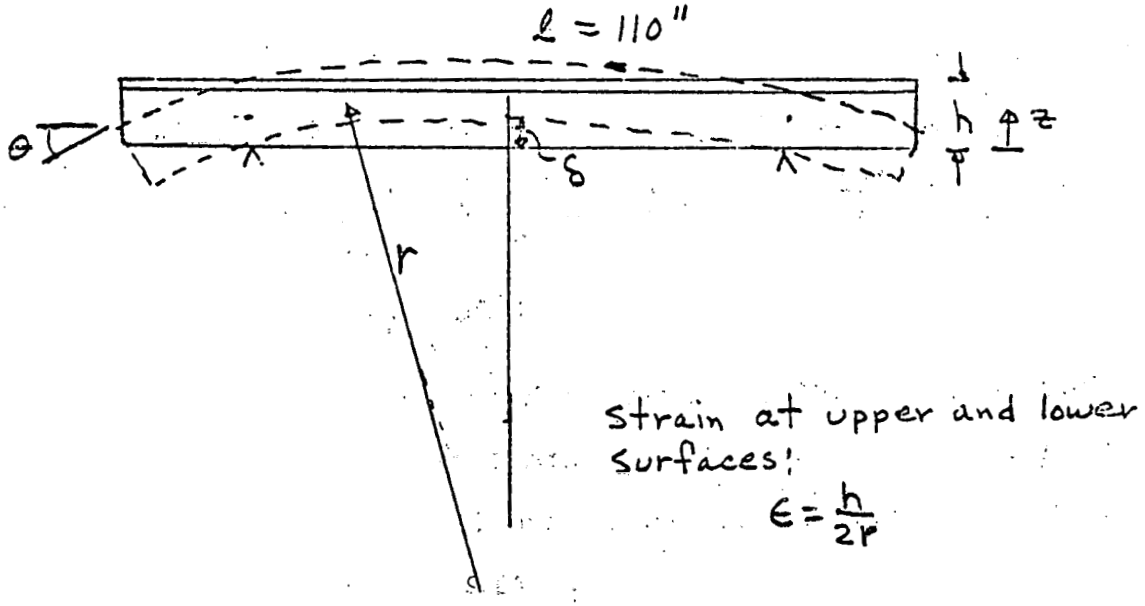

Assume a temperature gradient

$$T = \frac{\Delta T}{h}\left(z - \frac{h}{2}\right) \qquad (T=0 \text{ @ } z=\tfrac{h}{2})$$

Then,

$$\epsilon = \alpha T = \alpha \frac{\Delta T}{h}\left(z - \frac{h}{2}\right) \quad \text{(assuming no stress)}$$

$$\epsilon(z=0) = -\epsilon(z=h) = \frac{\alpha \Delta T}{2} = \frac{h}{2r}, \quad r = \frac{h}{\alpha \Delta T}$$

$$\frac{\ell}{2r} = \sin\theta = \frac{\ell \alpha \Delta T}{2h}$$

for $\alpha = 12 \cdot 10^{-6}$ /°F, and letting $\theta = 0.002$ rad.,

$\Delta T = 12^{\circ} F$

The conductivity for aluminum is

$$k = 90 \frac{BTU - ft.}{hr - ft.^2 - {}^{\circ}F} = 7.5 \frac{BTU - in.}{hr - in^2 - {}^{\circ}F}$$

The heat flow produced by a 12°F ΔT over 4 ins. is

$$Q = \frac{7.5(12)}{16(4)} = 1.5 \frac{BTU}{hr - in.} = 18 \frac{BTU}{hr - ft. \text{ of channel length}}$$

$$\text{incident heat} = 1 kw/m^2 \approx 0.1 \frac{kw}{ft.^2} = 360 \frac{BTU}{ft.^2 - hr}$$

Therefore, if 10% of incident heat flows down each side of the channel, a 12°F/4 in. temperature gradient will exist. It is doubtful, however, if 10% of the incident heat would be introduced at the flange of the channel. Also, maintaining a 12°F differential requires a heat path between the channel and H-frame which does not exist. A more likely process is for the channel to change temperature fairly uniformly to the point where it is in equilibrium with the surrounding structure and air. A uniform temperature change will produce a uniform change in length but will not warp the channel.

COOLING SYSTEM

The solar cells, with their high concentration ratio, require active cooling at least locally at the cells. Jet impingement cooling is used whereby a nozzle directs a flow of water onto the back surface of a heat conductive, electrically insulative disc attached to the cell. Because no makeup water is available at the site, a closed system is used to get rid of the waste heat. A volume of water is used as a heat sink to collect the heat during the day and to passively reject the heat primarily at night through convection and radiation. With this system, it is necessary to have sufficient volume of water to store the heat collected over a day without the cooling water exceeding some maximum temperature, say boiling, at any location in the system. Also, it is necessary to have sufficient surface area in the storage facility to reject the collected heat in a specified time, say conservatively, 10 hours. The surface area of a 55 gal. drum, including the top and sides, is 20 ft.^{2}. An experiment with a barrel showed that an average of 2 BTU/ft.^{2}-$^\circ$F-hour was rejected by a barrel over a 24 hour period and was about equally divided between convection and radiation. Therefore, a 55 gal. drum will reject about 40 BTU/$^\circ$F-hour. Also, 55 gals. (450 lbs. of water) will store 450 BTU/$^\circ$F. Assuming both processes are linear, the barrel will then reject its stored heat in about 11 hours. Because of this ideal surface area-to-volume ratio, low cost and availability, standard 55 gal. drums are used for storage. A sketch of the system is shown in figure 9. The inlet to the inlet header and the outlet for the outlet header are at are at opposite ends of the array to equalize

the pressure drop across the length of each channel. The bladder tank shown is to store the increased water volume due to thermal expansion. This amounts to about 20 gallons over the expected temperature range. The two extra tanks provide an excess air volume to limit the rise in pressure as the bladder tank fills. The system will be filled from the bottom (back-pumping into the barrels) and lines will be disconnected from the header at the top of the array to vent the air. The open type construction of the channels hopefully will provide considerable additional cooling. During the day, with the array at less than 90° elevation (horizontal), convective air currents within the channels should be generated by the hot cooling lines. A detailed analysis of the heat transfer at the cell and the required pumping power is given in Appendix E.

CELL ADJUSTMENT

The procedure for adjusting the cells is important to the successful development of the solar array. With 440 cells per array, the method of adjustment should be fast, accurate and reliable. The present method is based on the premise that one adjustment will be made. That is, the Y- and H-frames and the channels will be assembled without adjustments at the interfaces. The height of the cones will be ground to an accurate dimension (±0.025 in.) to provide the proper focal length. After the cone is attached to the channel, an error will exist in its angular orientation. Analysis by Varian has shown that if the direction of a line perpendicular to the lens is within 0.5° of the lens-sun line, the cell can be brought into adjustment by a lateral movement of not more than 0.1 inch. This freedom of motion is allowed in the cell adjustment. Tolerance errors at the various interfaces can accumulate and an estimate of the total error in pointing accuracy is given in the following.

H-Frame - flat within 0.010 in/ft, 0.165 in. total
Resulting rotation of channel, 0.165/60 = 0.0028 rad.

Channel - opposite flanges plane within 0.020 in.
rotation of attached cone, 0.020/7 = 0.0028

Channel gasket - thickness variation, 0.005/5 = 0.0010

Cone - cell mounting surface parallel to lens mounting surface within 0.015/7 = 0.0021

Cell - axis of cell perpendicular to cell mounting surface within 0.005/3 = 0.0017

Lens - flat within 0.005/9 = 0.0006

Total: 0.011 rad.
= 0.63°

$\sqrt{\text{Sum of squares}}$ = 0.0049 rad. = 0.28°

The root-square value is a reasonable estimate since it is improbable that all maximum errors will occur on a single lens unit and, if they do, some rotations will be perpendicular to other rotations. If a few lenses exceed the 0.5° error, they can be shimmed at the cone-channel interface. It is envisioned that a significant number of lens-cell units, just from a statistical standpoint, will not require adjustment. For instance, if 0.28° represents a 2σ value of a normal distribution (i.e. about 5% of cones will exceed this error), then 50% of the cones will have errors of less than 0.1°.

The maximum rotation of any point on the array under its weight is about 0.07° with the array horizontal and about 0.05° under a 30 mph wind with the array vertical. The cells can be adjusted when the array is in a specified position to cancel the error from a particular loading condition. To see what array position might be preferable for adjusting the cells, the following approximate analysis is given.

For an array inclined from the vertical at an angle α as shown in the following sketch, the rotations affecting the pointing accuracy are estimated and the results for θ/θ_o are shown in Table 1. The wind condition $\theta_1 = \theta_o$ (wind coming from in front of the array) corresponds to a southerly wind and $\theta_1 = -\theta_o$ corresponds to a northerly wind. A southerly wind is strongest during stormy weather when little power is generated whereas northerly winds are strong usually during clear weather so $\theta_1 = -\theta_o$ appears to be of more concern than $\theta_1 = \theta_o$. However, the no-wind condition in the middle of the day is of primary concern. If the cells are adjusted with the array at 45° and no wind blowing, a good compromise is achieved where the

tracking errors due to gravity and wind are considerably reduced.

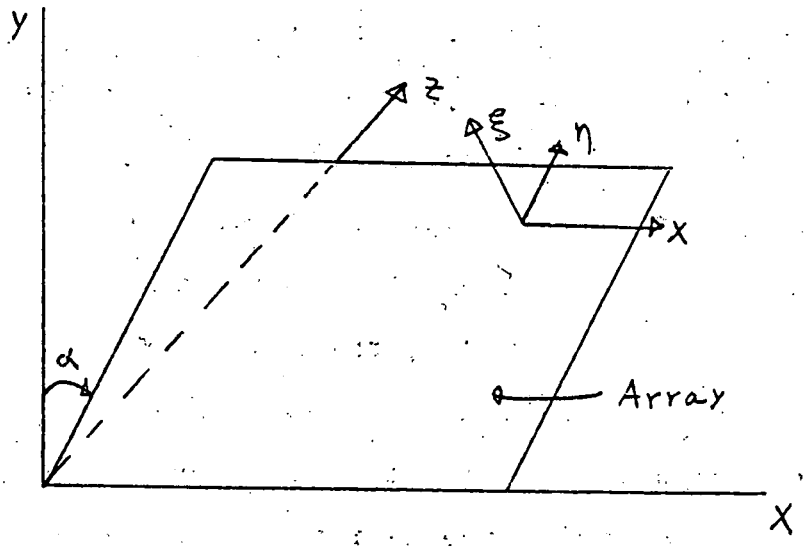

Assume: rotation about x axis, θ_x, is negligible

rotation about ξ axis, θ_ξ, does not affect cell accuracy.

max. rotation due to gravity: $\vec{\theta}_g = \theta_0 \sin\alpha \, \vec{e}_\eta$

max. rotation due to wind: $\vec{\theta}_w = \theta_1 \cos\alpha \, \vec{e}_\eta$

net rotation: $\theta = \theta_0 \sin\alpha + \theta_1 \cos\alpha$

α varies between 0 and 75°

	adjusted @ $\alpha = 0°$			adjusted @ $\alpha = 45°$			adjusted @ $\alpha = 90°$		
α	$\theta_1 = 0$	$\theta_1 = \theta_0$	$\theta_1 = -\theta_0$	$\theta_1 = 0$	$\theta_1 = \theta_0$	$\theta_1 = -\theta_0$	$\theta_1 = 0$	$\theta_1 = \theta_0$	$\theta_1 = -\theta_0$
0	0	1.0	-1.0	-0.71	0.29	-1.71	-1.0	0	-2.0
15	0.26	1.23	-0.71	-0.45	0.52	-1.42	-0.74	0.23	-1.71
30	0.50	1.37	-0.37	-0.21	0.66	-1.08	-0.50	0.37	-1.37
45	0.71	1.41	0	0	0.70	-0.71	-0.29	0.41	-1.0
60	0.87	1.37	0.37	0.16	0.66	-0.50	-0.13	0.37	-0.63
75	0.97	1.23	0.71	0.26	0.52	0	-0.03	0.23	-0.29
			Average Values						
	0.55	1.27	0.53	0.30	0.56	0.90	0.45	0.27	1.17

Table 1 – Values of θ/θ_0

Alternative Main Frame Structures

Several concepts of a main frame supported on a central column were considered and analyzed using SAP4 on a computer. Three concepts appeared promising. One, a truss composed of equilateral pyramids; two, a combined truss and frame; three, the chosen H-Frame. These are shown in Figure (10). Imposing the same stiffness requirement on all types (maximum rotation when subjected to gravity of .001 rad.), the analysis showed differences in weight between the three structural configurations but these differences were not significant enough to overrule practical considerations. For example, the H-frame members are primarily in bending. The stiffness of a bending member can be increased and the weight decreased by increasing the radius proportionately more than the thickness is decreased. The weight of the H-frame, therefore, can be heavier or lighter than the truss depending on whether small radius, thick walled or large radius, thin walled tubes are used. A practical limit on member size involving availability, cost per pound, and ease of handling limited the members in the present design to the 7 inch diam, 0.134 inch wall size. The resulting weight of the H-Frame was somewhat heavier (say, 20%) than estimates for the truss and truss-frame. However, the H-Frame has 11 members whereas the truss has 50 members, and the truss-frame has 40 members. The difficulty and cost of fabricating many members with many joints overrode the small weight advantage. Another disadvantage of the truss configuration is that their depth (about 3 feet compared to 7 inches for the H-frame) contributes to a large unbalance torque when the array is vertical. Considering these and other factors, the H-Frame was chosen for the design.

In the initial stages of the design, it was desired to determine the number of arrays versus array size, for a total of 50KW output, in a way to minimize the system cost. However, it became apparent that many costs were relatively insensitive to the number of arrays and were not well known for such a system. For example, the total number of cells, amount of rejected heat, number of secondary structural members and electrical wiring would remain relatively constant. The curves of cost versus array size would be too flat to attach any confidence to the location of minimum points. Therefore, other practical requirements determined the size of the array. It was considered important to have the option of assembling and adjusting each array and then shipping the unit, separate from its support, to the site for installation. This limited the size to less than about 10 x 40 ft. In addition, a shadowing study by Varian indicated the length-to-width ratio should be in the range of 2:1 to 4:1. Since the array was to be supported on a central column, the size of structural members and their weight increase rapidly as the length increases. Also the torque on the drive systems produced by wind loading increases as the square of the length. These considerations, along with using an integer multiple of the cell-cone dimensions, resulted in the size being set at 9.2 x 33.5 ft. At this size, structural members are of reasonable size and standard components can be used in the drive systems. Each array contains a field of 44 x 10 cells.

Alternative bed structures

Several concepts were considered for the bed structure that attaches to the main frame and supports the cell-cone units. Since a large flat surface was desired, hexagonal core honeycomb with aluminum face sheets was first considered. However, it was rejected because of high cost ($10/ft.^{2}), poor accessibility to cells and difficulty in attaching components to it. Numerous concepts of beam networks were considered. Some of these concepts were nearly comparable to the present design but were discarded in favor of the channels which offered a modular component to which attachment was easy and which provided a relatively safe and protective enclosure for the cells and electrical wiring. At the same time, the channels provided a path (open at the ends) for convective air flow to aid in the cooling of the cells. However, the present design does not efficiently combine with the presently required electrical wiring network and redesign of this portion of the structure considering electrical wiring requirements, plumbing, cell access and heat insulation for total energy systems appears worthwhile.

The channels are made of aluminum. Steel was considered in hopes of achieving lower cost but the thickness required to resist buckling for steel is about 2/3 that of aluminum. The weight of steel would be double that of aluminum and its cost therefore, would be comparable to aluminum (considering also, the effect of the increased weight on the remaining structure). Other reasons for choosing aluminum were its corrosion resistance and its larger thermal expansion coefficient which more nearly matched that of the plastic used in the lenses and cones.

Alternative Cooling Systems

The cells, with their high concentration ratio, require active cooling and, therefore, the basic design called for water to circulate near the back surface of the cell. Several alternative methods of removing heat from the water were considered. One groundrule that eliminated the possibility of evaporative systems was that no make-up water was available. For passive closed systems, simple calculations showed that a large surface area would be required to reject the heat by natural convection at the collection rate on a warm day. A forced air convective radiator was considered and appeared feasible. The hot water would be pumped from all arrays to a single radiator where a fan would produce the required cooling. However, the power needed for the radiator was significant and it seemed basically inefficient to collect heat, transport and reject the same heat during the hot part of the day. Therefore it was decided to use a volume of water as a heat sink and reject heat 24 hours a day. A given volume of water was needed to store enought heat while not allowing the cooling water to boil. On the other hand, a given surface area was necessary to reject this amount of heat over a 24 hour day. One scheme considered was to fill the tubular structural members with water and attach fins to the structure. The advantage of this method was that it would be self contained within the rotating array. However, the volume available was inadequate and the water nearly doubled the load on the structure. Large single tanks were also considered. However, these individual large single tanks have a low surface area to volume ratio which would require a forced air radiator. The common 55 gal. drum offered a good solution both from its

cost and heat rejection properties.

Alternate Adjustment Procedures

Of all the subsystems in the design, the cell adjustment procedure received the most attention. Even so, additional improvements may become evident after a system has been built and adjusted. All methods that came to mind were considered and no method clearly stood out as a superior scheme. Some methods involved adjustments at several interfaces. These methods included, for instance, spring loaded bolts with leveling nuts, etc. at the cone-channel and channel-H-frame interfaces and adjustment between the cell and cone. These were discarded partly because of the suspected large amount of time required to adjust 3 or 4 bolts at each location. Another scheme was patterned after an automobile headlight adjustment. The bottom of the cone would be a spherical surface (or have three pads lying on a spherical surface) and a matching spherical holder (a stamped aluminum dish) would be attached to the channel. By having the center of rotation at the center of the lens, it could be rotated without moving the lens laterally which would close the 0.050 inch gap between lenses. However, there appeared to be problems associated with locking the cones without affecting the adjustment and matching the spherical surfaces. Time was not available to build and test a model so a more straight forward procedure was chosen.

Appendix I-1 Foundation

Soil pressures:

The configuration of the foundation is shown below.

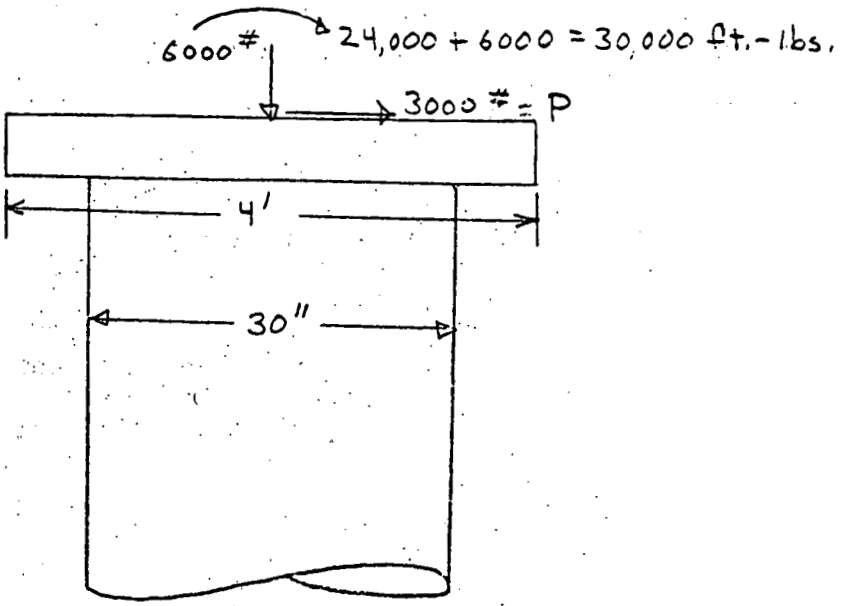

The net area of the pile cap is assumed to carry the vertical load. The soil pressure under the cap is

$$q_{av} = \frac{6000}{[4^2 - \pi(1.25)^2]} = 540 \text{ psf.}$$

For the lateral load and moment which are primarily short term loadings, the following load diagrams are assumed.

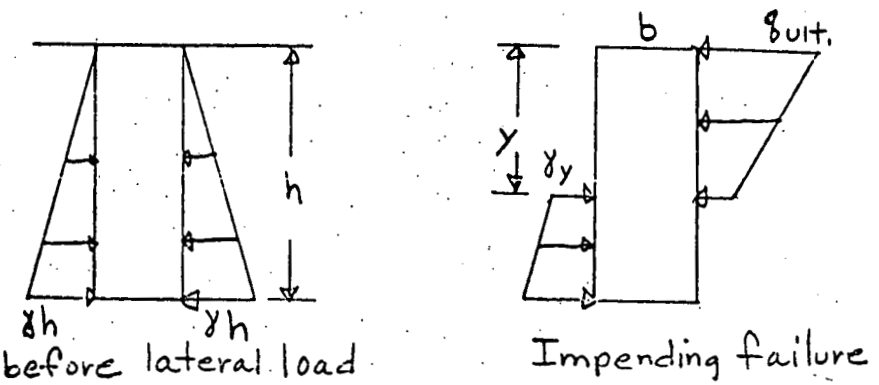

For equilibrium at failure, the lateral load is

$$\frac{P}{b} = \gamma\left(y^2 - \frac{h^2}{2}\right) + q_{ult.}\frac{y}{2} \tag{1}$$

Summing moments about the base gives,

$$\gamma\left(\frac{2}{3}y^3 - hy^2 + \frac{h^3}{6}\right) - \frac{q_{ult}}{2}\left(hy - \frac{y^2}{3}\right) + \frac{(Ph + 30{,}000)}{b} = 0 \tag{2}$$

assuming

$\gamma = 120\ \#/ft.^3$, $q_{ult.} = 2000\ psf$, $b = 2.5\ ft.$

Equation 1 becomes

$$y^2 + 8.333y - \left(\frac{h^2}{2} + 10\right) = 0 \tag{3}$$

Equation 2 becomes

$$y^3 - 1.5hy^2 + 0.25h^3 - 12.5hy + 4.167y^2 + 15.0h + 150 = 0 \tag{4}$$

we can solve eqs. 3 & 4 as follows. Assuming a value of h, eq. (3) can be solved for y. Using these values of h and y, the left side of eq. (4) can be computed and the zero value obtained from interpolation. Results are shown in the table below.

h	y	eq.(4)
6	2.568	+86
8	3.538	-10
10	4.629	-162

← $h \approx 8'$, use $h = 10'$

Reinforcing steel:

The pile is subjected at its top to 30,000 ft.-lbs. which can be applied from any direction. A conservative but simple calculation to obtain the area of reinforcing steel is to ignore the load capacity of the concrete both in tension and compression.

Replacing the bars with a continuous tubular member,

$$\sigma_s = \frac{M}{\pi r_s^2 t}$$

with, σ_s = 16,000 psi

r_s = 11.5 in.

M = 360,000 # in.

we get

$$t = 0.0542 \text{ in.}$$

The area of steel is, $A_s = 2\pi r_s t = 3.91 \text{ in.}^2$

for #5 bar, $A_s = 0.31 \text{ in.}^2$ $\quad N = \frac{3.91}{0.31} = 12.6$

use 12 - #5 bars

equally spaced.

A more detailed analysis would show that a smaller column was sufficient to transfer the loads from the array to the foundation but the controlling factor in determining the overall size is the transfer of load from the foundation to the poor soil.

Anchor bolts

The anchor bolts are positioned as shown.

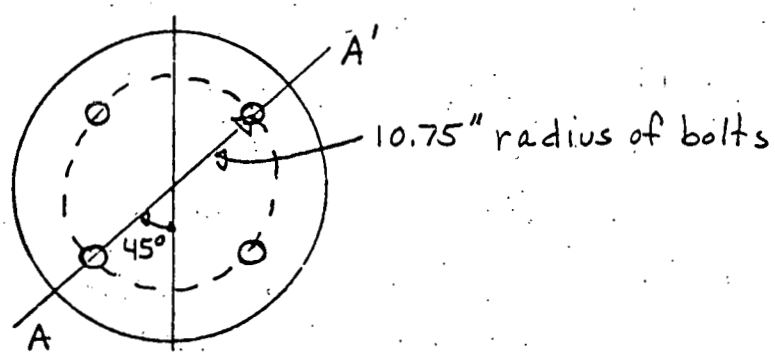

Assuming the moment acts about the weak axis A-A', the bolt force is

$$f_b = \frac{M}{10.75(2)} = \frac{360{,}000}{21.5} = 16{,}700\ \#$$

This neglects the contribution of the concrete (say, a gap exists between the grout and surface plate).

To prevent tension between base plate and concrete, the bolt load is determined as follows:

the base plate area : 40 x 36"

$$I = 40\left(\frac{36}{12}\right)^3 = 155{,}000\ \text{in.}^4$$

on this section:

$$\sigma = \frac{360{,}000(20)}{155{,}000} = 46\ \text{psi}$$

$$46(40)\left(\frac{36}{4}\right) = 16{,}500\ \#/\text{bolt}$$

bolt diam. for f = 16,700#

1.75"	9,000 psi = σ in bolt
1.50	12,000
1.25	18,000
1.00	29,000

pullout strength:

Allowable shear strength = 0.045 (2500) = 110 psi

$$\tau = \frac{P}{\pi d \ell} \qquad \ell = \frac{P}{\pi d \tau} = \frac{16{,}700}{\pi(110)d} = \frac{48}{d}$$

bolt diam.

d	ℓ, in.
1.75	26
1.50	31
1.25	37
1.00	46

baseplate thickness:

Two calculations will be made. One assumes the anchor bolt is in tension and the baseplate is separated from the foundation (i.e., the baseplate is sheared through by the anchor bolt). The second is that the anchor bolt is taking one fourth of the applied moment (4 anchor bolts). The stress is highest near the bolt and outer boundary conditions of simple supports and clamped supports are considered:

Case 1:

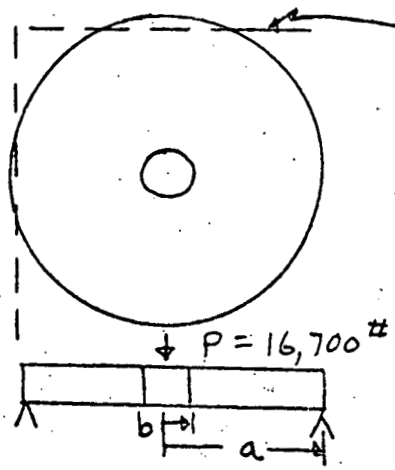

pedestal weldment

assume b = 1.5"

a = 7"

$\frac{a}{b} = 4.6$

'a' represents the average distance to the wall of the pedestal weldment, which transmits the moment to the baseplate.

The maximum stress is (Ref. Plates & Shells, Timoshenko)

simple supports: $\sigma_{max.} = 2.25 \left(\frac{16,700}{t^2}\right)$

for $\sigma_{max.} = 20,000$ psi

$$\underline{t = 1.37"}$$

clamped supports: $\sigma_{max.} = 1.15 \left(\frac{16,700}{t^2}\right)$

$$\underline{t = 0.98"}$$

Case 2

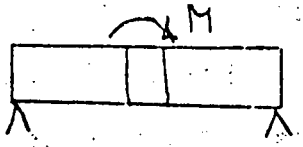

M = 7500 ft.-lbs.

for simple supports, the radial moment can be found to be (Timoshenko, Plates & Shells)

$$M_r = \frac{0.103}{a}\left(\rho - \frac{1}{\rho}\right), \quad \rho = \frac{r}{a}$$

@ $\rho = 0.214$, $a = 7''$

$$M_r = M\,\frac{(0.103)}{7}\left(0.214 - \frac{1}{0.214}\right) = -0.066M = -5940 \text{ \#in./in}$$

$$\sigma = \frac{5940(6)}{t^2}, \quad \text{for } \sigma = 20{,}000 \text{ psi}, \quad t = 1.33''$$

for clamped outer edges

$$\sigma_r = \frac{2.5\,M}{at^2}, \quad t = 1.27''$$

use $t = 1.50''$

Appendix I-2 Elevation and Azimuth Drives

The gears and interior components of the drive units are designed by the manufacturers to carry the rated loads. The external components including the shaft and flanges are analyzed here.

Elevation drive shaft:

The maximum moment in the shaft occurs when the array is vertical and subjected to a 60 mph wind. The loads, including torque, are

Moment = 93,000 #in.

Torque = 5,400 #in. (1/2 of survival torque in each shaft)

Shaft diameter = 3.0 in.

$$\sigma = \frac{4M}{\pi r^3} = \frac{4(93{,}000)}{\pi(1.5)^3} = 35{,}100 \text{ psi}$$

matl. yield stress = 59,000 psi

Shaft torsion

$$\tau = \frac{2M_T}{\pi r^3} = \frac{2(5400)}{\pi(1.5)^3} = 1{,}020 \text{ psi}$$

stress concentration for keyway: τ = 3,000 psi

Aximuth drive shaft

Torque = 36,000 #in.

$$\tau = \frac{2M_T}{\pi r^3} = \frac{2(36{,}000)}{\pi(1.8)^3} = 3{,}930 \text{ psi}$$

with keyway τ = 10,000 psi

Elevation drive bracket:

This bracket connects the elevation drive to the central column.

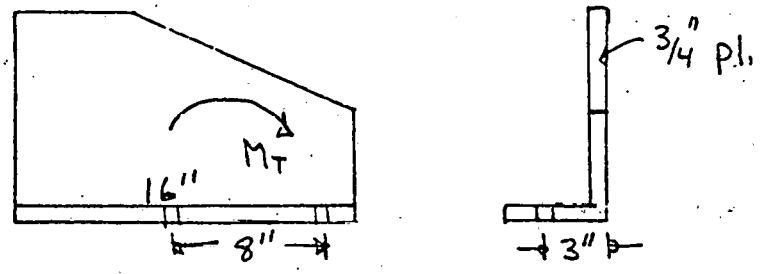

Torque:

M_T = 10,800 #in.

bolt load = $\frac{10,800}{8}$ = 1,350 #/bolt (1/2" bolts)

Moment capacity of plate

$$\sigma = \frac{M(6)}{16(.75)^2} \qquad M = 33,\frac{000(16)(.75)^2}{6} = 49,000 \text{ \# in.}$$

Under a 30 mph wind acting on half of the array (right or left side), the moment in the shaft is about M = 1/4 (93,000) = 23,000 #in. This moment can be safely carried by bracket. The symmetric moment produced by a 60 mph wind (93,000 #in.) remains in the shaft. The bolt load for 23,000 #in. is

$f_b = \frac{23,000}{3(2)}$ = 3,800 #/bolt

σ_b = 27,000 psi

use 1/2" bolts, grade 5

Flange Design

It is useful to obtain a general formula for sizing bolted flanges subjected to a bending load. Both internal and external flanges will be considered. The bolt preload will be assumed to be a distributed pressure over the area of the flange. The joint will be designed so that no tension (i.e. no separation) exists at the interface.

Bolt preload:

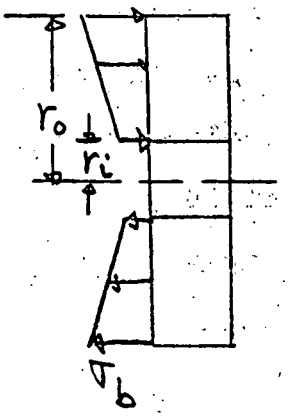

flange

n = number of bolts

The bending stress on the flange surface is

$$\sigma_b = \frac{4Mr_o}{\pi(r_o^4 - r_i^4)}$$

preload: $$P = \sigma_b A_{net} = \frac{4Mr_o}{r_o^2 + r_i^2}$$

bolt force: $$f_b = \frac{P}{n}$$

External flange:

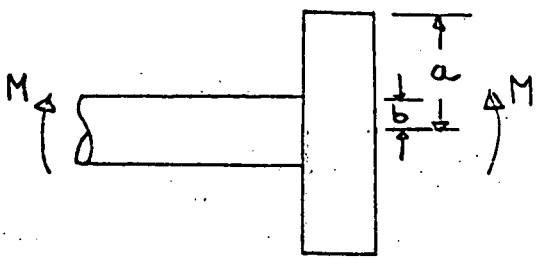

This can be treated as a plate with a rigid tube as shown:

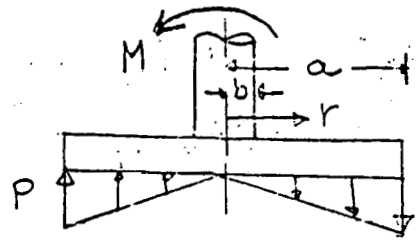

$\rho = \frac{r}{a}$

$\beta = \frac{b}{a}$

the deflection of the flange is, where θ is circumferential coordinate,

$$w = \frac{P a^4 \cos\theta}{192 D}\left[\rho^5 + A\rho + B\rho^3 + \frac{C}{\rho} + F\rho \log \rho\right]$$

where,

$$B = -2\left[\frac{4(2+\nu) + (1-\nu)\beta^2(3+\beta^4)}{(3+\nu) + (1-\nu)\beta^4}\right]$$

$$C = -2\left[\frac{4(2+\nu)\beta^4 - (3+\nu)\beta^2(3+\beta^4)}{(3+\nu) + (1-\nu)\beta^4}\right]$$

$$F = 12$$

The bending stress is maximum at $\rho = \beta$. The bending moments are

$$M_r = -\frac{P a^2 \cos\theta}{192}\left[\rho^3(20+4\nu) + (6+2\nu)B\rho + 2(1-\nu)\frac{C}{\rho^3} + 12\frac{(1+\nu)}{\rho}\right]$$

$$M_\theta = -\frac{P a^2 \cos\theta}{192}\left[(4+20\nu)\rho^3 + 2B(1+3\nu)\rho - 2(1-\nu)\frac{C}{\rho^3} + 12\frac{(1+\nu)}{\rho}\right]$$

for $\nu = 0.3$, $\theta = 0$, $P = \frac{4M}{\pi a^3}$, the moment can be calculated at $\rho = \beta$

β	B	C	$M_r\left(\frac{a}{M}\right) = h_r$	$M_\theta\left(\frac{a}{M}\right) = h_\theta$
0.2	-5.62478	0.231128	0.7372	0.2213
0.4	-5.74991	0.820994	0.2860	0.0859
0.6	-5.89176	1.48974	0.1121	0.0336
0.8	-5.98179	1.91415	0.02655	0.0080

$\sigma_r = \frac{6M_r}{t_f^2}$, $\sigma_\theta = \frac{6M_\theta}{t_f^2}$, $\sigma_p = -\frac{4M}{\pi a^3}$ (preload)

neglecting shear stresses. The effective stress (Von Mises criteria) is

$$\sigma^{*2} = (\sigma_R - \sigma_\theta)^2 + (\sigma_R - \sigma_p)^2 + (\sigma_p - \sigma_\theta)^2$$

$$= \left(\frac{6M}{t_f^2 a}\right)^2 \left[(h_R - h_\theta)^2 + \left(h_R + \frac{t_f^2}{1.5\pi a^2}\right)^2 + \left(h_\theta + \frac{t_f^2}{1.5\pi a^2}\right)^2\right]$$

$$T = t_f/a$$

$$\sigma^* \frac{a^3}{M} = \frac{6}{T^2}\left[(h_R - h_\theta)^2 + \left(h_R + \frac{T^2}{1.5\pi}\right)^2 + \left(h_\theta + \frac{T^2}{1.5\pi}\right)^2\right]^{1/2}$$

Internal flange:

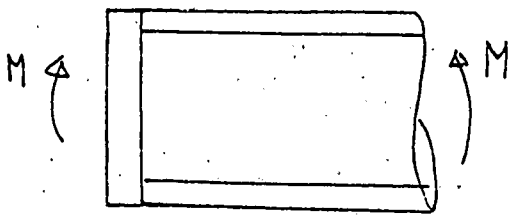

This can be treated as the following

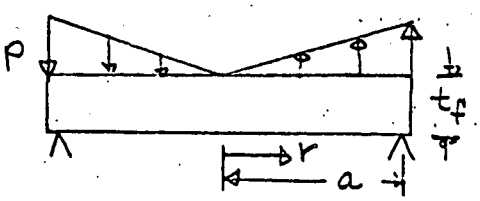

$$\rho = \frac{r}{a}$$

The maximum radial moment occurs at $\rho = 1/\sqrt{3}$ and is

$$M_r = \frac{p a^2 (5+\nu)}{72\sqrt{3}} = 0.0425\, p a^2 \qquad p = \frac{4M}{\pi a^3}$$

$$M_\theta = 0.0267\, p a^2$$

$$\sigma_r = 0.325 \frac{M}{a t_f^2}$$

$$\sigma_\theta = 0.204 \frac{M}{a t_f^2}$$

$$\sigma_p = -1.274 \frac{M}{a^3}$$

$$\sigma^* \frac{a^3}{M} = \frac{1}{T^2}\left[(0.121)^2 + (0.325 + 1.274 T^2)^2 + (0.204 + 1.274 T^2)^2\right]^{1/2}$$

Calculations are shown in the following graph.

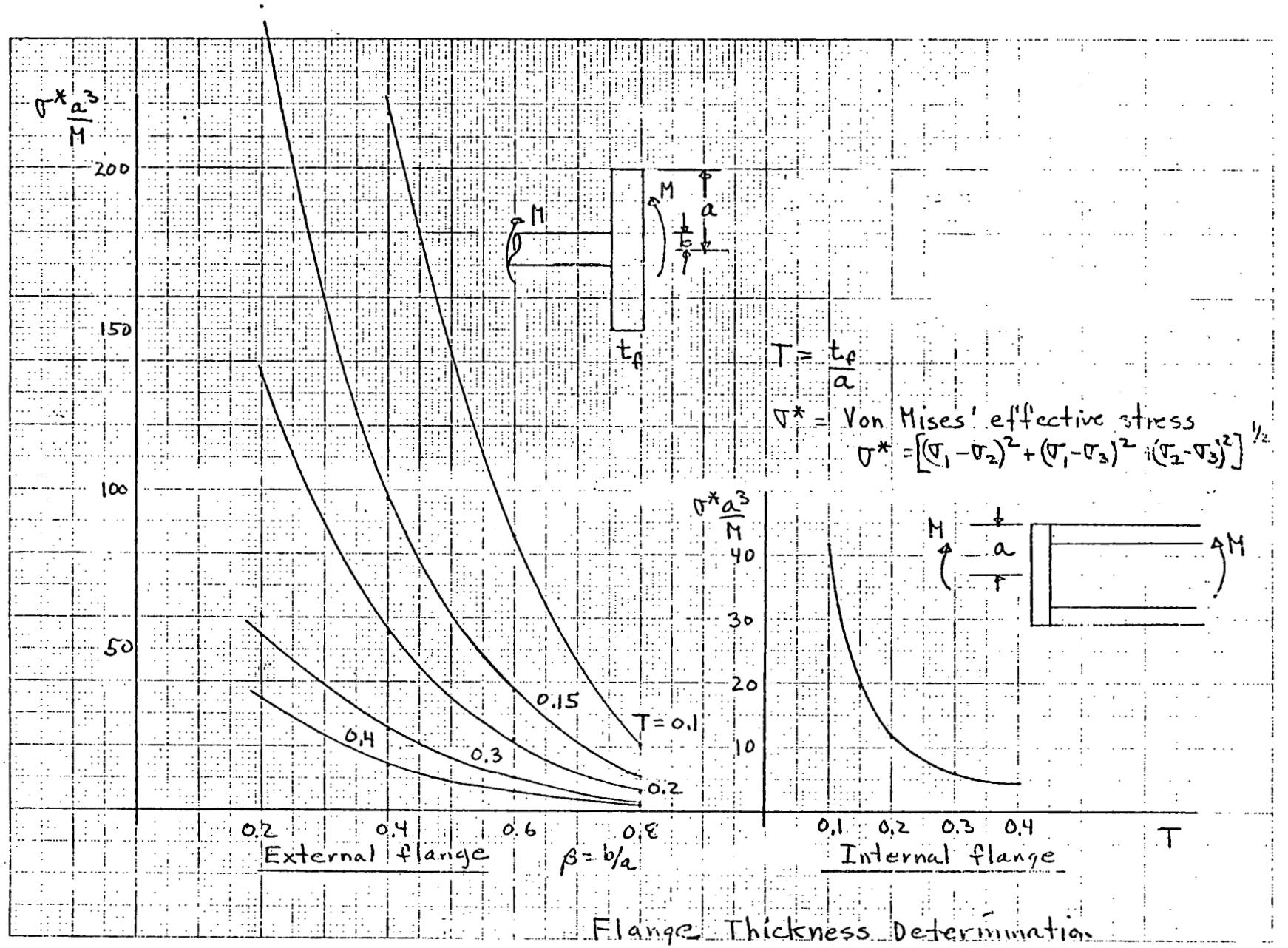

Flange Thickness Determination

Elevation drive:

flange at bearing at end of torque tube:

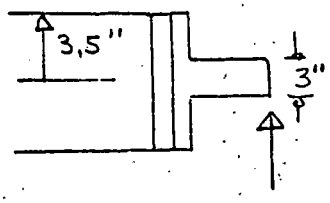

2000# gravity
1500# wind @ 90°
= 2500# resultant

$\frac{r_i}{r_o} = \frac{1.5}{3.5} = 0.43$

$M = 10,000$ #in.

use 6 bolts, preload = $\frac{4(10,000)(3.5)}{(3.5)^2+(1.5)^2} = 9,650$#

f_b = 1610 #/bolt (primarily from gravity)

σ_{bolt} = 20,000 psi use 6-3/8 bolts
SAE Grade 5

external flange: working stress = 20,000 psi

$\Gamma^* \frac{a^3}{M} = 20,000 \frac{(3.5)^3}{10,000} = 85.6$

$\beta = 0.42$

from graph $T = 0.16$ $t_f = .16(3.5) = 0.56"$

internal flange:

$t_f < 0.1(3.5) = 0.35"$ but require sufficient thickness for 3/8 in. bolt threads.

flange connecting elevation drive to torque tube:

from computer analysis:

M = 64,000 #in. wind
15,000 #in. gravity @ 90°

resultant 66,000 #in.

use 6 bolts, preload = $\frac{4(66,000)(3.5)}{(3.5)^2 + (1.5)^2} = 63,700$#

f_b = 10,600 #/bolt load is primarily from wind survival load which seldom occurs.

for 1/2" bolt, σ_b = 68,000 psi

use 6-1/2" bolts, grade 5

(σ_{proof} = 85,000 psi)

using σ^* = 30,000 psi

$$\sigma^* \frac{a^3}{M} = \frac{30,000}{66,000}(3.5)^3 = 19.5$$

External flange: $\beta = \frac{1.62}{3.5} = 0.46$

T = 0.30 $t_f = 0.30(3.5) = 1.1"$

Internal flange:

T = 0.15 $t_f = 0.15(3.5) = 0.53"$

use 3/4" for threads of 1/2" bolt

Azimuth Drive:

the wind moment is transferred to the bearing from the central column. This requires the following flange.

M = 290,000 #in. use σ^* = 30,000 psi

$$\sigma^* \frac{a^3}{M} = \frac{30,000(6)^3}{290,000} = 22.3$$

External flange: β = 0.65

T = 0.17 $t_f = 0.17(6) = 1.0"$

Appendix I-3 Pedestal Weldment

Load on bearing:

On the 17.0" bolt circle, the line loading applied to the bearing is

$$N = \frac{M}{\pi r^2} = \frac{22{,}000(12)}{\pi(8.5)^2} = 1160\ \#/in.$$

where M = 22,000 ft.-lbs. at height of bearing
Axial load ~ 100 #/in.

N_T = 1260 #/in.

Top plate:

The top plate is idealized as the circular plate shown

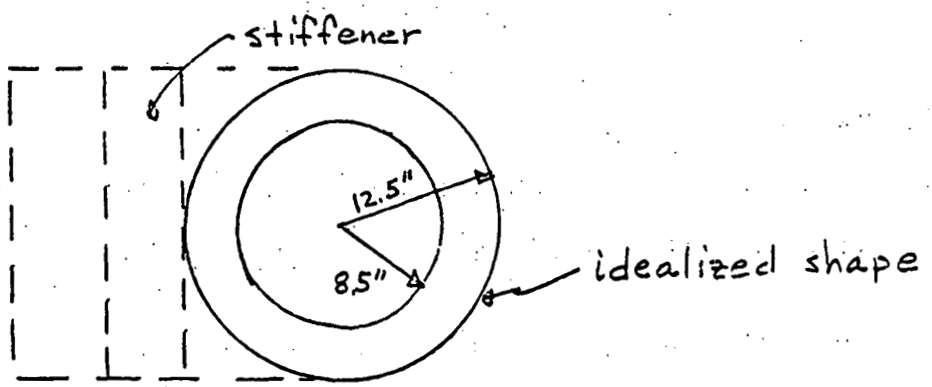

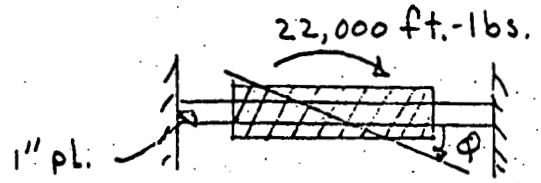

$\frac{8.5}{12.5} = 0.7$

from Timoshenko, Plates and Shells,

$$\theta = \frac{M}{7.8\,E t^3} = \frac{22{,}000(12)}{7.8(30)10^6} = 0.00011 \text{ rad.}$$

$$\sigma = \frac{36\,E t \theta}{r_i} = \frac{36(30)10^6(.00011)}{8.5} = 14{,}000 \text{ psi}$$

stiffener characteristics:

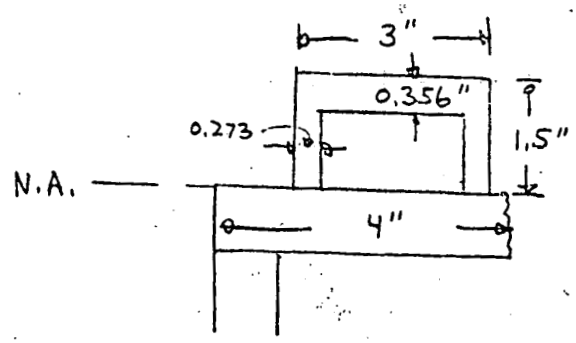

for this assumed cross section:

$I = 3.833 \text{ in.}^4$

assume a loading of

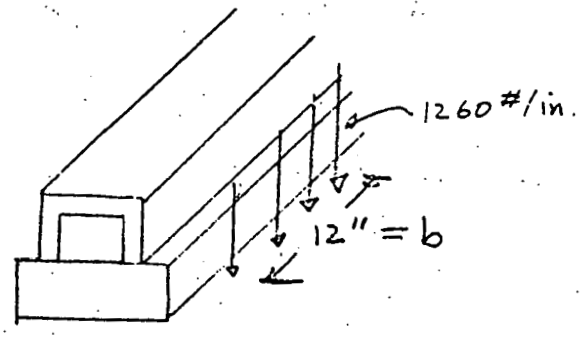

$$M = \frac{qbl}{4} - \frac{qb^2}{8} = \frac{qb}{8}(2l-b)$$

$$M = 1260\frac{(12)}{8}(50-12) = 71{,}820 \text{ \# in.}$$

$$\sigma = \frac{71{,}820(1.5)}{3.833} = 28{,}100 \text{ psi}$$

Shear in weld:

$$\tau = \frac{VQ}{IC} \qquad V = 1260(6) = 7560 \text{ \#}$$
$$Q = 4(1)(0.5) = 2 \text{ in.}^3$$
$$C = 0.273(2) = 0.546$$

$$\tau = \frac{7560(2)}{3.833(0.546)} = 7220 \text{ psi}$$

torsion:

$$\tau = \frac{M_T}{2At} \quad \text{where } A = 2.8(2.0) = 5.6 \text{ in.}^2,\ t = 0.273$$

$$\tau = \frac{1260(12)(2)}{2(2)(5.6)(0.273)} = 4{,}950 \text{ psi}, \quad \left[M_T = \frac{1260(12)(2)}{2}\right]$$

With the door removed, the top plate thickness is adequate to carry the maximum bending load.

Torsional twisting of side walls:

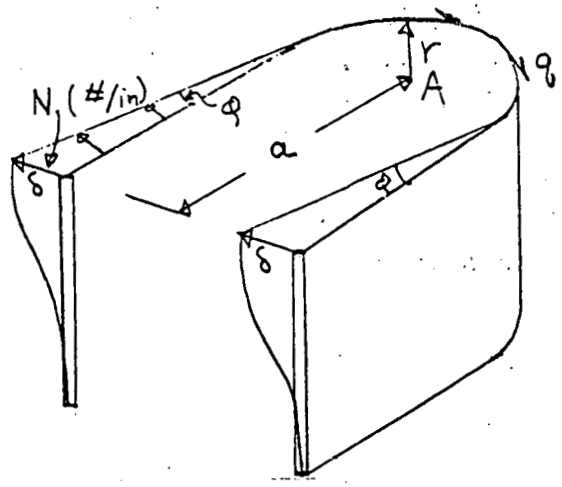

$a = 20''$
$r = 12.5''$

for a beam:

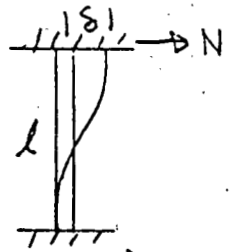

$$\frac{N}{\delta} = \frac{12EI}{l^3}$$

$$M = \frac{Pl}{2}$$

Torque: (about point A)

$$M_T = \frac{1}{2} N a \left(\frac{2}{3}a\right)(2) + \pi r^2 q = \frac{2}{3} N a^2 + \pi r^2 q$$

let $q = N$

$$M_T = 757\, N$$

for $M_T = 36{,}000$ #in., $N = 48$ #/in. (30 mph on half of array)

$$\phi = \frac{\delta}{a} = \frac{N l^3}{12EIa} = \frac{48(400)12}{12(30)10^6(.175)^3} = 0.0015 \text{ rad.}$$

$$M = 48\left(\frac{20}{2}\right) = 480 \text{ \#in./in.}$$

$$\sigma = \frac{480(6)}{(.175)^2} = 5{,}120 \text{ psi}$$

Bending:

for 60 mph wind, $N = \frac{3000}{60} = 50$ #/in.

Pedestal - baseplate screws:

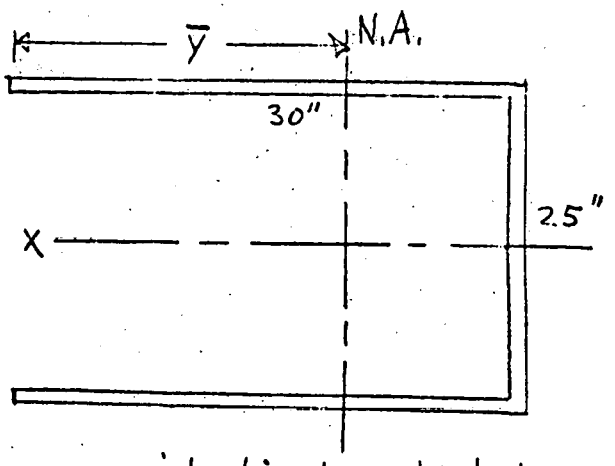

idealized pedestal

Neutral Axis:

$$2\frac{\bar{y}^2}{2} = 2\frac{(30-\bar{y})^2}{2} + 25(30-\bar{y})$$

$$\bar{y} = 19.4"$$

$$I_{N.A.} = 2t\left[\frac{(19.4)^3}{3} + \frac{(10.6)^3}{3}\right] + t(25)(10.6)^2 = 8470t$$

for $t = 0.75"$, $I_{N.A.} = 6350\ in.^4$

$$I_x = 2(30)t(12.5)^2 + t\frac{(25)^3}{12} = 10,680t = 8010\ in.^4$$

$$\sigma_{N.A.} = \frac{360,000(19.4)}{6350} = 1100\ psi$$

$$N = 1100(0.75) = 825\ \#/in.$$

for 3/4" screw: cap. = 10,000 #/bolt

$$spcg. = \frac{10,000}{825} = 12"$$

use 3/4" bolts @ 9"

Azimuth drive mounting plate:

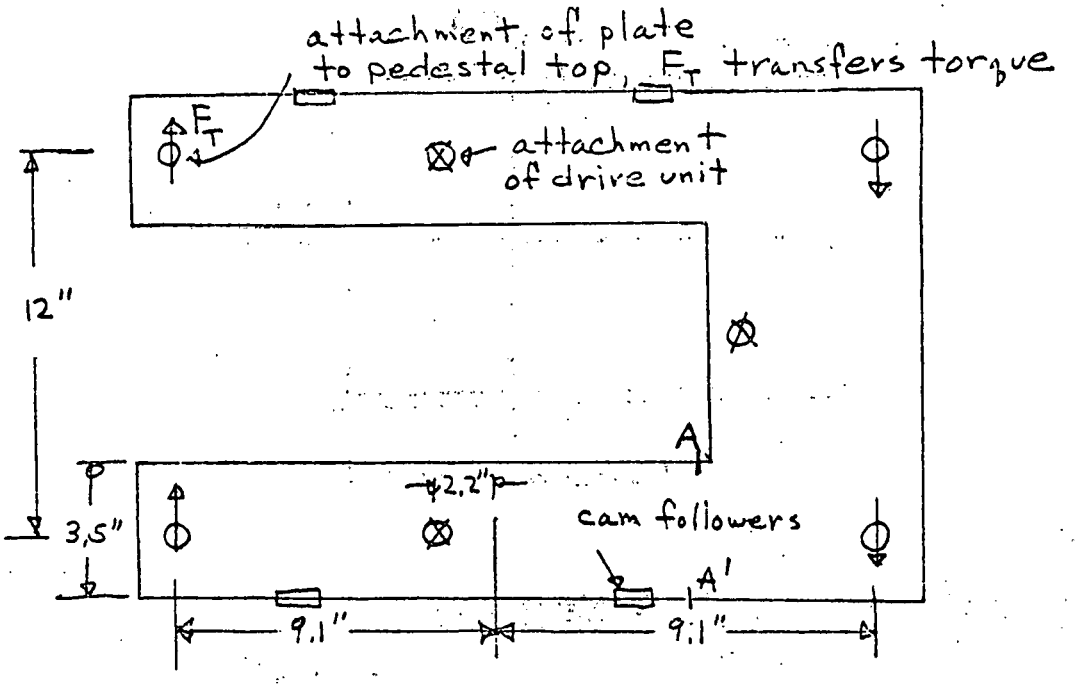

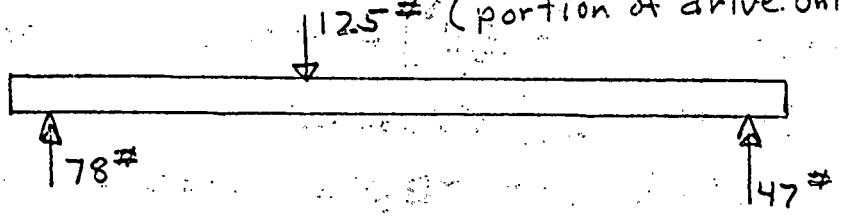

from weight of drive unit:

$$M = 78(6.9) = 540\ \#\text{in.}$$

$$\sigma = \frac{540(6)}{3.5(.75)^2} = 1{,}650\ \text{psi} \quad \text{(in mounting plate)}$$

$$\delta \approx \frac{Pl^3}{48EI} = \frac{125(18.2)^3 12}{48(30)10^6(3.5)(.75)^3} = 0.004"$$

from torque:

$$F_T = \frac{36{,}000}{2(18.2)} = 1{,}000\ \#/\text{bolt}$$

bending across A-A'

$$M = 1000(15) = 15{,}000\ \#\text{in.}$$

$$\sigma = \frac{15000(6)}{(3.5)^2(0.75)} = 9{,}800\ \text{psi}$$

Torsion from cam follower before weight is transferred to mounting plate.

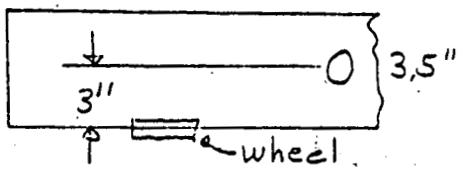

assume weight of unit is on 2 wheels.

Torque = 175 (3) = 525 # in.

$$\tau = \frac{M_T}{k_2 a b^2} = \frac{525}{0.29(3.5)(.75)^2} = 920 \text{ psi}$$

Appendix I-4 Channels

The cross section of the channel is shown below.

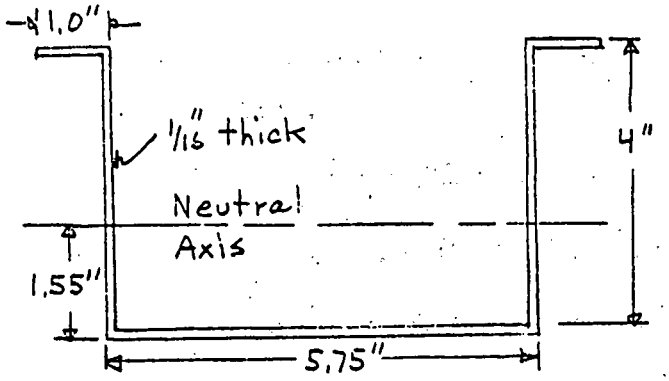

cross sectional area: $A = 0.976$ in.^{2}

moment of inertia: $I_{N.A.} = 2.35$ in.^{4}

The assumed loading is divided into the following:

Channel:	1 #/ft.
Cones, lens, cells	3 #/ft.
water lines, wiring	1 #/ft.
	$q = 5$ #/ft. $= 0.417$ #/in.

The overall dimensions are assumed to be, assuming symmetric supports, as shown.

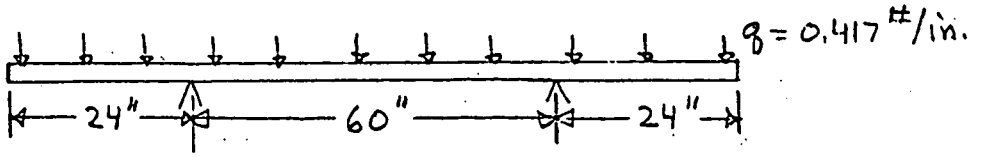

The bending deflection and rotation are:

Overhang: $\delta = \frac{q\ell^4}{8EI} = 0.0007"$ $(\ell = 24")$

$\theta = \frac{q\ell^3}{6EI} = 4.1 \cdot 10^{-5}$ rad.

midspan: $\delta = \frac{q\ell^4}{384EI} = 0.0007"$ $(\ell = 60")$

$\theta_{max.} \leq 4.1 \cdot 10^{-5}$ rad

Nonuniform Twisting of channels

The channel is an open cross-section, neglecting the stiffening effect of the attached cones, for which the warpage is restrained by the attachment to the H-Frame. A wind loading on the channels and cones will produce a distributed torque. The following analysis neglects the stiffening of the plastic cones (which may be very significant) but includes the warpage rigidity.

The equation for nonuniform torsion is

$$C_1 \frac{d^3\phi}{dz^3} - C\frac{d\phi}{dz} = -M_T$$

where C_1 = warpage rigidity

C = torsional rigidity

ϕ = rotation of cross section

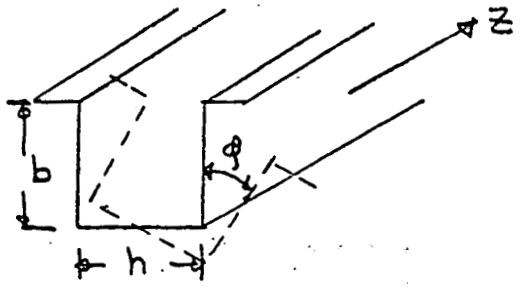

t = thickness

If the torque is of the form

$$M_T = M_o + M_1 Z$$

the solution for ϕ is

$$\phi = \frac{1}{C}\left(M_o z + M_1 \frac{z^2}{2}\right) + A_1 + A_2 \sinh \lambda z + A_3 \cosh \lambda z$$

where

$$\lambda = \sqrt{C/C_1}$$

$$C_1 = E\frac{b^3 h^2 t}{12}\frac{(3b+2h)}{6b+h} \qquad \text{(neglects flange on channel)}$$

$$C = \frac{E t^3}{6(1+\nu)}(2b+h)$$

The channel is supported at interior points so it will be considered as two segments as shown.

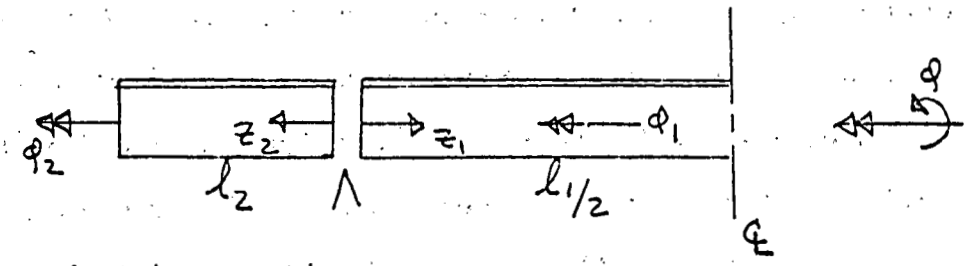

For the overhanging portion

$$M_T = M_A(\ell_2 - z_2), \quad M_A = \text{applied torque/unit length}$$

$$\phi_2 = \frac{M_A}{C}\left[\ell_2 z_2 - \frac{z_2^2}{2}\right] + A_1 + A_2 \sinh \lambda z_2 + A_3 \cosh \lambda z_2$$

B.C.

$$z_2 = 0; \quad \phi = 0 \quad \text{(support constraint)}$$

$$z_2 = \ell_2, \quad \frac{d^2\phi}{dz_2^2} = 0 \quad \text{(zero stress)}$$

These give

$$A_3 = -A_1$$

$$A_2 = A_1 \coth \lambda \ell_2 + \frac{M_A}{C\lambda^2 \sinh \lambda \ell_2}$$

$$\phi_2 = \frac{M_A}{C}\left[\ell_2 z_2 - \frac{z_2^2}{2} + \frac{\sinh \lambda z_2}{\lambda^2 \sinh \lambda \ell_2}\right] + A_1\left[1 - \frac{\sinh \lambda(\ell_2 - z_2)}{\sinh \lambda \ell_2}\right]$$

for the interior portion

$$M_T = M_A\left(\frac{\ell_1}{2} - z_1\right) \qquad \text{(the torque at the support is } M_A \ell_2 + M_A \frac{\ell_1}{2} = \frac{1}{2} M_A(\ell_1 + 2\ell_2)\text{)}$$

$$\phi_1 = \frac{M_A}{C}\left[\frac{\ell_1}{2} z_1 - \frac{z_1^2}{2}\right] + B_1 + B_2 \sinh \lambda z_1 + B_3 \cosh \lambda z_1$$

B.C.

$$z_1 = 0, \quad \phi = 0$$

$$z_1 = \frac{\ell_1}{2}, \quad \frac{d\phi}{dz_1} = 0 \quad \text{(symmetry at ℄)}$$

These conditions give

$$B_3 = -B_1$$

$$B_2 = B_1 \tanh \frac{\lambda \ell_1}{2}$$

$$\phi_1 = \frac{M_A}{C}\left(\frac{\ell_1 z_1}{2} - \frac{z_1^2}{2}\right) + B_1\left[1 - \frac{\cosh\lambda\left(\frac{\ell_1}{2} - z_1\right)}{\cosh\frac{\lambda\ell_1}{2}}\right]$$

For continuity of warpage displacement and longitudinal stress at the support,

$$@\ z=0 \qquad \frac{d\phi_1}{dz_1} = -\frac{d\phi_2}{dz_2}$$

$$\frac{d^2\phi_1}{dz_1^2} = \frac{d^2\phi_2}{dz_2^2}$$

This gives

$$A_1 = B_1 = -\frac{M_A}{\lambda C}\left[\frac{\ell_1}{2} + \ell_2 + \frac{1}{\lambda \sinh\lambda\ell_2}\right]\frac{\sinh\lambda\ell_2 \cosh\frac{\lambda\ell_1}{2}}{\cosh\lambda\left(\frac{\ell_1}{2} + \ell_2\right)}$$

Letting $\lambda_1 = \frac{\lambda\ell_1}{2}$, $\lambda_2 = \lambda\ell_2$

the rotations become

$$\phi_1\left(\frac{\ell_1}{2}\right) = \frac{M_A}{C\lambda^2}\left\{\frac{\lambda_1^2}{2} - \left[\lambda_1 + \lambda_2 + \frac{1}{\sinh\lambda_2}\right]\left[\frac{\sinh\lambda_2\cosh\lambda_1}{\cosh(\lambda_1+\lambda_2)}\right]\left(1 - \frac{1}{\cosh\lambda_1}\right)\right\}$$

$$\phi_2(\ell_2) = \frac{M_A}{C\lambda^2}\left\{\frac{\lambda_2^2}{2} + 1 - \left[\lambda_1 + \lambda_2 + \frac{1}{\sinh\lambda_2}\right]\left[\frac{\sinh\lambda_2\cosh\lambda_1}{\cosh(\lambda_1+\lambda_2)}\right]\right\}$$

with $b = 4.06$ $\quad \ell_1 = 60$

$h = 5.13$ $\quad \ell_2 = 24$

$t = 0.0625$

$$\phi_1\left(\frac{\ell_1}{2}\right) = 1.39 \cdot 10^{-4}\frac{M_A}{C\lambda^2}$$

$$\phi_2(\ell_2) = 1.13 \cdot 10^{-4}\frac{M_A}{C\lambda^2}$$

For a 30 mph wind, the pressure is 2.5 psf. This gives

$M_A = \frac{2.5(6)(12)}{144} = 1.25$ #in./in., assuming a 12" height and 6" moment arm.

$\phi_1\left(\frac{\ell_1}{2}\right) = 0.0007$ rad. $= 0.04°$ $\qquad \phi_2(\ell_2) = 0.00057$ rad. $= 0.03°$

A large balancing effect is provided by the torque on the overhang. To see this effect, assume no wind occurs on the overhang. Then,

$$\phi_1\left(\frac{\ell_1}{2}\right) = \frac{M_A}{\lambda^2 C}\left[\frac{\lambda_1^2}{2} - \left(\lambda_1 + \frac{\cosh\lambda_2}{\sinh\lambda_2}\right)\left(\frac{\sinh\lambda_2\cosh\lambda_1}{\cosh(\lambda_1+\lambda_2)}\right)\left(1 - \frac{1}{\cosh\lambda_1}\right)\right]$$

$$\phi_2(\ell_2) = \frac{M_A}{\lambda^2 C}\left[1 - \left(\lambda_1 + \frac{\cosh\lambda_2}{\sinh\lambda_2}\right)\left(\frac{\sinh\lambda_2\cosh\lambda_1}{\cosh(\lambda_1+\lambda_2)}\right)\right]$$

and,

$$\phi_1\left(\frac{\ell_1}{2}\right) = 0.0029 \text{ rad.} = 0.16^\circ, \quad \phi_2(\ell_2) = -0.0036 \text{ rad.} = -0.20^\circ$$

It is seen that, without the wind acting on the overhang, a reverse twisting occurs where the value at the center is 4 times larger and the value at the end is 6 times larger. This infers that the channel is sufficiently stiff under a steady wind but dynamic oscillations under wind gusts could cause a problem in the outside rows of cones that are subjected to wind load.

Another loading condition of interest is where a concentrated torque is applied at midspan. For these conditions,

$$A_1 = B_1 = -\frac{M_o}{2\lambda C}\frac{\cosh\lambda_1\sinh\lambda_2}{\cosh(\lambda_1+\lambda_2)}\left(1 - \frac{1}{\cosh\lambda_1}\right)$$

and,

$$\phi_1\left(\frac{\ell_1}{2}\right) = \frac{M_o}{2\lambda C}\left[\lambda_1 - \frac{\sinh\lambda_1}{\cosh\lambda_1} - \frac{\cosh\lambda_1\sinh\lambda_2}{\cosh(\lambda_1+\lambda_2)}\left(1 - \frac{1}{\cosh\lambda_1}\right)^2\right]$$

$$\phi_2(\ell_2) = -\frac{M_o}{2\lambda C}\left[\frac{\cosh\lambda_1\sinh\lambda_2}{\cosh(\lambda_1+\lambda_2)}\left(1 - \frac{1}{\cosh\lambda_1}\right)\right]$$

For our case,

$$\phi_1\left(\frac{\ell_1}{2}\right) = 0.003915\frac{M_o}{2\lambda C} = 6.124\cdot10^{-5} M_o$$

$$\phi_2(\ell_2) = -0.00459\frac{M_o}{2\lambda C} = 7.18\cdot10^{-5} M_o$$

The force applied at the top of the channel needed to deflect the cone 0.050" laterally is $F_T = \frac{Mo}{5}$

$0.050 = 6.124 \cdot 10^{-5}(18)\,Mo$

$Mo = 45.4$ #in. $F_T = 9.1$#

Lateral stiffness of channel

Assume the cones provide a rigid top on the channel. The side walls of the cones will provide most of this rigidity. The bottom of the channel is assumed to be flexible (say, at midspan).

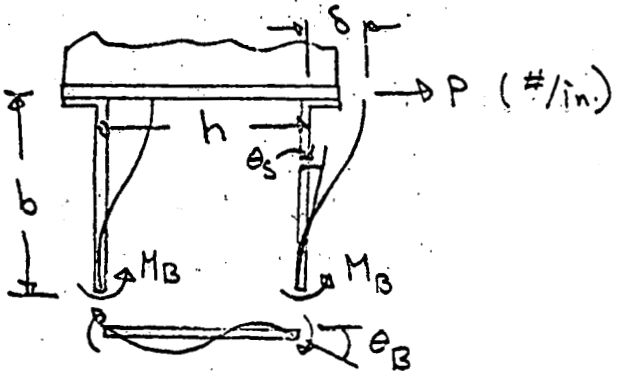

sidewall:

$$\theta_s = \frac{Pb^2}{4EI} - \frac{M_B b}{EI} \quad \text{(at bottom)}$$

bottom:

$$\theta_B = \frac{M_B h}{6EI}$$

$$\theta_s = \theta_B$$

$$\frac{M_B}{EI}\left(\frac{h}{6}+b\right) = \frac{Pb^2}{4EI}, \quad \text{or,} \quad M_B = \frac{Pb^2}{4}\left[\frac{1}{\left(\frac{h}{6}+b\right)}\right]$$

δ at top:

$$\delta = \frac{Pb^3}{2(3EI)} - \frac{M_B b^2}{2EI} = \frac{Pb^3}{6EI}\left[1 - \frac{3}{4\left(1+\frac{h}{6b}\right)}\right]$$

For our case,

$$\delta = \frac{P(4)^3(12)}{6(10^7)(.0625)^2}\left[1 - \frac{0.75}{1+\frac{5.75}{6(4)}}\right] = 0.0207P$$

A 30 mph wind applies about $\frac{2.5}{12} = 0.21$ #/in. to the cones and channels. This gives

$$\delta = 0.0207(0.21) = 0.004" \text{ deflection}$$

The lateral displacement of the lens due to a 30 mph steady wind is, including torsion and assuming a total height of 16",

$$\delta = 0.0007(16) + 0.004 = 0.015"$$

This is within the 0.050" spacing of the lenses. If a 30 mph gust acts only on the central portion of the channel, the displacement is

$$\delta = 0.0029(16) + 0.004 = 0.50"$$

For survival, a steady 60 mph wind applies about 0.84 #/in. This gives

$$\delta = 0.028(16) = 0.016 + 0.061"$$

This says that the exterior channels should be attached to adjoining interior channels.

Estimate of torsional natural frequency:

A solution is available for a 3 mass torsional beam that is unsupported. This can be used to obtain a reasonable estimate for our case. Consider our case to be modeled as shown below.

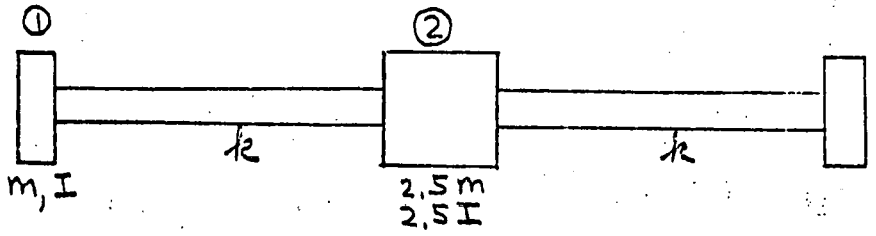

The equation for the frequencies of our model is

$$\omega^4 - 2.8\frac{k}{I}\omega^2 + 1.8\frac{k^2}{I^2} = 0$$

The roots are

$$\omega_{1,2}^2 = 1.0\frac{k}{I},\ 1.8\frac{k}{I}$$

The mode shapes are

$$\left(\frac{A_1}{A_2}\right)_1 = \frac{-k}{I\omega_1^2 - k} = \infty \quad \text{so } A_2 = 0$$

mode is antisymmetric about middle mass.

$$\left(\frac{A_1}{A_2}\right)_2 = \frac{-k}{I\omega_2^2 - k} = -1.25$$

mode is symmetric with outside masses rotating opposite to middle mass.

The lower mode is not possible because of the supports but the higher mode is a good estimate of the lowest mode of the system since the supports are at, or near, the node points of the model.

To estimate the stiffness of the channel we need to know the rotation at the end from the following load.

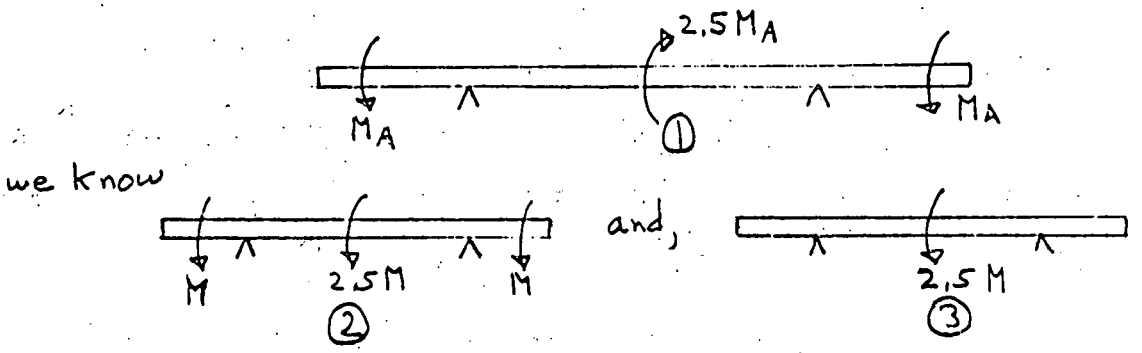

Therefore,

$$① = ② - 2③ \qquad \Delta\theta = \theta_{end} - \theta_{middle}$$

$$\Delta\theta_1 = (.00070 - 0.00057) - 2\,(.0029 + .0036) = -0.0129$$

where M = 1.25 (24) = 30 #in.

$$k = \frac{30}{0.0129} = 2330 \text{ \#in./rad.}$$

The total mass has been lumped into 3 masses. Assume the effective mass is 1/2 of total.

$$I = \int r^2 dm$$

$$dm = \frac{w}{g}\frac{dr}{h}$$

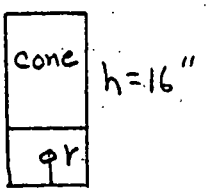

$$I = \frac{w}{gh}\frac{h^3}{3} = \frac{wh^2}{3g}$$

$$W_{eff.} = \frac{5}{2(12)} = 0.21 \text{ \#/in. of channel length}$$

$$I = \frac{0.21(16)^2}{3(386)} = 0.046 \text{ \#in.} \frac{sec.^2}{in}$$

$$I_{total} = 0.046\,(24) = 1.1 \text{ \#in. sec.}^2$$

$$\omega = \sqrt{\frac{1.8(2330)}{1.1}} = 61.7 \frac{rad}{sec.} = \underline{9.8 \text{ Hz}}$$

The supports not being at the nodes will cause the actual frequency to be higher than the estimated value so it can be taken as a lower bound estimate.

stiffening of channel:

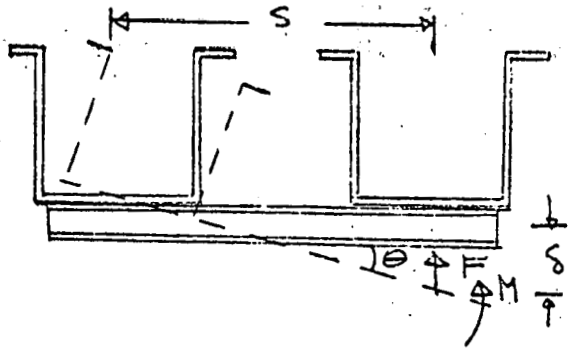

the rotation of the outside channel is

$\theta = \theta_A - \theta_F - \theta_M$ $\quad \theta_A$ from applied 60 mph wing

$\delta = \frac{F\ell^3}{48EI}$ (ℓ = length of channel)

$\delta = \theta S$ so, $F = \frac{48EI}{\ell^3}\theta S$

$M = J\theta$ we know $\theta_M = 6.124 \cdot 10^{-5} M_0$

so $J = 1.633 \cdot 10^4$ # in.

$\theta_F = FS(6.124 \cdot 10^{-5}) = 6.124 \cdot 10^{-5}(48)\frac{EI}{\ell^3} S^2\theta$

$\theta_M = \theta$

$\theta\left[2 + 6.124 \cdot 10^{-5}(48)\frac{EI\,S^2}{\ell^3}\right] = \theta_A = 0.0028$

$S = 9.1''$, $I = 2.35$ in.^{4}, $\ell = 60''$

$\theta = 9.8 \cdot 10^{-5}$ rad. $= 0.006°$

This provides sufficient stiffness for the channel.

stiffener size:

$$\delta_s = \frac{P\ell_s^3}{3EI_s} = 0.002 \quad , \quad P = 48\frac{EI}{\ell^3}(0.001)$$

$$I_s = \frac{48EI(0.001)\ell_s^3}{\ell^3(.002)3E} = 8I\frac{\ell_s^3}{\ell^3} = 8(2.35)\frac{(9.1)^3}{(60)^3} = 0.066\ in.^4$$

use Alum. I beam, channel or Tee.

Appendix I-5 Cooling System

Solar Array Cooling System

Typical solar cell dimensions, properties and heat fluxes are shown at right. Within each cell 40 watts of thermal energy is generated which is to be transferred away from the cell by the water cooling system. Any heat transfer through the plastic supports, E, will be neglected. It is well known that stagnation point flows afford the highest heat transfer rates thus the nozzle arrangement as shown. The nozzle parameters are chosen to provide the maximum heat transfer rates possible with the minimum flow losses. From Walz (Stanford University Department of Mechanical Engineering TR-61) figures 9 and 35 we have $\ell/D \sim 2.5$ and $\delta/D \geq 1$, thus the nozzle diameter $D \approx 3.2$ mm and the nozzle to cell distance $\delta \approx 6.4$ mm.

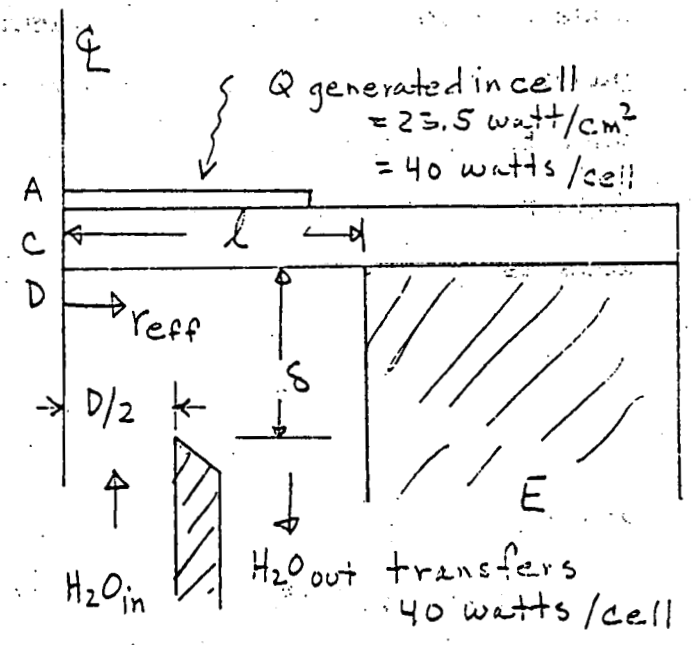

Material	thick. Δx (cm.)	effect. thermal radius reff (cm)	conduct. k w/cm°C
A-GaAs	.041	.635	0.43
B-solder(Ag)	.005	.635	4.15
C-BeO_x	.152	.775	2.68
D-H_2O B.L.	—	.775	—
E-Plastic	—	—	—

To optimize the cell cooling system, the electrical power loss due to increasing cell junction temperature and the hydraulic pumping power required to provide the required water flow rate must be minimized as a function of the water flow rate. From the data provided by Varian in the following figure the electrical power loss is-

$$-\dot{E}_{cell} = 0.0154\ (T_{junction} - T_{ref})$$

where

$T_{junction}$ = cell junction temperature

$= T_{H_2O} + \Delta T_{conduction} + \Delta T_{B.L.}$ (°C)

$T_{H_2O} = T_{start} + \frac{n}{2}\Delta T_{rise/cell} + N \cdot n\ \Delta T_{rise/cell}$

T_{ref} = cell ref. temperature from which temperature the power losses are measured (30°C)

ΔT_{start} = H_2O temp. at start of day (35°C)

$\Delta T_{rise/cell}$ = H_2O temp. rise per cell per pass

n = number of cells in series

N = number of times the total H_2O volume cycles through the system per 12 hr day

ΔT_{cond} = temp. drop across cell due to conduction resistance (=3.25°C)

$\Delta T_{B.L.}$ = temp. drop across boundary layer

Note that $N = \frac{12 \times \text{flow rate}}{\text{system volume (25 barrels)}} = 3.65\ \frac{\dot{m}}{n}$ ($\dot{m}$ in gm/sec.)

Assume that the inlet temp. rises instantaneously in proportion to the number of passes through the system.

Therefore the average H_2O temp. is (in the series loop)

$$T_{H_2O\ \text{average}} = T_{\text{start}} + n \frac{\Delta T_{\text{rise/cell}}}{2} (1 + 2N)$$

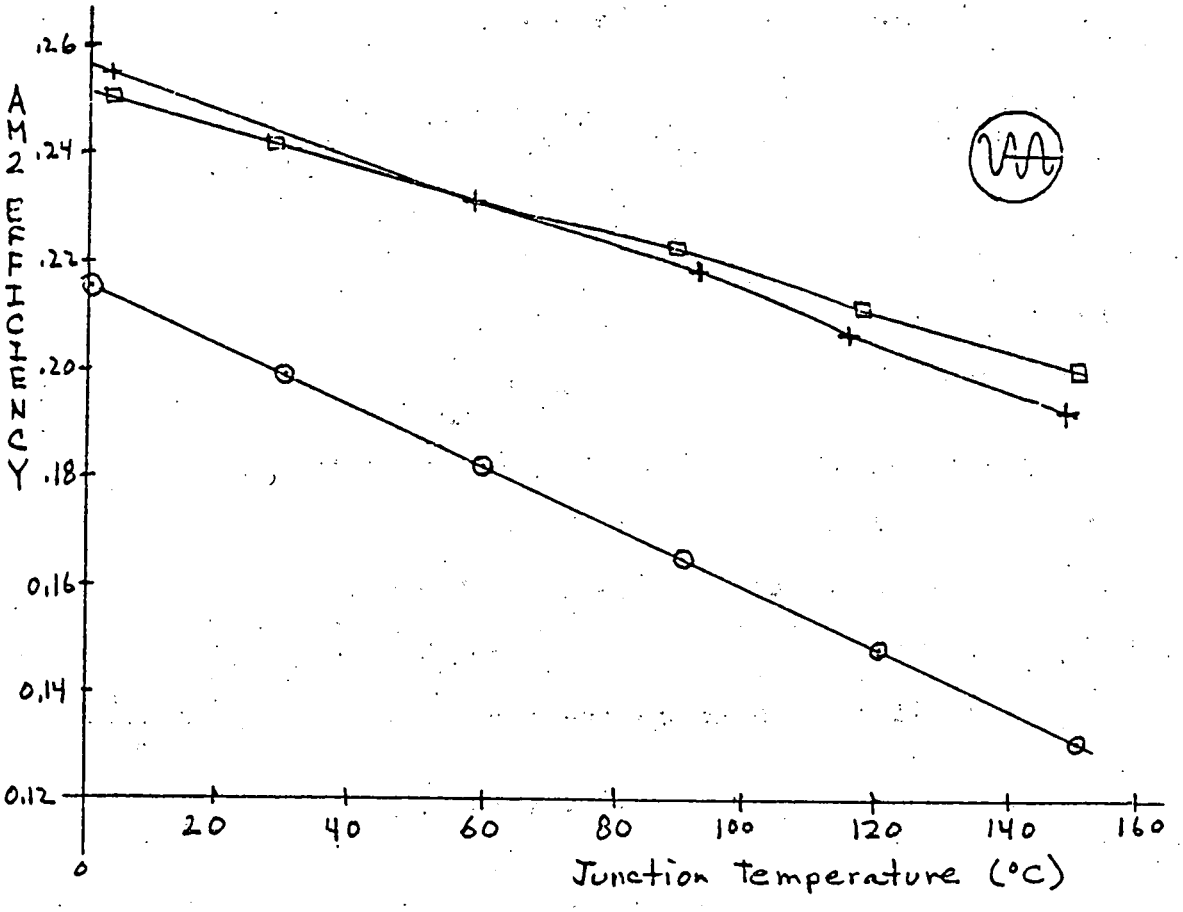

Cell Junction Temperature Power Efficiency

a) Conduction Temperature Drop

It can be shown that the temperature in the cell is nearly radially uniform (Kreith: Principles of Heat Transfer). A one dimensional analysis will then suffice

$$\Delta T = \frac{Q\ \Delta x}{\pi r_{eff}^2\ k} = \frac{Q}{\pi}\left\{\left(\frac{\Delta x}{r_{eff}^2\ k}\right)_A + \left(\frac{\Delta x}{r_{eff}^2\ k}\right)_B + \left(\frac{\Delta x}{r_{eff}^2\ k}\right)_C\right\} = 3.25°C$$

b) Boundary Layer Temperature Drop

From Walz equation (26) the average Stanton member is

$$St_{ave} = 0.47\ Re_{\ell}^{-0.434}\ Pr^{-0.64} = h_{ave}/G_{cp}$$

where

Re = Reynolds number = $G\ell/\mu$

G = mass flux at nozzle exit = $\frac{4\dot{m}}{\pi D^2}$

μ = coefficient of viscosity = .009 gm/sec-cm

Pr = Prandtl's number = 6.0

$\dot{m}$ = cooling water flow rate (gm/sec)

h_{ave} = average convective heat transfer coefficient

c_p = specific heat at constant pressure = 4.1876 $\frac{j}{gm°C}$

The temperature drop across the boundary layer is

$$\Delta T_{B.L.} = \frac{Q}{\pi \ell^2 h_{ave}} = 40.75/\dot{m}^{0.566} \quad (°C)$$

c) Water temperature rise per cell

$$\Delta T_{rise/cell} = \frac{Q}{C_p \dot{m}} = 7.165/\dot{m} \ (°C)$$

The resulting cell power loss is

$$-E_{cell} = .0154 \left[8.25 + \frac{40.75}{\dot{m}^{0.566}} + 3.583 \left(\frac{n}{\dot{m}} + 7.3\right)\right] \text{ for 25 barrels}$$

The table shows typical losses (watts/cell) for various numbers of cells in series and flow rates.

$-\dot{E}_{cell}$ $\dot{m}$ \ n	1	5	10	30	100
1	1.212	1.433	1.710	2.813	6.675
10	.706	.728	.755	.866	1.252
100	.577	.579	.582	.593	.631
1000	.542	.543	.543	.544	.548

Cooling System Flow Losses and Pressure Drops

A schematic of the cooling system for each solar array is shown below. The hydraulic losses associated with the system are: 1) Cell spot cooling, 2) Cell connecting tubing, 3) Array headers, 4) Plumbing from array headers, and 5) Barrels and Barrel headers. The dimensions of the plumbing are as shown. The sizes were selected to minimize pumping losses and fabrication costs.

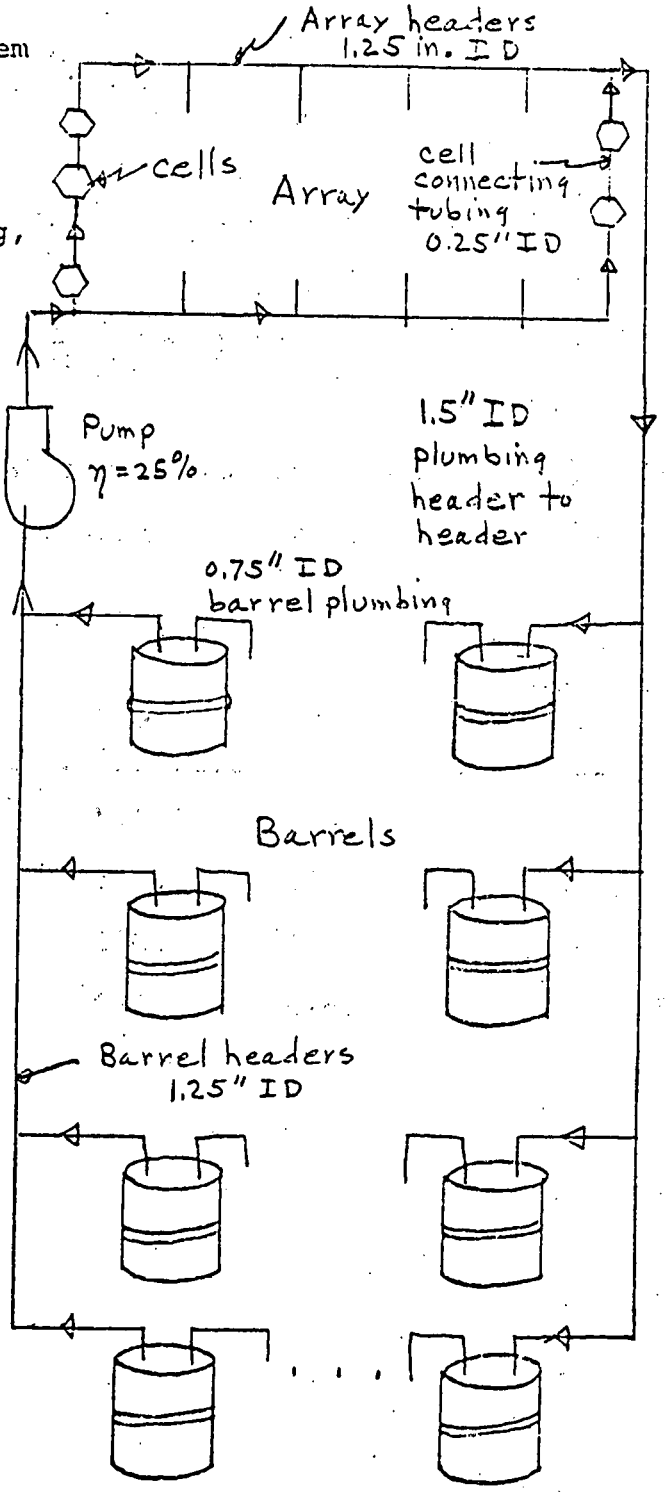

1. Cell spot cooling losses

We assume that all of the dynamic head at the cell nozzle exit is lost, thus

$$\Delta p_1 = \frac{1}{2}\frac{G^2}{\rho} = 1.27\times10^{-3}\ \dot{m}^2 \quad \text{(psi/cell)}$$

and the hydraulic energy loss is

$$\dot{E}_1 = \Delta p_1 \cdot \dot{m} = 8.78\times10^{-6}\ \dot{m}^3 \quad \text{(watts/cell)}$$

2. Cell connecting tubing losses

The cell connecting tubing consists of 12 inches of 0.25" ID smooth tubing with no elbows. The pressure and energy losses are

$$\Delta p_2 = K_2 \frac{\dot{m}^2}{d_2^{4.5}} = 2.5\times10^{-4}\ \dot{m}^2 \quad \text{(psi/cell)}$$

where

K_2 = friction factor

d_2 = tube internal diameter = 0.25"

$$\dot{E}_2 = \Delta p_2 \cdot \dot{m} = 1.74\times10^{-6}\ \dot{m}^3 \quad \text{(watts/cell)}$$

3. Array headers losses

The header on the array consists of a pipe with 440/n smoothly forged openings.

$$\Delta p_3 = \frac{K_3}{d_3^{4.5}}\frac{\dot{m}^2}{n} = \frac{1.8\times10^{-3}}{n}\dot{m}^2 \quad \text{(psi/header)}$$

$$\dot{E}_3 = \Delta p_3 \cdot \dot{m} = 1.25\times10^{-5}\frac{\dot{m}^3}{n} \quad \text{(watts/cell)}$$

where

K_3 = friction factor

d_3 = header internal diameter = 1.25"

4. Plumbing - array headers to barrel headers

$$\Delta p_4 = \frac{K_4}{d_4^{4.5}} \frac{\dot{m}^2}{n^2} = 0.383 \frac{\dot{m}^2}{n^2} \quad \text{(psi/loop)}$$

$$\dot{E}_4 = \Delta p_4 \cdot \frac{\dot{m}}{n} = 2.64\times10^{-3} \frac{\dot{m}^3}{n^3} \quad \text{(watts/cell)}$$

where

K_4 = friction factor

d_4 = plumbing internal diameter = 1.5"

5. Barrel plumbing losses

$$\Delta p_5 = \frac{K_5}{d_5^{4.5}} \frac{T}{Z^3} \frac{\dot{m}^2}{n^2} = 0.674 \frac{T}{Z^3} \frac{\dot{m}^2}{n^2} \quad (\text{psi}/T_{\text{barrels}})$$

where

K_5 = friction factor

d_5 = internal pipe diameter = 0.75"

T = total number of barrels

Z = number of rows of barrels

$$\dot{E}_5 = \Delta p_5 \cdot \frac{\dot{m}}{n} = 0.463 \frac{T}{Z^3} \frac{\dot{m}^3}{n^3} \quad \text{(watts/cell)}$$

6. Barrel header losses

$$\Delta p_6 = \frac{K_6}{d_6^{4.5}} Z \frac{\dot{m}^2}{n^2} = 0.024 Z \frac{\dot{m}^2}{n^2} \quad (\text{psi}/T_{\text{barrels}})$$

where

K_6 = friction factor

d_6 = header internal diameter = 1.25"

$$\dot{E}_6 = \Delta p_6 \cdot \frac{\dot{m}}{n} = 1.65\times10^{-4} Z \frac{\dot{m}^3}{n^3} \quad \text{(watts/cell)}$$

Combining the last two losses and minimizing the losses with respect to Z obtains for 25 barrels, 5 rows of 5 barrels each arrangement . For this optimum then the losses are

$$\Delta p_{56} = 0.255 \frac{\dot{m}^2}{n^2} \quad \text{(psi/25 barrels)}$$

$$\dot{E}_{56} = 1.75\times10^{-3} \frac{\dot{m}^3}{n^3} \quad \text{(watts/cell)}$$

The total hydraulic flow losses are

$$\dot{E}_{\text{total hydraulic loss}} = \dot{E}_1 + \dot{E}_2 + \dot{E}_3 + \dot{E}_4 + \dot{E}_{56}$$

$$= \left[10.52\times10^{-6} + \frac{1.25\times10^{-5}}{n} + \frac{4.39\times10^{-3}}{n^3}\right] \dot{m}^3 \quad \text{(watts/cell)}$$

Assuming a pump efficiency of 25% the pump power required is 1/0.25 times the total hydraulic loss. Both of these losses are shown in the following graph. The cooling system values and pressure drops at the optimum flow rates of 10 gm/sec/cell and 12.5 gm/sec/cell for n = 10 and 30, respectively, are shown in the following tables.

☆U.S. GOVERNMENT PRINTING OFFICE: 1979 640-258 1547

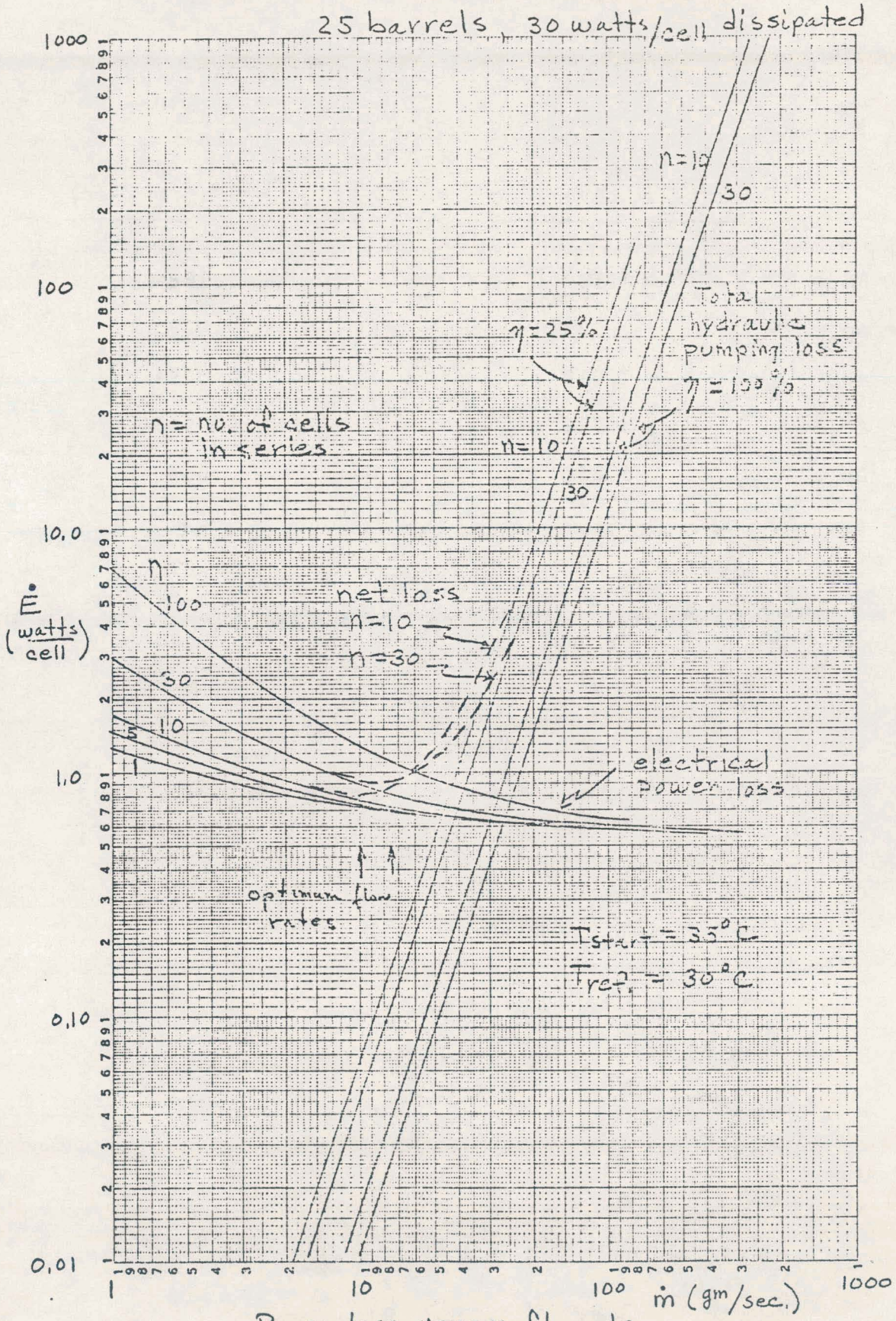

Power loss versus flowrate

PRESSURE DROPS AT OPTIMUM FLOW RATE (psi)

	n = 10 ($\dot{m}_{opt}$ = 10 gm/sec)	n = 30 ($\dot{m}_{opt}$ = 12.5 gm/sec)
Δp_1	0.127	0.198
Δp_2	0.025	0.0391
Δp_3	0.018	0.0094
Δp_4	0.383	0.0665
Δp_{56}	0.255	0.0443
Total	2.18	7.25

Cells in Series (n)	Net Loss (%)	Total Flow Rate (gpm)	Number of Passes per 12 hr day (N)	Required Pumping Power (watts)	Total Pressure Drop (psi)	$\Delta T_{B.L.}$ (°C)	$\Delta T_{rise/cell}$ (°C)	$\Delta T_{H_2O\ max}$ (°C)	$\Delta T_{H_2O\ max}$ (°F)
10	8.0	6.97	3.65	28.5	2.18	11.1	0.717	44.5	79.5
30	9.2	2.91	1.52	37.8	7.25	9.76	0.573	53.1	88.1

Note: These figures are for 25 Barrels and a pump efficiency of $\eta = 25\%$. The H_2O cooling system must absorb 30 watts/cell. The cell reference temperature is $T_{ref} = 30°C$. The H_2O starting temperature of the system is $T_{H_2O} = 35°C$.

Convection from Barrels

Assume some average amb temperature

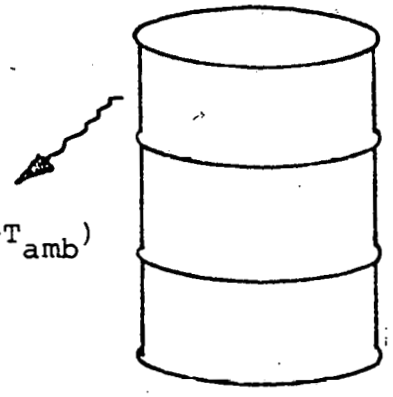

$$\dot{q} = Ab(T-T_{amb})$$

The temperature of H_2O in the barrel is

$$-M\,c\,\frac{dT}{d\tau} = \dot{q} = Ah(T - T_a)$$

Need to find T as a function of time

$$\frac{1}{(T-T_a)}\,\frac{d(T-T_a)}{d\tau} = -\frac{Ah}{mc} = -\alpha$$

$$\frac{d}{d\tau}\ell n(T-T_a) = -\alpha$$

$$\ell n(T - T_a)\Big|_{\tau=0}^{\tau=t} = -\alpha\tau\Big|_{\tau=0}^{\tau=t}$$

at t = 0 the H_2O temperature

$$\ell n\,\frac{T-T_a}{T_s-T_a} = -\alpha\tau$$

$$\frac{T-T_a}{T_s-T_a} = e^{-\alpha\tau}$$

Barrel Convection

Now $A = 20\ ft^2$

$h = 1$ BTU/hr-ft^2-°F

$c = 1$ BTU/lbm °F

$m = 55\ gal \times .1337 \frac{ft^3}{gal} \times 62.4 \frac{lb}{ft^3} = 458.86$ lbm

$\alpha = .0436/hr$

t(hr)	$(T-T_a)/(T_s-T_a)$	T(°C) T_s=80°C T_a=45°	(T_s-T) (°C)	T_s-T (°F)
1	.957	78.5	1.5	2.7
2	.9165	77.1	2.9	5.2
4	.840	74.1	5.6	10.1
8	.7056	69.7	10.3	18.5
16	.498	62.4	17.6	31.7
24	.35	57.3	22.7	40.9

Each barrel has a thermal capacity of 458.9 BTU/°F.

The total amount of thermal energy dumped into the H_2O is 5.01×10^5 BTU/day

Therefore the number of barrels required is

$$N = \frac{5.01 \times 10^5}{458.9 \times 40.9} = 26.7 \text{ barrels}$$

Heat Transfer of Barrel Array

We want to determine the change in heat transfer rate due to the barrel arrangement as opposed to the isolated barrel case.

The heat transfer for an isolated barrel is given by

$$N_{st}\, N_{pr}^{2/3}\, N_R^{0.4} = C_h$$

where C_h = 0.5 for an isolated cylinder.
(ref. Kreith, Principles of Heat Transfer, p. 411)

The empirical data for an array are shown in the following figure (ref. Kays & London, Compact Heat Exchanges).

Gas flow normal to an infinite bank of staggered circular tubes, heat transfer characteristics; a correlation of experimental data, average conductance around tube periphery. $N_{St} N_{Pr}^{2/3} = C_h N_R^{-0.4}$ $300 < N_R < 15{,}000$

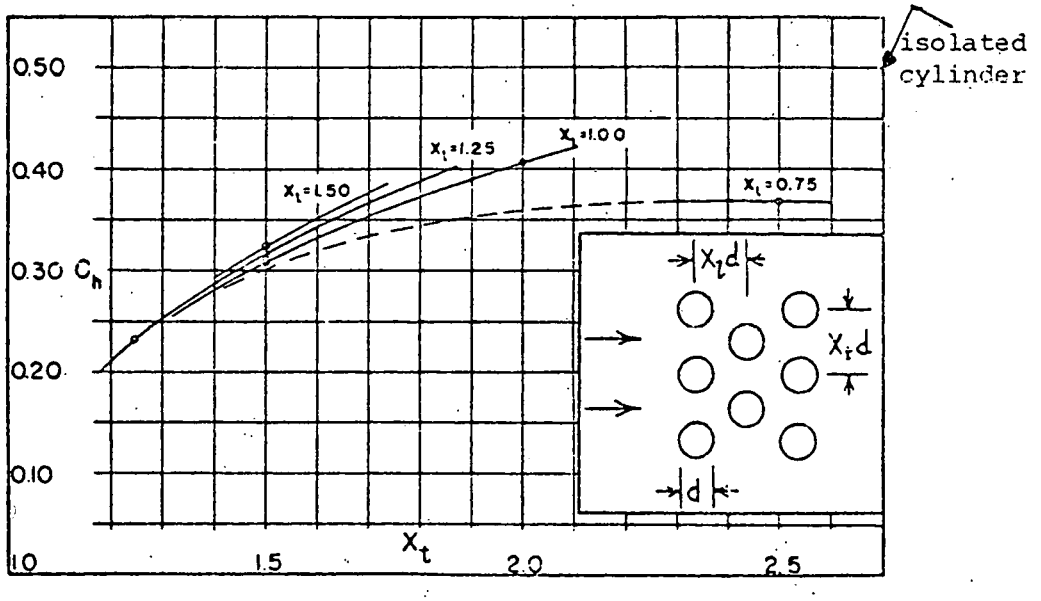

C_h = 0.50 for isolated cylinder

Flow normal to an infinite bank of staggered circular tubes, flow friction characteristics; a correlation of experimental data. $f = C_f N_R^{-0.18}$
$300 < N_R < 15{,}000$

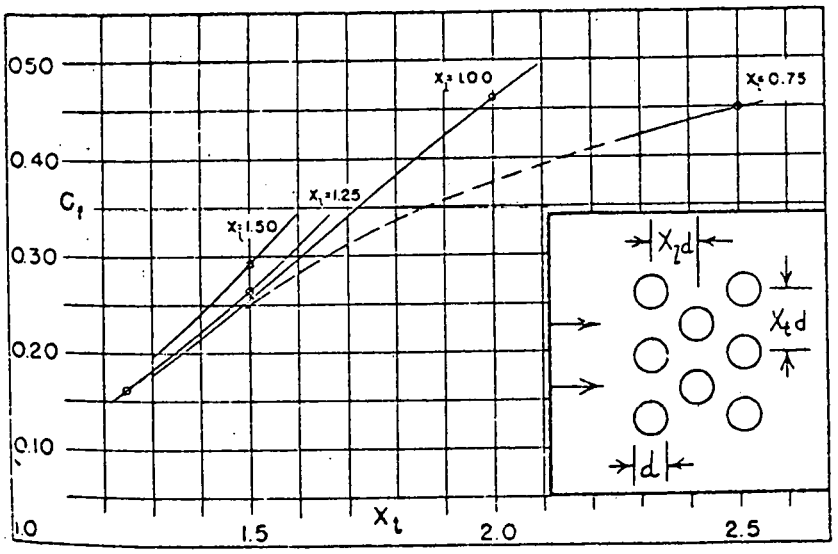

Ref. - Kays & London, " Compact Heat Exchanges".

Thus, if the barrels are spaced at least 2.5 barrel diameters apart then the array acts essentially like a set of isolated barrels.

Heat transfer of Isolated Cylinder (ref. Kreith, p. 411).

From the above figure between Reynolds number of 300 and 15000 we have

$$\log N_n = -.35 + \frac{3.60}{6} \log Re = \log .45 + \log Re^{.6}$$

$$N_n = .45\, N_R^{.6}$$

$$N_{st}\, N_R\, N_{pr} = .45\, N_R^{.6}$$

$$N_{st} = .45\, N_R^{-0.4}\, \frac{N_{pr}^{-1}}{N_{pr}^{2/3}}\, N_{pr}^{2/3}$$

$$= .45\, N_R^{-0.4}\, N_{pr}^{-2/3} \left(\frac{N_{pr}^{2/3}}{N_{pr}}\right) = 0.45\, N_R^{-0.4}\, N_{pr}^{-2/3}\, \frac{.779}{.7}$$

$$N_{st} = 0.5\, N_R^{-0.4}\, N_{pr}^{-2/3}$$

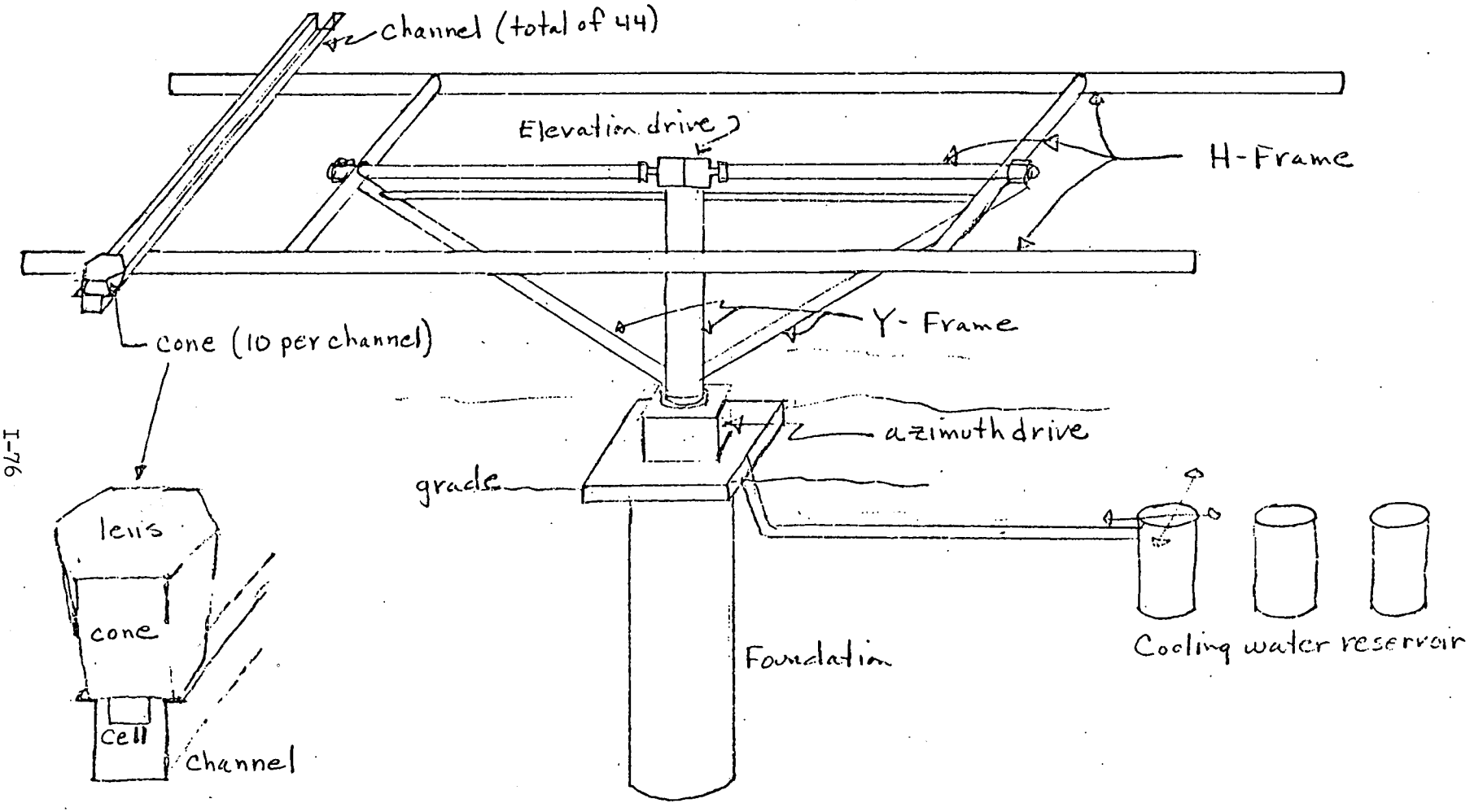

Figure 1 - Array subsystems

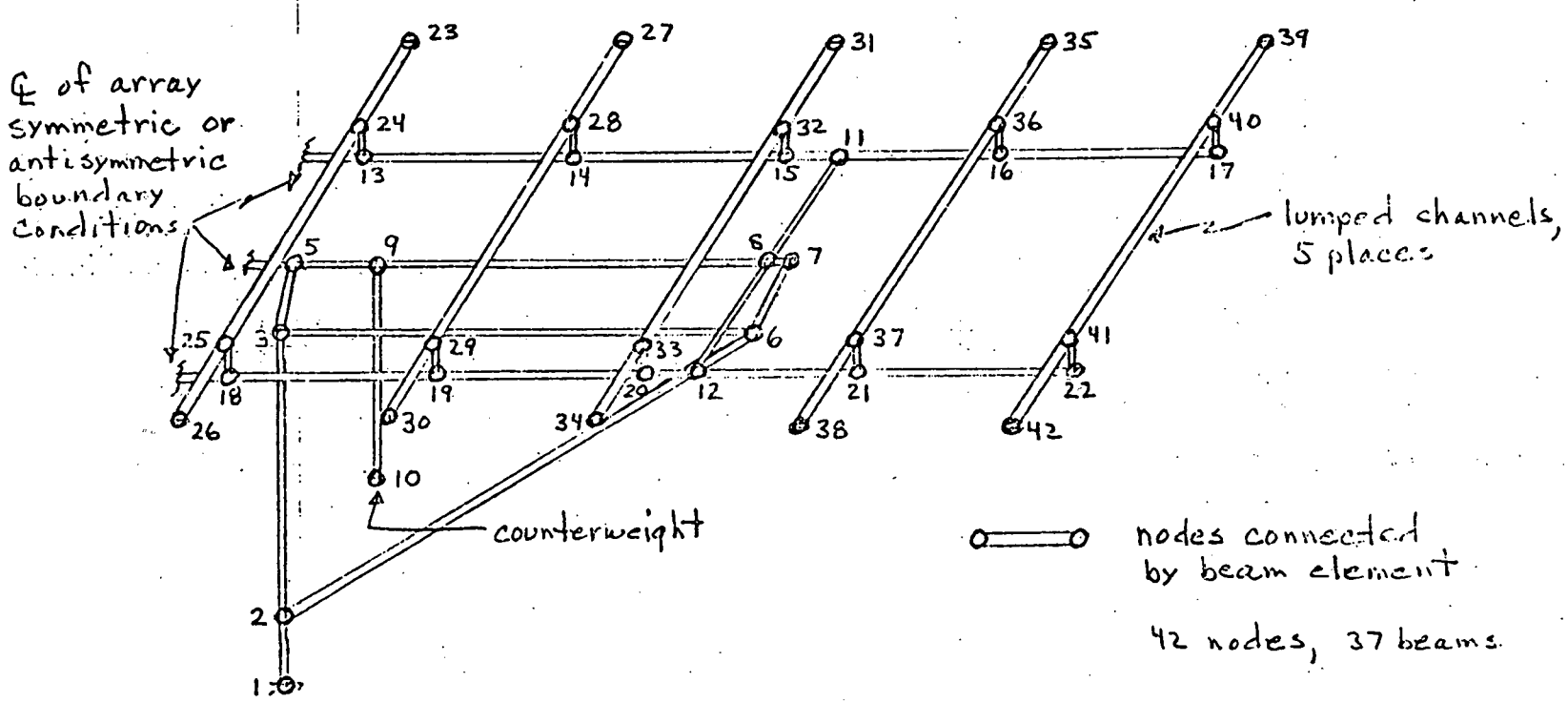

Figure 2 – Static Analysis Finite Element Model

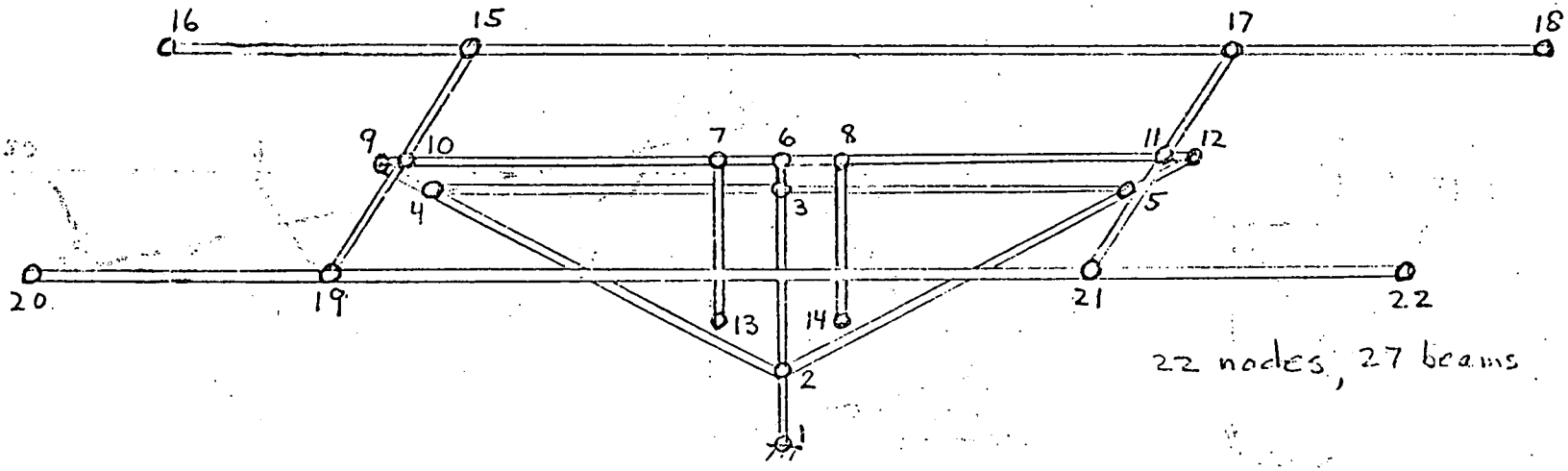

Figure 3 – Dynamic Analysis Finite Element Model

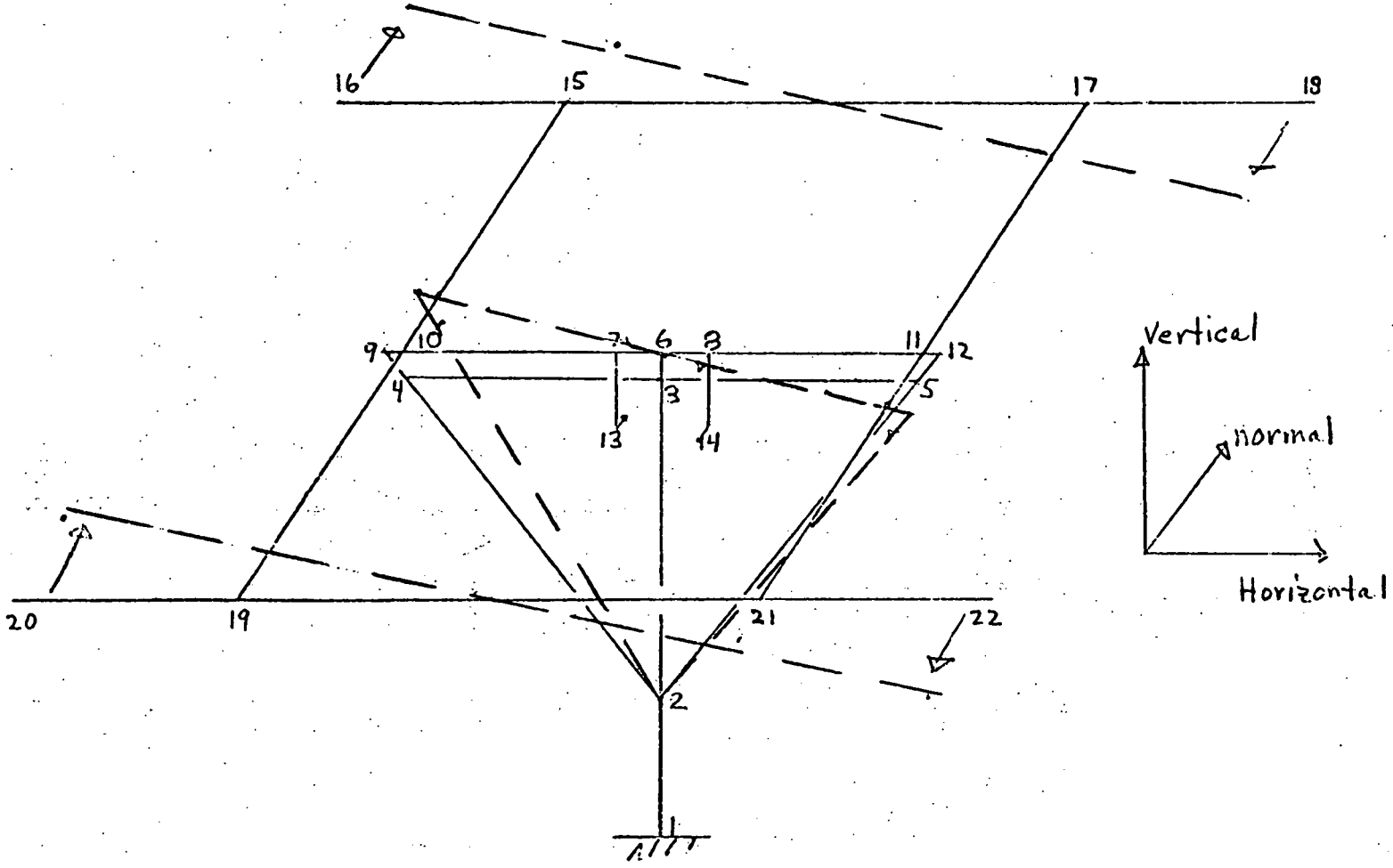

Figure 4 - Mode #1, Array horizontal, f = 2.42 Hz.

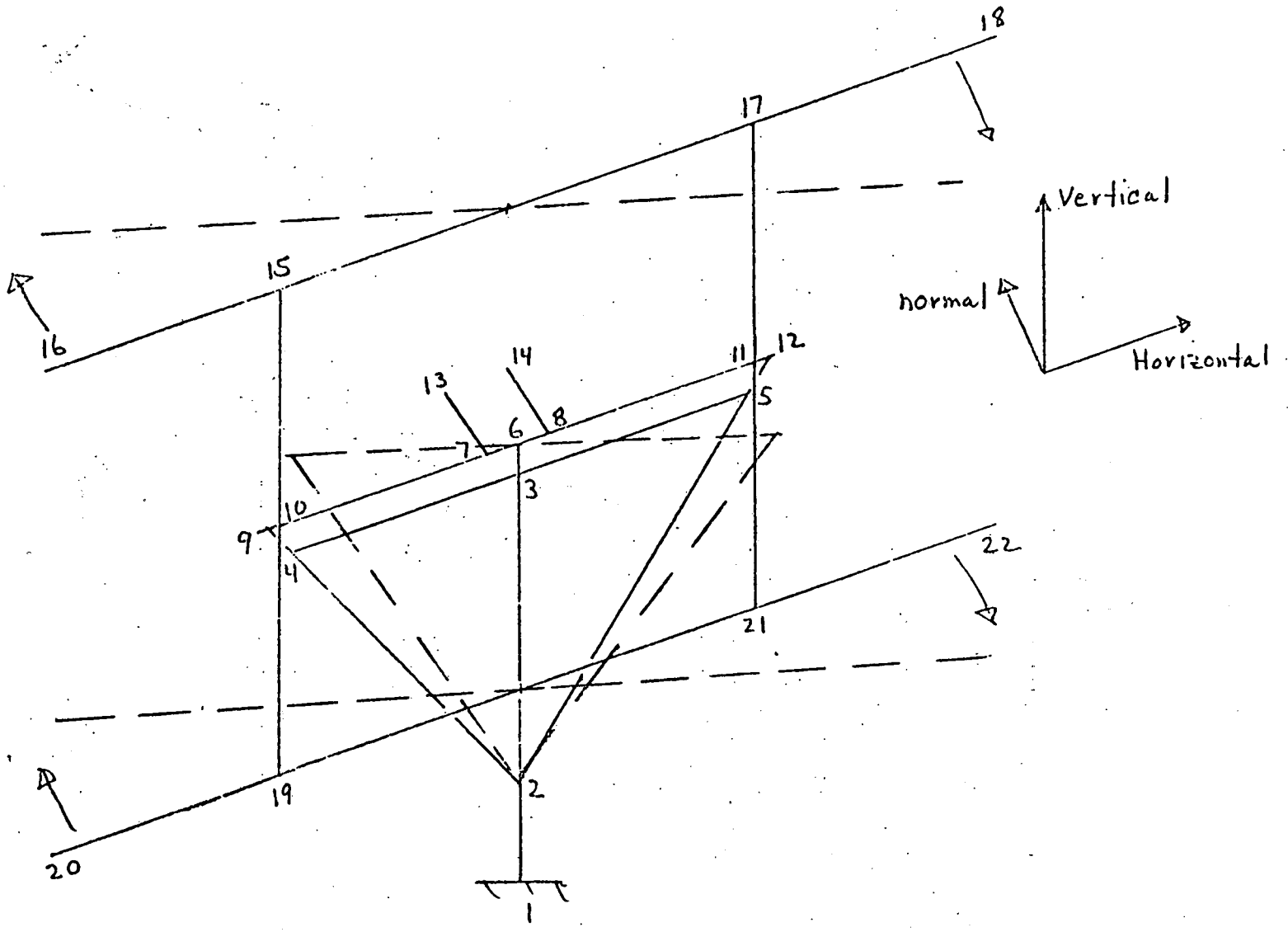

Figure 5- Mode # 2, Array Vertical, f = 2.46 Hz.

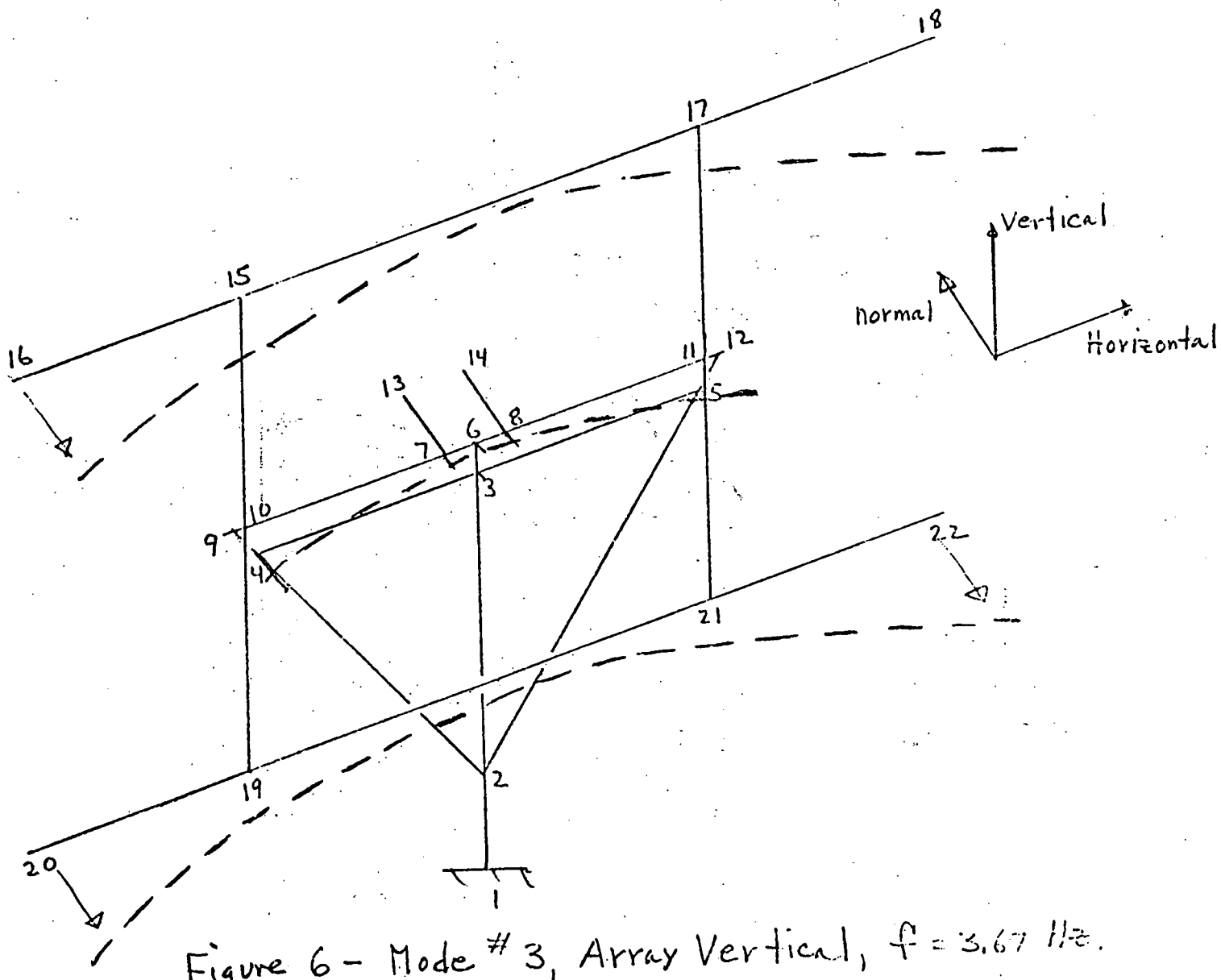

Figure 6 - Mode # 3, Array Vertical, f = 3.67 Hz.

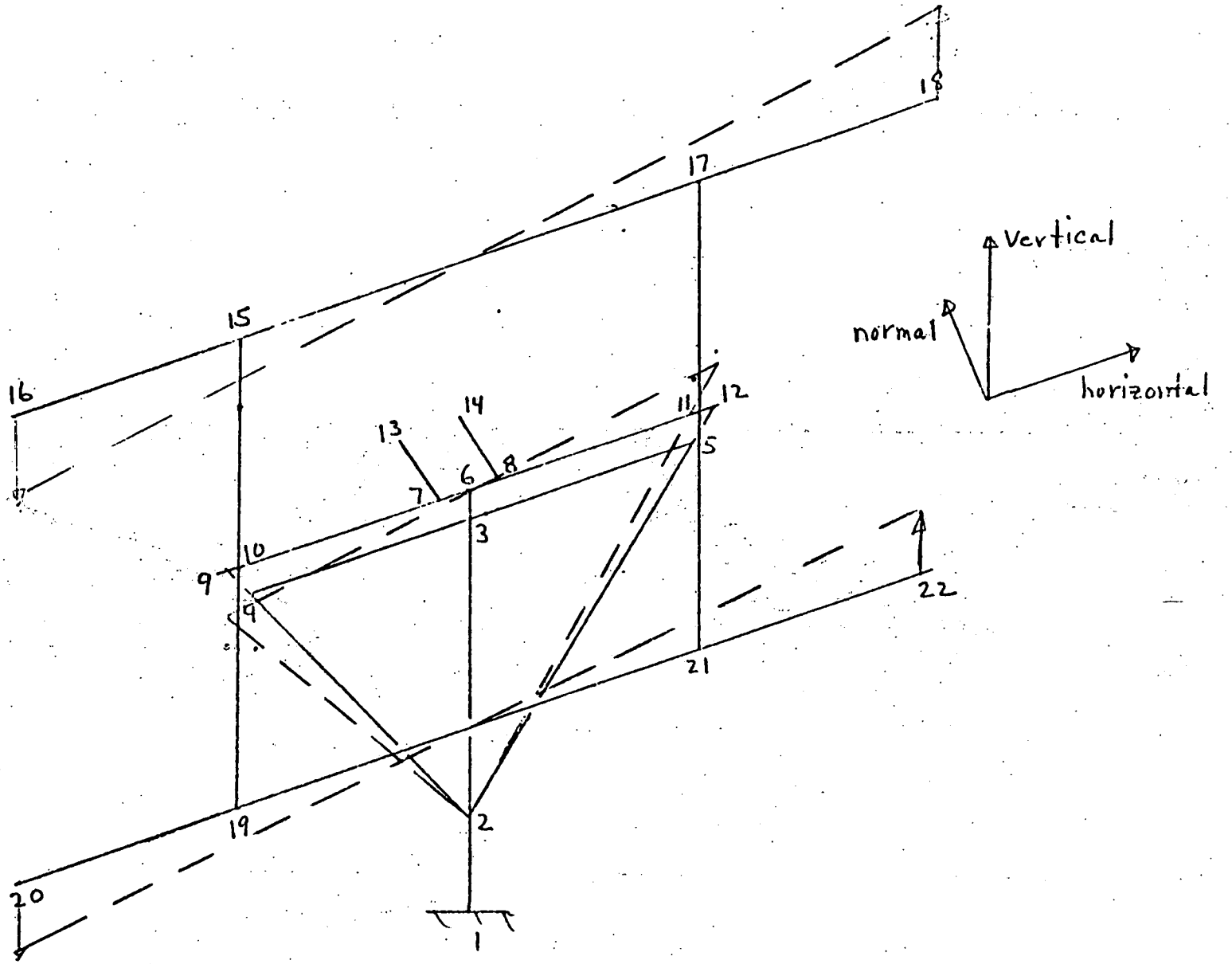

Figure 7 - Mode # 4, Array Vertical, f = 3.96 Hz.

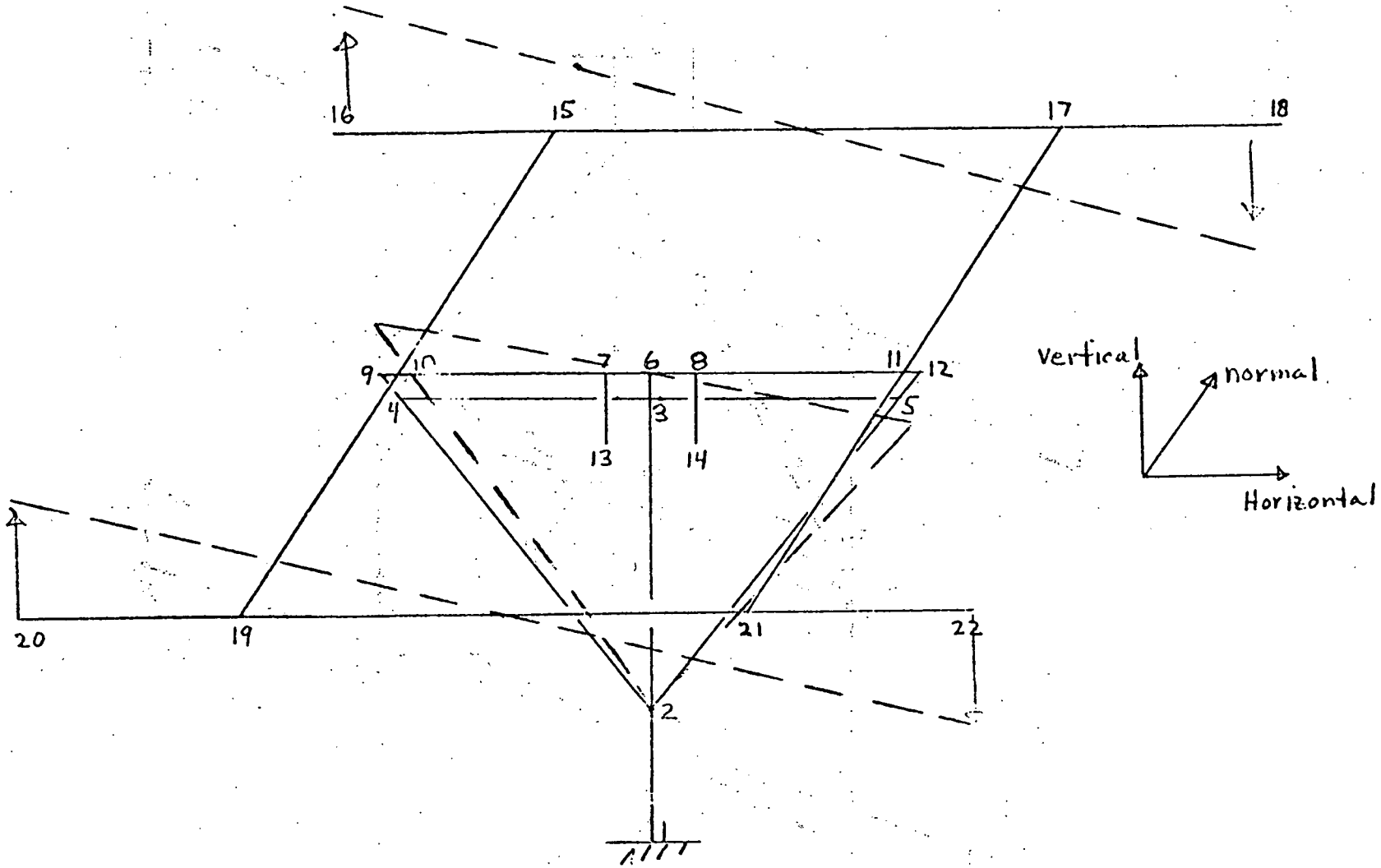

Figure 8 -- Mode # 5, Array horizontal, f = 4.03 Hz.

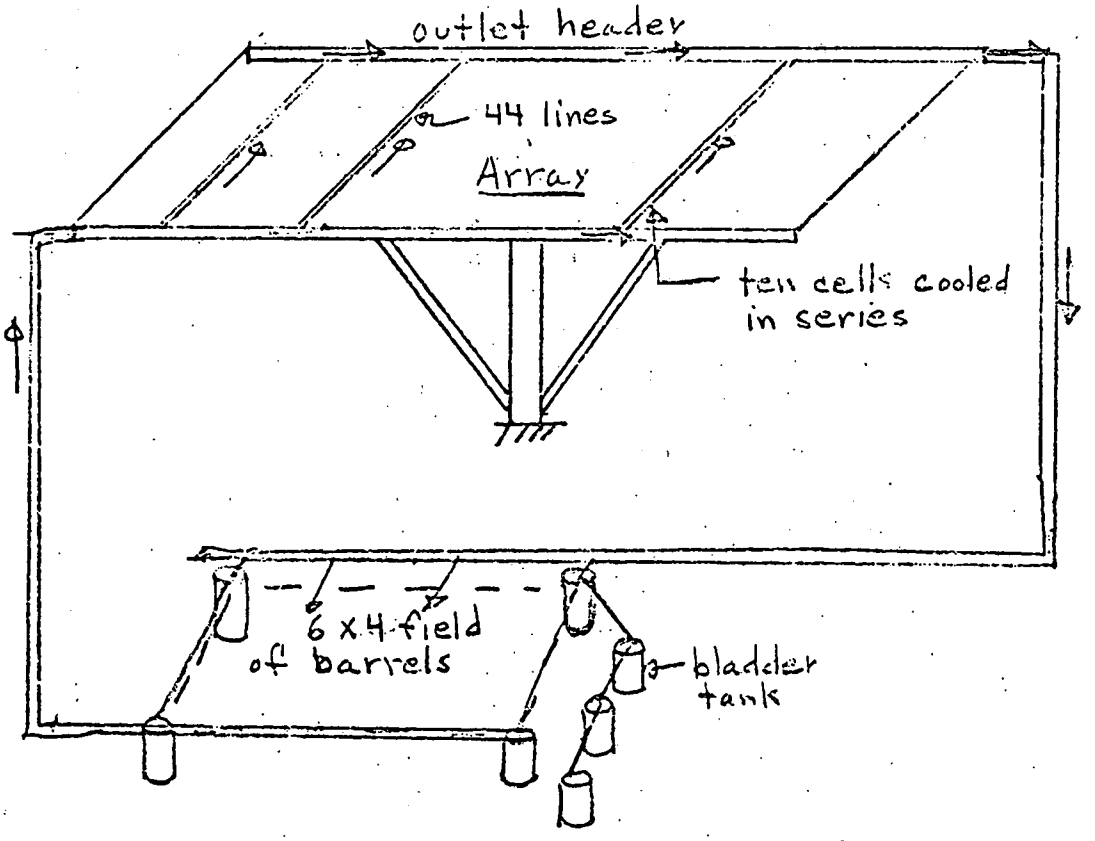

barrels covered with louvered roof to shade from sun.

Fig. 9 – Cooling system schematic

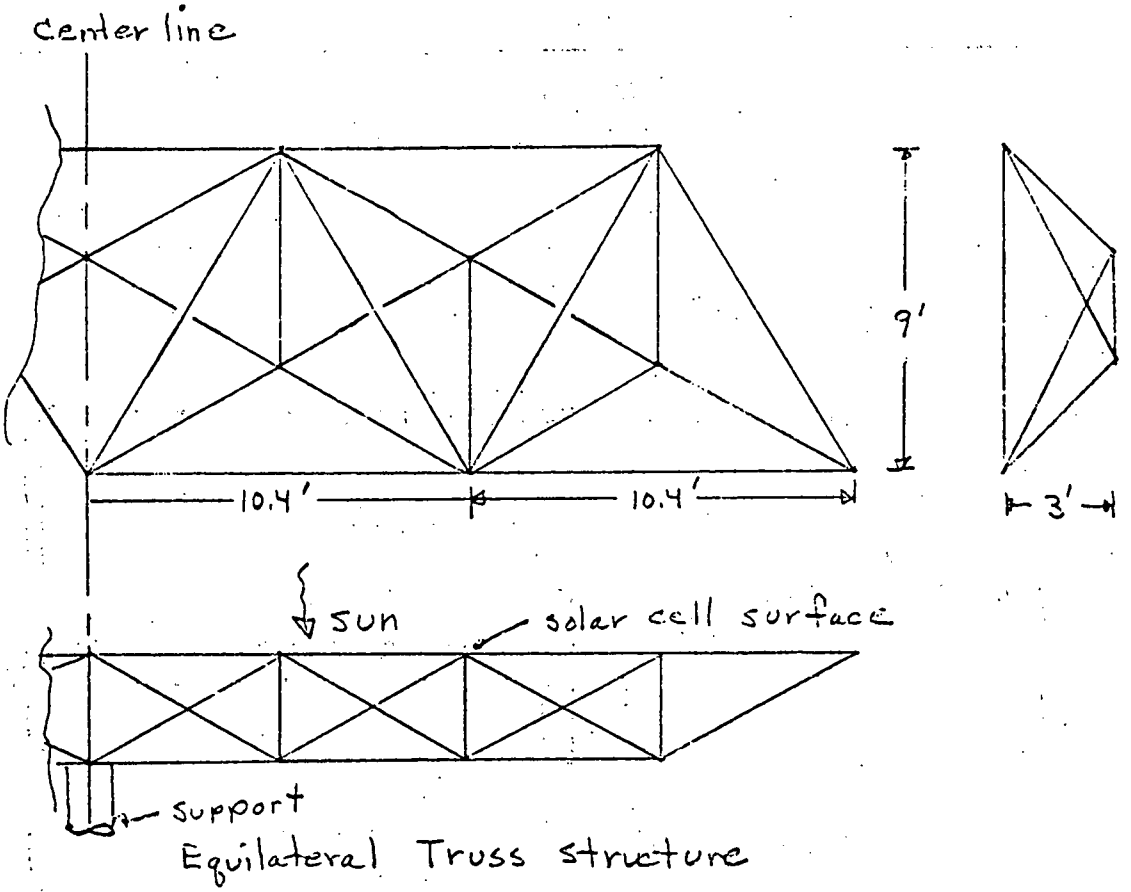

Equilateral Truss structure

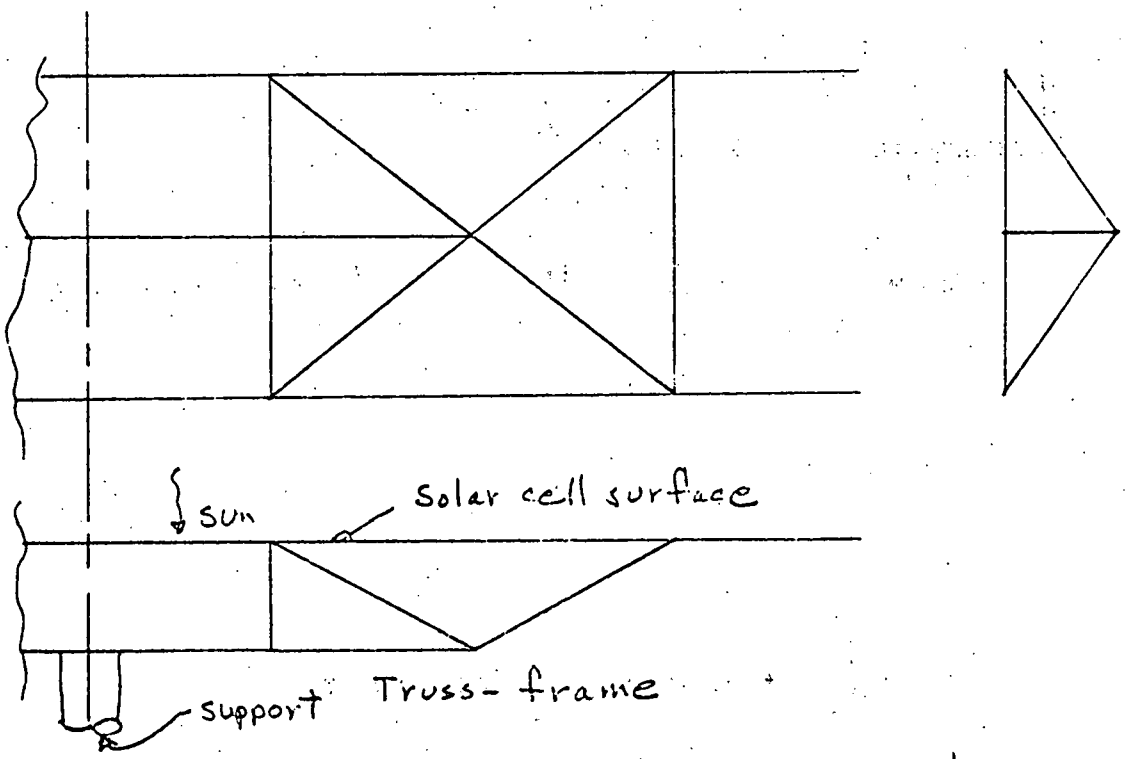

Truss-frame

Figure 10 – Alternative structures considered

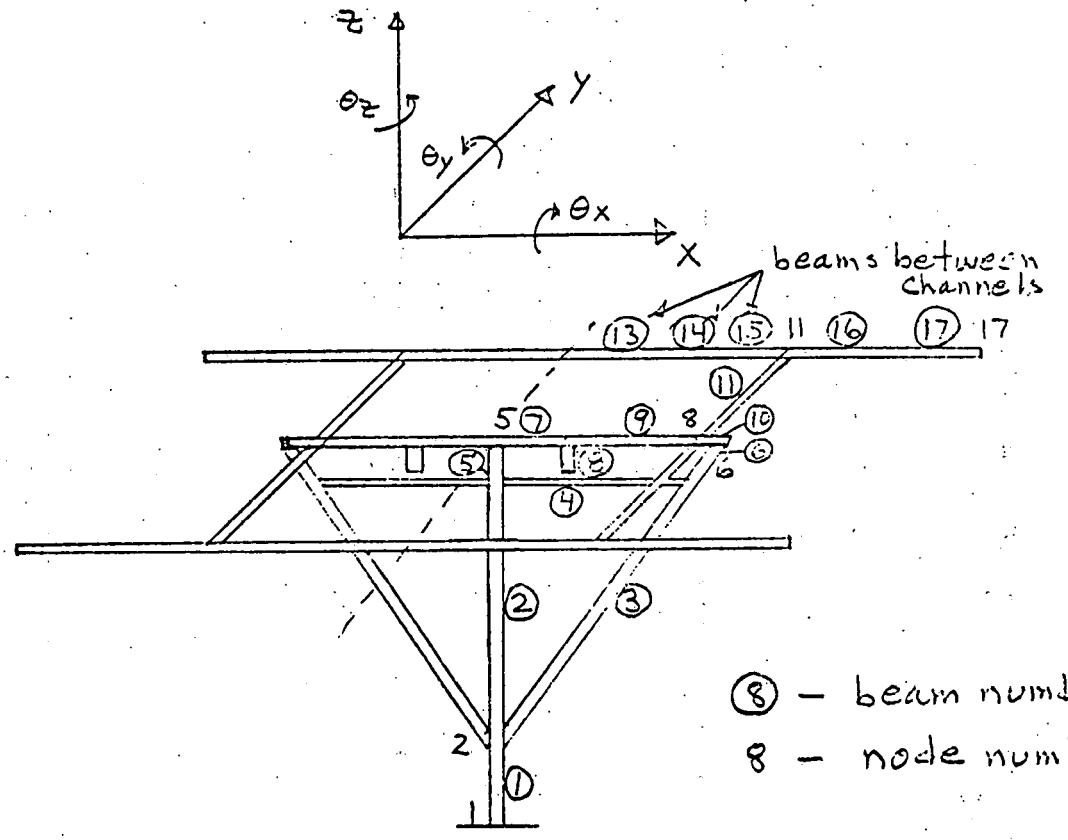

Node	Horiz. gravity			vert. gravity			60 mph wind		
	θ_x	θ_y	θ_z	θ_x	θ_y	θ_z	θ_x	θ_y	θ_z
1	0	0	0	0	0	0	0	0	0
2	0.00004	0	0	~0	0	0	−0.0005	0	0
5	0.00014	0	0	0.00014	0	0	−0.0012	0	0
6	0.00081	0.00002	−0.0003	−0.0008	−0.0004	~0	−0.0034	−0.0042	0.0011
8	0.00014	−0.00006	−0.00005	0.00017	−0.0004	−0.00001	0.00017	−0.0004	0.00008
11	0.00048	−0.00018	−0.00003	0.0001	−0.0003	0.00004	−0.0009	−0.0035	−0.00008
17	0.00043	−0.0015	~0	0.0002	−0.0003	0.0009	−0.0009	−0.0049	−0.00002

Table 1 – Rotations in radians of nodes under symmetric loading.

Beam	Horiz. gravity torsion	Horiz. gravity bending	Vert. gravity torsion	Vert. gravity bending	60 mph wind torsion	60 mph wind bending	Beam X sect. No.
1	0	10,700	0	1170	0	336,000	10
2	0	9,200	0	1810	0	193,000	10
3	2750	9,360	2,790	9160	5020	61,600	9
4	400	910	485	830	1,320	9,380	3
5	0	4,250	0	9,516	0	16,700	5
6	0	12,700	0	9,650	0	24,700	5
7	0	14,200	9,520	15,800	0	92,800	5
8	0	0	0	11,200	0	0	11
9	0	5550	1,710	7,930	0	64,750	5
10	0	9,830	0	9,580	0	3,630	4
11	2210	19,220	1,344	3,850	13,370	19,250	5
13	22	9,040	23	9,122	12	13,240	6
14	88	12,170	160	11,340	110	27,740	6
15	2460	16,150	455	15,290	2,370	31,700	6
16	670	18,360	125	14,000	730	18,400	6
17	150	6,720	50	4,930	150	6,720	6

Table 1 (concluded) – Maximum bending moments (in-lbs) in members.

Member stress:

torsion: $\tau = \frac{Mr}{I_p}$ r = radius; I_p = polar moment of inertia

bending: $\sigma = \frac{Mr}{I}$ I = moment of inertia

X sect. No.	Beam with max. stress	r/I_p $1/in.^3$	r/I $1/in.^3$	τ_{max} psi	σ_{max} psi
3	4	0.260	0.52	400	4900
4	10	0.100	0.200	0	1920
5	7	0.0862	0.172	1150	15,800
6	15	0.100	0.200	250	6,300
9	3	0.0862	0.172	450	10,600
10	1	0.0184	0.0368	0	12,400

Table 2 - stresses in beams of different cross-sectional properties.

APPENDIX J: HEAT TRANSFER COEFFICIENT OF BARRELS

To obtain an estimate for the number of barrels needed to dissipate the excess heat, tests were run to determine an approximate value of the heat transfer coefficient for a container of hot water in free air. The heat transfer was assumed to satisfy the following linear equation.

$$\frac{\Delta Q}{\Delta t} = kA\Delta T$$

where $\frac{\Delta Q}{\Delta t}$ = heat flux, BTU/hour

A = container surface area, ft^2

ΔT = average temperature difference between water and air, °F

k = heat transfer coefficient, $BTU/_{(ft.^2 - hr - °F)}$

The test results were obtained by placing a 19 inch diameter, 24 inch high (30 gal.), closed galvanized container of hot water outside in the shade. The water and ambient air temperature were monitored over a period of 24 hours. The first test was for water cooling during the night. The water was then reheated and its temperature monitored during the day. No attempt was made to monitor wind speed (which varied from still air to light wind of about 15 mph) or to separate radiative and convective heat dissipation.

The temperature variation with time is shown in Fig. 1 and the calculated values of the desired coefficient k are shown in Table 1. The surface area was taken to be the top and sides of the container ($A = 12$ ft.^{2}) and values of k were calculated using $\Delta t = 2$ hours. The heat loss is given by $\Delta Q = 30 \frac{(62.4)}{7.48} \left(T_{w_1} - T_{w_2} \right)$, where T_w is the water temperature. The initial value of k of 4.8 BTU/(ft.^{2} - hr - °F) should probably be disregarded because there may have been appreciable heat transfer through the bottom of the container into the initially cold ground. The remainder of the values of k show that k = 2 BTU/(ft.^{2} - hr - °F) is a reasonable value for these test conditions. However, the site conditions are expected to reduce the net heat transfer. The use of multiple barrels in an array under a roof (although vented) will reduce the heat transfer from radiation and forced convection. Therefore, a conservative number of k = 1 BTU/(ft.^{2} - hr - °F) was chosen to determine the number of barrels required. If this proves to be overly conservative during tests of MOD 0, the number of barrels can easily be reduced for the units installed at the site.

Time	T_w °F	$T_{w(ave.)}$ °F	T_{air} °F	ΔT °F	ΔQ BTU	k $\frac{BTU}{ft^2 - hr - °F}$
5:00 PM	145					
		131.5	73	58.5	6750	4.8
7	118					
		112	71.5	40.5	3000	3.1
9	106					
		101.5	70	31.5	2250	3.0
11	97					
		94	69	25	1500	2.5
1:00 AM	91					
		89	67	22	1000	1.9
3	87					
		85	66	19	1000	2.2
5	83					
		81	64.5	16.5	1000	2.5
7	79					
11 AM	130					
		124.5	68	56.5	2750	2.0
1:00 PM	119					
		114.5	69	45.5	2250	2.1
3	110					
		106	69.5	36.5	2000	2.3
5	102					

Table 1 - Calculation of k

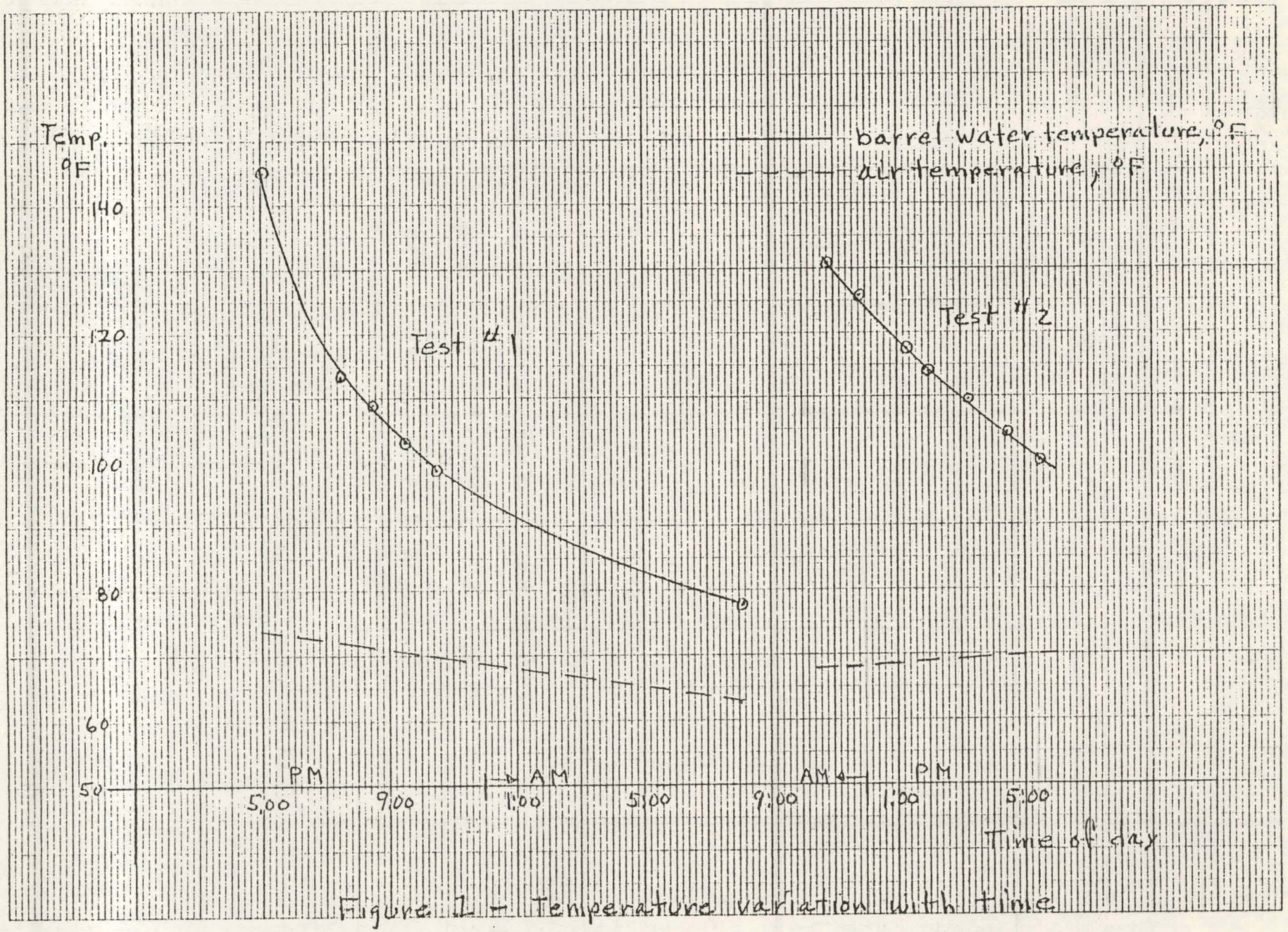

Figure 1 – Temperature variation with time.

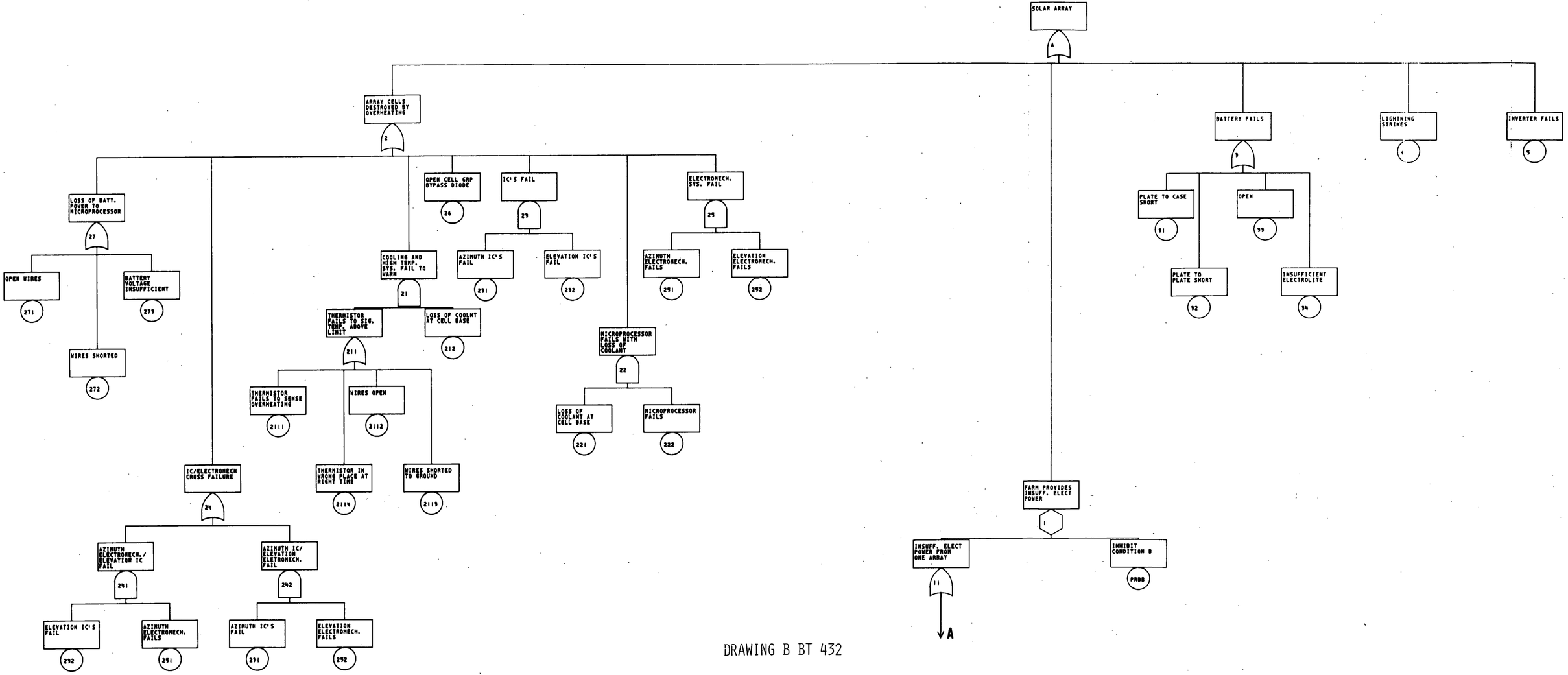

DRAWING B BT 432

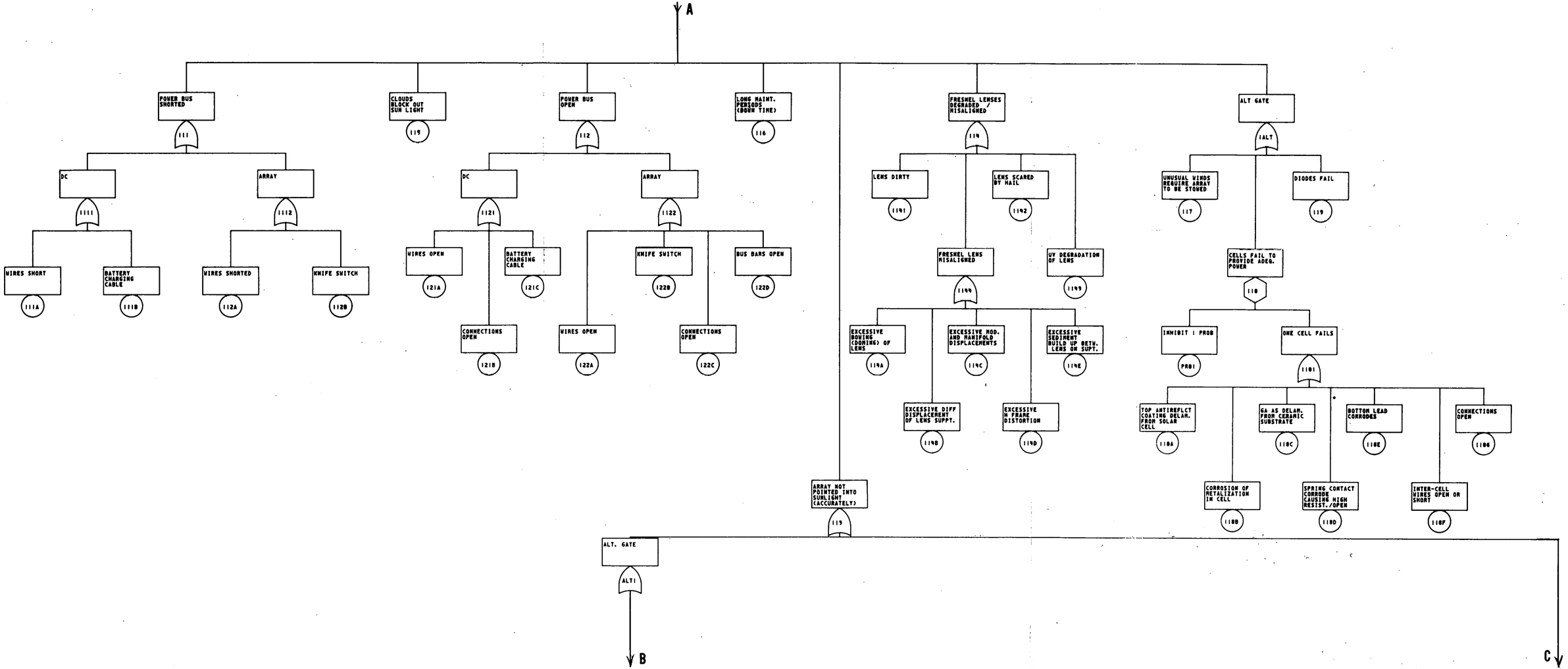

DRAWING B BT 432(CONTINUED)

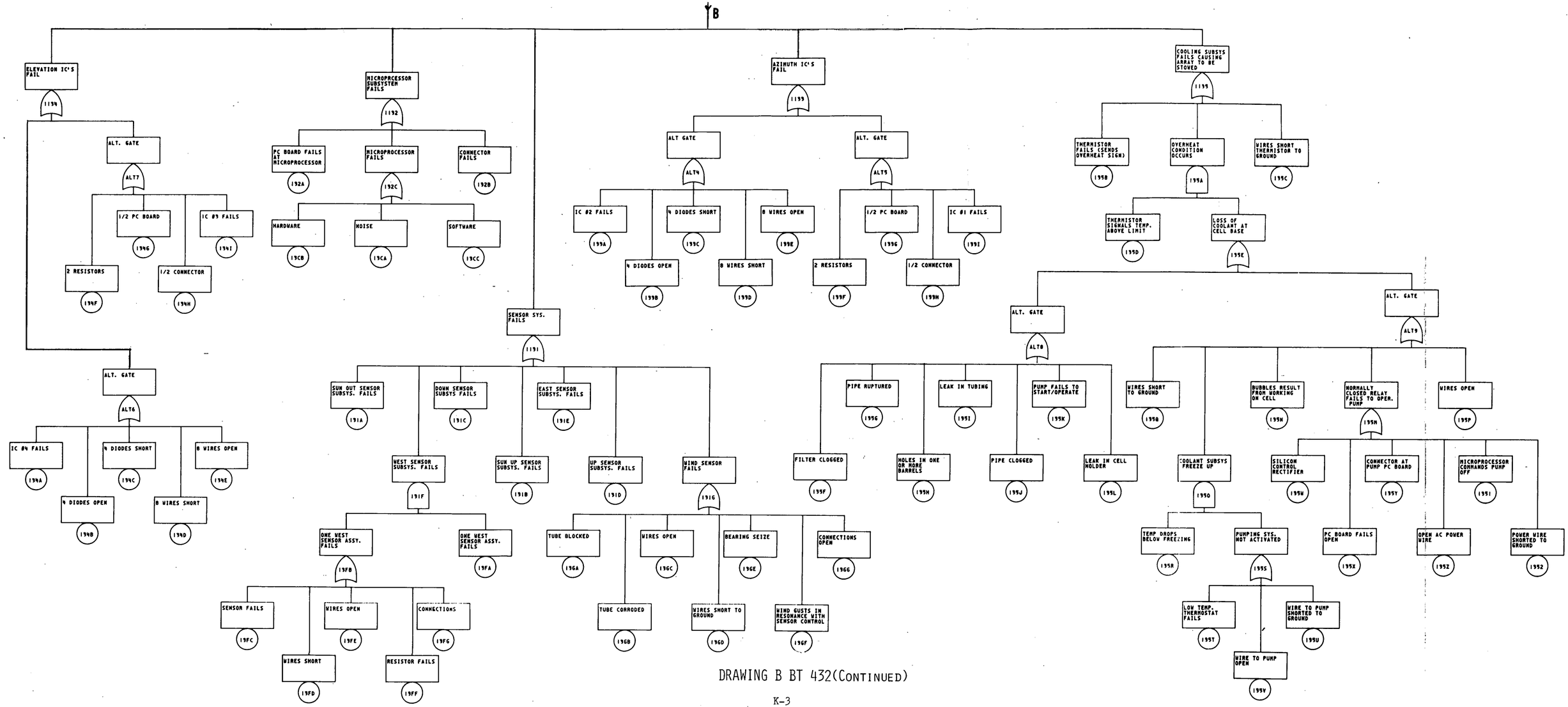

DRAWING B BT 432(CONTINUED)

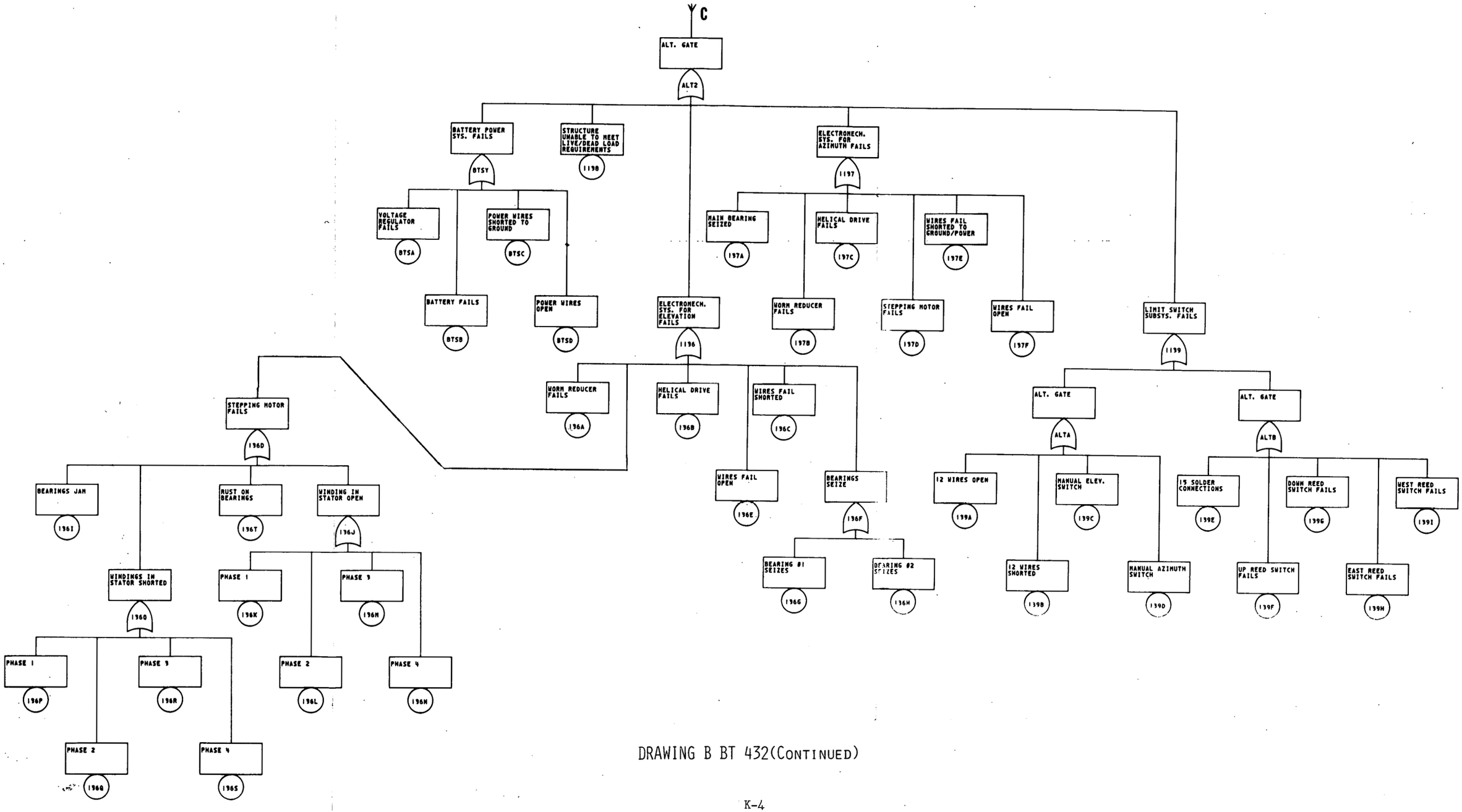

DRAWING B BT 432(CONTINUED)